Atom Probe Tomography analysis of Nb_3Sn superconducting wires for fusion reactor and particle accelerator applications



Laura Wheatley

University of Oxford

A thesis submitted for the degree of

Doctor of Philosophy

Michaelmas Term 2023

Supervisors: Professor Chris Grovenor and Professor Michael Moody

Abstract

First discovered in 1954, Nb_3Sn is a low temperature superconductor, which has had a resurgence in interest in recent years. Multiple projects, such as the Hi-Lumi upgrade to the Large Hadron Collider and the fusion reactor ITER have used Nb_3Sn superconducting magnets, and there are plans to use improved Nb_3Sn wires for a Future Circular Collider (FCC). Nb_3Sn is the second most commercially available superconductor after NbTi, which revolutionised the medical sector making MRI machines possible. However, NbTi has a maximum field of 14 T, compared to the higher maximum field of 28 T for Nb_3Sn.

The FCC target is 1500 Amm^{-2} at 16 T, much more challenging than previous applications of Nb_3Sn. To reach this target fluxons, which are 3 - 4 nm in radius in Nb_3Sn, need to be trapped at defects within the Nb_3Sn microstructure. Historically, grain refinement has been the main method of increasing the J_c by maximising the grain boundary area which can pin fluxons. Commercial Nb_3Sn wires have a grain size of $\approx$ 100 nm, however, it is difficult to reduce the grain size further and still produce a homogeneous Nb_3Sn layer with favourable superconducting properties. To increase J_c to reach the FCC target, artificial pinning centres (APCs), on the scale of the fluxons are required.

Considering the importance of the nanoscale structure on the superconducting properties of Nb_3Sn, little is known about nanoscale chemical segregation within Nb_3Sn. In this work, Atom Probe Tomography (APT) has been used to understand the nanoscale structure of two different types of Nb_3Sn wires, restacked-rod-processed (RRP®) and rod-in-tube (RIT) type wires. The first set of results focuses on a commercial RRP® wire doped with Ti and a comparative RRP® wire, irradiated at a neutron fluence of 2.82×10^{22} m^{-2} in the TRIGA II reactor. The inter-grain compositions, intra-grain compositions and any additional features such as dislocations were studied. Both RRP® samples had intra-grain compositions which were formed of two different, non-equilibrium compositions, one higher in Nb and one lower in Nb. The irradiated RRP® sample had a lower volume of high Nb compared to the as-received sample,

this suggests that irradiation induced diffusion has occurred due to the excess of vacancies produced during neutron irradiation.

The second set of results focuses on a RIT test wire which reached the high J_c requirement for the FCC. The pinning curve from this wire suggested the presence of APCs, despite no intentional source of oxygen added to the wire, to produce APCs through internal oxidation. An Electron probe micro-analyser (EPMA) and APT have been used to determine the oxygen concentration in the unreacted and reacted Nb-4Ta-1Hf (at%) alloy, with evidence of HfO_2 nanoparticles in the reacted Nb-4Ta-1Hf alloy. In a similar way to the RRP® samples, the intra-grain and inter-grain compositions of the Nb_3Sn layer have been measured, and the size and number density of HfO_2 APCs have been calculated. Additional features have been analysed, such as a residual Nb_6Sn_5 layer at the edge of the Nb_3Sn region and residual Cu rich phases trapped within the Nb_3Sn layer. Evidence of HfO_2 in the reacted Nb-4Ta-1Hf alloy and the Nb_6Sn_5 layer shows HfO_2 nanoparticles were formed prior to Nb_3Sn and that the HfO_2 nanoparticles may have acted as Zener pinning sites to reduce the grain size of the Nb_3Sn. Nb_6Sn_5 has been shown to have a higher Cu solubility than Nb_3Sn, perhaps explaining the trapped regions of Cu rich phases within the Nb_3Sn.

For future Nb_3Sn applications it is important to understand the effect of neutron irradiation and the presence of APCs on the nanoscale chemical segregation in Nb_3Sn wires in order to design Nb_3Sn with better superconducting properties. This work has shown that APT is a useful technique to analyse the nanostructure of Nb_3Sn wires.

Preface

The work presented in this Dphil has been carried out at the Department of Materials, University of Oxford from **October 2019 to November 2023** under the supervision of Professor Chris Grovenor and Professor Michael Moody. All research in this thesis is original and where the work of others has been included it has been clearly referenced and acknowledged. No part of this work has been submitted for a degree at this or any other university. Some of the work presented in this thesis has been published in peer-reviewed journals and been presented at conferences as detailed below:

Publications

C. Tarantini, F. Kumitake, S. Balachandran, S.M. Heald, **L.E. Wheatley**, C.R.M. Grovenor, M.P. Moody, Y. Su, P.J. Lee & D. Larbalestier. Origin of the enhanced Nb_3Sn performance by combined Hf and Ta doping. *Scientific Reports* 2021.

L.E. Wheatley, T. Baumgartner, M. Eisterer, S.C. Speller, M.P. Moody & C.R.M. Grovenor. Understanding the nanoscale chemistry of as-received and fast neutron irradiated Nb_3Sn RRP® wires using Atom Probe Tomography. *Superconducting Science and Technology* 2023.

Conference Presentations

L.E. Wheatley, B. Jenkins, C. Tarantini, P. Lee, D, Larbalestier, P. Bagot, S.C. Speller, M.P. Moody & C.R.M. Grovenor. *Atom Probe Tomography of doped Nb_3Sn wires*. Applied Superconductivity Conference, Tampa, Florida, U.S.A (virtual). November 2020.

L.E. Wheatley, B. Jenkins, C. Tarantini, P.J. Lee, D, Larbalestier, P. Bagot, S.C. Speller, M.P. Moody & C.R.M. Grovenor. *Atom Probe Tomography of Ti doped Nb_3Sn RRP® wires*. Applied Superconductivity seminar series (virtual). March 2021.

L.E. Wheatley, B. Jenkins, C. Tarantini, P.J. Lee, D, Larbalestier, P. Bagot, S.C. Speller, M.P. Moody & C.R.M. Grovenor. *Atom Probe Tomography of artificial pinning centres in doped Nb_3Sn wires*. European Conference on Applied Superconductivity, Moscow, Russia (virtual). September 2021.

L.E. Wheatley, B. Jenkins, C. Tarantini, P.J. Lee, D, Larbalestier, P. Bagot, S.C. Speller, M.P. Moody & C.R.M. Grovenor. *Advances in Nanoscale Analysis of Hf doped Nb_3Sn wires using Atom Probe Tomography*. Applied Superconductivity Conference, Honolulu, Hawai'i, U.S.A. October 2022.

L.E. Wheatley, T. Baumgartner, M. Eisterer, P. Bagot, S.C. Speller, M.P. Moody & C.R.M. Grovenor. *Nanoscale analysis of neutron irradiated Nb_3Sn for particle accelerator and fusion applications*. Applied Superconductivity Conference, Honolulu, Hawai'i, U.S.A. October 2022.

L.E. Wheatley, T. Baumgartner, M. Eisterer, C. Tarantini, P.J. Lee, D, Larbalestier, S.C. Speller, M.P. Moody & C.R.M. Grovenor. *Correlation of superconducting properties and nanoscale chemistry of Nb_3Sn wires using Atom Probe Tomography*. European Conference on Applied Superconductivity, Bologna, Italy. September 2023.

Awards

ESAS Best Young Researcher for Materials Awarded for the oral presentation: *Atom Probe Tomography of artificial pinning centres in doped Nb_3Sn wires*. European Society for Applied Superconductivity. September 2021.

ASC Best Student Paper for Materials Awarded for an extended abstract and oral presentation *Advances in Nanoscale Analysis of Hf doped Nb_3Sn wires using Atom Probe Tomography*. Applied Superconductivity Conference. October 2022.

Rolls Royce Prize awarded for best scientific poster titled *Understanding Nb_3Sn wires for high field and fusion applications*. Department of Materials. February 2023.

ESAS Best Young Researcher for Materials Awarded for the oral presentation: *Correlation of superconducting properties and nanoscale chemistry of Nb_3Sn wires using Atom Probe Tomography*. European Society for Applied Superconductivity. September 2023.

Acknowledgements

I would like to begin by thanking my supervisors Professor Chris Grovenor and Professor Michael Moody for providing me with the opportunity to undertake this DPhil project. Chris, you have championed my work from the very start, and you have gone above and beyond to support me throughout the DPhil. Michael, you guided me through my undergraduate course and through the DPhil, for your 8 years of support I will always be incredibly grateful. I would also like to thank Professor Susannah Speller for introducing me to superconductivity during my Master's project and for being a wonderful female role model for me throughout my time at Oxford.

I have been fortunate to work with collaborators from the National High Magnetic Field Laboratory and from the Vienna University of Technology during my DPhil. I would like to thank Chiara Tarantini, David Larbalestier and Peter Lee for their samples and thoughtful discussions throughout my DPhil. A special thank you to Shreyas Balachandran who produced some of my samples and was always willing to answer my calls when I had burning questions. I would also like to thank Michael Eisterer for providing samples and guidance, particularly on analysing superconducting measurements. It has been a pleasure to learn from world class researchers who are incredibly knowledgeable on Nb_3Sn.

Thank you to the Department of Materials, particularly DCCEM and DCMS without which this work would not have been possible. A special thank you to those staff who keep the department running, such as Philippa Moss, Rebecca Bradford and Diana Passmore and for their kindness over the years.

A huge thank you to the Atom Probe group who have made the DPhil such a wonderful experience. So many of the group I now call my friends so for that I am incredibly grateful. Paul and Christina, thank you for keeping all the equipment running, without you there would not be a functioning Atom Probe group. To Meg, you have been my college mum since day one at Trinity, thank you for guiding me for the last 8 years. Minyi, you are one of a kind, you

are so caring and funny and I will really miss you. Laura, it has been a pleasure training you and I cannot wait to see what you achieve. Ben, James D, James F, Megan, Victoria, Przemek, Martin, Yanru and Ruiying thank you for your wisdom and for the memories.

A massive thank you to the Fusion CDT and all my friends I have met through the programme. Rob, Yorick, Cyd and Arun I hope we will remain friends for life, who knew I could make such great friends with physicists. Also, thank you to the CDT programme for getting in contact with Jack Snape at GO-Science, without which, my internship and next steps would not have been possible.

Thank you to my wonderful college friends, Emma, Harry and Fabian who I will remain in touch with regardless which corners of the globe we end up living in. Michael, you are truly one of the kindest souls I have ever met, your support (and terrible dad jokes) have carried me through some of the hardest times in the Dphil, for that I will be forever grateful.

Finally, a huge thank you to my family and my long-term partner Ed, for all their love and support. Thank you to Ed for showing me the work ethic required to finish a DPhil project and for helping me to have a healthy work-life balance. To my dad for believing in me when I did not believe in myself, to my mum who always made sure I was looking after myself and to my sister who is my best friend and my biggest cheerleader.

Completing a DPhil has been an honour and an experience I will cherish for the rest of my life. If I could advise my younger self, I would say to worry less, work hard and surround yourself with wonderful people, and you will be surprised how much you can achieve.

Acronyms

$\Delta\kappa$ Ginzburg-Landau parameter

Γ_i Gibbsian Interfacial Excess

χ Susceptibility

AES Auger Electron Spectroscopy

APCs Artificial Pinning Centres

APT Atom Probe Tomography

$\mathbf{B}_{c2}$ Upper Critical Field

BCC Body Centred Cubic

BCS Bardeen Cooper Schreiffer

BSE Back Scattered Electrons

$\mathbf{d}_{eff}$ Effective Filament Diameter

DFT Density Functional Theory

DOS Density of States

EDX Energy Dispersive X-ray Spectroscopy

EPMA Electron Probe Micro-Analyser

EXAFS Extended X-ray Absorption Fine Structure

$\mathbf{F}_L$ Lorentz Force

$\mathbf{F}_p$ Pinning Force

$\mathbf{F}_p^{MAX}$ Maximum Pinning Force

FCC Future Circular Collider

FIB Focused Ion Beam Microscope

FWHM Full-width-half-maximum

$\mathbf{H}_{irr}$ Irreversibility Field

Hi-Lumi LHC High Luminosity upgrade to the Large Hadron Collider

HR-STEM High Resolution Scanning Transmission Electron Microscopy

isosurface Iso-concentration surface

IT Internal-tin

ITER International Thermonuclear Experimental Reactor

IVAS Integrated Visualisation and Analysis Software

$\mathbf{J}_c$ Critical Current Density

LEAP Local Electrode Atom Probe

LME Local Magnification Effect

LRO Long Range Order

LTS Low Temperature Superconductor

m/q Mass-to-charge-state ratio

MagLab National High Magnetic Field Laboratory

MSM Maximum Separation Method

N$_D$ Mean Number Density

PIT Powder-in-tube

RIT Rod-in-tube

RRP® Restacked-rod-process

RRR Residual Resistivity Ratio

SE Secondary Electrons

SEM Scanning Electron Microscope

SQUID Superconducting quantum interference device

SRF Superconducting Radio Frequency

T$_c$ Critical Temperature

TEM Transmission Electron Microscopy

Contents

Acronyms **ix**

1 Literature Review **1**

1.1 Introduction to Superconductors 1

1.1.1 Pinning and J_c 4

1.2 Nb_3Sn 5

1.2.1 Phases and Structure 7

1.2.2 Ordering and Lattice Variation 10

1.2.3 Maximising the Pinning Force 12

1.3 Pinning Mechanism for Nb_3Sn wires 14

1.4 Wires and their Methods of Fabrication 17

1.4.1 The Bronze Process 19

1.4.2 Powder-in-tube 19

1.4.3 Internal-tin Method 20

1.4.4 Restacked-rod-process 21

1.5 Ternary Phases and Heat Treatment 24

1.6 Titanium and Tantalum Additions 27

1.7 Artificial Pinning Centres 30

1.8 Radiation Induced Defects 35

1.9 Microstructural Analysis 38

2 Materials and Experimental Methods **47**

2.1 Materials 47

2.2 Characterisation Techniques . . . 48
2.2.1 Scanning Electron Microscopy . . . 48
2.2.2 Energy Dispersive Spectroscopy . . . 49
2.2.3 Electron Probe Micro-analyser . . . 49
2.2.4 Focused Ion Beam Microscope . . . 49
2.3 Atom Probe Tomography . . . 54
2.4 APT Parameter Selection . . . 57
2.4.1 Laser Energy . . . 57
2.4.2 Temperature . . . 59
2.4.3 Pulse Frequency . . . 60
2.4.4 Detection Rate . . . 61
2.5 APT Artefacts . . . 61
2.5.1 Local Magnification Effect . . . 61
2.5.2 Segregation to Crystallographic Poles . . . 62
2.5.3 Asymmetry of Laser Illumination . . . 64
2.5.4 Multiple Hit Detector Events . . . 64
2.5.5 Compound Ions . . . 65
2.5.6 Non-homogeneous Evaporation . . . 66
2.6 APT Data Analysis Techniques . . . 67
2.6.1 Peak Identification and Ranging . . . 67
2.6.2 Composition Analysis . . . 69
2.6.3 Concentration Profiles and Proxigrams . . . 69
2.6.4 Gibbsian Interfacial Excess . . . 71
2.6.5 Solute Cluster Analysis . . . 74
2.6.6 Cluster Analysis Method . . . 75

3 RRP®: A Comparison of As-received and Neutron Irradiated Samples 80

3.1 Superconducting Results . . . 81
3.1.1 Calculating T_c . . . 81

3.1.2 F_p . . . 82
3.1.3 Estimated B_{c2} . . . 85
3.2 Sample Preparation for Atom Probe Tomography . . . 87
3.3 Atom Probe Tomography Experimental Parameters . . . 89
3.3.1 Reconstruction Parameters . . . 89
3.4 Results from Atom Probe Tomography: As-received Sample . . . 90
3.4.1 Intra-grain Compositional Analysis . . . 90
3.4.2 Grain Boundary Concentration Profiles . . . 95
3.4.3 Gibbsian Interfacial Excess . . . 96
3.4.4 Additional Features of Interest . . . 101
3.5 Results from Atom Probe Tomography: Irradiated sample . . . 107
3.5.1 Intra-grain Compositional Analysis . . . 107
3.5.2 Grain Boundary Concentration Profiles . . . 108
3.5.3 Gibbsian Interfacial Excess . . . 108
3.5.4 Additional Features of Interest . . . 112
3.6 Comparison of As-received and Irradiated results . . . 117
3.6.1 Overall Composition . . . 117
3.6.2 Grain Boundary Segregation . . . 119
3.6.3 Additional Features of Interest . . . 121
3.7 Discussion . . . 123
3.8 Conclusions . . . 127

4 APC RIT Sample **128**

4.1 Pre-heat Treatment Nb-4Ta-1Hf Alloy . . . 131
4.1.1 EPMA . . . 131
4.1.2 Atom Probe Tomography . . . 133
4.2 Reacted Nb-4Ta-1Hf alloy . . . 138
4.2.1 EPMA . . . 139
4.2.2 Atom Probe Tomography . . . 142

4.3 APT analysis methods for the Nb_3Sn Layer . . . 146
4.3.1 Identifying the Nb_3Sn . . . 146
4.3.2 Atom Probe Tomography Experimental Parameters . . . 147
4.3.3 Ranging the Mass-to-charge-state Spectra . . . 147
4.3.4 Peak Overlaps in the Mass-to-charge-state Spectra . . . 152
4.3.5 Cluster Analysis Considerations . . . 154
4.4 Analysis from the Nb_3Sn Layer . . . 157
4.4.1 Intra-grain Compositional Analysis . . . 157
4.4.2 Grain Boundary Concentration Profiles . . . 162
4.4.3 Gibbsian Interfacial Excess . . . 164
4.5 Solute Cluster Analysis from the Nb_3Sn Layer . . . 169
4.5.1 Number Density and Size of HfO_2 Clusters . . . 169
4.5.2 Location of HfO_2 Clusters . . . 172
4.6 Residual Cu Rich Phases . . . 178
4.7 Carbon and Nitrogen Rich Particles . . . 182
4.8 Overall Composition of the Nb_3Sn . . . 183
4.9 Residual Nb_6Sn_5 . . . 186
4.9.1 Intra-grain Compositional Analysis . . . 188
4.9.2 Number Density and Size of HfO_2 Clusters . . . 192
4.10 Linking Cluster Properties to Superconducting Properties . . . 194
4.11 Discussion . . . 197
4.11.1 Pre- and Post-heat treatment Nb alloys . . . 197
4.11.2 Nb_3Sn . . . 199
4.11.3 HfO_2 Clustering . . . 201
4.11.4 Residual Cu Rich Phases . . . 202
4.11.5 Nb_6Sn_5 . . . 202
4.11.6 Linking Cluster Properties to Superconducting Properties . . . 203
4.12 Conclusions . . . 204

5 Conclusions **205**

5.0.1 Intra-grain Compositional Analysis 206

5.0.2 Inter-grain Compositional Analysis 206

5.0.3 Overall Nb_3Sn composition 207

5.0.4 Summary 208

6 Future Work **209**

6.1 RRP® and Neutron Irradiation 209

6.2 Optimising APC Wires 210

Chapter 1

Literature Review

1.1 Introduction to Superconductors

A superconductor is defined as a conductor which has zero resistance below T_c. Heike Kamerlingh Onnes first discovered superconductivity in 1911 when he cooled mercury with liquid helium [1] and later went on to win the Nobel prize for his work in 1913. A superconductor is defined by three critical parameters: T_c, J_c and B_{c2}. These three parameters can be used to define a critical surface, below which the material is a superconductor and above which the material is in the normal state, as seen in Figure 1.1.

There are two different types of superconductor: type I and type II superconductors, as shown by their magnetisation in Figure 1.2. The surface currents induced in a superconductor are in the opposite direction to the applied field, hence the magnetisation of superconductors is negative, as shown in Figure 1.2. Type I superconductors display the Meissner effect, behaving as perfect diamagnets by expelling all magnetic field until T_c when the material becomes 'normal' and flux penetrates straight through the material, these only have one upper critical field B_c. An example of a type I superconductor is pure aluminium with a $T_c = 1.2$ K and $B_c = 0.01$ T, however in practice type I superconductors are not used for commercial applications as they cannot tolerate impurities and have a low critical field. A type II superconductor displays the Meissner effect up to a certain critical field (B_{c1}) when magnetic flux then penetrates through

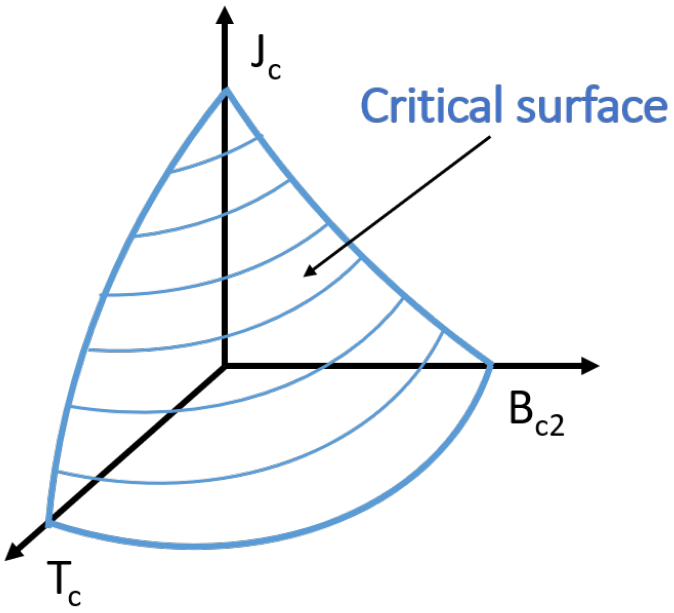


Figure 1.1: Critical surface of a type II superconductor

the material in discrete fluxons. As the field increases towards B_{c2} the number of fluxons increase as more of the material becomes 'normal' until B_{c2} where the material is no longer in the superconducting state. The direction of the current is perpendicular to the field and the motion of the fluxons as seen in Figure 1.3, this must not be confused with the screening current which is produced around each fluxon.

There are two different types of type II superconductor: LTS and high temperature superconductors (HTS). LTS properties are determined by BCS theory, which was first published in 1957 [2] and later won a Nobel prize in 1972. The theory states that superconductivity is possible via Cooper pairs. Below T_c electrons close to the Fermi level become unstable, therefore the electrons can overcome the Coulomb potential forming pairs approximately 100 nm apart which are held together by phonon interactions. This is due to an electron in the lattice attracting a positive ion, which distorts the lattice and attracts an electron with the opposite spin, the two electrons then become correlated (evidenced by the isotope effect shown by two groups in 1950 [3, 4]). A valid mechanism for HTS has not yet been discovered, however the mechanism for LTS took 46 years from first discovery of superconductivity, so as HTS

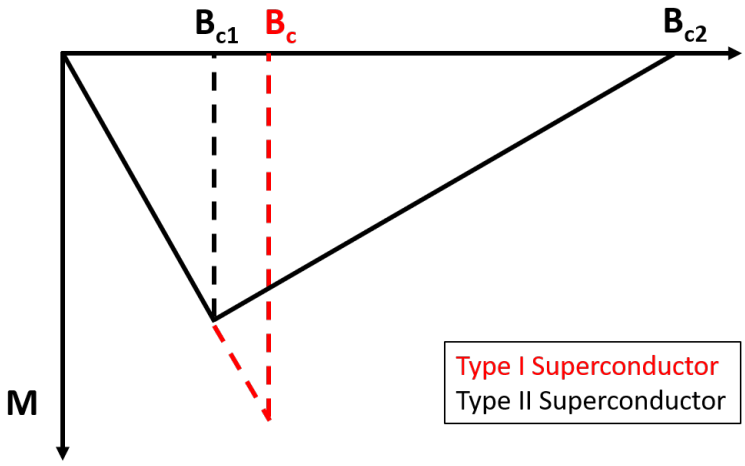


Figure 1.2: Magnetisation against $B_{applied}$ for type I and type II superconductors. The Meissner effect is displayed up to the B_c for type I and B_{c1} for type II superconductors with $B_{c1}<B<B_{c2}$ showing the mixed state. The relative sizes of B_c to B_{c1} are purely for diagrammatic purposes.

superconductors were first discovered in 1986 [5] we may be waiting until at least 2032 for an answer. The LTS with the highest T_c is magnesium diboride with a T_c of 39 K, however at extreme pressure (150 GPa), H_2S has been shown to have a T_c of 203 K (the highest T_c ever recorded) and follow BCS theory [6]. A conventional HTS has a T_c larger than the temperature of liquid nitrogen (77 K), this enables less energy to be lost in cooling than that for an LTS which uses helium at 4.2 K. Also nitrogen is far more abundant in the atmosphere than helium, which is a scarce resource. HTS materials can trap larger fields than conventional LTS materials, with the world record for the largest trapped field set by a REBCO magnet at Florida State University, recording 45.5 T in 2019 [7]. Despite the benefits of HTS materials their development is years behind that of LTS materials, they are currently very expensive and difficult to process in large quantities with no HTS materials used in commercial magnets. The next stage in developing higher field commercial magnets therefore lies in optimising LTS materials, such as Nb_3Sn, to increase B_{c2} and J_c to meet challenging requirements, such as a next generation particle collider [8].

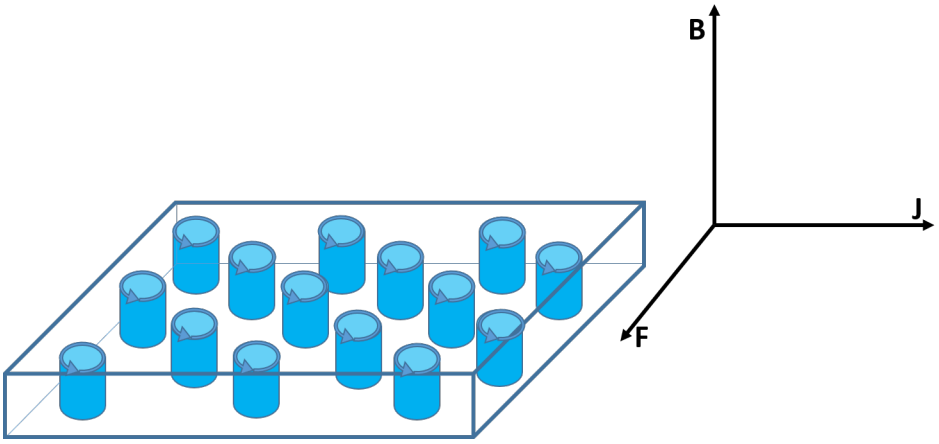


Figure 1.3: Vortices penetrating a type II superconductor in the mixed state. The screening current around each vortex shown with dark blue arrows.

1.1.1 Pinning and J_c

Nb_3Sn is operated in the mixed state between B_{c1} and B_{c2}. At B_{c1} flux penetrates the material in quantised fluxons ($\phi_0 = h/2e$, where ϕ_0 is a fluxon, h is Planck's constant and e is the charge of an electron), originally called Abrikosov vortices. These vortices only penetrate the material to a skin depth which is determined by the London penetration depth (approximately 65 - 89 nm for Nb_3Sn [9]). For schematic simplicity in Figure 1.3 the vortices are shown to penetrate through the material.

A F_L is produced orthogonal to both the field and current, as shown in Figure 1.3. Without an opposing force, the F_L produced would cause all the trapped flux to leave the material and the superconductor would return to the 'normal' state. To maintain the superconducting state an opposing F_p is needed:

$$F_L = J \times B_{c2} = -F_p \tag{1.1}$$

J is the current density and B_{c2} is the upper critical field. When the F_L is applied to individual vortices the force per unit length can be written as $F_L = J \times \Phi_0$. The force at a given location between two vortices is due to the field around one vortex and the current density arising from the neighbouring vortex. F_L acts to expel vortices out of the material, therefore

a pinning force is required. If F_L is temporarily large (e.g increase in temperature) then flux creep will occur, this is where vortices move a short distance before re-pinning. Additionally, the flux lines can de-pin via thermal activation causing flux flow and expelling the vortices from the superconductor.

A pinning force is a short-range force which acts to pin the core of the vortex in place. There are many types of defect which can provide a pinning force including: point defects (e.g. vacancies), screw dislocations, inclusions, intra- or inter-granular non-superconducting regions, grain boundaries or dopants. The effectiveness of pinning relates to the coherence length of the material and the size of the pinning defect. The coherence length is the correlated distance from superconducting material to the normal material. In a mixed state superconductor the coherence length is the radius of a vortex, and for maximum pinning a defect should be twice this length. The pinning force is material dependent and therefore the properties of Nb_3Sn are vital in our understanding of pinning behaviour.

1.2 Nb_3Sn

Superconductivity in Nb_3Sn was first reported in 1954 by Matthias *et al* [10] to have a T_c of 18.05 $\pm$ 0.1 K, only the second superconducting A15 phase (explained in section 1.2.1) to be discovered, a year after V_3Si in 1953 [11]. The highest reported T_c for pure Nb_3Sn was 18.3 K in 1964 [12], however the average T_c is commonly quoted as 18.1 K. Historically Nb_3Sn has been second in commercial applications to NbTi, which is less brittle and therefore far easier to process. However, NbTi has a maximum B_{c2} value of $\sim$ 14.4 T at 0 K, whereas Nb_3Sn can have a B_{c2} of up to $\sim$ 28 T at 0 K [13].

Nb_3Sn has been selected as the chosen superconductor for the tokamak ITER, the Hi-Lumi LHC and for a FCC. The first large scale project to utilise this higher B_{c2} in Nb_3Sn was the Hi-Lumi LHC [14] which was specified to increase the field from 8.3 T using old NbTi wires, to 11 T using Nb_3Sn, hence increasing the number of ion-ion collisions by a factor of three [15, 16]. Nb_3Sn has also been selected for the toroidal field coils in ITER to meet the design requirement of an operating field of 11.8 T [17]. During 2008 to 2015 there was a 10 fold

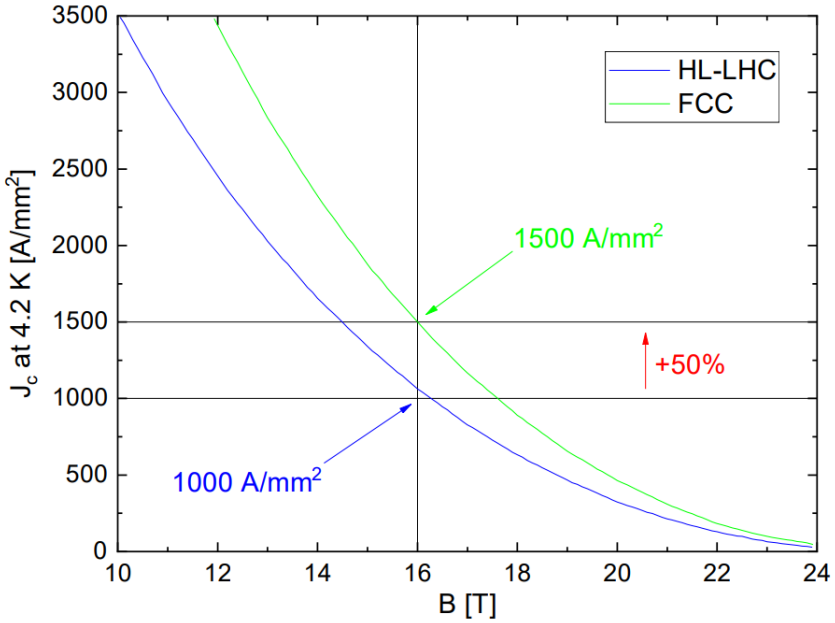


Figure 1.4: Comparison of the J_c required for the FCC compared to the Hi-Lumi LHC [20]

increase in production of wires to produce the Nb_3Sn required for ITER [18]. Most recently, Nb_3Sn has been selected as a primary choice for a FCC, which will need $>$ 16 T magnets with a J_c $= 1500$ Amm^{-2} (at 4.2 K) to be able to reach the 100 TeV required [19]. The increase in J_c required from Hi-Lumi LHC to the FCC requirement can be seen in Figure 1.4. The highest performing Nb_3Sn wires, at preliminary research stage, do meet some of the FCC requirements, however further microstructural understanding is needed to commercially produce these wires.

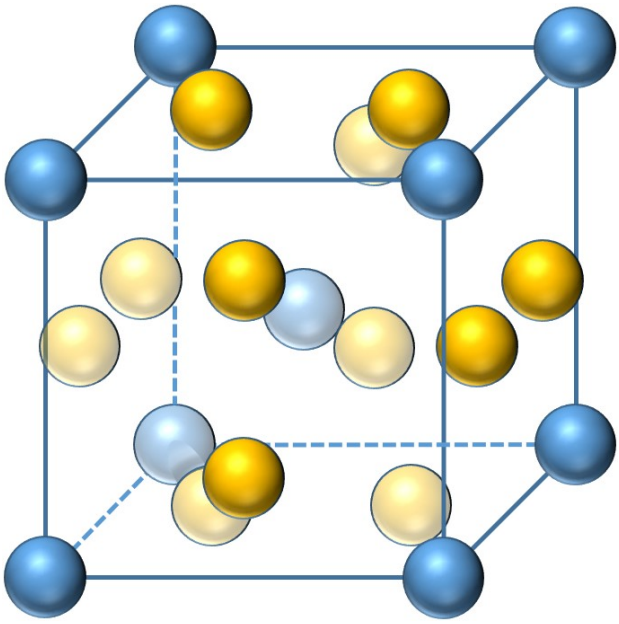


Figure 1.5: Nb_3Sn A15 crystal structure with niobium in yellow and tin in blue

1.2.1 Phases and Structure

Nb_3Sn has a cubic A15 crystal structure (A_3B) with a lattice parameter of 0.529 nm containing Sn in a BCC structure at (0,0,0) and (1/2, 1/2, 1/2) and two Nb atoms at each face centre (0, 1/2, 1/4), (0, 1/2, 3/4), (1/2, 1/4, 0), (1/2, 3/4, 0), (1/4, 0, 1/2) and (3/4, 0, 1/2), as shown in Figure 1.5.

The crystal structure is based on the superconductor Nb, which exists as either a BCC structure ($T_c \sim 9.2$ K) or metastable Nb_3Nb, with the same A15 structure as Nb_3Sn, which has a $T_c \sim 5.2$ K [21]. The location of Nb and Sn within Nb_3Sn structure greatly affects the DOS and therefore the T_c values. When there is a deficiency in Sn, vacancies are produced on the B site which are then filled by Nb atoms, this can cause a rounding off of the DOS and therefore a lower T_c. As a result Nb will produce a second broader d-band, which will be at the expense of electrons in the Nb chain [22, 23]. The change in DOS caused by a deficiency in Sn from the ideal 3:1 ratio is the largest cause of reduction in the superconducting properties of binary Nb_3Sn wires.

In this work, Nb_3Sn will be referred to as Nb_3Sn, however, the A15 structure has a range of compositions. Nb_3Sn is more precisely $Nb_{1-\beta}Sn_\beta$ where $\sim 0.18 < \beta < 0.25$ [24]. The

other two Nb-Sn phases are the line compounds Nb_6Sn_5 and $NbSn_2$ at $\beta = 0.45$ and 0.66 respectively. $Nb_{1-\beta}Sn_\beta$ can superconduct anywhere within the range of $0.18 < \beta < 0.25$, however higher T_c and J_c values are reported closer to $\beta = 0.25$ [25] due to the DOS reduction from stoichiometry. This phase band is according to the widely accepted phase diagram by Charlesworth *et al* from 1970, which has been adapted by A. Godeke in Figure 1.6. Nb_3Sn can be formed from an Nb-Sn melt above 930 °C or from solid state reactions between Nb, Nb_6Sn_5 and $NbSn_2$ at lower temperatures [26]. The phase diagram shows a dashed line in the Nb_3Sn region as there is substantial evidence to suggest that nucleation of the Nb_3Sn phase is more favourable at lower temperatures, tending to produce a curved solidus rather than the original straight one [27–29], however the exact detail of the curved solidus is somewhat speculative. The inset diagram in Figure 1.6 displays a tetragonal phase between $0.245 < \beta < 0.252$, by a shear transformation below $\sim$ 43 K with a c/a ratio $\sim$ 1.0026-1.0042 [22, 30–33]. Both Nb_2Sn and Nb_6Sn_5 are superconducting with $T_c < 2.68$ K [34] and $T_c < 2.8$ K respectively [35, 36]. These phases, although superconducting, are not desirable in the matrix as their superconducting temperatures are below that of liquid helium (4.2 K). Any residual Nb_6Sn_5 or $NbSn_2$ in Nb_3Sn wires due to incomplete reaction reduces the size of the A15 area and can reduce the J_c produced [37].

The effect of Sn content on T_c and B_{c2} in Nb_3Sn is highly irregular compared to other A15 compounds. All A15 compounds ($A_{1-\beta}B_\beta$) have a linear relationship with B content (at%) and T_c or B_{c2}, apart from $Nb_{1-\beta}Sn_\beta$ and $V_{1-\beta}Si_\beta$ where T_c and B_{c2} level off at $\beta = 0.25$, as seen in Figure 1.7. Both the T_c [24, 38, 39] and B_{c2} [24, 39–43] relationship with Sn concentration can be seen from Figure 1.7 with B_{c2} showing a peak at 24 at% before a drop off in pure Nb_3Sn (the clean limit).

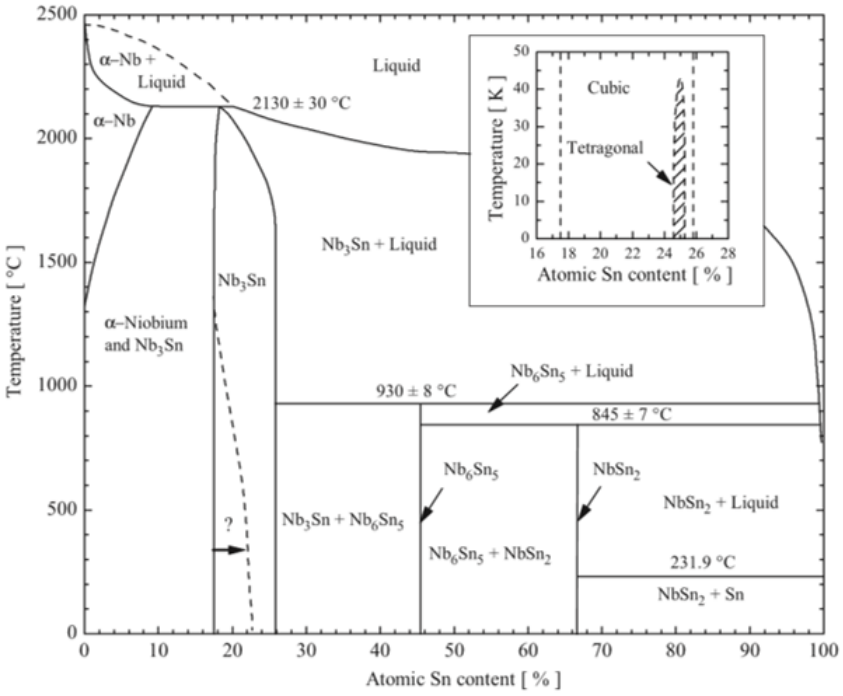


Figure 1.6: Nb-Sn phase diagram originally from Charlesworth *et al* 1970 [44] adapted by A.Godeke [26]

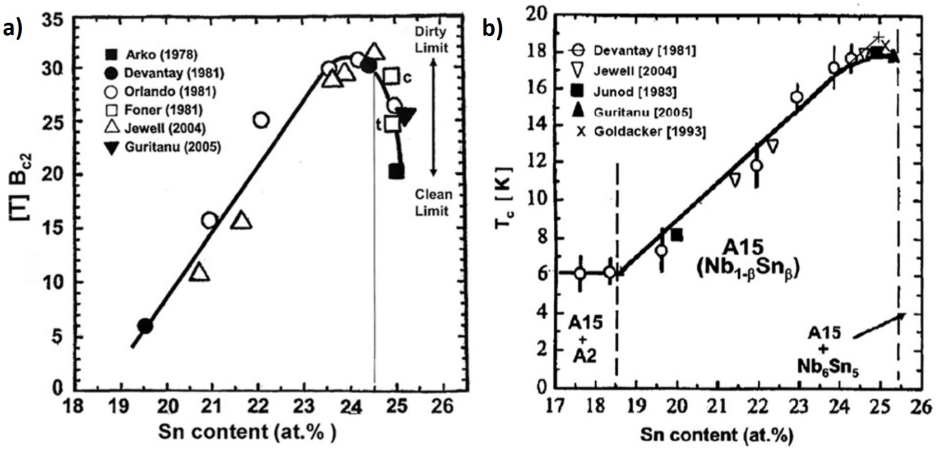


Figure 1.7: a) Variation of B_{c2} with Sn content in $Nb_{1-\beta}Sn_{\beta}$ b) Variation of T_c with Sn content in $Nb_{1-\beta}Sn_{\beta}$ [45]

1.2.2 Ordering and Lattice Variation

The T_c of $Nb_{1-\beta}Sn_\beta$ varies with the Sn at% (as mentioned in section 1.2.1) and the LRO parameter for each site. The two order parameters are S_a and S_b for the A and B sites respectively in an $A_{1-\beta}B_\beta$ crystal structure. These are found by the following equations explained in detail by Flükiger [25]:

$$S_a = \frac{r_a - \beta}{1 - \beta} \quad \text{and} \quad S_b = \frac{r_b - (1 - \beta)}{1 - (1 - \beta)} \tag{1.2}$$

The ordering parameters are expressed in terms of two occupation factors r_a and r_b for the A and B sites. Perfect ordering occurs when $S = S_a = S_b = 1$ and $S = 0$ represents perfect disorder. For perfect order this would require $\beta = 0.25$, the ideal stoichiometry for Nb_3Sn. The term S is used to describe any type of LRO (e.g. off-stoichiometry, quenched in thermal disorder or neutron irradiation induced disorder) which reduces the T_c [25]. The variables β, r and S are quantitatively linked within the A15 composition range, which makes it possible to link them back to Sn concentration. Both Devantay *et al* and Vieland *et al* showed that as the Sn content increased from $\sim$ 18 at% to 25 at% there was a linear increase in lattice parameter up to 5.29 Å at $\beta = 0.25$, as shown in Figure 1.8. Godeke used data from Devantay *et al* to plot the first line and extrapolation from 5.29 Å at $\beta = 0.25$ to a value of 5.25 Å at $\beta = 0$ for Flükiger's line [21]. Importantly there is a reduction in the lattice parameter below 25 at% Sn in the A15 phase range because Nb substitutes onto Sn lattice sites producing a reduction in the quality of the A15 phase. Nb_3Sn is dominated, in the binary state, by antisite disorder, with computer modelling in the 1980's showing that the lowest energy point defect structure is a Nb on a Sn site with an associated Nb vacancy [46]. The fraction of vacancies by comparison has been shown to be 7 orders of magnitude smaller than that of antisite defects at 1000 K [47]. More recently, DFT has shown that these Nb antisite defects cluster together to form Sn depleted regions in association with grain boundaries in SRF cavities [48]. SRF cavities are produced to be monocrystal, therefore this defect of increased Nb concentration can be seen at the surface of SRF cavities. However, there is little understanding as to how this could be impacting polycrystal Nb_3Sn.

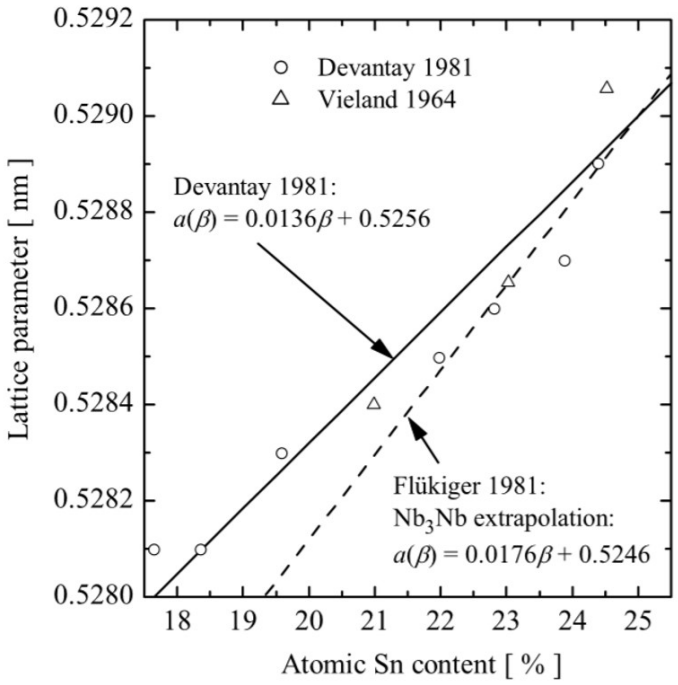


Figure 1.8: Lattice parameter as a function of Sn content produced by A. Godeke [26] with data from Devantay *et al* [24] (with earlier data from Devantay's paper from Vieland) and Flükiger *et al* [25]

1.2.3 Maximising the Pinning Force

As mentioned in section 1.1.1 the pinning force in a type II superconductor is maximised when the defects providing the pinning force are on the scale of the coherence length. Current commercial Nb_3Sn wires have grain sizes of $\sim$ 100 - 150 nm, which is far from optimised. However, there are reasons why commercial wires do not yet have smaller grain sizes, as discussed in section 1.5. The field at which the F_p^{MAX} occurs depends on the relationship between the lattice and the flux lines [49]. In Nb_3Sn and other A15 phases, grain boundaries are generally assumed to represent the primary pinning centres, supported by experimental evidence that the F_p^{MAX} is proportional to the reciprocal grain size ($1/d_{av}$) as shown in Figure 1.9 [26, 50–54]. The data summarised until 2002 of non-Cu J_c (the non-copper area of the wire) all follow the same linear trend shown in Equation 1.3, including the non-Cu J_c values added by Fischer. When Fischer then redefined the area to be the A15 area, not the non-Cu area, the pinning force then increased due to higher J_c values, as shown in equation 1.4.

$$22.7ln\left(\frac{1}{d_{av}}\right) - 10(GNm^{-3}) \tag{1.3}$$

$$39.2ln\left(\frac{1}{d_{av}}\right) - 10(GNm^{-3}) \tag{1.4}$$

The most objective wire comparisons can be made when the pinning force is normalised to the grain boundary length, giving an effective pinning force Q_{GB}:

$$Q_{GB} = \left(\frac{1}{\eta}\right)\left(\frac{F_P}{GB_{l/A}}\right) \tag{1.5}$$

η is the efficiency of normalisation (1/3 for equiaxed grains) and $GB_{l/A}$ represents the grain boundary length per unit area. Q_{GB} is useful for determining the effective pinning of a boundary however $GB_{l/A}$ is not easy to calculate [26].

In order to maximise the pinning force an optimum grain size can be calculated, based on the principle that there is one pinning site per flux line and that grain boundaries produce the primary source of pinning in Nb_3Sn. Under the assumption that there is a triangular flux line

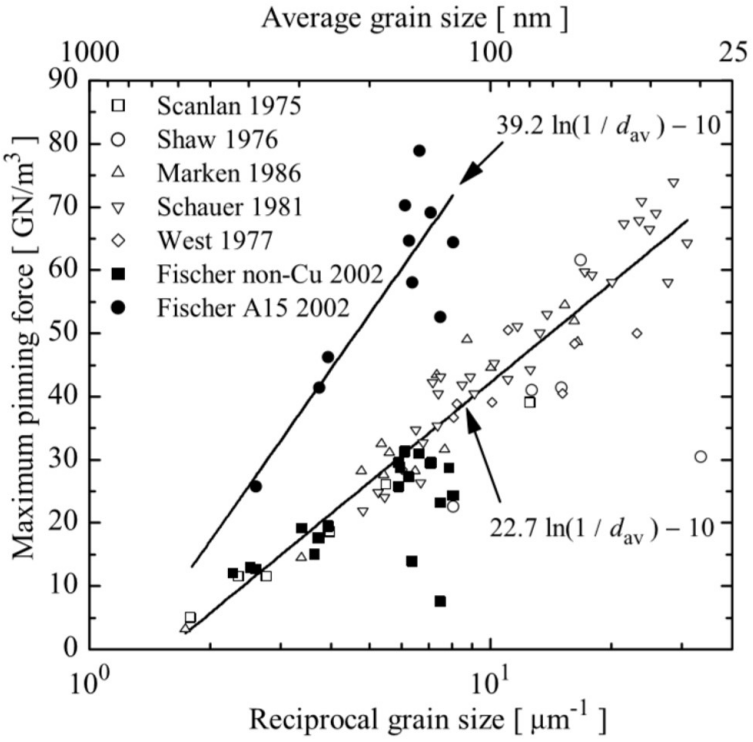


Figure 1.9: F_p^{MAX} as a function of reciprocal grain size, A Godeke [26]

lattice the optimum grain size can be calculated:

$$a_{\triangle}(H) = \left(\frac{4}{3}\right)^{1/4} \left(\frac{\phi_0}{\mu_0 H}\right)^{0.5} \tag{1.6}$$

At an operating field of 16 T required for the FCC this would give an optimum grain size of $\sim$ 12 nm, approximately 10 times smaller than current commercial Nb_3Sn wires. In NbTi the ideal limit has been closely approached by producing non-superconducting α-Ti precipitates approximately 1 - 4 nm thick [55]. In Nb_3Sn, as explained in section 1.5, it is not possible to reduce the grain size to 12 nm without degrading other properties of the wire, however nano-engineering NbTi has shown that nanostructural characterisation is important in optimising an LTS, whether that is by introducing pinning precipitates, refining the grain size or analysing the constituents at the grain boundaries.

1.3 Pinning Mechanism for Nb_3Sn wires

Dew-Hughes published a variety of different mechanisms in 1974, with which type II superconductors can pin flux lines [49]. The mechanisms of interest for Nb_3Sn all have a dependency of:

$$F_{p,max}(H) \propto \left(\frac{H}{H_{irr}}\right)^p \left(1 - \frac{H}{H_{irr}}\right)^q \tag{1.7}$$

This equation can be written in terms of B as B/B_{c2} or H as H/H_{irr} depending on how the data is collected. H_{irr} is where the hysteresis curve is no longer reversible due to vortex movement and is used in chapter 4. Equation 1.7 assumes shearing of the flux lines to be the main de-pinning mechanism between $0.05 < \frac{H}{H_{irr}} < 0.8$, and operation at 16 T fits this model [56, 57]. Historically B_{c2} has been beyond the fields available in most laboratories (which were often limited to $\sim$ 15 T) so therefore B_{c2} needed to be extrapolated using the Kramer function $Kr(H) = J_c^{0.5}(\mu_0 H)^{0.25}$. Despite good correlation between experiments and the pinning model at lower fields, Kramer extrapolations at high fields (over 15 T) have not been experimentally verified in modern doped Ti/Ta wires where the dopants are added in order to increase B_{c2} [58].

Standard polycrystal Nb_3Sn wires are governed by surface pinning [50, 52, 57, 59, 60], which has exponents of $p = 1/2$ and $q = 2$ with the F_p^{MAX} occurring at $0.2H_{irr}$. The mechanism is defined as a normal core interaction with a surface (in this case a grain boundary). There are a few instances where there are shifts in the pinning curve:

- A change in grain shape from equiaxed to columnar grains
- Additional normal pinning centres added in the form of secondary phases or radiation induced defects
- A change in the $\Delta\kappa$ caused by changes in the normal-state resistivity. This can be produced by composition fluctuations or non-uniform distributions of dislocations [49, 61, 62].

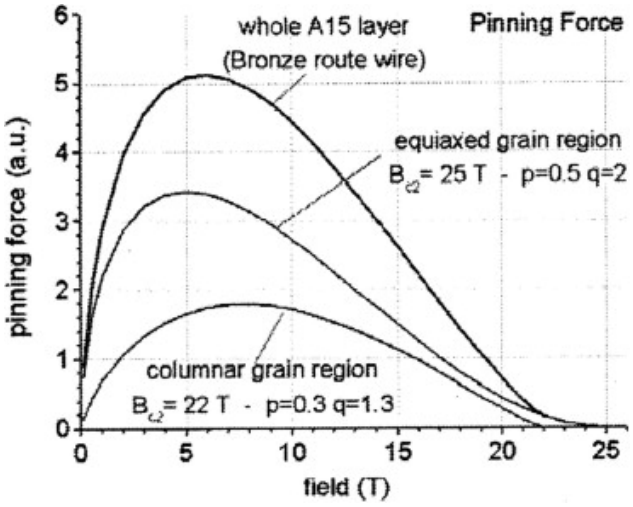


Figure 1.10: Pinning force curve against field for a bronze route processed Nb_3Sn wire with contributions from equiaxed and columnar pinning [45]

The Kramer model assumes equiaxed grains, however in bronze route wires (with $> 30\%$ columnar grains) there is a lower J_c which has been explained by fitting the contribution of columnar grains as $p = 0.3$ and $q = 1.3$, as shown in Figure 1.10 [63]. PIT and RRP® wires tend to have a higher fraction of equiaxed grains [45], therefore the contribution of columnar grains will not be considered further in this work.

Additional pinning centres are non-superconducting secondary phases or vacancies which act to pin flux lines. For the greatest effect on pinning and J_c the additional pinning centres should be on the scale of the coherence length. Dew-Hughes modelled normal additional pinning centres with the coefficients of $p = 1$ and $q = 2$ [49] in equation 1.7, where F_p^{MAX} occurs at $0.33H_{irr}$, higher than surface pinning. In recent years, focus has been placed on adding additional pinning centres to Nb_3Sn wires, either in the form of APCs [64, 65] or through irradiation damage [66], to increase the pinning force and maximise J_c . Competition to use APCs in Nb_3Sn to reach the FCC requirement has increased in recent years with Hf and Zr additions seen as likely candidates, further information can be found in section 1.7. For applications such as fusion reactors, it is important to understand how irradiation affects the pinning in Nb_3Sn, however irradiating Nb_3Sn for increased pinning is not practical.

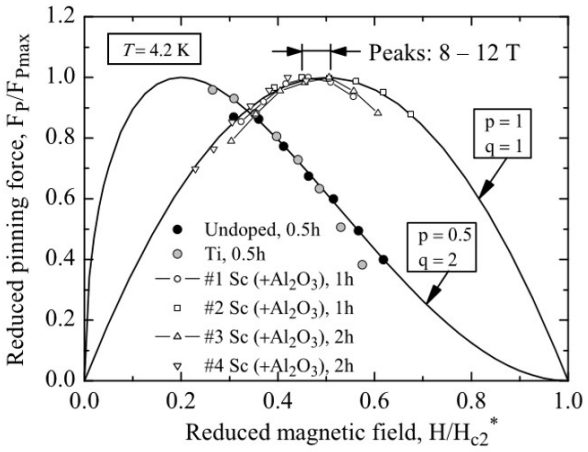


Figure 1.11: Reduced pinning force as a function of reduced magnetic field for undoped and doped Nb_3Sn [67]

A change in κ signifies that there is an area of the superconductor with a differing superconducting performance e.g differing T_c or a normal phase which is smaller than the coherence length and therefore causes a change in κ due to the proximity effect. The $\Delta\kappa$ pinning mechanism has coefficients of $p = 1$ and $q = 1$ [49] and an F_p^{MAX} at $0.5H_{irr}$. Figure 1.11 shows $\Delta\kappa$ pinning has been seen on Nb_3Sn tapes, with a very small grain size of 15 – 30 nm [67], however there is still a long way to go until this can be achieved with a homogeneous A15 layer in commercial Nb_3Sn wires.

As the A15 is inhomogeneous throughout each wire there will be shifts in the pinning curve due to multiple pinning mechanisms all taking place in different areas of the wire. However, modern PIT and RRP® wires with APCs can be assumed to follow the function:

$$F_{p,max} \propto x\left(\frac{H}{H_{irr}}\right)^{0.5}\left(1-\frac{H}{H_{irr}}\right)^{2}+(1-x)\left(\frac{H}{H_{irr}}\right)\left(1-\frac{H}{H_{irr}}\right)^{2} \tag{1.8}$$

Where x is the contribution of surface pinning and $1-x$ is the contribution of point pinning. The contribution from $\Delta\kappa$, and columnar grains may shift these values slightly, however this is negligible compared to the effect of APCs. Shifting F_p^{MAX} to higher fields is important for operation at 16 T and can improve the low field stability as there is a smaller magnetisation at low fields, which is important for the stability of accelerator magnets [68].



Figure 1.12: Untwisted Rutherford cable [73]

1.4 Wires and their Methods of Fabrication

The first commercial Nb_3Sn magnets were produced in the 1960s and composed of wound Nb_3Sn tapes which were flexible enough to be made into coils [69]. The first wire was fabricated by J.E Kunzler via the PIT method, explained in section 1.4.2. In 1965 a Cu matrix was introduced as a larger Cu fraction appeared to produce a significantly more stable wire [70]. In 1968 wires were sub-divided into sub-elements in a Cu matrix which reduced the wires' resistance to flux jumps [71]. This idea was based on permanent magnets as finer Fe in a Cu matrix had been shown to produce a higher coercivity (resistance of the wire to de-magnetisation) [72]. For future applications and regardless of wire type, each wire will be bundled into a Rutherford cable, as shown in Figure 1.12. The relevant types of wire which have been developed will be discussed and their relative chances of achieving the FCC target.

Two parameters which are vital for the stability in commercial wires are: the d_{eff} and the thermal conductivity of the Cu matrix, which is very sensitive to impurities at low temperatures. In order to have a figure of merit for wires a RRR is used, which is defined by the electrical resistivity at 273 K divided by the resistivity at 20 K. To produce the best wires a high RRR ratio is desired for maximum stability, with a value of RRR $>$ 150 as the design requirement for the FCC [74].

A Cu matrix is vital for a successful Nb_3Sn wire for many reasons:

- Reduction of the A15 formation temperature, initially demonstrated on V_3Ga tapes [75], enabling smaller grain sizes to be produced and reducing the manufacturing costs as discussed in section 1.5.
- Cu acts as a cryostabiliser allowing heat to be removed from the filaments. High purity Cu produces the largest RRR ratio and is therefore the most desirable for high performance wires.
- The Cu matrix can conduct heat away from the superconductor if any sudden instabilities or temperature increases occur preventing damage to the superconductor.
- In certain wires Sn can be added in the form of a Cu-Sn alloy. The initial increase in Sn in the alloy increases the J_c produced in the final wire, however if there is a too much Sn then Cu-Sn phases will form in the A15 region greatly reducing the J_c [76].
- Cu helps to process wires as it is harder than Nb and softer than Sn, aiding in the drawing process.

Cu is also known to have no solubility within the Nb_3Sn grains and is purely confined to the grain boundaries [77, 78].

1.4.1 The Bronze Process

The bronze process was developed in 1969 with the first multi-filamentary wire patent produced in 1973 [79]. The method includes drilling rod length holes into an α-bronze matrix and inserting Nb filaments. Often Ti is included in the Cu-Sn matrix to suppress intermetallic precipitation of other Cu-Sn phases. Impure Cu reduces the RRR [80], and although a high purity Cu layer can be used as a diffusion barrier, bronze processed wires have too low a RRR for the FCC specification. Modern bronze processed wires can reach $\sim$ 900 Amm^{-2} at 12 T and 4.2 K [81, 82], well below that required for FCC, but four of the nine Nb_3Sn wires selected for ITER are bronze processed [83]. There is one large benefit to the bronze process: this method has the lowest hysteresis loss (this is the loss of trapped field due to irreversible motion of the vortices) out of all the methods of Nb_3Sn fabrication (as small as $\sim$ 200 mJ/cm^3 for $\pm$ 3 T [73]).

1.4.2 Powder-in-tube

The PIT method is a high J_c technique and is one of the two methods considered for particle colliders [84]. The first wires date back to 1961 where Nb_3Sn powder and Sn powder were placed in a Nb tube and heated to over 970 °C [85]. However, modern multi-filamentary wires, with the addition of Cu to manufacture at 600 - 700°C, were not produced until 1977 [86]. Often, modern PIT wires have powdered $NbSn_2$ and Cu which is placed inside a thin Cu sheath in a Nb (or Nb-7.5wt% Ta) tube, which acts as a diffusion barrier, to form a subelement [87]. These tubes are stacked to form a wire, which when optimised by doping and heat treating, can reach non-Cu $J_c \sim$ 2700 mm^{-2} at (12 T, 4.2 K) and have a an d_{eff} of 30-50 μm [88]. The relative simplicity of PIT wires enables small d_{eff} to be produced compared to, for example RRP®. An example of a multi-filamentary PIT microstructure and an individual filament are shown in c) Figure 1.13. A modification to the PIT design is the RIT design which is the opposite geometry with a Nb rod in the centre of wire surround by a Cu/Sn powder encased in an outer barrier layer.

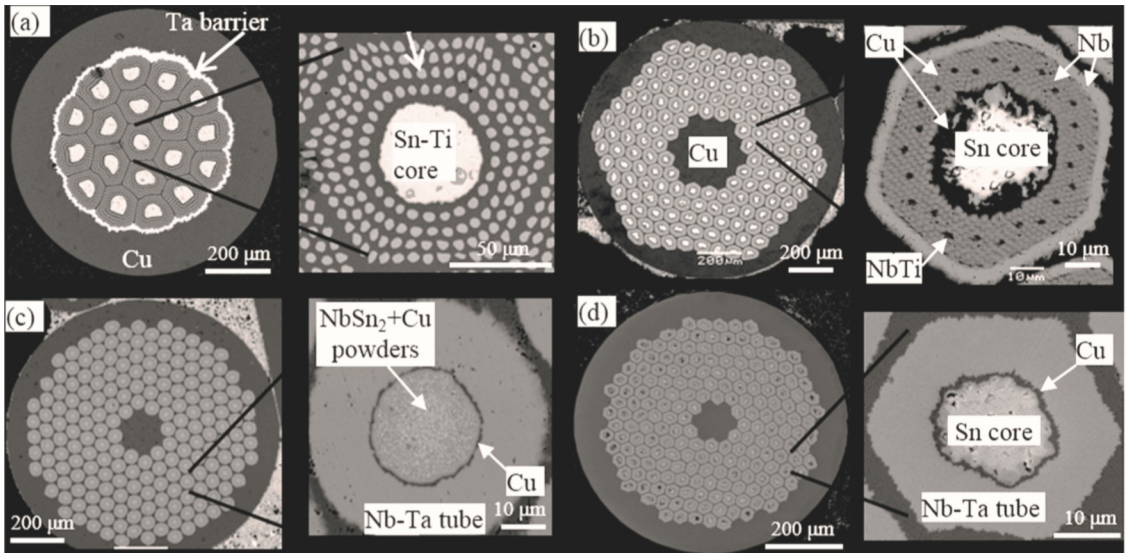


Figure 1.13: SEM images a) Single barrier IT b) RRP® c) PIT d) Tube-type Nb_3Sn wires [89]

1.4.3 Internal-tin Method

The IT method was developed in 1974 [90] to reduce the need for frequent annealing in the drawing process and at the time had a J_c four times that of the bronze process [76]. There are two variations to this method: the single-barrier IT and distributed-barrier IT. Single-barrier IT can be seen in a) Figure 1.13 with originally a pure Sn core (often Sn-Ti in modern wires) surrounded by Nb filaments in a high purity Cu matrix. There is a single Ta barrier around the filaments and then a Cu sheath around the wire. During heat treatment the Cu and Sn react first to form Cu-Sn alloys which then react with the Nb, this produces a large range of Nb/Sn/Cu compositions, much greater than that of the bronze method. To produce the A15 phase it is important to have high ratios of Nb/Cu and Sn/Cu, but still have Cu to nucleate A15 at a lower temperature and provide stability. The reduction of Cu is not as easy with single-barrier IT wires as the subelements can fuse together to form a very large d_{eff}, greatly decreasing J_c . Distributed-barrier IT wires have smaller Cu areas and therefore higher J_c values representing one of the best methods to manufacture wires to meet the FCC specification.

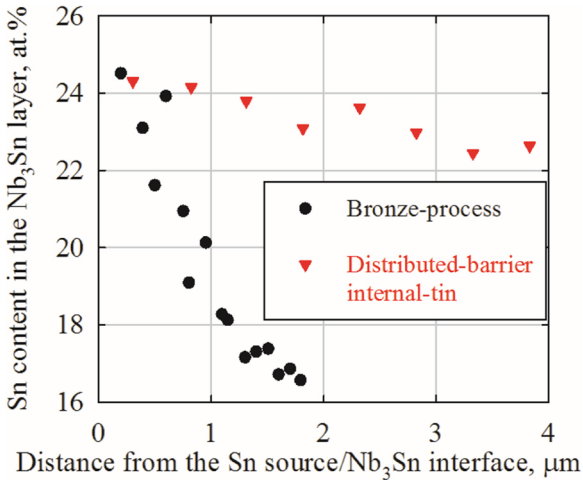


Figure 1.14: Sn at% profile against distance from the Sn source/Nb_3Sn interface for bronze [91] and distributed barrier wires [92] from Xu *et al* [89]

1.4.4 Restacked-rod-process

The main distributed-barrier IT method is the RRP®. Each subelement has its own diffusion barrier, therefore there is a lower Cu content between Nb filaments than the single-barrier method and subelements can be closer in proximity to each other. Sn diffuses through the Cu network produced between the Nb filaments [89], diffusing to even the outer Nb rods, so the overall gradient in Sn concentration is relatively low, as shown in Figure 1.14. Expansion during the A15 reaction enables bonding between filaments, producing a ring of Nb_3Sn with d_{eff} equal to the subelement size [93]. An example RRP® wire can be seen in b) Figure 1.13. The RRP® method has produced the highest non-Cu J_c values for Nb_3Sn wires (not including additional pinning centres) recording: 3000 Amm^{-2} at (12 T, 4.2 K) in 2005 [94], however the d_{eff} is still far from optimised. The larger diameter means RRP® wires suffer from greater hysteresis loss compared to other wire types, but the best combination of high J_c and d_{eff} is on average 2900 Amm^{-2} (12 T, 4.2 K) and 55 μm [73]. Despite record breaking J_c results, RRP® could only be used for the FCC specification if the d_{eff} is reduced. Attempts to reduce d_{eff} have historically resulted in reduced J_c , as seen in Figure 1.15.

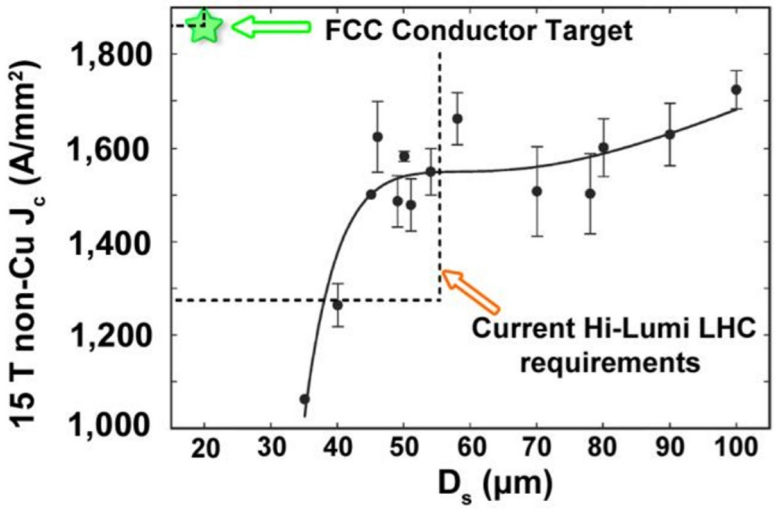


Figure 1.15: J_c as a function of subelement size (D_s) for RRP® wires. The High-Lumi LHC upgrade and FCC specifications are shown, highlighting much more development is needed to reach the FCC specification. In RRP® wires the D_s is the same as the d_{eff} [73]

The Hi-Lumi LHC uses RRP®, only commercially produced by Bruker, with a three stage heat treatment to the wires (210°C, 400°C and 660°C) for $\sim$ 48 hours at each stage [95–97]. A standard commercial stack of 108 subelements around a 127 centred hexagonal holder produces a reasonably consistent $d_{eff} = 55$ μm and $J_c \sim 1200$ Amm^{-2}, however this is far from the FCC specification. RRP® wires always resemble something similar to Figure 1.16, however any extra Nb rods e.g Nb-Ti or Nb-Ta are dependent on the wire design. Both RRP® and PIT wires have high J_c performance, with their main properties compared in Figure 1.17. The simpler design of PIT wires does mean that finer d_{eff} can be produced than RRP® wires, however the larger area of fine grain Nb_3Sn in RRP® is a distinct advantage over PIT wires.

The samples discussed in this work are RRP® and RIT type wires.

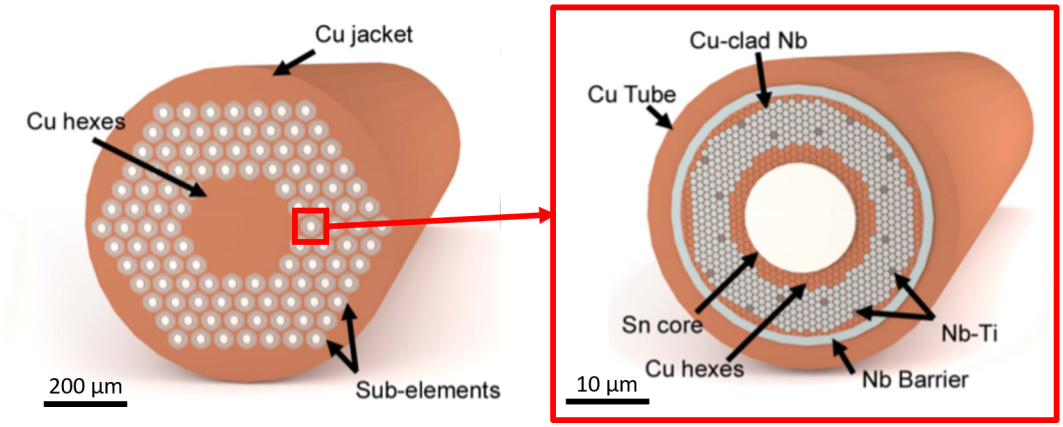


Figure 1.16: A sketch of an RRP® wire with subelements surrounding Cu hexes and in a Cu jacket, and a sketch of an individual subelement from the wire. The subelement has a Sn core surrounded by Cu hexes, Nb-Ti, Cu-clad Nb, Nb barrier and a Cu tube. The Sn core is inserted in a drilled hole once the Nb and Cu has bonded. Adapted from [98]

	Fine grain Nb_3Sn fraction	B_{c2} @ 4.2 K (T)	Grain size (nm)	F_p^{MAX}
Present best RRP®	$\sim 60\%$	$25-27$	$120-150$	$\sim 0.2B_{c2}$
Present best PIT	$40-45\%$	$25-27$	$100-150$	$\sim 0.2B_{c2}$
Optimum limit	$\sim 65\%$	~ 28	<15	$0.5B_{c2}$

Figure 1.17: Comparison of Nb_3Sn fractions, B_{c2} and flux pinning characteristics from the best modern wires [89]

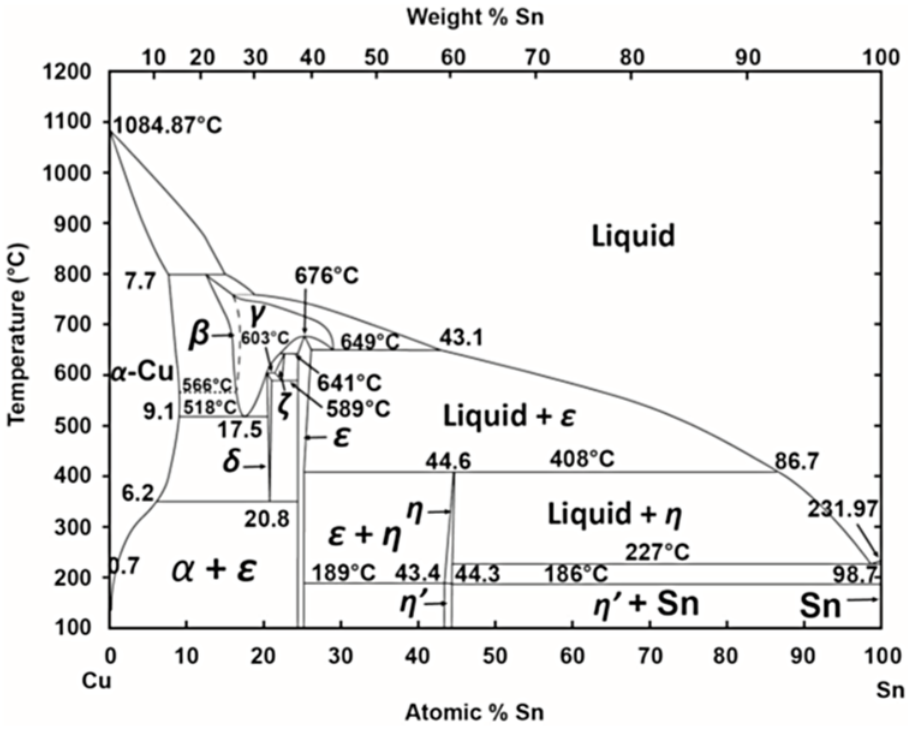


Figure 1.18: The Cu-Sn phase diagram [98, 99]

1.5 Ternary Phases and Heat Treatment

Each Nb_3Sn wire, regardless of manufacturing technique, requires a heat treatment stage to form the final A15 phase. Copper is important in the production of Nb_3Sn wires, as previously listed in section 1.4, therefore the Cu-Sn phase diagram is included in Figure 1.18. With all IT wires heat treatments at low temperatures are used to mix the Cu-Sn before reaction with the Nb filaments, this reduces the impact of liquid phases and produces primary bronze phases which then react to form the final A15. The steps for forming the A15 phase referenced here are in the context of RRP® wires, however the fundamental chemistry is very similar for all forming methods.

RRP® wires are produced through three standard heat treatment steps where the first two steps are Cu-Sn mixing steps and the final heat treatment is the A15 formation (Figure 1.19). The first step is a heat treatment at $\sim$ 210 - 220°C [98] which is claimed to 'wet' the phase boundaries preventing large voids and tin bursting due to liquid Sn production, which destroys

the superconductor [95, 100, 101]. Figure 1.19 shows after the first step at $\sim$ 210 - 220°C η (Cu_6Sn_5) forms on the Sn rich core with some ϵ (Cu_3Sn) surrounding in the Cu rich region and residual Sn powder.

The second step is at 400°C where the remaining Sn first liquefies and reacts to produce η and then ϵ. The ϵ and η react with Nb producing a phase called Nausite ($Nb_{0.75}Cu_{0.25}Sn_2$), shown as a white ring in c) Figure 1.19. Nausite has been suspected to decompose into porous $NbSn_2$ [98, 102], which upon further heating transforms via Nb_6Sn_5 (at 590°C) into disconnected pieces of coarse grain Nb_3Sn at the inner ring of the filament, characteristic of low performance wires. During the ramp up of heating to 665°C the residual η phase liquefies at 408°C, as seen in Figure 1.18, producing a ring of large faceted grains of nausite.

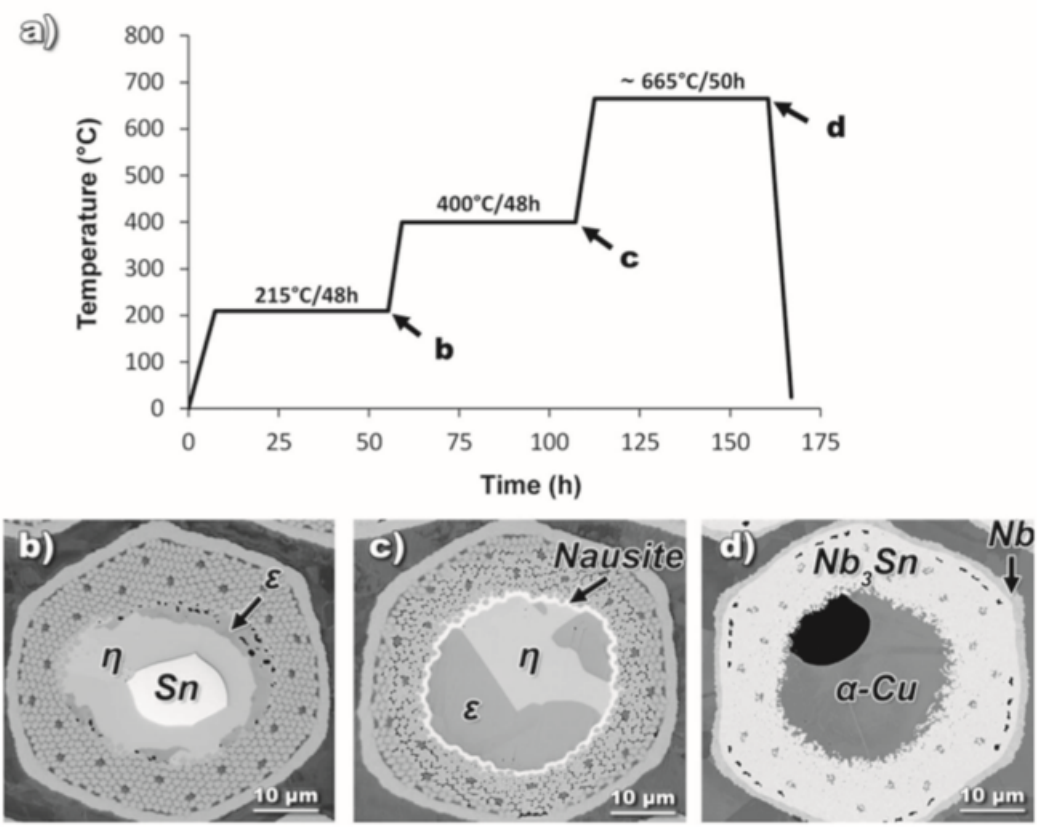


Figure 1.19: Heat treatment of a standard RRP® wires and their associated microstructures b) 215°C/48hrs c) 400°C/48hrs d) final microstructure after 665°C/50hrs which includes a large pore in the core [98]

At 665°C there is a transformation of the stacked Nb filaments to the A15 phase, producing smaller grains which are higher quality than those transformed via Nb_6Sn_5 decomposition [102]. One benefit of RRP® wires is that lower fractions of Nb_6Sn_5 are produced compared to PIT or RIT wires as the A15 phase appears to form at lower temperatures than the Nb_6Sn_5 in this manufacturing method (as low as 510°C [103]). The final structure can be seen in Figure 1.19 d) with the A15 phase shown in white surrounding an α Cu-Sn core.

As discussed previously, a reduction in grain size substantially increases the J_c within a Nb_3Sn wire, with a theoretical optimisation occurring at grain sizes 10 times smaller than current commercial wires. A reduction in the temperature of processing can produce a finer grain size, however if the temperature is too low then there is a reduction in the amount and quality of the A15 produced causing a reduction in B_{c2} [89]. The final heat treatment has been varied between $\sim$ 630 - 700°C with an increased J_c and B_{c2} at the highest treatment temperature, however a decreased RRR $\sim$ 50 [104] due to the A15 phase breaching the diffusion barrier.

The three-step process was aimed at wires operating between 11 - 12 T, however to operate at the 16 T required for FCC, improvements to the heat treatment were needed. In 2018 Sanabria *et al* showed that you could replace the first two steps with a single step at 350°C for 400 hrs [98]. The key development made by Sanabria in improving the J_c of RRP® was achieved by controlling the nausite reaction, which between 300 - 400 °C acts as an osmotic membrane to inhibit the Sn diffusion whilst supporting strong Cu counter diffusion. Sanabria *et al* showed that the new two-step heat treatment produced an average of 36% higher J_c at 16 T than that of the three-step wires (on average 1223 Amm^{-2} with a d_{eff} of 35 μm was achieved). This novel approach suggests that the presence of voids before the final heat treatment does not hinder the final J_c performance as previously suggested (extensive concerns about limited diffusion and cracking have previously been expressed) [105–107]. The decrease in thickness of the nausite layer ($\sim$ 55%) resulting from the lower temperature and increased diffusion of Cu into the core due to the longer reaction time resulted in a lower amount of η before liquefaction - this reduced the amount of Nb lost to dissolution and therefore increased J_c [98]. Sanabria

et al concluded that although the heat treatment had now been optimised, to reach the J_c required for the FCC, a homogeneous dispersion of Ti or Ta would be required in the A15 layer [98].

1.6 Titanium and Tantalum Additions

Any commercial Nb_3Sn wire contains either Ti or Ta to increase B_{c2}. Ti and Ta are dopants, they do not form secondary phase particles but instead lie on the A15 lattice. Ta was initially added to Nb_3Sn in 1964 [108] and further pioneered by Livingston in 1978 where Ta was added to the Nb filaments in bronze processed wires [109]. Ti was added later in 1981 by Tachikawa *et al* [110] to the Nb filaments, however Ti can also be alloyed to the Cu-Sn matrix.

In 1986 Suenaga *et al* showed that up to $\sim$ 1.5 at% Ti and $\sim$ 4 at% Ta, when added to separate bronze processed wires, produced a maximum increase in B_{c2} at 4.2 K from $\sim$ 23.4 T in pure Nb_3Sn to $\sim$ 27 T [111–113]. Suenaga *et al* suggested that the primary reason for the increase in B_{c2} was an increase in electron scattering produced by alloying, but that excessive amounts of Ti and Ta reduced the T_c and B_{c2} as shown in Figure 1.20. Ti/Ta have also been attributed to suppressing the tetragonal phase [111], and allowing for increased heat treatment times without excessive grain growth, compared to binary Nb_3Sn [45].

Dopants can either be introduced in the Cu-Sn region or the Nb filaments, however the most success with increasing J_c has been with introducing Nb-Ti or Nb-Ta rods into the Nb region [114]. This is likely due to the Nb region being the location where the A15 is produced, whereas any dopants in the Cu-Sn core need to diffuse to the A15 region. Multiple attempts have been made to use Ti+Ta together to increase J_c with mixed results. Abächerli *et al* used a bronze route, however this was found to not perform as well as the singularly Ti doped sample [115].

Flükiger *et al* created two pseudobinary phase field diagrams for Nb-Sn-Ti and Nb-Sn-Ta from previous data between 700°C and 750°C in Figure 1.21 [109, 111, 115–119]. These phase fields have been developed from micron scale measurements, however the nanoscale fluctuations in Ti/Ta doped Nb_3Sn are not well understood.

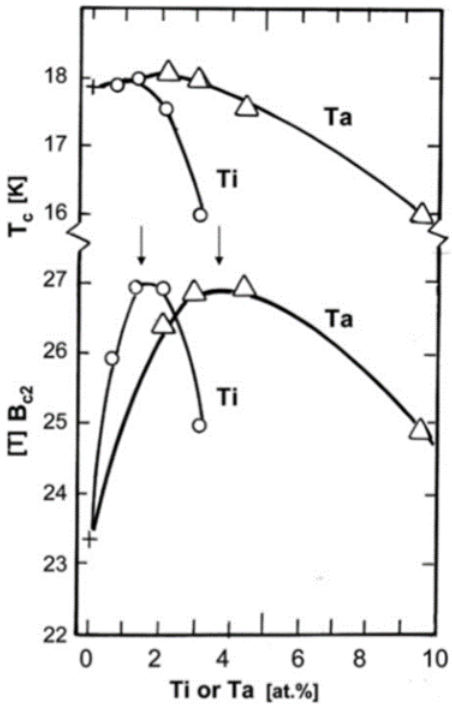


Figure 1.20: Variation in T_c and B_{c2} in Nb_3Sn monofilamentary wires as a function of Ti and Ta content, with arrows indicating the values of Ti and Ta for a maximum B_{c2} [45].

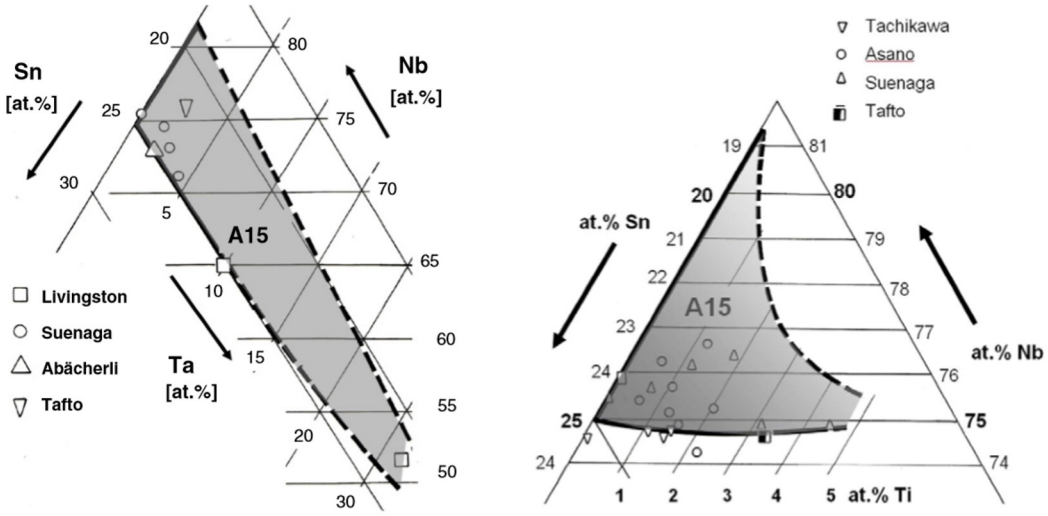


Figure 1.21: Pseudobinary A15 phase field for Nb-Sn-Ta and Nb-Sn-Ti respectively [116]

The sites which Ti and Ta occupy in the A15 was disputed for many years. Initial results in 1984 suggested both substituted on the Nb sites [117], however this failed to explain the differences in lattice parameter or maximum amount of Ti/Ta and which leads to the highest B_{c2} values. Flükiger *et al* revisited the topic in 2008 suggesting the differing resistivity slopes for Ti and Ta suggested different sites of occupation [116]. More recently, work carried out using EXAFS showed that Ta doped samples mismatched the Nb site spectra, still with significant occupation of Nb sites, but with a best fit to the data when Ta occupied between 21% to 32% of Sn sites. This suggests that the formula which should be used to work out the correct ratio, where Ti and Ta are both present, is (Nb+Ti+(1-x)Ta)/(Sn+xTa) where x would vary between 0.21 and 0.32. Furthermore, Ti spectra exactly matched that of the Nb lattice sites, suggesting that Ti only occupies Nb sites [120]. The calculated stoichiometries were further away from perfect stoichiometry with this new method of calculation, however Heald *et al* suggested this was due to large amounts of antisite disorder skewing the ratio. The EXAFS results were collected using a 3 μm beam which averaged over many grains (grain size $\sim$ 100 - 200 nm) and potentially some non-A15 area. Nanoscale analysis is required to determine whether the occupation ratios are valid on the scale of individual grains.

1.7 Artificial Pinning Centres

Once the grain boundary density is maximised and Ti/Ta doping is used to increase B_{c2}, the most common way to increase J_c further is by adding APCs to the Nb_3Sn. APCs have been pursued since the 1980s with limited success in commercial wires.

Initially combinations of NbTi or Ta ribbons were used to provide inclusions which would limit grain growth [121], however despite enhancing B_{c2}, there was discussion as to whether the APCs were provided by secondary phase particles or dopants within the matrix [122]. Later Cu ribbons were added to produce APCs, however this failed to increase J_c , likely due to the high heat treatment temperatures which prevented the Cu ribbons from maintaining their dimensions [123, 124]. None of Ta, NbTi or Cu ribbons produced any form of substantial improvement [89].

Other attempts have been made to include APCs in the Nb precursors by selecting elements with low solubility in Nb. One such attempt used rare earth elements (Y or Gd) pre-alloyed with the Nb [125]. F_p increased for both additions at lower fields, and there was a larger increase for the Y sample which had smaller grains, however at higher fields the increase in F_p became far weaker [125]. In this method the APCs hardened the material [125], so to reduce this problem the APCs need to be formed during the heat treatment and drawing processes.

The most successful attempt at APCs has been internal oxidation, whereby a metal with a higher affinity for oxygen is added to the Nb (e.g. Hf, Zr). This method has been seen to both refine the grain size through Zener pinning and add APCs to improve pinning performance. In the 1960s there was success on Nb_3Sn tapes [126], refining the grain size by 10 times using Nb-1at%Zr and an anodising environment [127]. As wires replaced tapes in the 1970s oxygen could not be introduced via anodising as the Cu sheath prevented the oxygen diffusing through. Group IVB elements such as Zr and Hf, together with Ta, have been studied as an alternative to increase pinning performance in modern wires. In the 1980s and 1990s further additions of Zr and Hf to Nb_3Sn were explored [111, 113, 127, 128]. Early attempts in 2005 to introduce oxygen as SnO_2 [129], hardened the alloy and did not demonstrate grain refinement, this was likely due to insufficient oxygen to the Nb-Zr.

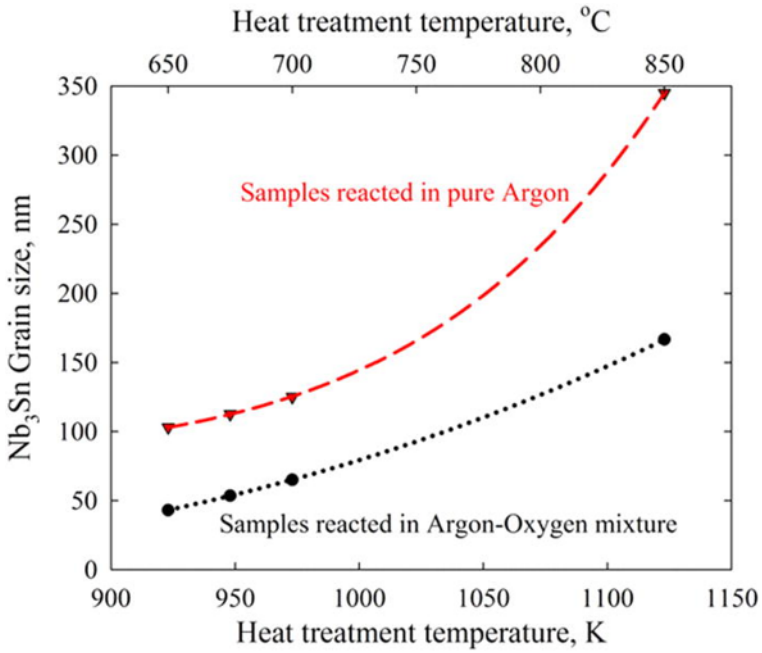


Figure 1.22: Average grain size as a function of temperature for argon and argon-oxygen atmospheres, measured at 650°C, 675°C, 700°C and 850°C [65], measured using TEM

The first successful attempt of internal oxidation on Nb_3Sn wires was in 2014 where Xu *et al* formed wires with a Nb-1Zr outer tube surrounding a Cu-Sn core and exposed the wires to both an argon and argon-oxygen atmosphere, as seen in Figure 1.22 [65]. Under the oxygen atmosphere the average grain size was refined to 36 nm and F_p^{MAX} shifted to $1/3\frac{H}{H_{irr}}$ evidencing that a finer grain size shifts the peak towards the limit of $0.5\frac{H}{H_{irr}}$ (as discussed in section 1.1.1), improving the wire for high field applications [130]. TEM evidence of the ZrO_2 particles can be found in section 1.9. Xu concluded for APCs to enhance performance, oxygen needs to be absorbed by the Nb-1at%Zr before the A15 phase forms so that grain refinement can occur [89].

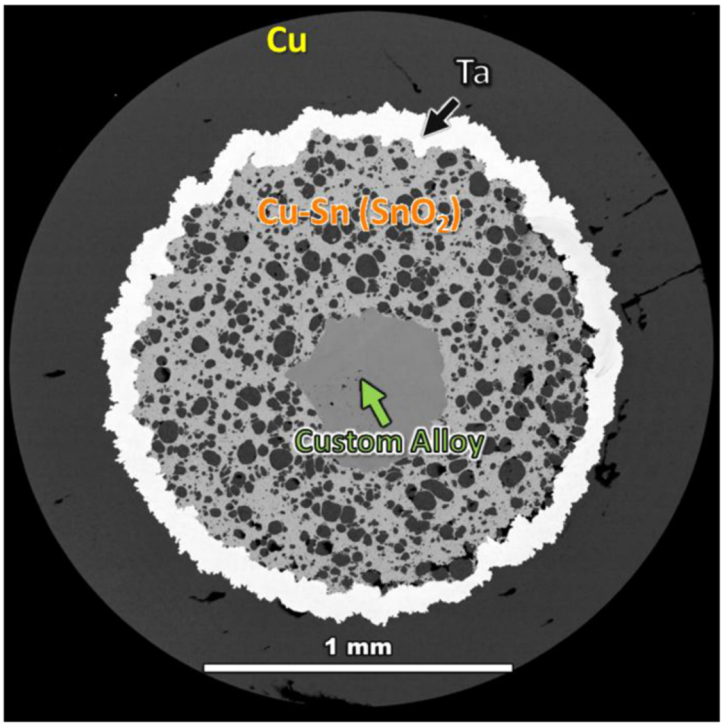


Figure 1.23: BSE-SEM image of an unreacted RIT cross section showing the custom alloy Nb-4Ta-1Hf (at%) or Nb-4Ta-1Zr (at%) in the centre surrounded by Cu-Sn(SnO_2) in an external Ta-Cu tube [64]

Following on from Xu's success, Balachandran *et al* used Nb-4Ta-1Hf (at%) and Nb-4Ta-1Zr (at%) alloys, in a monofilamentary RIT wire, discussed in chapter 4 of this work. Figure 1.23 shows an unreacted monofilament which was heat treated at 550°C/100 hrs to allow oxygen to diffuse from the SnO_2 powder, and 670°C/100 hrs to form the A15 layer. The best performing wire did not contain SnO_2 and instead only contained 1 at% Hf, achieving a predicted J_c of 3710 Amm^{-2} at 16 T and 4.2 K. When this wire was compared to the area fraction of A15 in a usual RRP® wire, an equivalent J_c was calculated of 2230 Amm^{-2}, theoretically reaching the FCC J_c target. TEM was used to analyse the microstructure of the wires, with the best forming Nb-4Ta-1Hf wire producing a grain size of 68 $\pm$ 25 nm and visible precipitates between the A15 grains, as shown in Figure 1.24. Although the Nb-4Ta-1Hf wire without SnO_2 was the best performing sample, the nature of the nanoscale precipitates and how or if any oxygen had entered the sample was unknown.

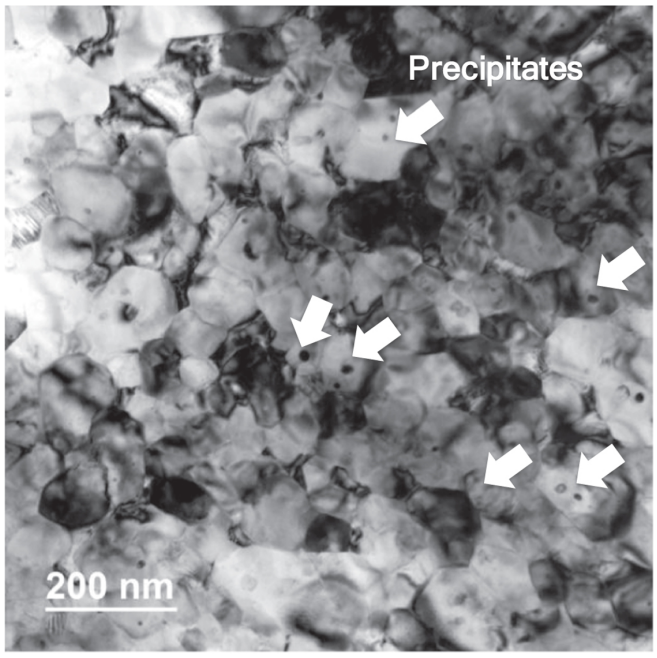


Figure 1.24: Bright field TEM image taken of the A15 phase close to the alloy-rod interface in the Nb4Ta1Hf sample with SnO_2 treated at 550°C/100 hrs and 670°C/100hrs [64]

More recently, multiple groups have developed multi-filamentary PIT wires with the addition of Zr to the starting Nb alloy to produce ZrO_2 through internal oxidation [131, 132]. The University of Geneva replicated the work first developed by Xu *et al* in 2014 on monofilamentary wires and were able to show that CuO could also be used for oxidation instead of SnO_2 [133]. Xu *et al* have made substantial progress in recent years, with a PIT multi-filamentary wire doped with Zr which reached the FCC specification [134]. The wires were produced by filling mixtures of Sn, Cu and SnO_2 powders into Nb-7.5wt%Ta-1wt%Zr tubes before drawing and heat treating at 685°C or 700°C [134]. All of their internally oxidised wires outperformed the best commercial RRP® and PIT wires, and when extrapolated to higher fields, the non-Cu J_c reached the FCC specification as seen in Figure 1.25. Limited TEM and APT has been carried out on these samples and will be discussed in section 1.9. In 2023 Xu *et al* modified their multi-filamentary design to improve the wire quality and the electromagnetic stability, with an RRR value of 84 and 91 for a Hf doped wire and a Zr doped wire respectively [135]. These values are still below the FCC RRR target of 150, but are a substantial improvement on an RRR value of 22 for their multi-filamentary Zr doped APC wire from 2019. The University of

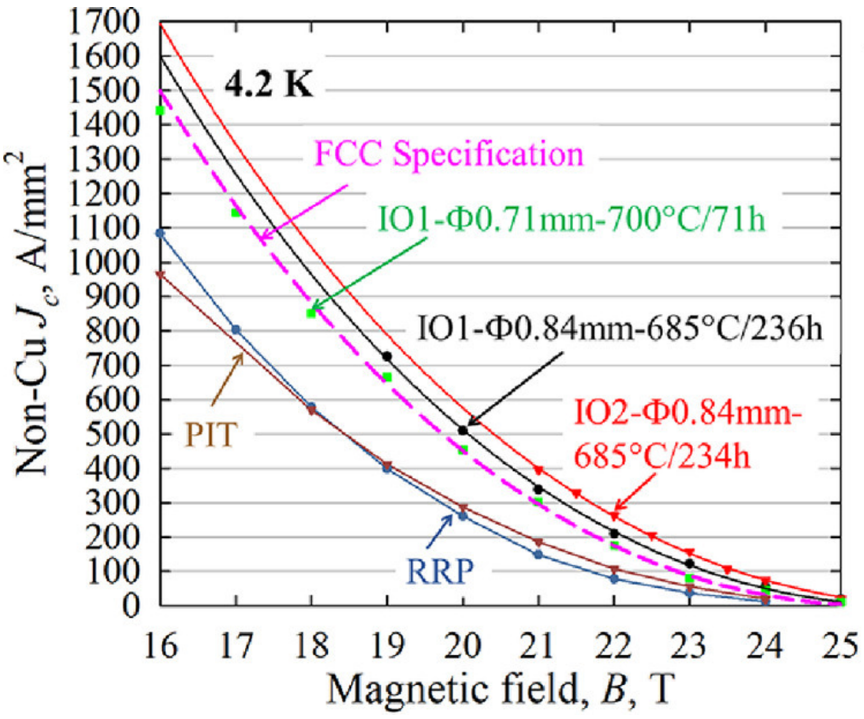


Figure 1.25: Two IO1 wires with the same O content reacted at different temperatures for different time periods and an IO2 wire with a different O content. Non-Cu J_c against the B field for each wire compared to non-oxidised RRP® and PIT wires, and the FCC specification [134]

Geneva have further tested the geometry of internally oxidised wires producing 12-filament RIT wires doped with either Hf or Zr in two different configurations [136], one with oxygen in the Nb filaments and one with oxygen between the filaments and the Cu tube. The Hf doped wire, with oxygen between the filaments and the Cu tube, performed the best with a J_c of up to 3000 Amm^{-2} at 4.2 K and 16 T and a very high B_{c2} of 29.3 T.

Further research into forming internal oxidation wires is needed to: reduce the chance of cracking, increase RRR, reduce d_{eff}, increase the non-Cu J_c and increase the lengths of wires that can be formed [137]. However, to understand how F_p and J_c are affected it is important to understand the nanoscale structure which is altering these properties.

1.8 Radiation Induced Defects

For applications such as fusion reactors and particle accelerators, it is important to understand how the properties on Nb_3Sn vary with irradiation damage during the magnet lifetime. Although superconducting magnets are shielded from 14.8 MeV neutrons produced from Deuterium-Tritium fusion, each magnet needs to withstand an amount of neutron irradiation, for example, for ITER the Nb_3Sn wires needed to withstand a maximum energy of 0.1 MeV at a fluence of 10^{22} neutrons/m^2 [138, 139]. This is equivalent to a displacements per atom dose of 1×10^{-4} dpa, compared to an expected dose of 2.4×10^{-4} dpa for the Hi-Lumi LHC and up to 3×10^{-3} dpa for the FCC [20]. Nb_3Sn magnets will also be subjected to irradiation damage from electrons and protons, however neutrons will cause 90% of the irradiation damage, therefore understanding neutron damage is important for future applications [20].

Many studies on neutron irradiating Nb_3Sn and other A15 compounds were undertaken in the 1970s [140–142]. The main findings after irradiation were a drop in T_c and an increase in J_c. Correlated TEM studies found there were disordered regions within the Nb_3Sn matrix [143–145] which were 2 - 10 nm in size. The radiation induced disorder has been suggested to include defects such as vacancies, interstitials and Frenkel pairs which act to reduce the LRO (as discussed in section 1.2.2) above a critical threshold and reduce the T_c [140, 146]. To explain the drop in T_c, Pande developed a model which assumed that the strongly disordered regions (with reduced T_c) were initially far apart and had no impact on T_c due to the proximity effect, but as the irradiation increased the distance between these regions decreased to within the coherence length, greatly suppressing T_c [143]. The drop in T_c under 14.8 MeV neutrons is described by equation 1.9 [146]. $T_c(0)$ is the T_c before irradiation and C is a fit parameter around 10^{-23} m^{-2} therefore the fit is almost linear at low neutron fluences.

To test whether Nb_3Sn magnets would survive the radiation imposed lifetime limit of 2.4×10^{-4} dpa for the Hi-Lumi LHC, a Ta doped RRP® and a Ta doped PIT wire were irradiated at various proton and neutron fluences. The key finding was that the T_c of the Nb_3Sn would only drop by 0.3 K during the lifetime of the Hi-Lumi LHC regardless of the type of radiation used [147].

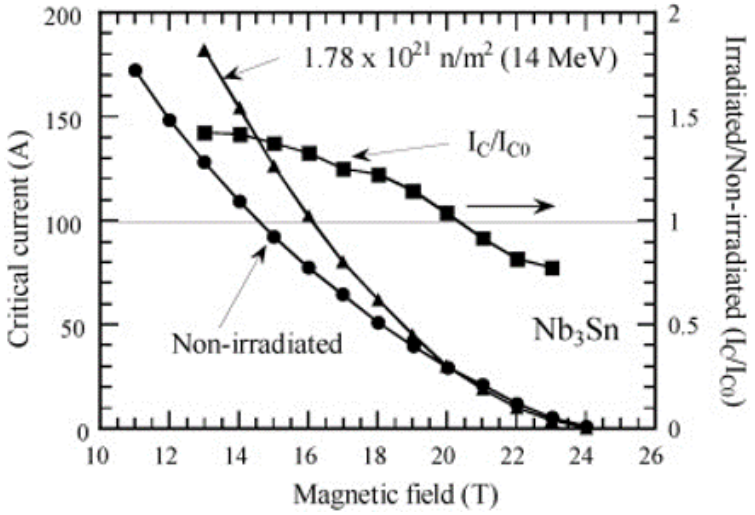


Figure 1.26: Change in critical current density of Nb_3Sn with 14 MeV neutron irradiation against field [149]

$$T_c(\Phi t) = T_c(0)\exp^{-C\Phi t} \tag{1.9}$$

Irradiation increases the volume pinning force, increasing J_c [66] and shifting F_p^{MAX} towards $\frac{H}{H_{irr}}$ ~0.33 suggesting the introduction of point pinning [148, 149]. Figure 1.26 shows that at a neutron fluence of 1.78 $\times$ 10^{22} neutrons/m^2 at 14 MeV increased the J_c of a Nb_3Sn wire bundle [149], particularly at lower fields (12 T - 18 T). Irradiated wires tend to shift the pinning curve from solely surface pinning which has exponents $p = 0.5$ and $q = 2$ in equation 1.7 to point defect pinning $p = 1$ and $q = 2$ and increase the F_p^{MAX} due to the irradiation induced defects produced in the sample [58, 66], as evidenced in Figure 1.27. The induced regions of disorder, on the scale of the coherence length, are likely causing the additional pinning. However, it is unknown as to what happens to the grain boundary structure under irradiation and whether this is also modified due to the additional point defects produced from irradiation.

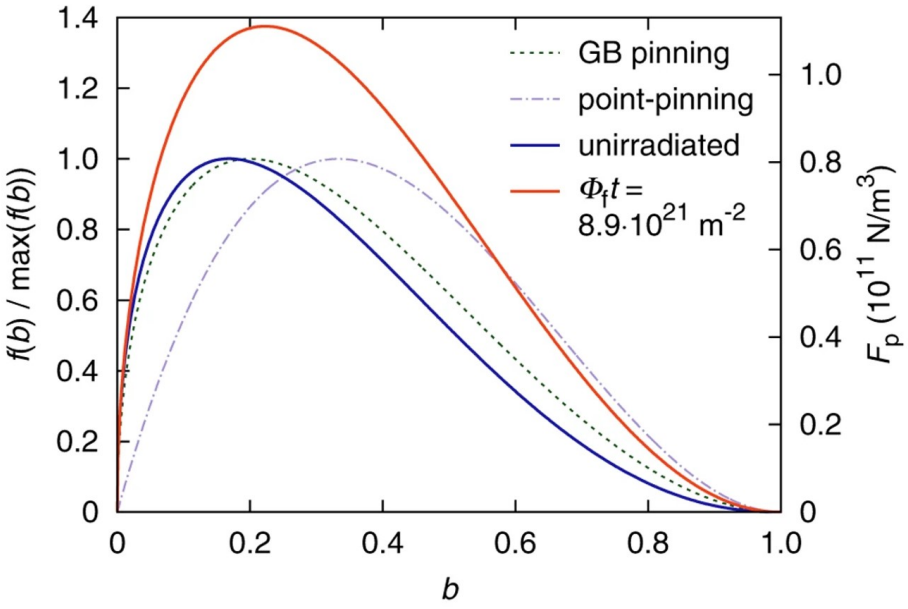


Figure 1.27: Normalised pinning force against fraction of the B field for an as-received Nb_3Sn wire and a Nb_3Sn wire irradiated at a neutron fluence 8.9 $\times$ 10^{21} m^{-2} with the grain boundary and point pinning functions shown with dashed lines [66]

Neutron irradiation has been seen to produce a weak increase in B_{c2}, with early studies claiming the increase in B_{c2} increased the normal state resistivity [66]. However, Cullen and Novak appear to be the first to suggest that the increase in J_c cannot be dependent on just the normal state resistivity but instead there must be nanoscale defects acting as additional pinning centres [150].

An extensive study was undertaken by Baumgartner to irradiate RRP®, PIT and IT wires to fluences 1.6 $\times$ 10^{22} m^{-2} under fast neutron irradiation (E>0.1 MeV) [151]. Baumgartner used the same samples throughout the irradiation, taking measurements at each radiation dose. F_p increased with the irradiation dose until a plateau was reached at the end of the experiment, and a significant deviation from surface pinning was seen after each stage of irradiation. In 2015 Baumgartner *et al* suggested that evidence for improved J_c of Nb_3Sn from radiation defects could lead to further enhancement of Nb_3Sn wires irradiating samples for additional point pinning [66]. Understanding the effects of irradiation damage is important, however using irradiation damage to introduce point pinning is not practical.

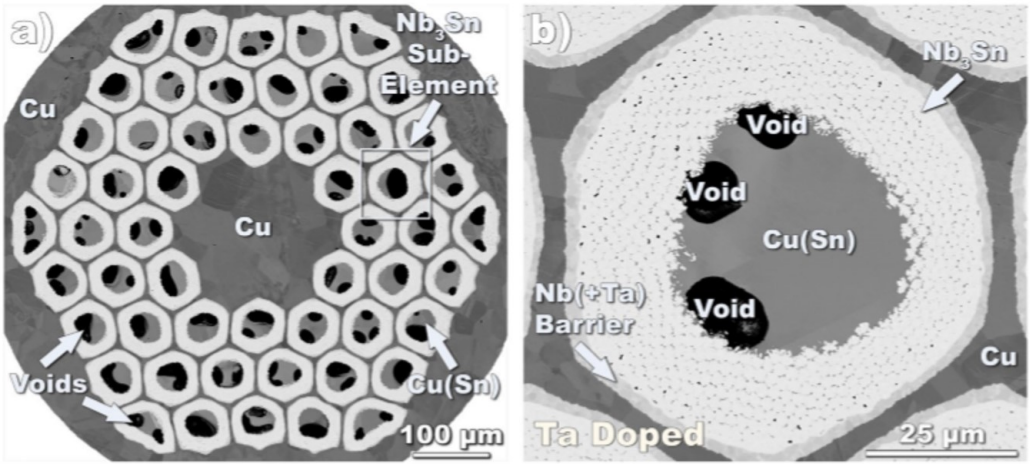


Figure 1.28: SEM-BSD image of: a) an RRP® 54 element stack and b) a Ta doped subelement from the stack [120]

1.9 Microstructural Analysis

The pinning performance and J_c of polycrystalline Nb_3Sn is governed by defects on the scale of the coherence length, as explained in section 1.1.1. To truly understand the superconducting performance of Nb_3Sn it is therefore important to understand any nanoscale defects in the selected wire. Despite extensive measurements of the superconducting properties of wires, often by J_c or resistivity measurements, very few techniques have been used to analyse the microstructure. Often wires have SEM-BSD images taken on the micron scale to show the structure of the wire and any filaments which the wire is composed of, as shown in Figure 1.28.

In 1983 Suenaga *et al* used AES to probe grain boundaries in Nb_3Sn tape and bronze processed wires [77]. To the author's knowledge, this is the first investigation into grain boundaries in Nb_3Sn and showed that Cu segregated to grain boundaries, Nb content was depleted by nearly 40% and the Sn content was enriched by $\sim$ 20% compared to the bulk. In the same year, high resolution TEM images were used to image commercial bronze processed Nb_3Sn at a variety of different heat treatment temperatures. Wu *et al* showed that a sample heat treated at 700°C contained dislocation arrays within the columnar grains formed, and that the frequency of these arrays and pileups increased near the outer periphery of the columnar shell [152]. The formation and migration of dislocations is due to the strain produced during

the A15 reaction, with evidence of dislocation pile-ups shown in Figure 1.29. Wu also suggested that any fine-grained Nb_3Sn which is produced is dominated by low angle grain boundaries [152].

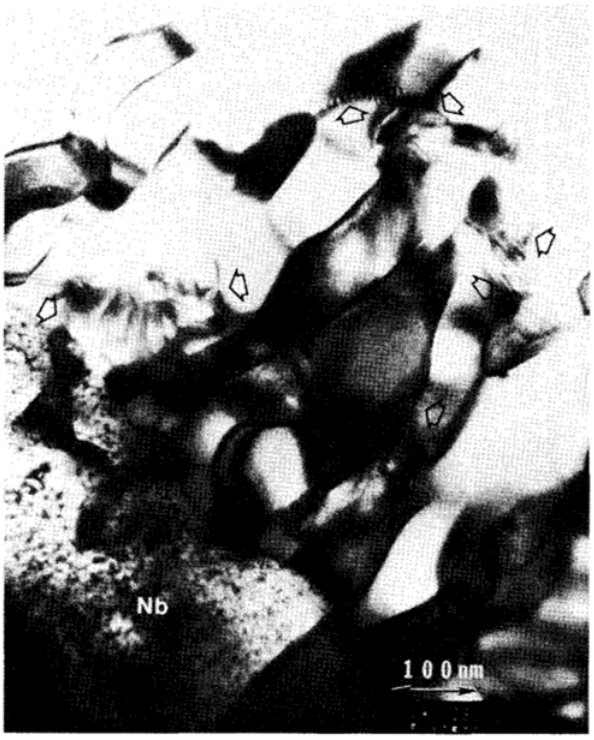


Figure 1.29: High resolution TEM image showing dislocation pileups in columnar grains indicated by arrows. The sample was aged for 6 days at 700°C [152]

In 1986 field ion microscopy, a precursor to APT, analysed an undoped bronze processed wire and both an enrichment of Sn and Cu were present at the one grain boundary identified [153]. More recently TEM and APT have been used to analyse grain boundaries in Ti doped bronze processed wires, with an excess of Cu, Ti and a depletion in Nb seen at the grain boundaries [154, 155]. TEM EDX analysis can only detect a minimum of $\sim$ 1 at% of any element and the electron beam which interacts with a TEM lamellar interacts with the whole thickness of the sample ($\sim$ 100 nm), therefore TEM is not helpful for accurate nanoscale chemical segregation analysis. However, using APT, sub-nanometre chemical segregation can be performed, therefore making APT a more favourable technique to analyse local chemistry changes.

As discussed in section 1.8, TEM has been used to analyse regions of disorder within a range of Nb_3Sn tapes and wires. Pfeiffer recently analysed irradiation damage in two differently doped RRP® wires [20], one an RRP® sample doped with 2 at% Ti which will be explored further in this thesis. The RRP® sample was irradiated by fast neutron irradiation (E>0.1MeV) in the TRIGA II reactor to a neutron dose of 2.82 $\times$ 10^{22} m^{-2}. HR-STEM analysis of the irradiated sample showed disordered regions, as shown in Figure 1.30 with an estimated defect density of 11589 μm^{-2} and size of 3 - 4 nm [20]. Further defects observed were dislocation loops and disordered regions which are on the scale of 10 nm. TEM images have also been taken to show precipitation of APCs, e.g. Figure 1.31 or Figure 1.24 as seen in section 1.7.

The first APT paper by Sandim *et al* on bronze processed wires used an EBSD scan to show the grain sizes in the A15 layer were on average 99 nm and 116 nm in the transverse and longitudinal directions [154]. Figure 1.32 shows a TEM EDX profile which was taken from the matrix to the inner edge of the A15 layer, evidencing the significant Nb and Sn gradients present within the Nb_3Sn. APT analysis was then carried out on several grain boundaries and two intra-grain regions, as shown from the APT reconstruction in Figure 1.33. For the grain boundaries the main findings were that Cu and Ti segregate to the boundaries with a $\sim$ 15% depletion of Nb at the grain boundaries, supporting evidence from Suenaga *et al*. The intra-grain regions contained 18 and 19% Sn, which is relatively low Sn, but still equilibrium Nb_3Sn.

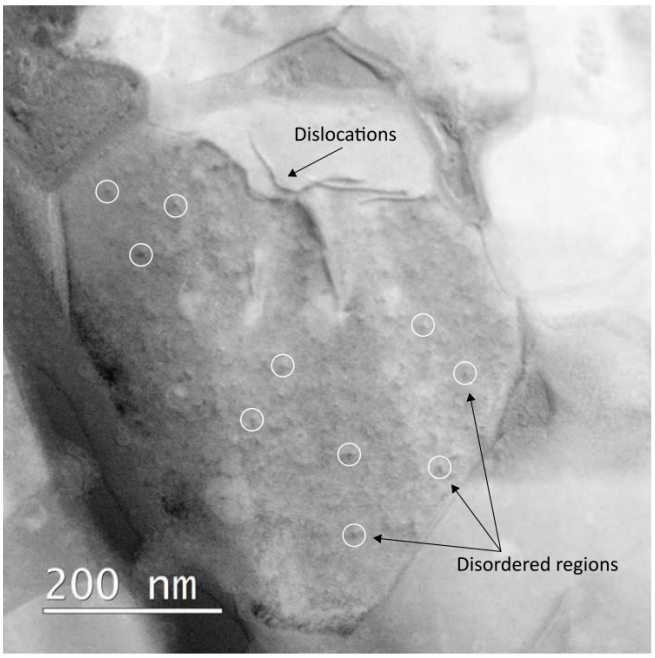


Figure 1.30: HR-STEM image of an irradiated Nb_3Sn wire containing disordered regions, likely induced by irradiation damage [20]

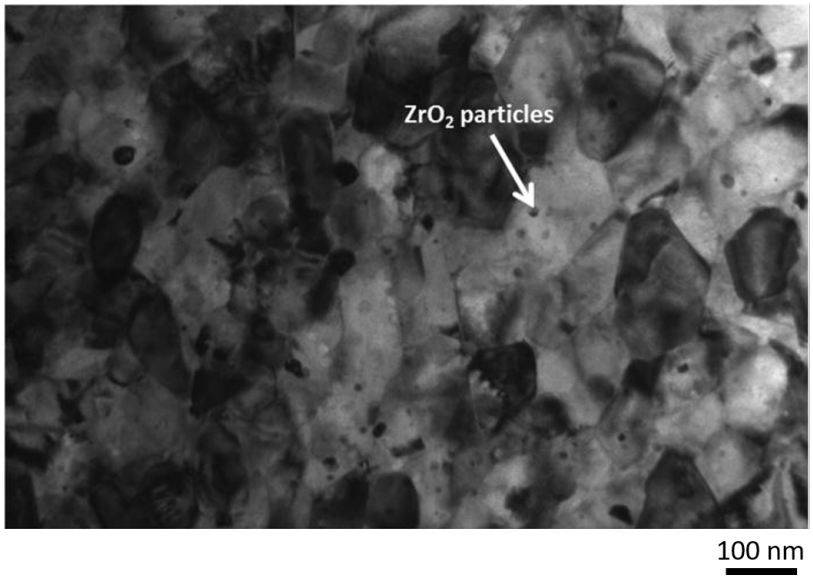


Figure 1.31: TEM image of a sample processed in a Nb-1%Zr tube at 700°C for 55 hours, with obvious ZrO_2 nanoparticles [65]

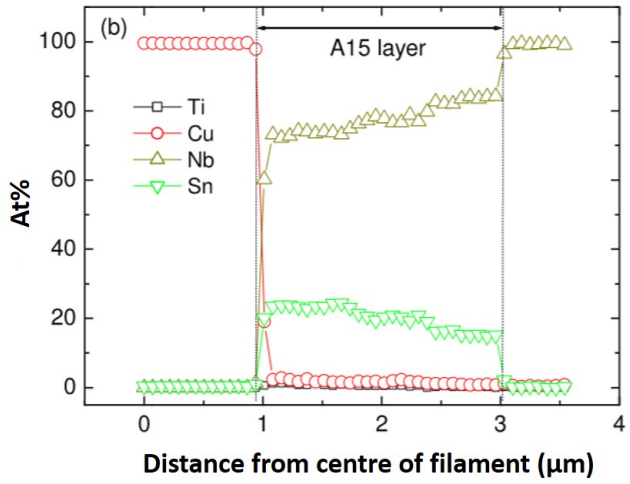


Figure 1.32: Composition (at%) of the A15 layer from the outer matrix at 0 μm to the Nb core at 3 μm [154]

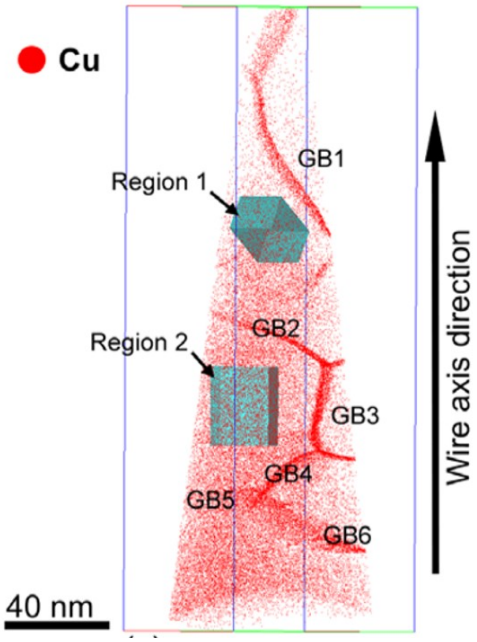


Figure 1.33: APT reconstruction of a bronze processed Nb_3Sn wire showing 6 grain boundaries and two regions far from boundaries, with only the Cu shown in the reconstruction [154]. Composition measurements for the grain boundaries and the intra-grain regions were calculated.

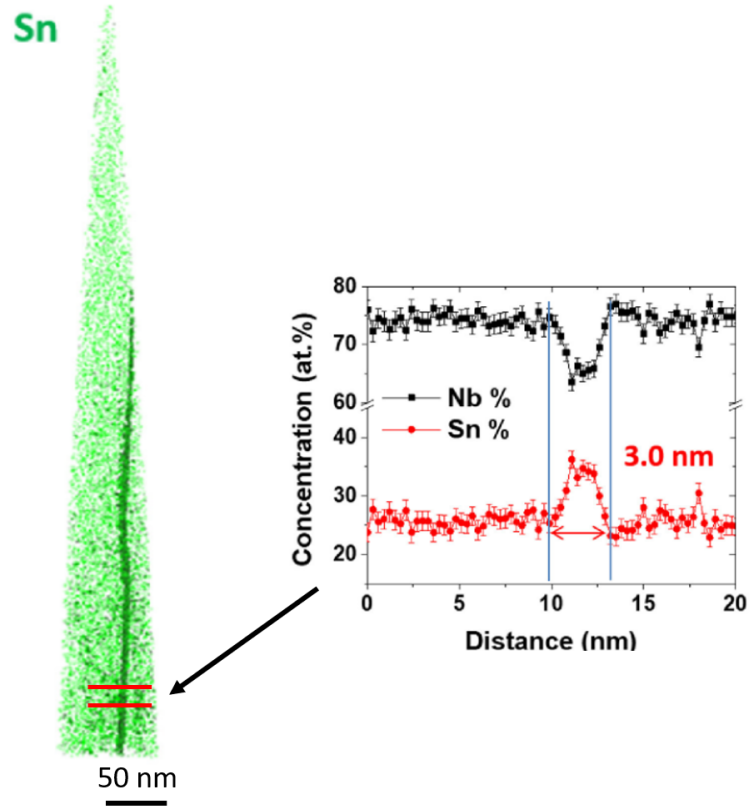


Figure 1.34: APT reconstruction of an Nb_3Sn grain boundary in a superconducting cavity and a 1D profile showing the Nb and Sn at% at the grain boundary, adapted from Lee *et al* [156]

No further literature using APT for the analysis of wires was published until 2019. Lee *et al* published novel HR-STEM images and some supporting APT to analyse undoped Nb_3Sn for SRF cavities [156]. For SRF cavities the kinetics of Sn diffusion are important for Nb_3Sn layer growth. Sn segregation at grain boundaries within the film indicated a maximum of 35 at% Sn in the grain boundaries, as shown in Figure 1.34 - much higher than that expected for the bulk A15. Also in 2019, Santra *et al* conducted some APT work on Ti doped samples, seen in Figure 1.35, which found a Nb depletion of $\sim$ 20% at the grain boundaries [157]. However, no excess Ti was found at grain boundaries, this was likely due to incomplete mixing of the original powder which produced residual pure Ti in the final microstructure.

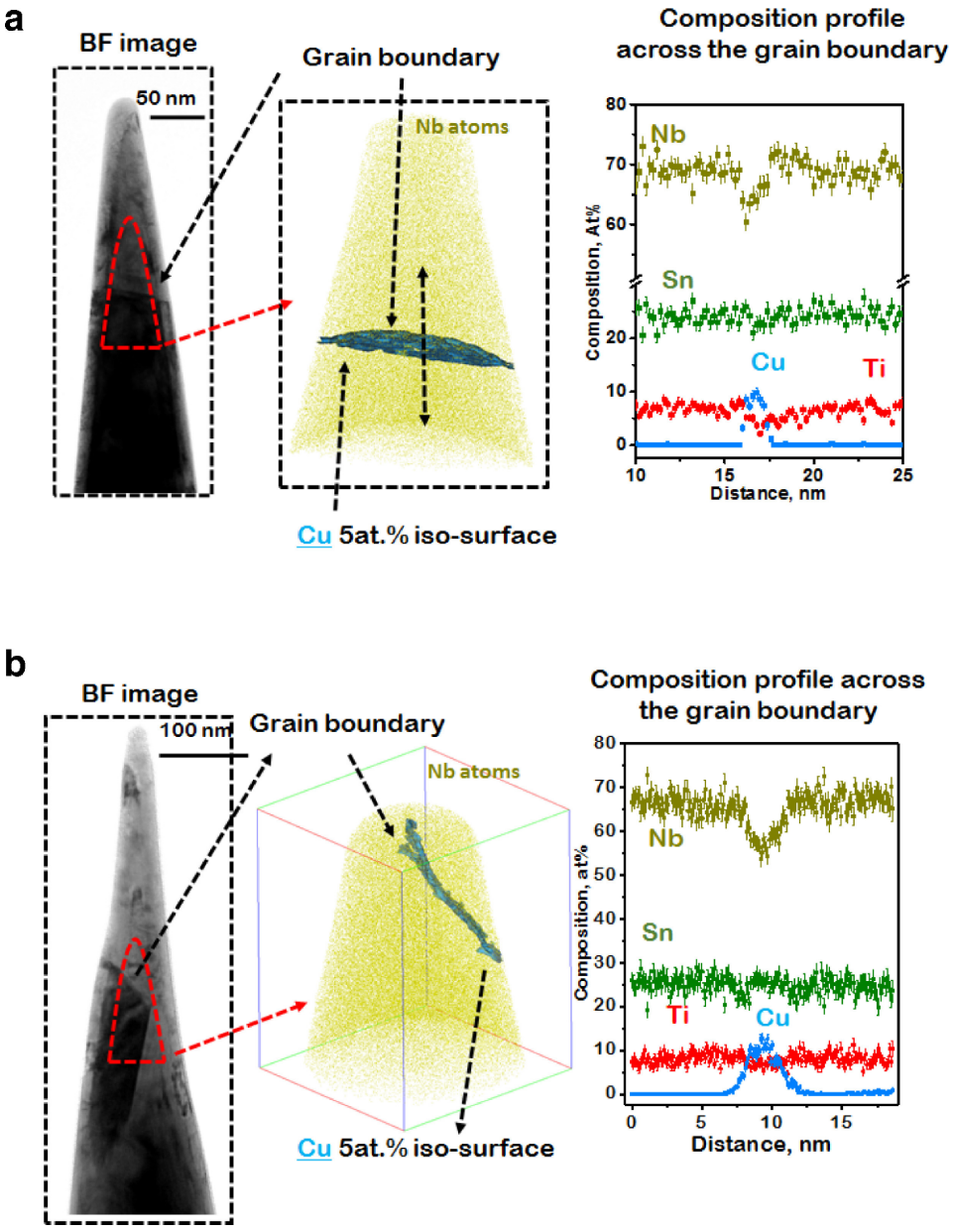


Figure 1.35: Bright field STEM images highlighting the location of an APT reconstruction at a grain boundary in a bronze processed wire a) Cu(5.5Sn,0.2Ti)/Nb b) Cu(5.5Sn)/Nb(Ti). Composition profiles were taken across the grain boundaries is shown on the right [157]

The first works using APT on internally oxidised wires were published in 2020. Xu *et al* published two papers utilising APT to understand the microstructure of new internally oxidised wires. The first paper was evidence of ZrO_2 particles in an IO1 wire, as explained in section 1.7 [134], and the second used APT to study the interface between Nb_3Sn/Nb in a Zr and O doped wire [158]. Neither paper states the quantities of Zr or SnO_2 used in the wires and both only show one APT reconstruction with no detail as to how each reconstruction was produced. Figure 1.36 shows a TEM image of what is assumed to be ZrO_2 particles and an associated APT reconstruction showing ZrO_2 particles. The TEM image and APT data are clearly not correlated with the same location, and species shown in the APT reconstruction are not labelled so it is unclear whether the so called 'grain boundary' shown is rich in Sn or another species. There is very little quantitative information on the scale of the precipitates, with a rough estimate suggesting most of the precipitates are below 10 nm. Xu *et al* have only touched the surface with how APT can assist in understanding the microstructure of Nb_3Sn wires.

The second paper shows the Nb/Nb_3Sn interface, as shown in Figure 1.37, with peaks of Zr, O and Cu at the interface with an increasing amount of Cu into the Nb_3Sn phase and a decreasing quantity of O. Very little detail or quantitative analysis can be gained from either reconstruction, however the premise of the paper discusses the rate limiting step in producing the A15 phase, which is important for A15 growth. Nb_3Sn has low bulk diffusivity, therefore most of the Sn diffusion takes place along the grain boundaries, which Xu *et al* claim leads to higher B_{c2} values due to the higher Sn content in the internally oxidised wires (with Zr and SnO_2). This is a bold claim which requires further investigation, especially as the extra pinning on the scale of the flux lines from ZrO_2 is thought to be the main reason for the higher B_{c2} values for internally oxidised wires.

The limited APT characterisation which has been conducted on bronze processed wires and internally oxidised wires does not discuss inter- and intra-grain composition and does not quantify a number density to the APCs which may be contributing to the additional pinning. There are no published APT studies on irradiated Nb_3Sn by other authors, so any localised changes in composition which could be affecting superconducting properties are unknown.

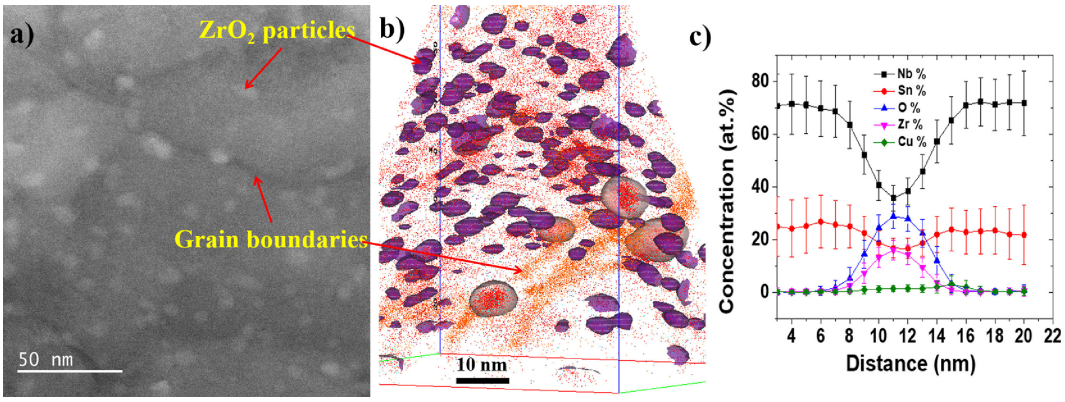


Figure 1.36: a) TEM image of an IO1 wire drawn to a diameter of 0.71 mm processed at 700°C/71hrs b) a 3D APT reconstruction of the wire c) composition profile across a large particle [134]

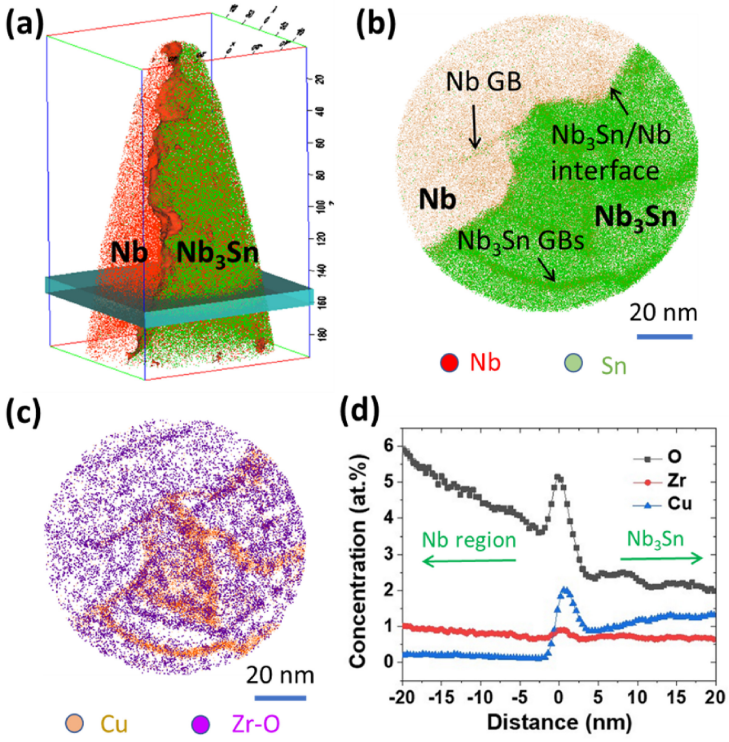


Figure 1.37: a) APT reconstruction of a internally oxidised wire containing Zr and SnO_2 b) Distribution of Nb and Sn at the Nb/Nb_3Sn interface c) Distribution of Cu and Zr-O ions d) Concentration of Zr, Cu and O across the interface [158]

Chapter 2

Materials and Experimental Methods

2.1 Materials

For fusion applications or the FCC, it is important to understand the effects of irradiation damage and APCs on the pinning landscape in Nb_3Sn wires. This work is split between two sample types: a comparative study of an as-received and fast neutron irradiated RRP® wire and a RIT APC wire.

Table 2.1 shows the RRP® samples compared in this work. The irradiated sample was irradiated in the TRIGA-II fission reactor with a fast neutron fluence of 2.82×10^{22} m^{-2} ($E > 0.1$ MeV). The RRP® samples are commercially produced with AC susceptibility measurements and irreversible magnetic moment data taken by collaborators at TU Wien. The data has been processed to produced susceptibility and pinning force curves for both RRP® samples, more details in chapter 3.

Sample Name	Manufacturer	Wire Type	Dopant at%	Heat treatment	Irradiation	APT
As-received	Bruker-OST	RRP	2 at% Ti	210 °C (48 h) 400 °C (48 h) 665 °C (50 h)	No	Yes
Irradiated	Bruker-OST	RRP	2 at% Ti	210 °C (48 h) 400 °C (48 h) 665 °C (50 h)	Yes	Yes

Table 2.1: RRP® Nb_3Sn sample list

Table 2.2 details two custom Nb alloys which have been studied in addition to the APC Nb_3Sn wire. The as-received Nb alloy is the central rod in the unreacted APC wire and the reacted Nb alloy is the central alloy in the APC wire post heat treatment. The Nb alloys have been studied to determine the original distribution of oxygen in the wire prior to heat treatment and to help understand the density and location of oxide nanoparticles in the final APC Nb_3Sn layer, further details in chapter 4. Other phases which are discussed in relation to APT data are Nb_6Sn_5 and Cu-Sn or Nb-Sn-Cu phases found in the APC sample.

Sample Name	Manufacturer	Wire Type	Dopant (at%)	Heat Treatment	APT	EPMA
APC	Florida	RIT	4 at% Ta and 1 at% Hf	550 °C (100 h) 670 °C (100 h)	Yes	Yes
As-received Nb alloy	Florida	RIT	4 at% Ta and 1 at% Hf	Arc melted 50 kPa in argon	Yes	Yes
Reacted Nb alloy	Florida	RIT	4 at% Ta and 1 at% Hf	550 °C (100 h) 670 °C (100 h)	Yes	Yes

Table 2.2: RIT Nb_3Sn and Nb alloy sample list

2.2 Characterisation Techniques

A range of characterisation techniques, on different length scales, have been used to analyse samples in this work. Care has been taken to also use complementary techniques on a larger micron scale, in order to determine that nanoscale APT data taken is representative of the larger sample.

2.2.1 Scanning Electron Microscopy

SEM's utilise a focused electron beam which interacts with the material. There are three key signals which are produced by this interaction: BSE, SE and X-rays. BSE are electrons from the original beam which are deflected by interactions with the material and SE are electrons knocked off from constituent atoms in the material by the incident electron beam. BSE images produce compositional information from the material and due to the small interaction volume of secondary electrons at the surface of the sample, SE images produce topographic information. X-rays are produced when electrons near the nucleus in the material are excited by the electron beam to a higher energy level, this leaves holes which higher energy level electrons can move into and release X-rays characteristic of the material. The interaction volume of the beam can

be altered by changing the current and applied voltage. There is a linear increase of probe size with current, however if the current is too low this limits the signal. The optimal voltage is dependent on the atomic number of the material and the size of the features of interest. Within this body of work BSE imaging has been used to show the region of Nb_3Sn in each wire.

2.2.2 Energy Dispersive Spectroscopy

EDX detects the characteristic X-rays from the SEM to map the distribution of elements in the material. A voltage which resolves the characteristic X-ray lines of the elements in the material should be selected. There is a limit on the minimum at% of an element EDX can detect which is ~ 1 at% if no peak overlaps occur in the resulting X-ray spectrum. For each Hf sample there is less than 1 at% of Hf in the Nb_3Sn layer therefore Hf is undetectable through EDX in these samples. EDX has been utilised to determine the Nb_3Sn region of each sample so that selective regions can be targeted for Atom Probe Tomography.

2.2.3 Electron Probe Micro-analyser

An EPMA uses wavelength dispersive spectroscopy (WDS) to acquire quantitative chemical information about the sample. A focused electron beam excites atoms in the sample to produce characteristic X-rays, which is the same as EDX, however EPMA has a range of crystal spectrometers which enables chemical analysis at a higher sensitivity than EDX. Prior to an EPMA scan a series of standards are used to calibrate the instrument for the sample of interest, for example pure Nb and pure Sn samples. The spot size for EPMA is around 1 μm, very similar to EDX, and therefore EPMA can be used as a complimentary tool to APT to provide micron scale quantitative chemical information. EPMA has been used in this work to look at oxygen concentrations and chemical segregation on the micron scale in a custom Nb alloy.

2.2.4 Focused Ion Beam Microscope

A FIB is a versatile technique which uses an ion beam to image, sputter and mill a material. The ion beam is commonly produced from a liquid metal source, usually gallium,

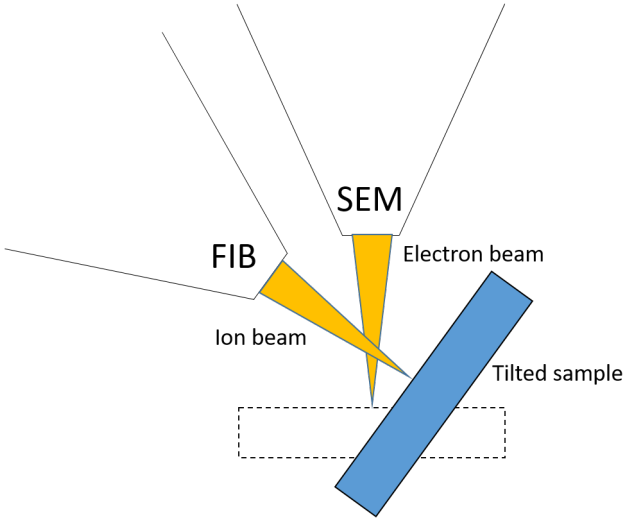


Figure 2.1: FIB angled at 54° to the SEM beam. Sample has been tilted 54° and re-centred to focus the beam on the same location as initially seen in the SEM

which consists of a piece of gallium attached to a tungsten needle. The tungsten is heated which melts the gallium, this then flows to the tip and is subsequently ionised and accelerated by the electric field towards the sample. A Zeiss Nvision and Crossbeam were used to make all samples for this work, both use a Ga^+ beam and when used for milling were operated at 30 kV, apart from the final polishing stage in tip production where 5 kV was used. The Crossbeam FIB is a Dual FIB-SEM with the FIB at 54° to the SEM column. To FIB the sample perpendicular to the sample surface the stage was tilted to 54° as shown in Figure 2.1 and the working distance adjusted to the point of coincidence between the FIB and SEM fields of view. Each FIB and SEM column has a slightly different working distance depending on how the machine has been set up, this varied between 5.1 mm to 5.3 mm for all samples in this work.

To produce an Atom Probe tip from a FIB there are four distinct stages: production of a lift-out cantilever, mounting each wedge on a silicon post, milling the wedges under a series of annulus shaped milling patterns to form a tip and a final polish to remove Ga damage [159].

In this work the procedure of using the FIB to produce a lift-out cantilever is described below. Each of the steps can be seen in Figure 2.2.

1. Measure out a beam of approximately 30 μm in length and 4 - 5 μm in thickness, as shown in a) Figure 2.2.

2. Deposit a layer of Pt/W, depending on the FIB which is used, over the beam area of approximately 2 μm in thickness. Pt/W is required as a protective layer which is eventually removed later in the milling process.

3. Mill three sides of the rectangular beam, starting at one of the short ends and then milling the two long sides, as shown in b) Figure 2.2. For the RRP® wires 3 nA 30 kV was used for each sample, for every other sample 1.5 nA 30 kV was used.

4. Once satisfied with the depth of each trench tilt the stage to 24° to undercut the two longer sides of the rectangular beam. A rotation of 180° is required between undercutting each side.

5. When there is a clear gap between the cantilever and the rest of the sample the manipulator can be attached for a lift-out, as seen in c) Figure 2.2.

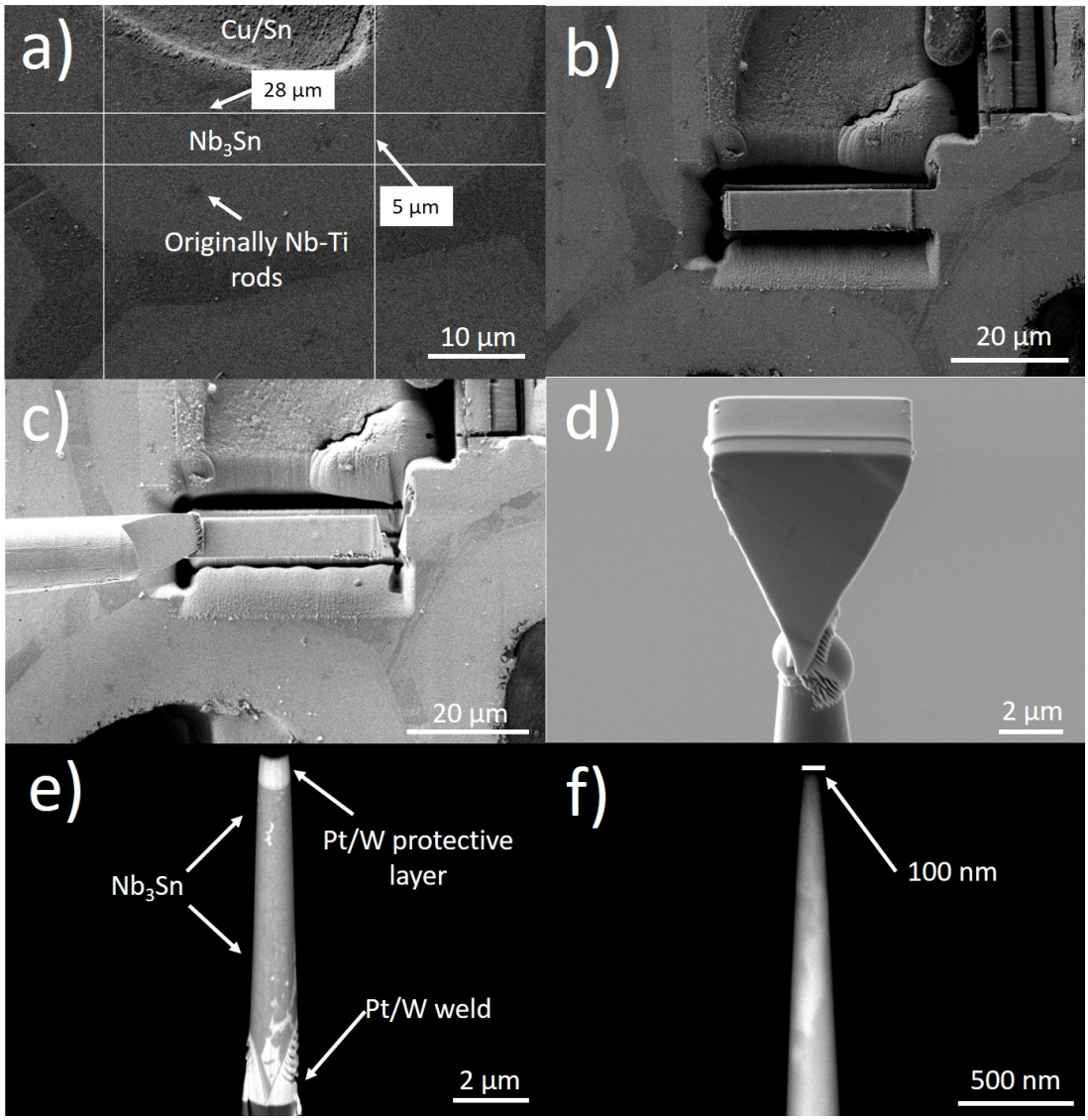


Figure 2.2: FIB preparation from original wire to finished Atom Probe tip. a) Measuring the beam for extraction b) Mill three trenches to produce a cantilever beam c) Attach the manipulator once a clear undercut can be seen at the bottom of the beam d) A mounted wedge on a silicon post cut from a section of the cantilever beam e) A wedge milled into a cylinder using an annular milling pattern f) A finished tip with a radius much smaller than 100 nm at the very top

Once the cantilever is lifted out, the rest of the sample is removed from the FIB and a coupon with an array of silicon posts is placed in the FIB. The cantilever produced can be split into $\sim$ 10 samples which are mounted on silicon posts before polishing into tips. The production of tips occurs in the following steps:

1. Place the free end of the cantilever on a silicon post and secure with a 1 μm layer of Pt/W 50 - 100 pA 30 kV.

2. Mill the end free using 700 pA 30 kV and then repeat the process with each post.

3. Rotate the posts 180° to secure the other side of the wedges with Pt/W.

4. From the mounted wedge (Figure 2.2 d) mill the left and right sides down respectively, to create a cuboid shape. This step ensures that there is material in the centre with a direct path to the silicon post, this is particularly important when tips are mounted to one side. For the Nb alloys 1.5 nA 30 kV was used, whereas for all Nb_3Sn 700 pA 30 kV was selected.

5. Change the FIB pattern to an annular mill gradually reducing the current from 700 pA to 50 pA with decreasing radii until around 50 nm is reached at the tip.

6. Finally, polish each tip at 10 pA 5 kV to remove Ga damage which may have occurred during milling. Remove approximately 300 nm from the top of each tip (finished tip shown in Figure 2.2).

2.3 Atom Probe Tomography

APT is a three-dimensional sub-nanometre characterisation technique with high chemical sensitivity, able to detect elements in parts per million. An electric field is applied to the specimen which causes highly controlled ionisation and field evaporation of atoms from the surface. The electric field at the tip is determined by equation 2.1 where F is the field at the tip, V is the positive voltage applied during the experiment, k_f is the field factor which accounts for the tip shape and the electrostatic environment, and r is the radius of the tip [160].

$$F = \frac{V}{k_f r} \tag{2.1}$$

The basic setup of the APT experiment can be seen in Figure 2.3. A sample of radius $\sim$ 50 nm is placed into an ultra-high vacuum of $< 10^{-8}$ Pa and cooled to cryogenic temperatures ranging from 20 - 80 K [160]. The most common atom probes are LEAPs which have a stage that can be moved freely in three dimensions to align the specimen a few tens of microns away from a counter electrode [161]. A direct current high-voltage power supply ranging from 1 - 15 kV is connected to the specimen to generate the electrostatic field.

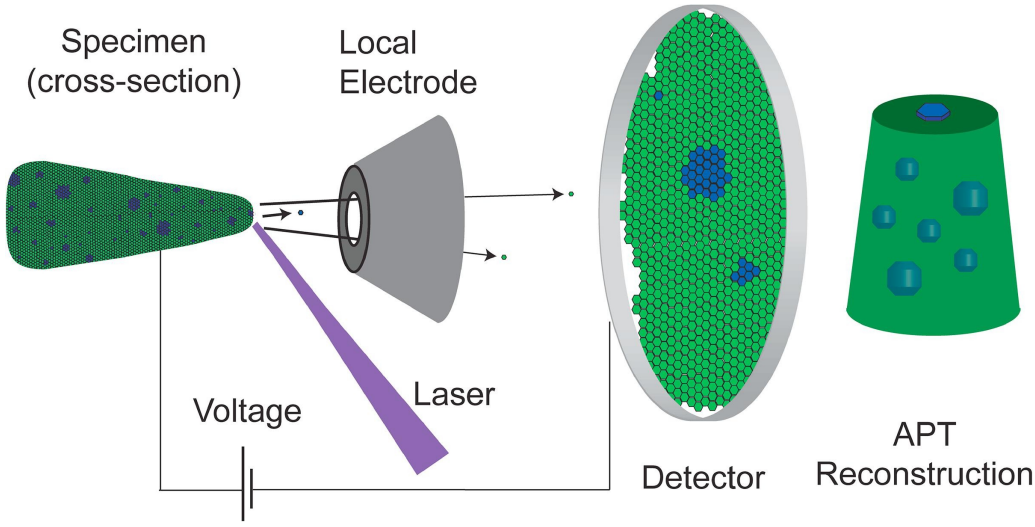


Figure 2.3: Schematic of local electrode atom probe tomography demonstrating the experimental set up and an APT reconstruction [162]

Ions are evaporated off the tip and accelerated though an electric field towards a detector. Due to the relationship between time-of-flight (t) and the known distance between the tip and the detector (L) (see equation 2.2) a m/q spectrum can be determined for the evaporated ions. Originally atom probes had a straight ion flight path, however some modern atom probes incorporate an energy compensating device called a reflectron. Due to the fact that in voltage mode ions are accelerated using an electrical voltage pulse of finite width, this leads to an uncertainty in kinetic energy and therefore a reduction in mass resolution [163]. As the DC field is constant during laser-assisted evaporation the variance in arrival times can be attributed to the finite heating duration from the laser pulse.

$$\frac{m}{q} \approx 2eV \left(\frac{t}{L}\right)^2 \tag{2.2}$$

When an ion hits the position sensitive detector, a microchannel plate in the detector triggers an electron cascade, signalling the time of arrival of the ion onto a delayed line detector. The ion detection event creates electric signals which calculate the position of the ion on the detector [161]. Each ion is assigned an X-Y coordinate and the tip is reconstructed using a reverse point projection algorithm [164] first pioneered by Bas *et al* [165]. The algorithm assumes that the apex of the tip is a perfect hemisphere, the radius of which is measured at each instantaneous point during the experiment. The sequence of ion evaporation and a geometric correction based on the radius of the tip is used to provide a Z coordinate and therefore a set of 3D coordinates is available for each detected ion. Incremental changes have been added to the original algorithm to create better iterations of analysis software. For this work IVAS 3.8.4 - 3.8.16 have been used for all analysis.

The LEAP can operate in two modes: voltage and laser assisted evaporation, both require a base DC voltage. To operate in voltage mode the counter electrode is attached to a negative pulsing high voltage, with each pulse lasting several nanoseconds. For laser assisted evaporation a UV laser pulse, on a timescale of picoseconds to femtoseconds, is required in addition to a base voltage. The benefit of using laser-assisted atom probe is that the applied voltage, and therefore the field, is held constant during evaporation. In voltage mode the cycling of an

intense pulsed electric field causes mechanical stress on the specimen which may cause the sample to break before significant data is collected from the experiment. In voltage mode the evaporation of ions is dependent on the voltage and therefore the field applied, whereas in laser mode the addition of short laser pulses means that ions can be evaporated at a lower field than that of voltage mode [166].

In laser mode, if the thermal energy is not dissipated quickly then there is an increasing chance of evaporation occurring which is not correlated to each pulse, this affects the time-of-flight measurement and produces long thermal tails in the m/q spectrum. The high temperature can also produce enhanced surface diffusion of atoms prior to their evaporation, which can lead to artefacts, such as compositional inaccuracies, and reduced spatial resolution [167, 168]. In this work all data sets have been analysed in laser-assisted mode, because applying a laser pulse enables a lower field to be applied to the sample, this is particularly important for a brittle sample such as Nb_3Sn.

In APT there are a variety of different experimental parameters which need to be considered to collect data in laser-assisted mode:

- Laser energy - The energy of the laser pulse used for thermally assisted evaporation
- Temperature - The temperature of the specimen stage, kept constant during the experiment
- Pulse frequency - How frequently a laser pulse is applied to the tip
- Detection rate - The fraction of ions detected per pulse, for example a pulse rate of 0.3% corresponds to 3 ions detected per 1000 pulses

Using a higher laser energy reduces the field on the tip, therefore for more brittle samples, such as Nb_3Sn with HfO_2 nanoparticles, a higher laser energy can optimise the chances of successful analysis. Unfortunately, as the laser energy increases, increased surface diffusion of certain species, such as, Sn migration in zirconium alloys [169], can occur. The migration of different species is sample dependent and can be accounted for by checking whether certain species appear to be more concentrated on the side of the tip closest to the laser pulse.

2.4 APT Parameter Selection

In this thesis LEAP 5000 instruments were used for all APT samples. The primary instrument used was the LEAP 5000 XS with a straight flight path and high detection efficiency of 80%. Some samples were, however, analysed on the LEAP 5000 XR which has a lower detection efficiency of 52% but a higher mass resolution as it contains a reflectron. Compared to samples such as steels, which can contain a large variety of additional elements which lie close together on the m/q spectrum, the Nb_3Sn samples contained relatively few peaks close together therefore the LEAP XS with a higher detection efficiency was more suitable for these samples than the LEAP XR with increased mass resolution.

Operation conditions were initially selected from the only APT paper which had analysed Nb_3Sn, as of 2019. Sandim *et al* selected a laser energy of 0.4 nJ, a frequency of 250 kHz, a detection rate of 1 ion per 1.25×10^5 pulses and a temperature of 60 K [154]. However, Sandim *et al* used a LEAP 3000X HR which had a 532 nm wavelength compared to the LEAP 5000 355 nm wavelength laser. As no further work had been conducted on Nb_3Sn using APT prior to the start of this work, it was important to see how the LEAP 5000 parameters affected the Nb_3Sn samples. Initial parameter sweeps were carried out on the as-received RRP® sample and a composition ratio of Nb/Sn calculated for each parameter.

2.4.1 Laser Energy

Laser energy is well known to affect the measured composition of different materials, therefore it is important to select a laser energy which is a compromise, low enough for reasonable composition measurements and high enough for brittle samples to produce enough data prior to fracture [160]. Nb and Sn have very different evaporation fields, Nb is 37 V/nm and Sn is 23 V/nm at 77 K, therefore it is important to determine the laser energy which reduces any unexpected compositional differences caused by the difference in evaporation field. The first sample tested was the as-received RRP® wire at 60 K. A laser energy sweep of 30 pJ, 40 pJ and 50 pJ with a pulse frequency of 250kHz and a detection rate of 0.3 was conducted on the LEAP 5000 XS, with 3 million ions detected per energy. The laser energy sequence was randomly

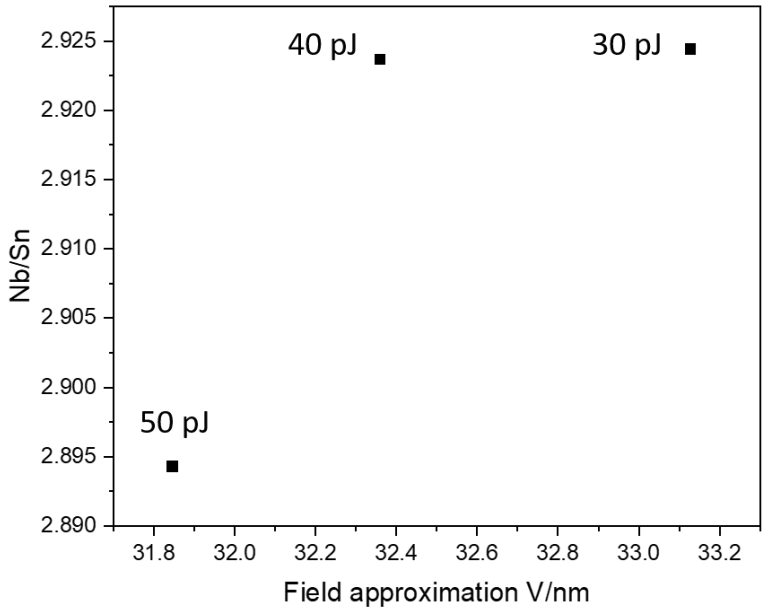


Figure 2.4: Nb/Sn ratio against predicted field based on the CSR of Nb^{3+} to Nb^{2+} using the Nb Kingham curve [160]

selected to be 30 pJ, 50 pJ and 40 pJ to make sure the laser energy did not systematically increase with the tip radius. Care was taken to remove the top surface of the tip containing any residual oxygen or gallium before a comparison was made.

The ratio of a given species evaporating in two different charge states can indicate the field strength at the apex of the tip, as predicted by post-ionisation theory by Kingham and Haydock [170]. To predict the field strength at the tip, the charge-state-ratio (CSR) of Nb^{3+} to Nb^{2+} peaks from the m/q spectrum was used with the Nb Kingham curves [171] to generate an approximation for the field at each laser energy, as shown in Figure 2.4. The ratio of Nb/Sn has been plotted against the predicted field strength to give a first estimation to how the field may be affecting the composition. The field approximation is higher than the field expected for Sn (23 V/nm at 77 K), therefore it may be expected that some Sn could be being lost between pulses, however the Nb:Sn is actually slightly low in Nb compared to the predicted composition of $Nb_{3-4.44}Sn$ [44].

On first appearance the laser energies of 30 pJ and 40 pJ appear to be closest the minimum equilibrium Nb/Sn ratio of 3. However, the part of the tip analysed at 50 pJ contains a small amount of grain boundary, which has a reduction in Nb at the boundary, as discussed in chapter 3. The reduction in Nb at the grain boundary will be reducing the overall ratio of Nb:Sn. Each of the Nb_3Sn samples analysed in this work have grain sizes $\leq$ 110 nm, therefore multiple grain boundaries are present within each tip and therefore each APT reconstruction. Considering the limited effect of laser energy, compared to the overall effect of the microstructure of the samples, and the brittle nature of Nb_3Sn, a laser energy of 50 pJ was selected for all RRP® samples to maximise the amount of data which could be collected. To properly calibrate the correct laser energy for Nb_3Sn, a sample with a grain size larger than 100 nm should be used. However, as discussed in chapters 3 and 4 even the intra-grain chemistry varies quite substantially in Nb_3Sn, so it is very difficult to choose the 'right' laser energy.

Initially a laser energy of 50 pJ was selected for the Hf doped Nb_3Sn, however the presence of HfO_2 nanoparticles meant the APT tips were more brittle and therefore the majority of the tips were fracturing. In order to reduce the field on the Hf doped Nb_3Sn the laser energy was increased to 80 pJ for all Hf doped samples. Further details can be found in chapter 4.

2.4.2 Temperature

APT needles are cooled to cryogenic temperatures to reduce the thermal agitation of the surface atoms. The cryogenic temperatures can enhance the spatial resolution of the reconstruction, minimising the chance that atoms are redistributed by the electric field [160]. Cooler temperatures are more likely to lead to fracture in brittle materials, hence the selected temperature should be a balance between data quality and data quantity. An as-received RRP® tip was analysed at 30 pJ, 250 kHz and at a detection rate of 0.3 across a range of base temperatures: 50 K, 55 K and 60 K. Each analysis contained approximately 2 million ions and between each analysis the tip was left for 30 minutes to adjust to the new temperature. The results are shown in Figure 2.5, with 60 K producing a ratio closer to an equilibrium value for Nb_3Sn. The CSR values for each temperature were also generated with only a small difference

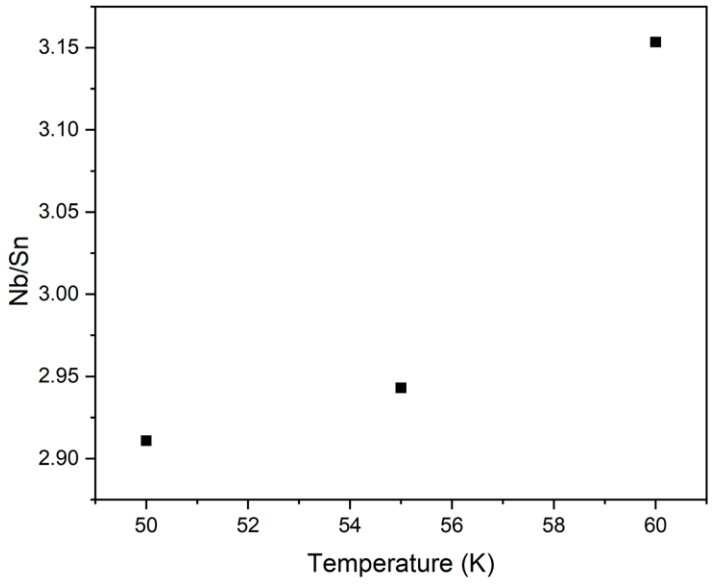


Figure 2.5: Nb/Sn against temperature for an as-received RRP® sample

between the predicted fields at 50 K and 60 K (33.3 V/nm at 50 K and 33.7 V/nm at 60 K). As the grain size in Nb_3Sn is less than 110 nm, the presence of grain boundary in these experiments affected the ratio more than the temperature. Therefore, to maximise spatial resolution, the less brittle samples, such as the RRP® wires, were analysed at a base temperature of 50 K and the more brittle Hf doped samples were analysed at 60 K where an increased yield could be achieved.

2.4.3 Pulse Frequency

A higher pulse frequency reduces the data accumulation time and produces a better signal-to-noise ratio. The pulse frequency has been selected based on the highest m/q species present within each sample and the specific instrument used for analysis. For the majority of experiments were conducted on the LEAP XS, which has a straight flight path, 250 kHz was used to collect data so that even the largest m/q peaks e.g TaO^+ at at m/q = 196.9 were resolvable. Due to the increased flight path the LEAP XR was operated at 125 kHz, as this was sufficient to resolve even the largest m/q peaks.

2.4.4 Detection Rate

Every experiment in this work has been conducted at a constant detection rate, this can be maintained as the voltage adapts during the experiment. For all RRP® samples the detection rate was set at 0.3% and for Hf doped samples the detection rate was decreased to 0.2% which appeared to lead to fewer fractures of the Hf doped samples.

2.5 APT Artefacts

2.5.1 Local Magnification Effect

The quality of the reconstructed APT data is dependent on the parameters of operation, however there can be significant material dependent artefacts. All of the Nb_3Sn samples in this thesis contain average grain sizes of $\leq$ 110 nm, and therefore tips with a z-dimension of a few hundred nanometres are likely to contain multiple grains. Although this is beneficial for grain boundary analysis, the nature of field evaporation at boundaries can produce artefacts. Grain boundaries contain an excess of defects and have a disordered structure compared to bulk grains, therefore the field required to evaporate ions can be different at the boundaries compared to the bulk of the material. A change in field at a boundary can cause a LME which can skew the local composition and width measurements of the boundary [160]. This localised change in shape at the surface of the specimen changes the ion projection properties and affects the reconstruction of the tip as the tip is assumed to be a perfect hemisphere at all points during the experiment.

LME at interfaces has been shown to minimised when the interface is perpendicular to the analysis direction during field evaporation [172], therefore grain boundaries in the z-direction are usually less affected by LME. To compare the effect of LME on Nb_3Sn samples one irradiated RRP® tip contained a boundary in the x-y plane and another along the z direction, discussed in section 2.6.4, with Cu Gibbsian excess values of 10.2 $\pm$ 0.1 atoms/nm^2 and 28.1 $\pm$ 0.9 atoms/nm^2 respectively. The reduced Γ_i of the boundary in the x-y plane is due to the erroneously increased width of the boundary due to LME.

In Γ_i calculations it is possible to partially correct for LME using the local atomic density to scale distances of each species [173, 174], however this assumes that the atomic density in this region of the specimen is consistent. Density corrections are usually performed when one boundary is present within a tip and there are no other significant changes to density e.g. precipitates, therefore these corrections are not reasonable for the complex nano-grain Nb_3Sn tips. Although LME is present to some extent in the Nb_3Sn data, a large sample size of boundaries has been collected over a large variety of angles to minimise any skew in data between samples.

LME can also be produced when there is a presence of precipitates in the material with a different evaporation field to the matrix, this can cause trajectory aberrations which affect the measured size of the precipitates. For example a precipitate with a higher evaporation field will tend to protrude on the surface, leading to a smaller local radius which will project the ions to a larger area of the detector, therefore producing an image of the precipitate which is larger in the x-y plane. The size of the precipitates will always be slightly distorted in the reconstruction, therefore a size distribution for HfO_2 clusters in Nb_3Sn and Nb_6Sn_5 has been given in terms of the number of ranged ions in each cluster in chapter 4, this measurement is not distorted by the reconstruction.

2.5.2 Segregation to Crystallographic Poles

Poles produced by the crystallography of the sample produce artificial density fluctuations within the reconstruction, as shown in Figure 2.6. High field gradients produced at poles tend to favour a lower atomic density at the centre due to trajectory aberrations [160]. The high gradient in the field can in turn cause surface migration of atoms towards poles, as shown in Figure 2.6 and 2.7, which will be dependent on the crystallographic index of the pole. There are poles within all the Nb_3Sn samples in this work, which show segregation preferentially of either Nb or Sn. The higher the laser energy used, produced stronger segregation due to increased thermal energy driving migration of the surface atoms. Each ROI selected for Γ_i calculations has been chosen to avoid poles which will distort composition measurements.

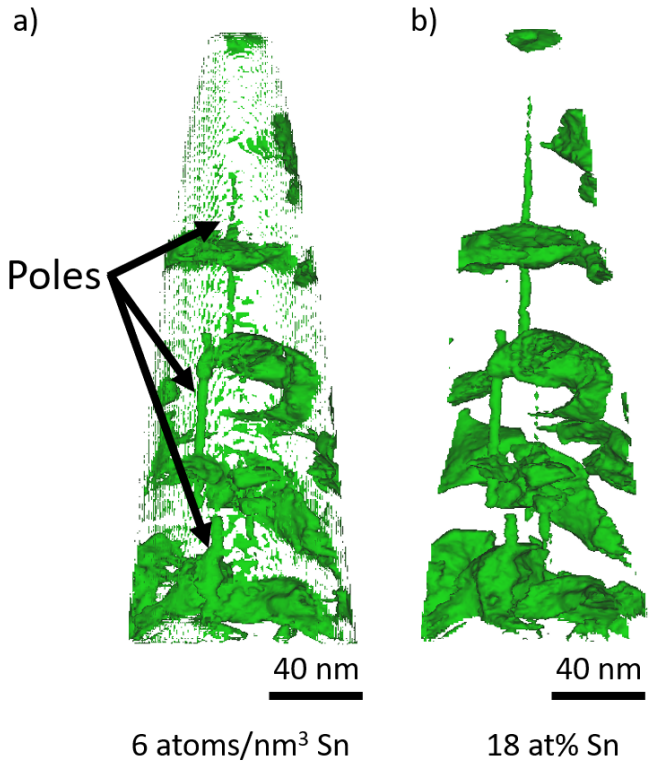


Figure 2.6: a) Reconstruction of an as-received RRP® sample showing an isosurface of 6 atoms/nm^3 of Sn highlighting 3 poles b) A concentration isosurface of 18 at% Sn showing a lower concentration of Sn than in the surrounding regions of the grains. This lower concentration of Sn corresponds with increased Nb segregation to these poles. Sn is shown here as it is the clearest species to visualise.

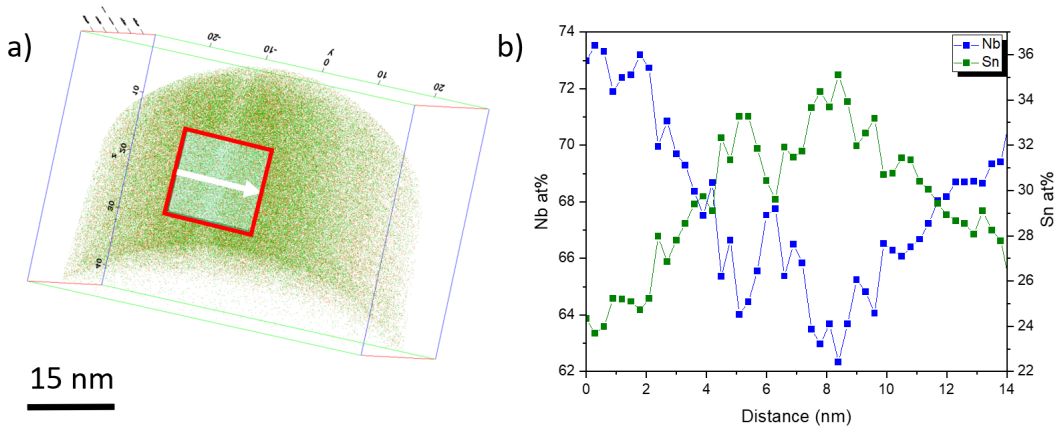


Figure 2.7: a) Reconstruction of an as-received RRP® sample showing an ROI across a pole feature, b) A 1D concentration profile showing an increase in Sn at the pole by up to 40 at% depletion of Nb of up to 16 at%

2.5.3 Asymmetry of Laser Illumination

In laser mode the laser illumination is at an angle to the surface of the tip, for example on the LEAP XS the laser is on the -x -y detector quadrant of the sample and this can cause preferential evaporation on this side of the tip. The density of the Nb_3Sn tips and the concentration of primary species Nb and Sn were checked after each reconstruction to see if there was significant variation in the laser illuminated quadrant. If significant variation was found then that data was discarded. Nb_3Sn is conductive and therefore the asymmetry of the laser illumination proved negligible.

2.5.4 Multiple Hit Detector Events

Multiple ion events occur when the detector receives multiple hits per pulse [160]. The multiple hit spectrum does not necessarily correlate with the composition of the overall material because certain species can preferentially evaporate as multiple ion events [175]. Due to limitations in detection efficiency, many multiple hit events will not be detected, therefore multiple hits data is an important way of determining which species may be systematically lost during the experiment. Figure 2.8 shows the m/q spectrum generated only from contributions

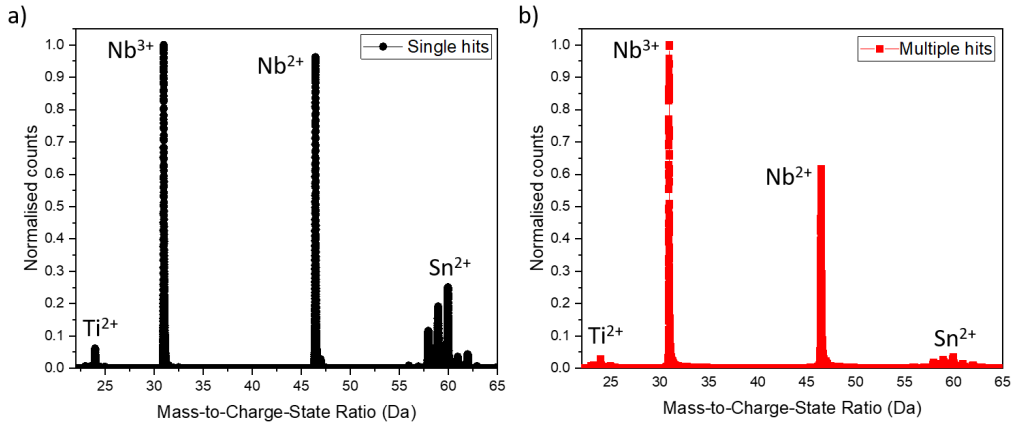


Figure 2.8: a) Normalised single hit spectrum from an as-received RRP® sample showing the key Nb, Sn and Ti peak ranges b) Normalised multiple hits spectrum from the same as-received RRP® sample showing the key Nb, Sn and Ti peaks

of multiple hit events for an as-received RRP® sample. The spectrum shows a change in ratio of the Nb^{2+} and Nb^{3+} peaks but not a significantly larger proportion of Nb multiple hits than any other species. Under the conditions which this experiment was conducted (30 pJ 50 K) the multiple hits spectrum does not show a systematic loss of species. This analysis had 20% multiple hits, substantially higher than other analyses sampled, and the composition of the reconstruction still lay within the expected equilibrium composition, as discussed in section 1.2.1, therefore the impact of multiple hits will not be discussed further in this work. A lower detection rate has also been seen to reduce the likelihood of multiple hits [176], therefore low detection rates of 0.002 and 0.003 ions per pulse were selected for all samples.

2.5.5 Compound Ions

In the RIT m/q spectra there is evidence of compound peaks, such as: HfO or Nb_2 ion peaks. The presence of these peaks does not necessarily mean that the ion was present in this compound form within the material, but that it is more energetically favourable to ionise, for example, as a HfO ion than to evaporate as adjacent Hf and O ions. To determine the difference between HfO_2 and residual Hf the individual spatial distribution of the ion peaks Hf,

O and HfO in the m/q spectrum need to be reconstructed. First the correlation between these species needed to be assessed and then individual measurements of the total number of Hf and O needed to be calculated, further details in chapter 4. Once the HfO ion peak is confirmed to reflect HfO_2 within the material then the additional oxygen ion must be found elsewhere in the spectrum. As discussed in chapter 4, the species with additional oxygen in the vicinity of HfO_2 are TaO and NbO ions which appear at the outer edge of HfO_2 precipitates and appear to be 'real' in the reconstruction, when instead these are compound ions produced due to additional oxygen in the local area.

2.5.6 Non-homogeneous Evaporation

As mentioned in section 2.4.1 each element has a different field of evaporation. The way in which ions evaporate is also dependent on their local crystallographic environment. When the RIT tips were reconstructed and the distribution of Cu ions isolated, it was clear that the boundaries did not have a regular structure, but instead appeared to show clustering of Cu, as shown in Figure 2.9. This effect is only present in the RIT sample which is doped with Ta and Hf, both Ta and Hf have higher fields of evaporation than Cu (44 V/nm for Ta and 39 V/nm at 77 K compared to 30 V/nm for Cu). As discussed in chapter 4, Ta is present at grain boundaries, therefore Ta atoms likely protrude on the surface, locally increasing the field before Ta ions can evaporate. Once the Cu atoms are exposed it is likely they are evaporating in bursts due to the higher field required to evaporate the Ta atoms, this burst then produces defocused 'clusters' of Cu atoms which are discontinuous in the z-direction. A similar effect has been observed in steels with carbides which have a higher field to the matrix and therefore appear defocused in the reconstruction [177].

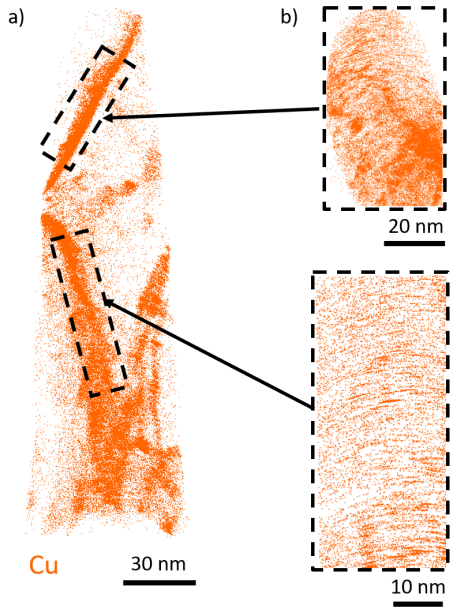


Figure 2.9: a) A Nb_3Sn tip from the RIT sample showing only Cu atoms with two grain boundaries highlighted b) Two ROIs taken which look at the plane of each grain boundary from a) showing uneven Cu segregation

2.6 APT Data Analysis Techniques

2.6.1 Peak Identification and Ranging

To determine composition measurements for atom probe samples it is important to correctly identify ionic species and be able to reproducibly range peaks in the APT m/q spectra across multiple datasets. For each peak in the m/q spectra the user must define the extent of each peak, balancing this with associated signal-to-noise ratio. The identification of m/q peaks is carried out manually by the experimentalist and the exact method of ranging the peaks varies between experimentalists.

Initial ranging using the FWHM method was selected so that there would be no issue with overlapping ranges (e.g. the Nb^{3+} thermal tail and Cu^{2+} peaks) however the FWHM method produced a Nb/Sn ratio lower than would be predicted for the Nb_3Sn composition range, particularly for the RIT samples. As can be seen from Figure 2.10, the Nb^{3+} peak has a large thermal tail which is not taken into account if the FWHM method is used. The Nb^{3+} peak

is significantly wider than the 10 Sn^{2+} peaks, therefore significant counts of Nb are unaccounted for in the final composition measurement. To compare the compositions for both the FWHM and full width method, an as-received RRP® reconstruction has been ranged and the overall ratio of Nb/Sn compared. The full width method is defined as the whole peak, including the peak tail, once the background counts are removed, for example the Cu^{2+} peaks in Figure. 2.11. The as-received RRP® reconstruction had a Nb/Sn ratio of 2.80 for the FWHM method and 3.18 for the full peak width method, with a change of Nb content from 71.9 at% to 74.4 at%. The counts in the thermal tails are due to the dissipation of heat between pulses, therefore if the temperature remains high enough after the finite duration of the pulse, then delayed evaporation can occur [160]. The delayed counts are real and have therefore been accounted for in all samples in this work.

Once known elements contained in the sample were initially identified e.g. Nb^{+}, Nb^{2+}, Nb^{3+} ion peaks for Nb, unknown peaks were identified using a program called weights developed by D. Haley [178].

2.6.2 Composition Analysis

To determine composition, two background corrections are first performed on the m/q peaks using the local range assisted background model. The model is the sum of a time-of-flight background count which is independent from voltage or laser pulsing and a contribution from the high mass tail of the peak immediately to the left of the ranged peak [160]. The local peak correction acts to fit a power law to the tail of each peak [179], in laser mode this spread in time-of-flight is due to delayed evaporation from thermal excitation.

Nb is the dominant species in all samples and at lower laser energies (e.g. 50 pJ used for RRP® samples), the Nb^{3+} peak is the dominant Nb peak. There is an overlap with the Cu^{2+} peaks when the full width of the peaks is ranged, which makes it difficult to quantify the amount of Cu in each reconstruction. Figure 2.10 shows the lack of overlap when the peaks are ranged by the FWHM method, however the FWHM underestimated the amount of Nb in the sample so cannot be used. The overlap problem can be reduced when smaller volumes of each reconstruction are extracted, as there is smaller thermal tail, therefore intra- and inter- granular data on the RRP® samples does not suffer from overlaps. Although the RIT sample does not suffer from Nb^{3+}/Cu^{2+} overlaps due to its less prominent Nb^{3+} peak, additional peak overlaps are found between Sn^{2+} and Hf^{3+}, further details found in chapter 4.

For composition measurements incorporating data from the whole reconstruction, the Cu^{2+} peaks have been ranged so that when the background counts are removed the Cu^{2+} peaks are distinct and separate from the Nb^{3+} peak, as shown in Figure 2.11.

2.6.3 Concentration Profiles and Proxigrams

To demonstrate spatial changes in chemical segregation, 1D concentration profiles have been employed across features of interest, such as grain boundaries. Each profile has been extracted as an ROI and ranged as explained in section 2.6.1. For profiles where a 3D interface is defined, a proxigram has been defined to measure the difference in composition with respect to distance from the interface, effectively a summation of many 1D concentration profiles from different points at the interface.

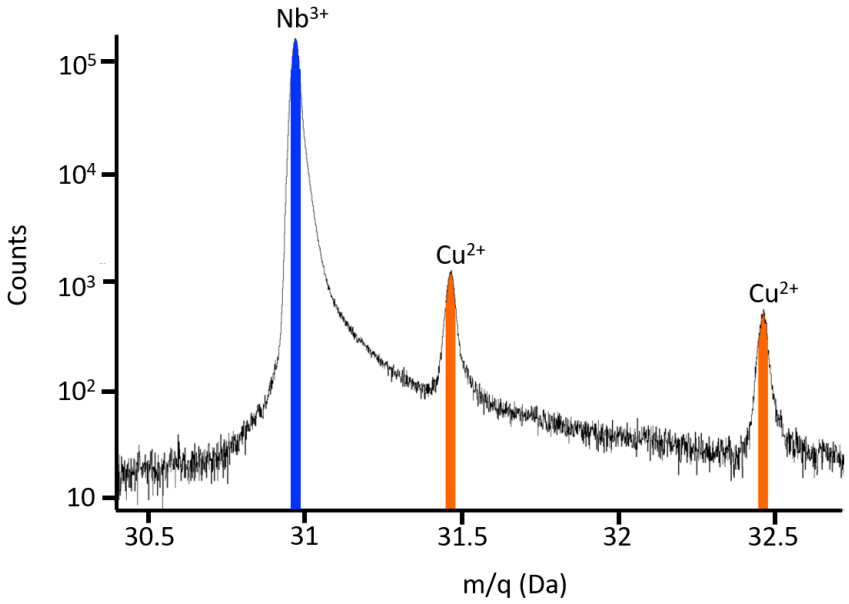


Figure 2.10: FWHM ranging of a Nb^{3+} overlap with Cu^{2+} peaks for a whole as-received RRP® reconstruction

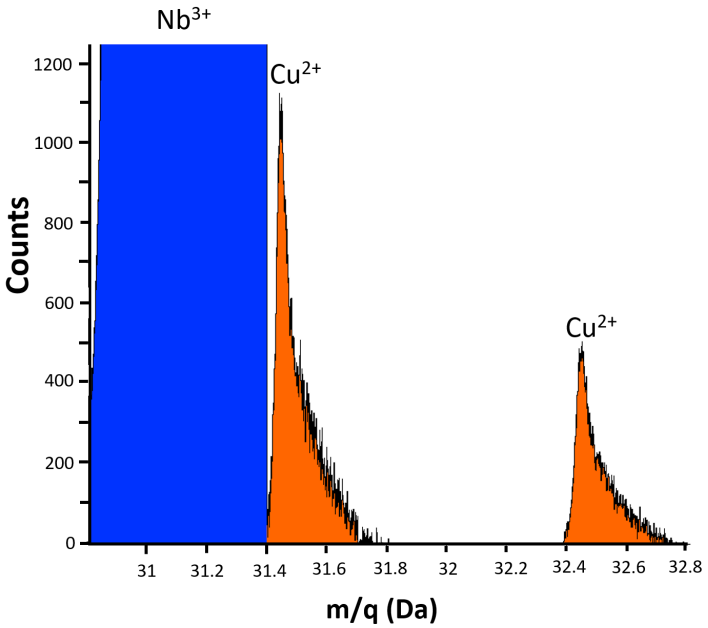


Figure 2.11: Background corrected m/q spectrum of a as-received RRP® sample displaying discrete Cu^{2+} peaks when the full width of the Cu^{2+} peaks are selected

2.6.4 Gibbsian Interfacial Excess

A common method of quantifying segregation at a boundary is Γ_i which is a measure of the number of excess solute atoms of solute i there are at an interface per unit area. First proposed by Krakauer and Seidman [180], Γ_i can be calculated from APT data through either a count or a concentration method, as shown in equation 2.3.

$$\Gamma_i = \frac{N_i^{excess}}{\eta A} = \frac{1}{\eta A}(N_i^{Total} - N_i^{\alpha\xi} - N_i^{\beta\xi}) = \frac{N_i^{Total}}{\eta A}(C_i^{Total} - C_i^{\alpha}\xi - C_i^{\beta}(1-\xi)) \quad (2.3)$$

Where N_i^{excess} is the excess number of atoms of type i at the interface, η is the detection efficiency of the atom probe used for the experiment, A is the area of the interface being sampled, ξ is the Gibbs interface, N is counts, C is concentration, α and β refer to the amount/concentration of type i solute either side of the boundary. The equations can be graphically solved by plotting the cumulative counts of atom i against all atoms as seen in Figure 2.12.

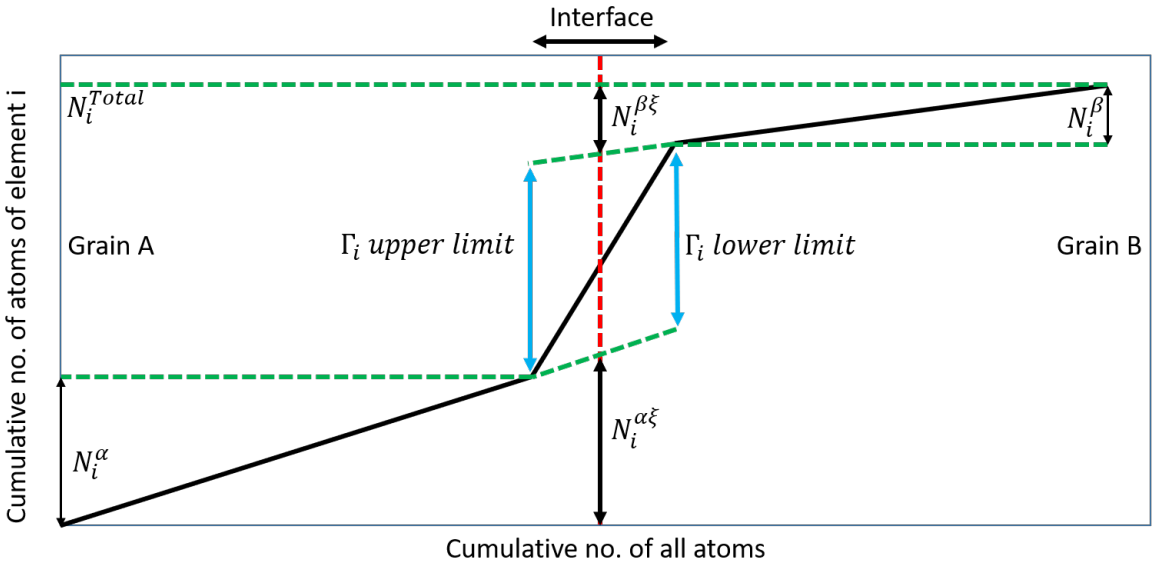


Figure 2.12: Schematic ladder diagram adapted from B. Jenkins thesis showing the change in cumulative counts of atom i through an interface and how the variables in equation 2.3 can be extracted to determine Γ_i [181].

To solve for Γ_i, code written by B. Jenkins was used to determine the excess quantities of segregating species at grain boundaries using the steps below.

- An ROI was placed across the selected boundary, with the analysis direction perpendicular to the boundary. A 1D segregation concentration profile was measured across the boundary to make sure a clear solute peak was defined.
- The m/q spectrum was isolated and re-ranged to only include ions within the ROI, and a 1D segregation profile was measured across the boundary. If the profile was wide suggesting a curved interface, or if small segregant side peaks which produced additional noise were present, then the ROI was retaken to be perpendicular to a flat region of boundary.
- The segregant profile was plotted as counts against distance. The original distance in the ROI was calculated and divided into 0.3 nm wide bins e.g. a 9 nm profile would have 30 bins, 0.3 nm is a realistic length scale for minimum APT resolution and was a sensible balance between spatial resolution and signal-to-noise ratio.
- A Poisson distribution was fitted to the concentration profile of the segregant. The interface is then defined by a threshold value selected by choosing a statistically unlikely amount of counts, below which the interface cannot exist, for this work p $<$ 0.05 was selected across all interfaces. The interface is then defined as the first and last bin which the threshold value is reached. This method removes the uncertainty of the user selecting limits of the interface [181].
- The final value of Γ_i is given as the median of the highest and lowest excess values, as can be seen graphically from Figure 2.12.

The calculation of Γ_i does have multiple limiting factors which need to be accounted for. In real APT data there is often an unphysical increase in density of atoms at an interface, due to the LME [160] and the structural defect of a boundary. At interfaces certain elements can preferentially evaporate or prove more difficult to evaporate leaving grooves or protrusions at the boundary which produces a variation in the LME, this is minimised when the interface aligns with the z-direction of the tip [172]. Even simulated reconstructions with a homogeneous evaporation field, which contain an interface, have shown the interface affects the measured atomic density [182]. Interfaces are often inhomogeneous with large variations in segregation over small distances, to minimise this variation each ROI was selected to have the largest area of interface possible, whilst maintaining a perpendicular analysis direction. Another limitation of Γ_i calculations is that the value calculated only takes account of the region in which it is sampled, this could be an issue if there is a variation in the concentration in the species within the grains or if the ROI only samples the region close to the boundary [181].

In this work Γ_{Cu} has been extracted for all grain boundaries in the Nb_3Sn samples where an ROI could be placed reasonably across the boundary. As discussed in chapter 3, Cu has very low solubility in Nb_3Sn, therefore clear Cu segregation profiles could be fitted as the Cu concentration either side of the boundary was negligible. Γ_i values for i $=$ Ti,Sn have not been calculated in this work, even when there in an increase of these species of the boundary. The local peak concentration of Ti and Sn is less pronounced than Cu, therefore there are larger errors associated with the selection of the interface.

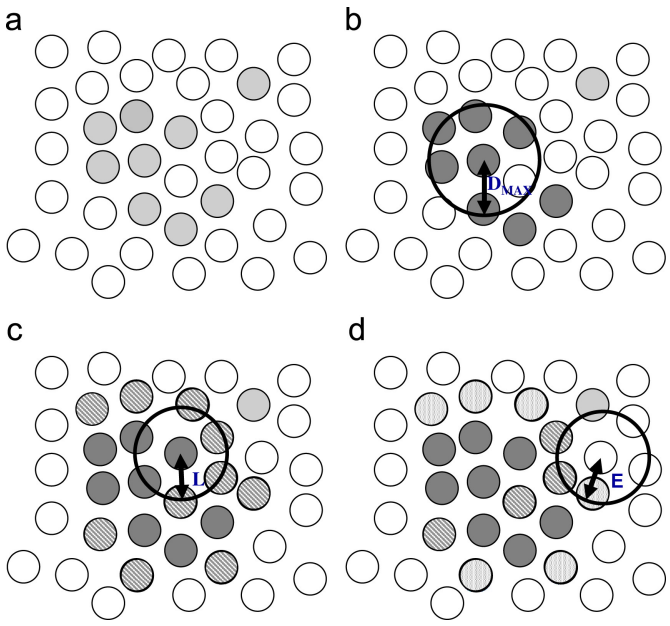


Figure 2.13: Schematic of MSM: a) solute atoms are shown shaded b) solute atoms within d_{max} are shaded dark (core atoms) c) other atoms within a distance L of the core (hatched) and d) atoms within a distance E from any other atom are removed [186]

2.6.5 Solute Cluster Analysis

The best way to define solute clusters occurring within APT data is a topic that is greatly debated in the Atom Probe community. The most common method of defining clusters in the APT community is the MSM [183–185]. This method is based on the idea that the average distance between neighbouring solute atoms incorporated within a cluster is less than that separating neighbouring solute atoms within the surrounding matrix, as shown in part a) and b) in Figure 2.13. This method requires key parameters in relation to the solute ions selected:

- A defined solute species expected in the cluster, e.g. HfO ions for the RIT sample
- d_{max} - The maximum distance between a solute atom and its nearest neighbour solute atom for them to be defined as clustered, this is typically between 0.3 - 0.7 nm.
- N_{min} - The minimum amount of atoms which can define a cluster.

Further development of the MSM was made by Vamousse *et al* [183], who performed a cluster search using the MSM, before introducing an envelope (L) step to enable the incorporation of solvent atoms into the cluster, shown in c) in Figure 2.13. All the atoms within a distance L of the core cluster of solute ions are defined as part of the cluster. This produces a shell of matrix atoms on the edge of the cluster which can then be removed by the use of an erosion (E) step, as shown in Figure 2.13 d). The erosion step helps to remove matrix atoms which may be included in the cluster analysis which may not actually be present within the real cluster. The MSM has sensitivity to local density fluctuations, and may suffer from the single-link effect (when two physically distinct clusters are joined), which can produce excessively large and unphysical clusters, and could produce many very small clusters [187]. A modification to the MSM is the core-linkage method which contains an additional parameter, order (O). Order is the number of solute atoms that must be within d_{max} of a solute atom to be defined as a core cluster atom. In the MSM $O = 1$, whereas the possibility of fluctuating O in the core-linkage method, which is a density-based algorithm, allows for greater discrimination between clustered and unclustered solute [186, 187]. The benefit of the core-linkage method becomes more pronounced as the solute concentration increases.

Limitations to the cluster core-linkage method are that all the parameters selected are defined by the user and therefore final cluster results can be strongly influenced by the parameter selection [186]. Careful selection of parameters is therefore required and the exact method and selection of parameters for each cluster search should be reported.

2.6.6 Cluster Analysis Method

The majority of cluster analysis in this work refers to identification and analysis of HfO_2 clusters in the APT reconstructions, therefore the method defined here is specific to HfO_2 clusters, however parameters for defining Cu clustering can be found in chapter 3.

To estimate the amount of HfO_2 clusters present, HfO ion isosurfaces were plotted at 1 ionic% (as shown in Figure 2.15), 2 ionic% and 3 ionic%, where the 1 ionic% tended to overestimate the amount of clusters and 3 ionic% tended to underestimate the amount of

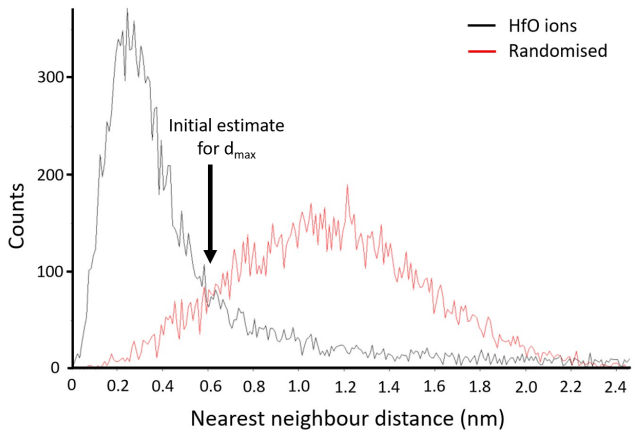


Figure 2.14: Nearest neighbour distribution of HfO ions and randomised ions for the RIT sample which contains obvious HfO_2 clustering, with an arrow showing the initial estimate for d_{max}

clusters. When cluster analysis was undertaken on IVAS these estimates helped to discount results which were vastly different to expected. To define the clusters in this work initially the MSM was selected, however, it was clear that the order needed to be increased as some of the clusters were split into multiple smaller clusters. This erroneous characterisation of clusters would have produced a reduced size distribution and increased N_D of clusters.

The steps used to define the clusters were:

1. A nearest neighbour algorithm between HfO ions at an initial $O = 1$. Using IVAS a nearest neighbour distribution measured from a complimentary randomised reconstruction is also plotted alongside the HfO ion distribution, as shown in Figure 2.14. The randomised distribution contains no clusters and therefore the initial estimate of d_{max} is the point at which the two curves cross, which in Figure 2.14 is 0.6 nm.

2. A size distribution is then measured with the initial estimate for d_{max} and $O = 1$. A distribution of cluster sizes is plotted for the original dataset and a distribution of cluster sizes is also plotted for the randomised dataset. Any clusters which are larger than the largest cluster in the random dataset are therefore not due to statistical fluctuations.

3. A count distribution, which counts the number of clusters present with a given d_{max},

is then performed with the predicted N_{min} and O = 1 to test whether the d_{max} value produced matched with the initial d_{max} from the nearest neighbour distribution. If the d_{max} value is lower than predicted by the nearest neighbour algorithm, then the process is repeated from step 1 until there is consistency in d_{max} values. If the d_{max} value is higher, such that the distance appears to be within the nearest neighbour distance of the randomised dataset, then the order parameter is increased and the process is repeated from step 1.

4. When the d_{max} values are consistent cluster analysis using the d_{max}, N_{min} and the relevant order parameter are used. Initially E = 0 because this made visualising the clusters easier as there were more counts per cluster, therefore it was simpler to see which parameters gave a better approximation to the 'true' clusters. L = 0.5d_{max} because if L is too high it can include too many additional atoms on the edge of the clusters and if L is less than half there may be gaps forming within the clusters.

5. Finally, E = 0.5d_{max} to remove excess matrix which may have been included in the cluster search.

The majority of datasets required approximately 5 iterations before the final parameters were selected, an example of appropriate parameter selection is Figure 2.15. After extracting the cluster data, further analysis of the data can produce size, composition and N_D information for the clusters present. Some clusters in each dataset will not be contained wholly within the reconstruction, these clusters are denoted as edge clusters. Including edge clusters in calculations may bias the average size of the clusters and bias compositional measurements for each cluster if the composition varies radially for each cluster.

$$N_d = \frac{N_{Total} - (0.5 \times N_{Edge})}{V_{Total}} \tag{2.4}$$

$$V_{Total} = \frac{N_{ions}}{\eta \times \rho} \tag{2.5}$$

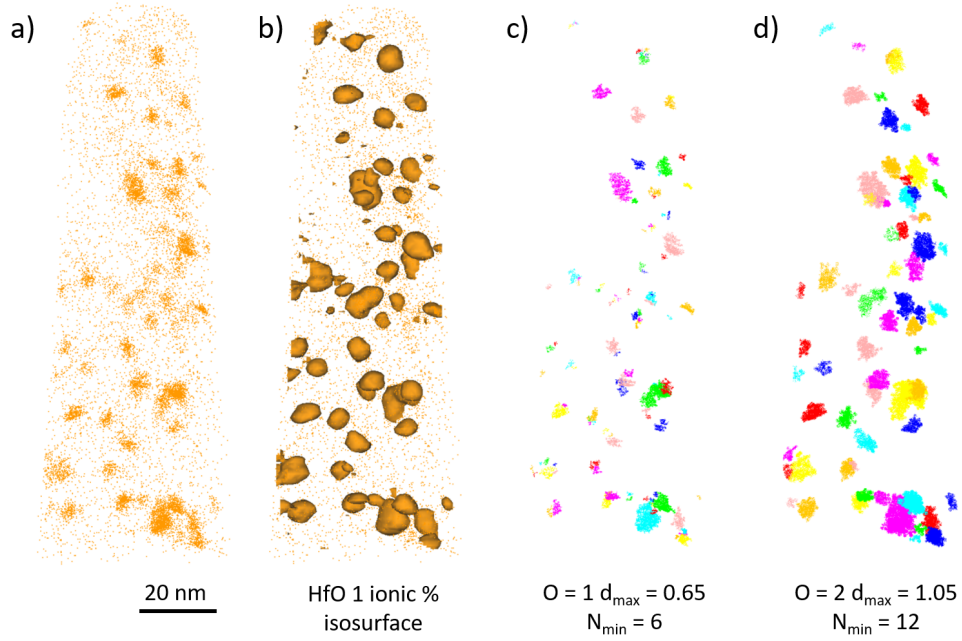


Figure 2.15: a) APT reconstruction of Nb_3Sn in an RIT tip with only HfO ions shown b) A HfO 1 ionic% isosurface defining 58 clusters, an initial cluster estimate c) A O = 1 cluster search where the clusters are erroneously defined, appearing too small and some clusters are split into multiple clusters, 110 clusters are defined d) The final selected cluster parameters for this sample with 65 clusters defined

N_d of clusters is therefore calculated using equation 2.4 where N_{Total} is the total number of clusters detected in the cluster search, N_{Edge} is the number of edge clusters in each dataset and V_{Total} is the total volume of each dataset. To calculate V_{Total} equation 2.5 is used where N_{ions} is the total number of ranged ions in the dataset, η is the detection efficiency of the atom probe (80% for the LEAP XS and 52 % for the LEAP XR) and ρ is the number of Nb and Sn atoms per m^3 in the A15 structure (54.05×10^{-27} m^3). For each sample with clustering, the mean of the N_d and its standard deviation are calculated.

Volume fraction percentages (V_f) are calculated using equation 2.6.

$$\sigma_{V_f} = \frac{N_{Ranged}^{Cluster} - N_{Nb}^{Cluster} - N_{Sn}^{Cluster}}{N_{ions}} \times 100 \tag{2.6}$$

To produce an estimate for the volume of each cluster equation 2.7 assumes each cluster is spherical, as evidenced by aspect ratio and oblation data in chapter 4, and that the atomic density of the clusters is the same as the atomic density of the matrix. Nb and Sn counts have been subtracted from the volume calculations under the assumption that Nb and Sn are not part of the final clusters, this applies to any clusters in the A15 structure or Nb_6Sn_5, however in clusters in the Nb alloy, only the Nb counts are subtracted. Cluster diameters were then calculated from the cluster volumes for each reconstruction. The diameter of each cluster is an estimated value, therefore a more robust approach is to display the ranged ion count as a measure of cluster size for each cluster. The total number of ions is not shape dependent, therefore it is not dependent on the change in field at the cluster which may cause aberrational narrowing or widening of the cluster in the atom probe reconstruction. Estimations of diameter are important to the superconducting community, however also included is a size distribution of the clusters based on ranged ions to show the spread of clusters within each region.

$$V_{Cluster} = \frac{N_{ions} - N_{Nb} - N_{Sn}}{\eta \times \rho} \tag{2.7}$$

Analysis of cluster data was carried out using code developed by B. Jenkins, adapted by M. Carter and further adapted by the author of this work.

Chapter 3

RRP®: A Comparison of As-received and Neutron Irradiated Samples

As explained in section 1.8, understanding how neutron irradiation affects the properties of Nb_3Sn is important for its application in both fusion reactors and particle accelerators. Presented in this chapter is an analysis of two commercial RRP® wires produced by Bruker-OST, one in the as-received condition and the other irradiated in the TRIGA-II reactor with a fast neutron ($E > 0.1$ MeV) fluence of 2.82×10^{22} m^{-2}, as calculated by S.Pfeiffer [20]. It should be noted that, although the samples are the same type of wire, the two samples are from two different sections of an original RRP® wire. Further details on the samples can be found in section 2.1.

A Quantum Design MPMS XL SQUID magnetometer was used by collaborators at TU Wien to measure the irreversible magnetic moment (m_{irr}) of the two samples over a range of temperatures (4.2, 5, 6...,15 K) using field steps of 0.2 T up to a maximum field of 7 T. The samples were 4 mm lengths of wire with their axes perpendicular to the applied field (B). J_c values were calculated using the Bean critical state model from the m_{irr} data as explained by T Baumgartner *et al* [151]. T_c has been calculated from AC susceptibility measurements (m_{ac}) using a frequency of 30 Hz and field of 30 μT. Further analysis of the J_c and m_{ac} data has been carried out by the author of this work.

3.1 Superconducting Results

3.1.1 Calculating T_c

To determine T_c the m_{ac} data was converted to χ data using equation 3.1, where D_m is the demagnetising factor, which is 0.5 for a transversal cylinder. V is the volume of all the filaments, which has been approximated as a hexagon containing both the Nb_3Sn layer and the outer Nb layer for the cross section of each filament, multiplied by the total number of filaments in each wire (108). Nb is also superconducting with a transition temperature at $\sim$ 9 K [188] so therefore needs to be included in the superconducting volume. The non-superconducting region in the centre of each subelement will be shielded by the outer superconducting region and therefore needs to be included in the superconducting volume. Equation 3.1 resulted in values slightly below -1, likely due to the a slight off axis misalignment of the sample in the magnetometer. For simplicity χ was set below the transition to -1 for both samples. To calculate the T_c of the two samples, the mid-point of the superconducting to normal transition has been taken. The as-received sample had a Nb T_c of 8.9 $\pm$ 0.7 K and a Nb_3Sn transition of 17.6 $\pm$ 0.4 K, whereas the irradiated sample had a Nb T_c of 9.0 $\pm$ 0.3 K and a Nb_3Sn transition of 16.6 $\pm$ 0.6 K. The width of the T_c transition is dependent on the properties of the whole material, and a sharper T_c is reflective of a Nb_3Sn wire which has a very similar Sn content throughout the wire. The irradiated sample has a broader width of Nb_3Sn transition, at approximately 1.2 K compared to 0.8 K, which suggests that there is a larger variation in the bulk Sn content through the irradiated wire.

$$\chi = \frac{1}{1 - D_m} \frac{m_{ac}\mu_0}{BV} \tag{3.1}$$

The decrease in T_c of Nb_3Sn wires due to fast neutron irradiation is well documented in the literature [140, 142, 190]. Reasons for this decrease in T_c are explained in section 3.7.

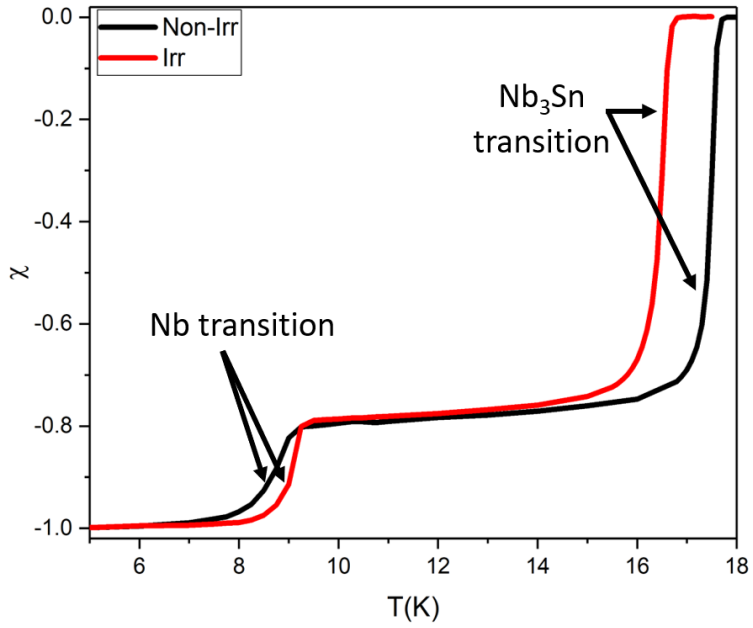


Figure 3.1: χ against Temperature (T) for the as-received and irradiated samples, with both the outer Nb and the Nb_3Sn transitions included [189]

3.1.2 F_p

$$F_p = |\vec{B} \times \vec{J_c}| \tag{3.2}$$

To calculate the volume pinning force, equation 3.2 has been used with the J_c data produced from the Bean critical state model provided by collaborators in Vienna. Equation 3.2 can be simplified to $F_p = J_c B$ due to the applied field and the irreversible currents being approximately perpendicular. The pinning force in as-received, polycrystalline Nb_3Sn can be fitted by the Dew-Hughes model for surface pinning at grain boundaries [49] with exponents $p = 0.5$ and $q = 2$ for equation 1.7 in section 1.3. However, previous work on neutron irradiated Nb_3Sn has shown a shift in F_p towards point pinning [191], which has exponents for equation 1.7 of $p = 1$ and $q = 2$. To verify whether the data for the as-received and irradiated samples follow this trend the normalised pinning forces curves have been plotted against reduced field for each sample. An explanation for how B* was calculated can be found in section 3.1.3. Data below 7 K are not included in the normalised pinning plots because the peak pinning forces

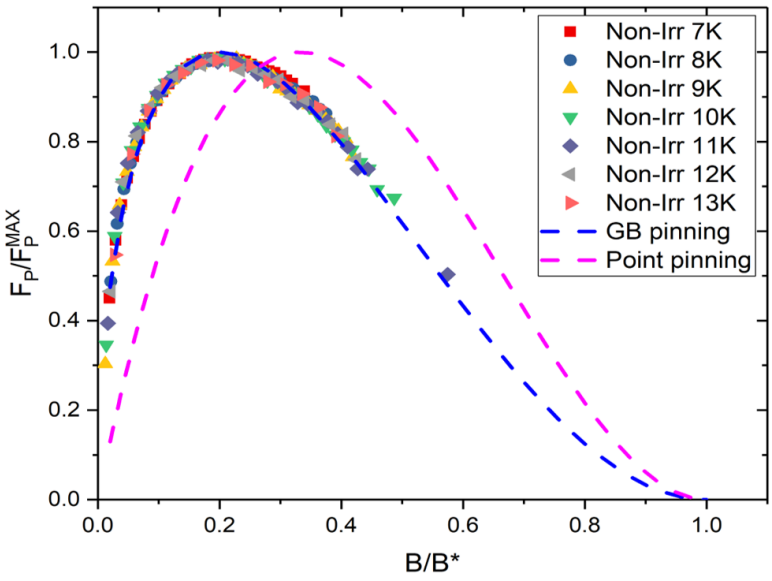


Figure 3.2: Plots of F/F$_p$ against B/B* at temperatures between 7 - 13 K for the as-received sample [189]. The data points clearly follow the grain boundary pinning model.

were not reached within the 7 T field range, and data at 14 K and 15 K is not included because there were too few data points available. OriginPro software has been used to plot the grain boundary and point pinning functions. The normalised pinning plot for the as-received sample can be seen in Figure 3.2, with the data closely following the grain boundary surface pinning function. The normalised pinning plot for the irradiated sample in Figure 3.3 is shifted right towards the point pinning function, demonstrating that the irradiated sample contains a mixture of grain boundary and point pinning.

In the literature, F$_p$ is often compared between samples at 4.2 K, [66, 151, 192] which is likely to be the temperature used for any application of Nb_3Sn. The increase in pinning force of the irradiated sample compared to the as-received sample can be seen in Figure 3.4, where there is 58% increase in the overall pinning force from 84.3 GN/m^3 to 134 GN/m^3 and a clear shift in the pinning force from a peak at 5.1 T to 7.1 T. An increase in pinning force has previously been seen in RRP® wires after fast neutron irradiation [66, 151, 191].

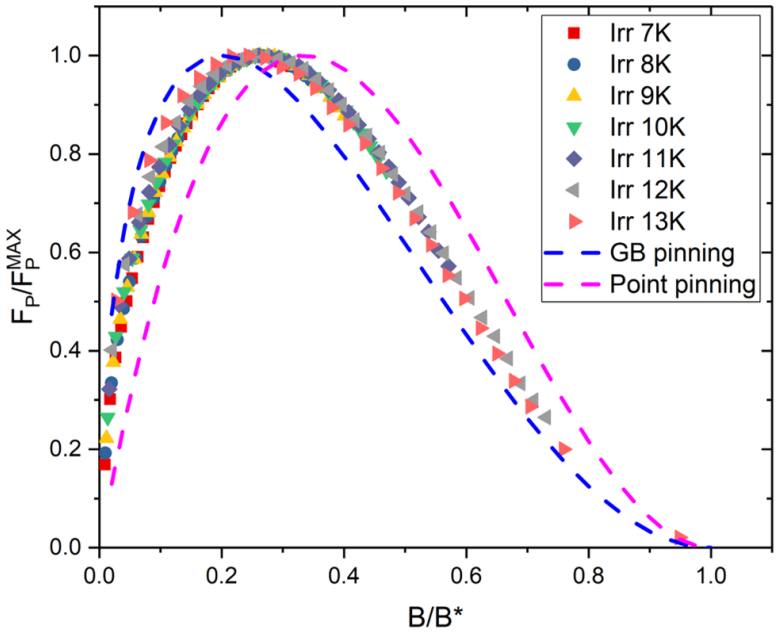


Figure 3.3: Plots of F/F$_p$ against B/B* at temperatures between 7 - 13 K for the irradiated sample [189]. The data points are shifted towards point pinning, implying a combination of grain boundary and point pinning mechanisms are present.

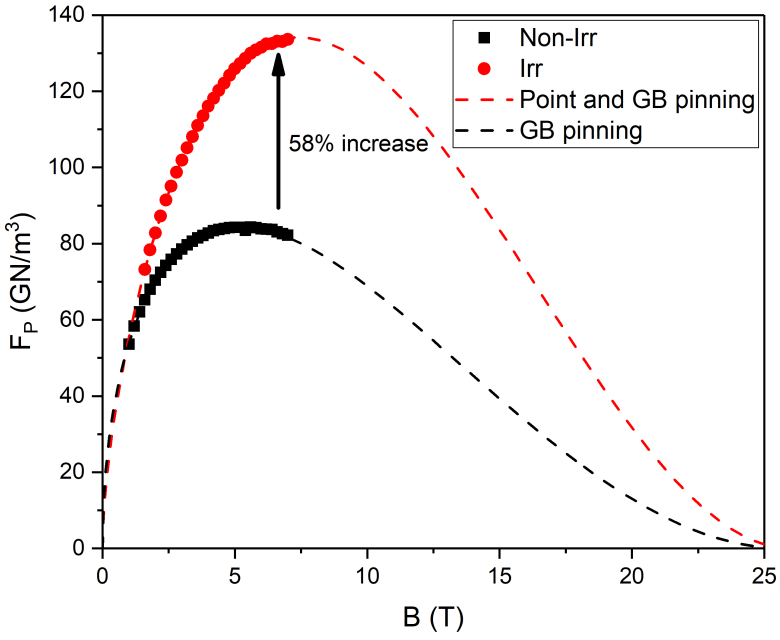


Figure 3.4: F$_p$ plotted against B at 4.2 K for the as-received and irradiated samples. There is an increase in F$_p^{MAX}$ and a increase in the field at which F$_p^{MAX}$ occurs after irradiation.

3.1.3 Estimated B_{c2}

To produce an accurate value for B_{c2} normal resistivity measurements are required, however this data was unavailable for the both RRP® samples, therefore B_{c2} has been estimated. To plot the reduced field graphs in Figures 3.2 and 3.3, an estimate for B_{c2} was made by fitting the respective pinning force exponents to the as-received and irradiated sample using OriginPro software which iterates using the Levenberg-Marquardt algorithm. The best fit from the software then produced an estimate for B_{c2} which will be called B^*. All the extrapolated B^* values for the 7 - 13 K temperature range can be found in Figure 3.5. Unfortunately extrapolation of B^* produces unrealistic values for $B^*(0)$ of 37.7 $\pm$ 0.6 T and 39.4 $\pm$ 0.9 T for the as-received and irradiated sample respectively, this is likely due to the limited maximum field of 7 T available.

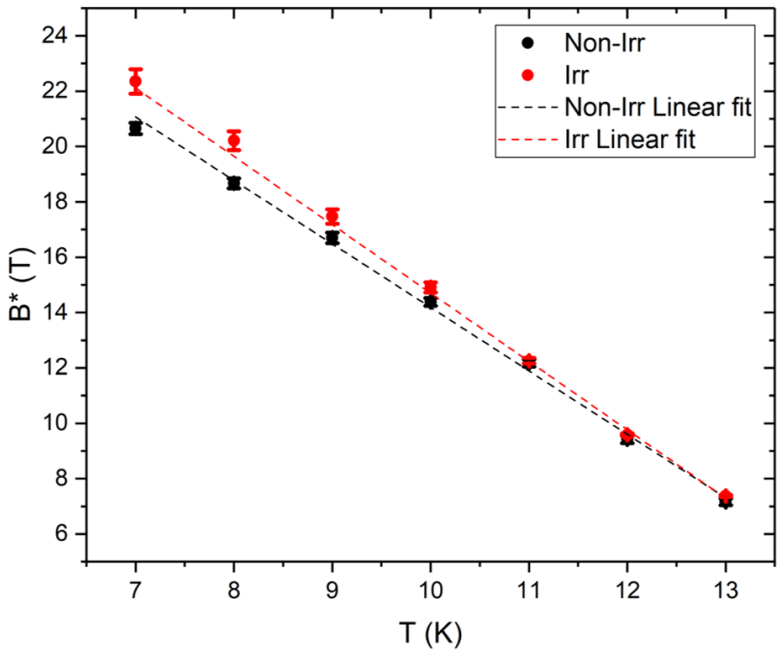


Figure 3.5: Plots of B^* against T for the as-received and irradiated sample, with error bars in B^* associated with the best fit in OriginPro [189].

Often the Kramer function ($Kr = J_c^{0.5}B^{0.25}$) is plotted against B to approximate for the $B_{c2}(0)$ [27, 193, 194]. This relationship was postulated to be valid beyond the F_p^{MAX} where Kramer assumed de-pinning occurs through synchronous shear of the flux line lattice [56]. However, because the field of the SQUID used was limited to 7 T not enough of the Kramer plot produced gave a reliable linear relationship from which $B_{c2}(0)$ could be extracted leading to the severe overestimations of $B_{c2}(0)$. Previously, deviations in linearity in the mid-field range were thought to be caused by variation in Sn content in the Nb_3Sn regions of wires [45], however recent work on modern Ti, Ta and Hf wires has shown similar extrapolations can lead to an overestimation in $B_{c2}(0)$ [58].

$$h^*_{fit}\left(\frac{T}{T_c}\right) = 1 - \frac{T}{T_c} - C_1\left(1 - \frac{T}{T_c}\right)^2 - C_2\left(1 - \frac{T}{T_c}\right)^4 \tag{3.3}$$

$$B_{c2}(T) = \frac{B_{c2}(0)}{0.693}h^*_{fit}\left(\frac{T}{T_c}\right) \tag{3.4}$$

To estimate the effect of irradiation on the upper critical field at 0 K ($B_{c2}(0)$) an approximation to B_{c2} using the Helfand and Werthamer method [195] was made. T. Baumgartner developed an approximation to the dirty limit of the Helfand and Werthamer method by using parameters $C_1 = 0.153$ and $C_2 = 0.152$ with equations 3.3 and 3.4 [151]. The approximation to B_{c2} when fitted between 10 - 15 K gave values of $B_{c2}(0) = 31.4 \pm 1.6$ T and $B_{c2}(0) = 32.5 \pm 1.9$ T, where the error is determined by the largest error in gradient given by the linear fit. Although these values for $B_{c2}(0)$ are approximate, both values are consistent with normal resistivity measurements on similar RRP® wires [151]. These calculated values will be discussed in the light of APT results on as-received and irradiated samples.

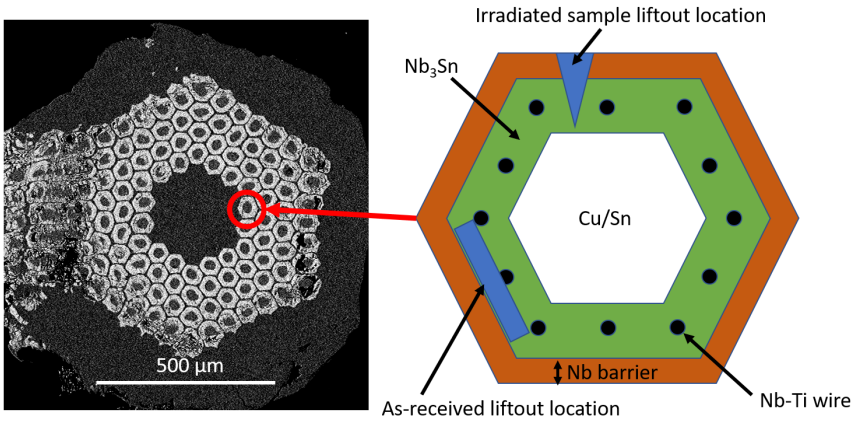


Figure 3.6: SEM image of a cross-section of the as-received wire after mounting, grinding and polishing with a schematic of a subelement displaying the Nb_3Sn region in green. The lift-out geometries for both the as-received and irradiated sample are displayed with the as-received lift-out within the plane of the page and the irradiated lift-out into the plane of the page.

3.2 Sample Preparation for Atom Probe Tomography

The as-received sample arrived as one short piece of RRP® wire approximately 1 cm in length. The sample was cut using a slow saw to produce two sections of approximately 0.5 cm in length wire. One length of the wire was mounted in bakelite then ground and polished to leave a cross-section of the original RRP® wire, as shown in Figure 3.6. The thinness of the sample limited the amount of grinding possible, therefore only the central filaments of the wire were suitably ground and polished for FIB preparation, with residual saw damage on the outer filaments. Figure 3.6 also shows a schematic of a subelement with an outer Nb barrier layer, an inner Cu/Sn region and a Nb_3Sn region containing Nb-Ti wires which dope the Nb_3Sn to an estimated 2 at% Ti. The irradiated sample arrived as subelements stuck onto carbon tape, Figure 3.7. Separating the subelements reduced the level of radiation produced and therefore made transporting and handling the sample easier. Prior to a FIB liftout procedure on the irradiated sample, an EDX map, Figure 3.8, was produced on a tilted end of one of the subelements to check the thickness of the Nb layer which would later need to be removed prior to producing APT tips. The Nb layer measured approximately 1.2 μm, which could then be accounted for during final annular milling stages in the preparation of tips.

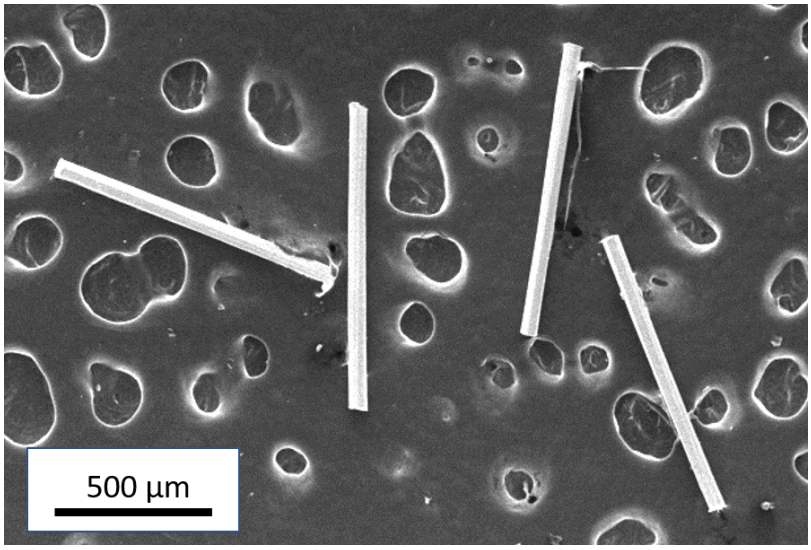


Figure 3.7: SEM image of four subelements of the irradiated sample stuck onto carbon tape

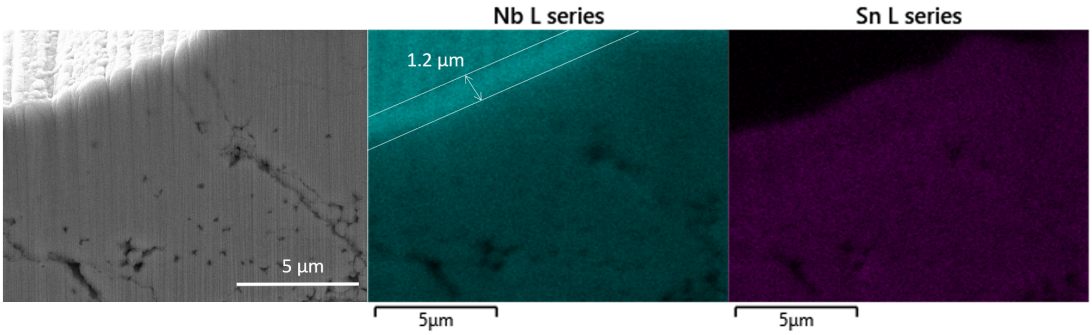


Figure 3.8: EDX map of the edge of the cross-section of an irradiated subelement displaying the Nb and Sn element maps

Weak Sn concentration gradients are known to be present within Nb_3Sn RRP® wires [196], with a higher Sn content associated with proximity to the central Cu/Sn region. Lower temperature heat treatments are used such that Sn can diffuse through the original Nb elements, then a higher heat treatment is applied (665°C) to encourage the reaction to form the A15 compound. To make sure that the APT tips were taken from approximately similar locations with equivalent Sn contents, FIB liftouts were taken along the outer edge of the cross-section for the as-received sample and taken from the top of the subelement for the irradiated sample, as indicated in the schematic in Figure 3.6. The standard FIB liftout and sharpening procedure was then followed as detailed in section 2.2.4.

3.3 Atom Probe Tomography Experimental Parameters

Both the as-received and irradiated atom probe tips were analysed at a laser pulse energy of 50 pJ, a base temperature of 50 K or 60 K, and a detection rate of 0.2 - 0.3 on both the LEAP 5000 XS and LEAP 5000 XR. The initial experiments were conducted at 60 K, due to the brittle nature of Nb_3Sn, however once the temperature was shown to have little effect on the m/q spectrum and that the experiments were viable at 50 K, this lower temperature was used to limit thermal surface diffusion on the tip, as discussed in section 2.3. The majority of experiments were conducted on the LEAP 5000 XS with a pulse frequency of 250 kHz and two experiments were conducted on the LEAP 5000 XR at 125 kHz when the LEAP 5000 XS was unavailable.

3.3.1 Reconstruction Parameters

All data was reconstructed using IVAS 3.8.14 software from CAMECA. Each reconstruction was based on the voltage curve, with standard time-of-flight and voltage corrections applied to the m/q spectrum. As Nb is the most abundant element in Nb_3Sn, the initial radius of the reconstruction was estimated using the voltage and the electric field required to evaporate pure Nb, which is 37 Vm^{-1} at 77 K.

3.4 Results from Atom Probe Tomography: As-received Sample

In total 7 atom probe tips from the as-received sample were analysed and 11 atom probe tips from the irradiated sample. The volume of each tip was measured by placing a density isosurface over the reconstructed and ranged tip and encapsulating the volume inside. The LEAP detection efficiency is already accounted for in the δz calculation during reconstruction so does not need to be applied to measured volumes. The total volume of APT data analysed for the as-received samples was 8.6 $\times$ 10^6 nm^3 and 5.8 $\times$ 10^6 nm^3 for the irradiated sample. The final volumes are dependent on the exact reconstruction parameters used, and care was taken to use the same reconstruction parameters for each analysis. The main analysis of the tips can be separated into intra-grain compositional analysis (inner grain composition), inter-grain compositional analysis (grain boundary segregation and Γ_i) and additional features which have been identified within the tips (dislocations and residual Nb).

3.4.1 Intra-grain Compositional Analysis

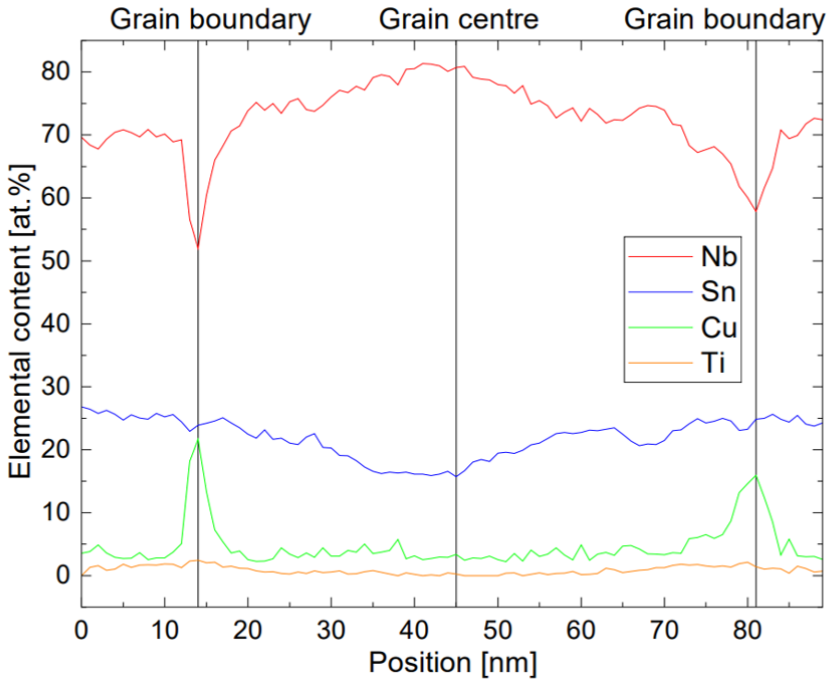


Figure 3.9: TEM EDX profile across a 2 at% Ti doped RRP® wire [20]

On the micron scale, binary Nb_3Sn is known to have an equilibrium concentration of 18 - 25 at% Sn [44] and recent EXAFS experiments have shown that when Ti is doped in Nb_3Sn that Ti atoms only substitute on the Nb sites in the A15 structure, not the Sn sites [120]. However, little is known about the intra-grain composition of Nb_3Sn wires, to the author's knowledge, only one published TEM EDX profile of an RRP® wire from one grain boundary through the grain to a second boundary [20], as shown in Figure 3.9. The TEM EDX profile shows a depletion of Nb at the grain boundaries and an increase up to approximately 80 at% Nb at the centre of the grain.

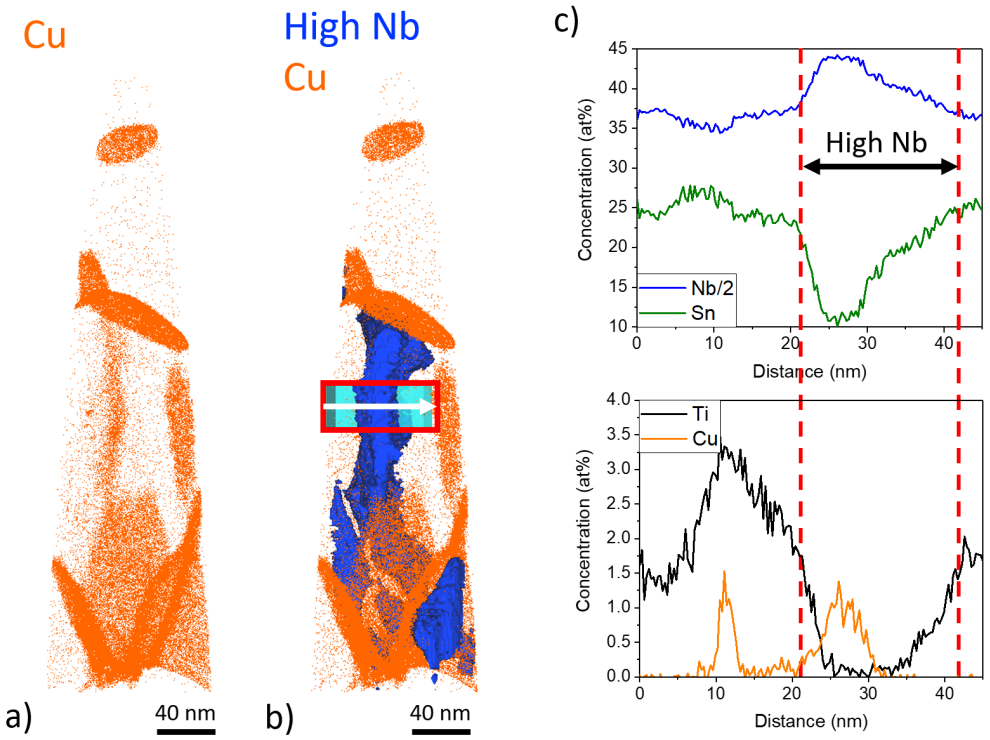


Figure 3.10: a) APT reconstruction of an as-received tip showing just the Cu atoms which are segregated to the grain boundaries b) An isosurface of 82 at% Nb and Cu atoms to show the locations of the grain boundaries and an ROI shown in blue from which a 1D profile is calculated in the direction of the arrow. The high Nb regions in this tip are $\sim$ 16% of the tip volume and the grain boundaries (defined by Cu 2 at% isosurface) are $\sim$ 14% of the total tip volume c) A 1D profile from a low Nb Nb_3Sn region to a high Nb Nb_3Sn region. Composition of the high Nb and low Nb regions in this tip and all other as-received tips sampled is included in Figure 3.35.

Initial APT investigations into the intra-grain compositions showed distinct regions of Nb_3Sn which differ in composition. Figure 3.10 shows a typical APT dataset containing regions of Nb_3Sn outside the equilibrium composition range, highlighted in blue. These high concentration Nb regions show a reduction in Ti and an increase in Cu content from an initial 1D concentration profile, as shown in Figure 3.10. In Figure 3.10 the first peak in the 1D profile is due to the incorporation of a Cu cluster at one end of the ROI. In this work regions of Nb_3Sn outside the equilibrium composition range (18 - 25 at%) will be defined as 'low Nb' with $\leq$ 75 at% Nb and 'high Nb' with $\geq$ 82 at% Nb. To analyse the intra-grain compositions further, isosurfaces were used to separate the differing regions of low Nb and high Nb regions and the compositions were calculated.

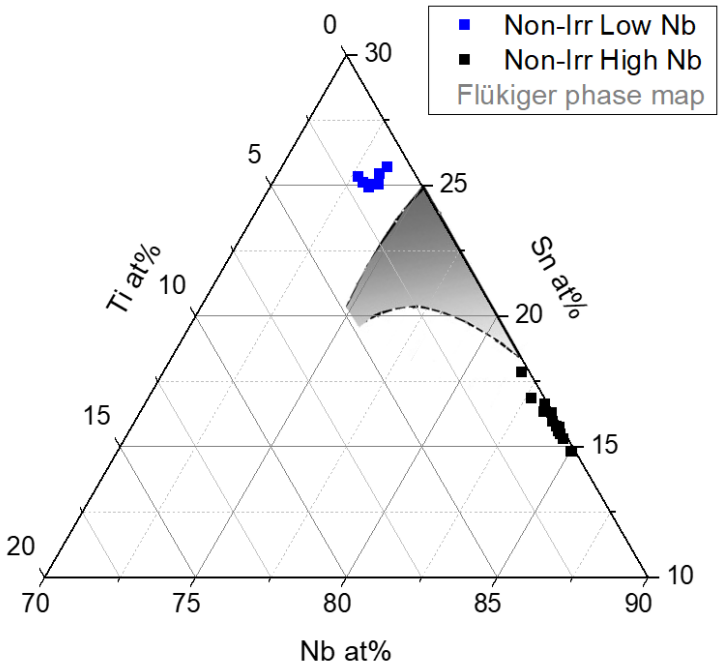


Figure 3.11: A ternary composition map showing the composition measurements of the high and low Nb regions in the as-received sample and a superimposed ternary composition map of the expected A15 composition when Nb_3Sn is doped with Ti from Flükiger *et al* [45]

ROI composition measurements were taken in the regions of high Nb and low Nb respectively to determine the composition of these regions across the 7 atom probe tips sampled. The volume of the ROIs was limited by the shape and size of the high Nb regions which were not as large or common as the low Nb regions. Figure 3.11 shows a ternary composition map calculated by Flükiger *et al* in grey which shows the expected equilibrium phase composition range for Nb_3Sn doped with Ti [45], with data taken from previous work between 700 - 750°C [111, 117, 119, 197]. The phase map by Flükiger *et al* is based on bulk data collected on the micron scale, via SEM EDX [111, 197] or EPMA [117, 119] analysis which cannot measure compositional variations within individual grains. To produce the ternary composition map Nb, Sn and Ti were assumed to be the only constituents in the microstructure and their contents were assumed to produce 100% of the microstructure. Figure 3.11 shows there are two distinct compositional ranges of A15 present in the microstructure.

The average composition across 7 low Nb and 12 high Nb regions can be found in table 3.1. High Nb regions are smaller and less common in the microstructure, therefore more high Nb regions were extracted to produce an average composition. Despite the obvious increase in Nb and decrease in Sn in the high Nb regions there is also a reduction in the amount of Ti and the presence of a small amount of Cu. To provide evidence that this small concentration of Cu can be correctly interpreted with confidence, Figure 3.12 shows a selected section of the m/q spectrum from 55 - 66 Da. The mass spectra originating from the low Nb region of the data shows Sn^{2+} peaks and no evidence of Cu^{+} peaks, however the spectrum from the high Nb region shows distinct Cu^{+} peaks. The two spectra in Figure 3.12 were taken for volumes of 6930 nm^3 for the low Nb region and 6940 nm^3 for the high Nb region, from the reconstruction in Figure 3.10.

Nb_3Sn regions	Nb at%	Sn at%	Ti at%	Cu at%
Low Nb	73.1 ± 0.6	25.5 ± 0.8	1.4 ± 0.4	0
High Nb	83.7 ± 0.9	16.0 ± 0.8	0.2 ± 0.1	0.1 ± 0.1

Table 3.1: Average composition of the high and low Nb regions, from APT data in the as-received sample

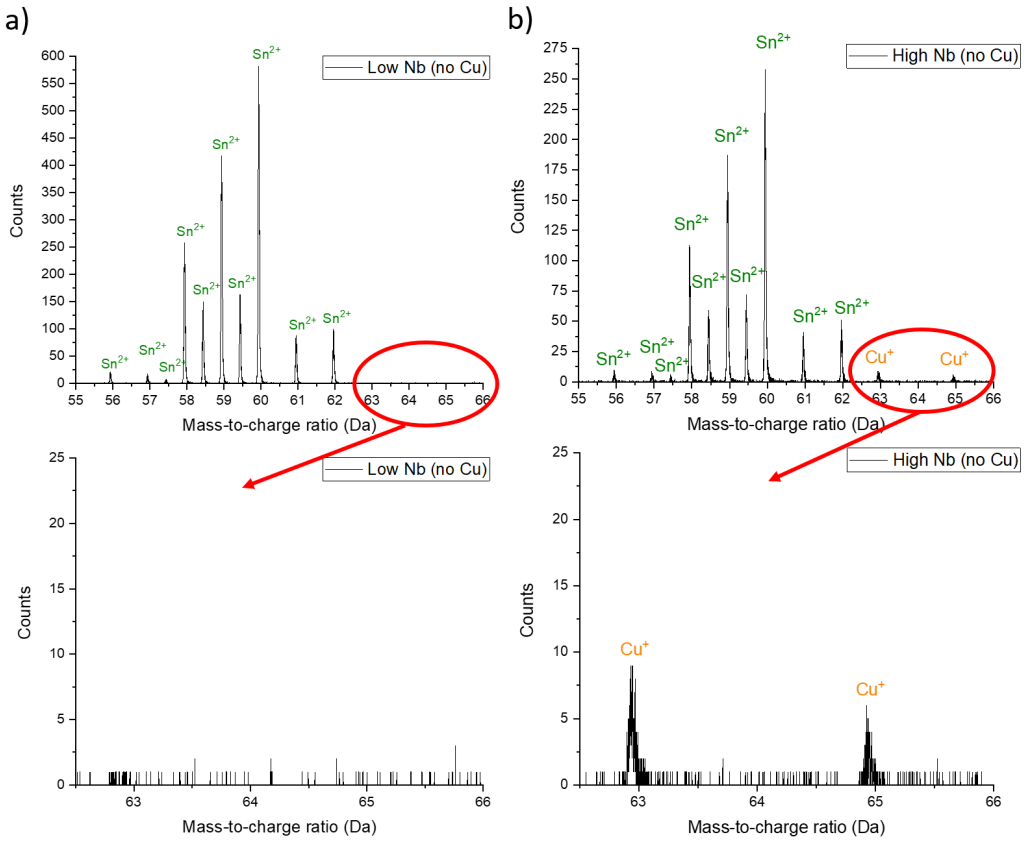


Figure 3.12: a) A section of the m/q spectrum over 55 - 66 Da for the low Nb region for the as-received sample showing no Cu^+ peaks between 63 - 66 Da b) A section of the m/q spectrum over 55 - 66 Da for the high Nb region for the as-received sample showing visible Cu^+ peaks between 63 - 66 Da

3.4.2 Grain Boundary Concentration Profiles

As previously discussed in section 1.9, Nb_3Sn wires doped with Ti have shown Nb depletion at grain boundaries, enrichment of Cu and often enrichment of Sn at the grain boundaries using AES and field ion microscopy [77, 153]. More recent work on Ti doped Nb_3Sn wires using APT and TEM, found that Ti also segregated to grain boundaries [154, 155]. However, no previous studies have analysed grain boundary segregation in modern RRP® wires or neutron irradiated Nb_3Sn wires.

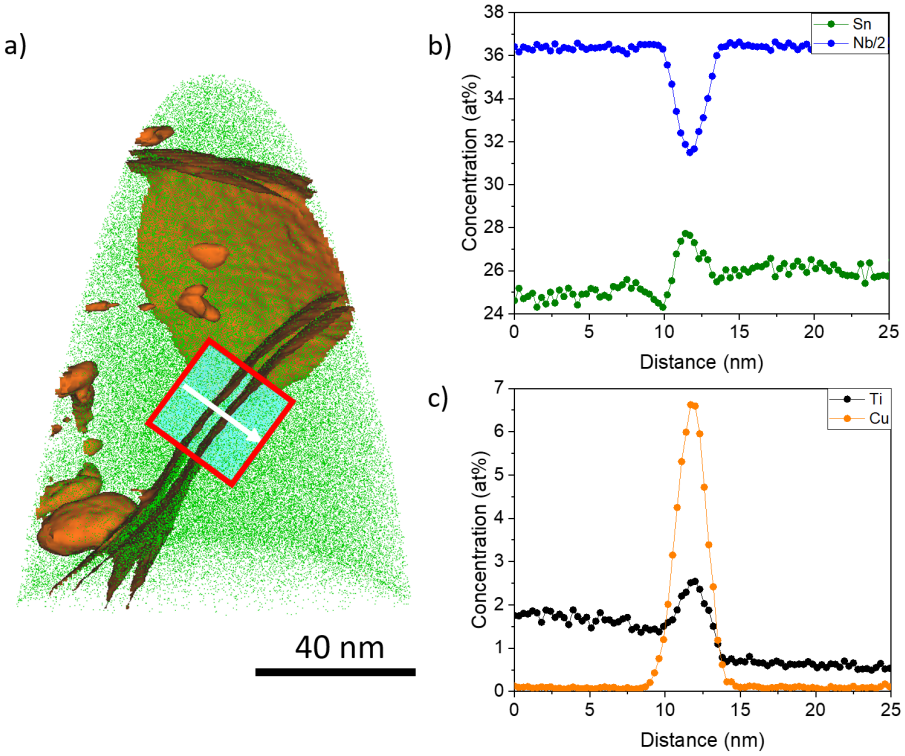


Figure 3.13: a) APT reconstruction from the as-received sample with an ROI across a grain boundary, an isosurface of 2 at% Cu in orange and Sn atoms in green b) A 1D concentration profile of Nb/2 and Sn at% across the grain boundary c) A 1D concentration profile of Cu and Ti at% across the grain boundary

A typical concentration profile measured across a grain boundary for the as-received sample can be seen in Figure 3.13 where there is a depletion of Nb, an enrichment of Sn, an enrichment of Ti and a sharp increase in Cu, which aligns with what has been seen previously

in the literature. However, as discussed in section 3.4.1, because the grain composition is not consistent in each grain due to the regions of high and low Nb Nb_3Sn respectively, this produces variations in the compositional profiles across the grain boundaries. Figure 3.13 has a 72 at% Nb region on either side of the boundary which would classify each adjacent grain as low Nb. To categorise the boundaries, Figure 3.14 plots the Sn concentration of one of the grains, denoted here as Grain A, in comparison to the Sn concentration of the adjacent grain, Grain B. 'Equilibrium' boundaries are defined as boundaries which either have equilibrium Sn content (between 18 - 25 at% [44]) in grain A and B or boundaries with low Nb (and therefore higher Sn content) in Grain A and Grain B. Equilibrium and low Nb boundaries have been grouped together due to their similar segregation behaviour, and are shown in blue on Figure 3.14. Boundaries which have high Nb in both Grain A and Grain B are defined as 'high Nb' boundaries, shown in red, and boundaries which have high Nb within one of the grains are defined as 'mixed' boundaries, shown in purple in Figure 3.14. All three types of boundary contain strong Cu segregation and a sharp Nb depletion, however the amount of Sn and Ti segregation appears to vary between the three boundary types.

3.4.3 Gibbsian Interfacial Excess

The Γ_{Cu} has been measured according to methodology in section 2.6.4 for each of the 30 grain boundaries analysed from the as-received sample. The Γ_{Cu} values have been separated into the three types of grain boundary defined in section 3.4.2. These grain boundaries have been numbered 1 - 30 and plotted against their Γ_{Cu} values with their associated errors in the measured excess dependent on fit only, Figure 3.15. The mean Γ_{Cu} of the equilibrium boundaries is 15.8 $\pm$ 4.8 atoms/nm^2, mixed boundaries is 14.5 $\pm$ 4.0 atoms/nm^2 and the mean of the high Nb boundaries is 10.8 $\pm$ 1.7 atoms/nm^2. The boundaries between high Nb regions consistently have a lower Γ_{Cu} value than that of the equilibrium or mixed Nb boundaries.

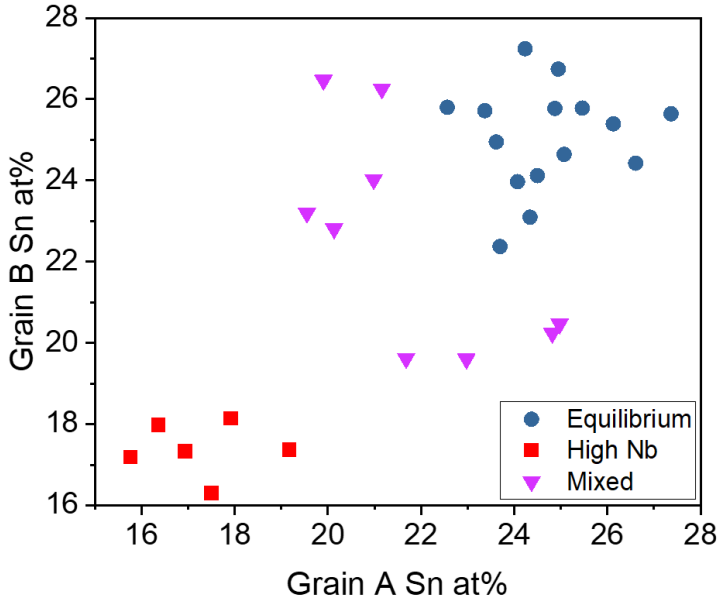


Figure 3.14: Respective Sn concentration in the adjacent grains on both sides of the grain boundaries in the as-received sample. There are boundaries which have high Nb grains adjacent to the boundary as shown in red, boundaries with equilibrium or low Nb content shown in blue and mixed boundaries in purple.

The amount of Nb depletion of the boundaries has been measured in Figure 3.16 by calculating the percentage difference between the average amount of Nb in the grains and the measured interface value for Nb generated by the Γ_i analysis. The error bars are the Nb depletion percentages for either side of the grain boundary, therefore boundaries with larger differences in Grain A and Grain B will have larger error bars. The mean values of Nb depletion are 10.2 $\pm$ 2.0 % for the mixed boundaries, 8.1 $\pm$ 2.3% for the equilibrium boundaries and 9.6 $\pm$ 0.8% for the high Nb boundaries. Since there is no obvious difference in the amount of Nb depletion across the different types of boundary, this suggests that the high Nb boundaries show Γ_{Cu} values due to the fact that they retain more Nb at the grain boundaries, therefore less Cu can be accommodated at these boundaries.

The effect on Ti can be analysed by considering the composition of Ti either side of each boundary. As discussed in section 3.4.1 a reduced amount of Ti is accommodated within the

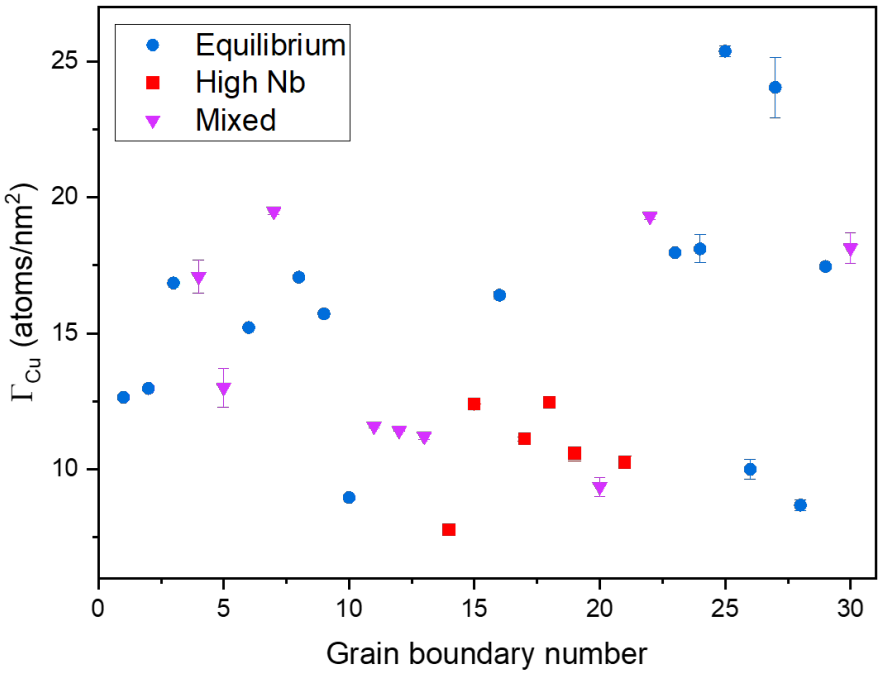


Figure 3.15: Γ_{Cu} at the grain boundaries in the as-received material. Equilibrium concentration on either side of the boundary shown in blue, high Nb either side of the boundary shown in red and a combination of low and high or high and low shown in purple. The error bars attached are those generated by the fit of the Poisson distribution to the solute profile.

high Nb regions. This is confirmed at the grain boundaries when the average composition of Ti either side of the boundary is plotted in Figure 3.17. The mean values for Ti composition adjacent to the boundaries are 1.2 $\pm$ 0.5 at% at mixed boundaries, 1.5 $\pm$ 0.6 at% at equilibrium boundaries and 0.2 $\pm$ 0.1 at% at high Nb boundaries, which supports evidence from section 3.4.1 that high Nb regions contain less Ti. The average composition of Ti at the interface is shown in Figure 3.18 where there is clearly lower Ti at the high Nb boundaries compared to equilibrium and mixed boundaries. Γ_i values have not been calculated for Ti because of the difficulty of precisely identifying the extents across the grain boundary using the Ti concentration profile therefore the Γ_i values have large associated errors.

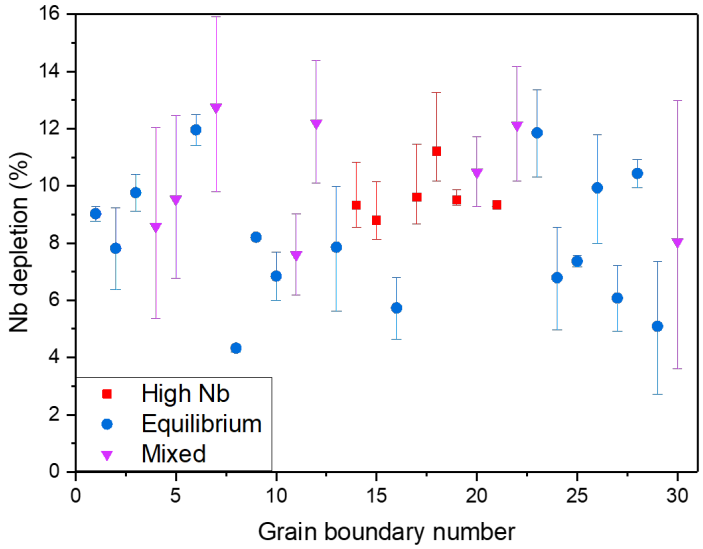


Figure 3.16: Nb depletion % of each grain boundary with the error bars taking into account the maximum and minimum Nb content on each side of the boundary.

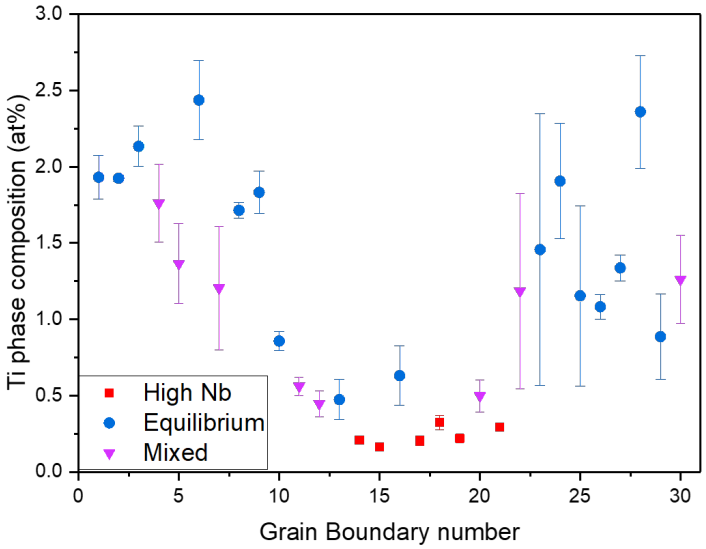


Figure 3.17: Average Ti at% of the grains either side of each boundary with the error bars taking into account the maximum and minimum Ti content on each side of the boundary.

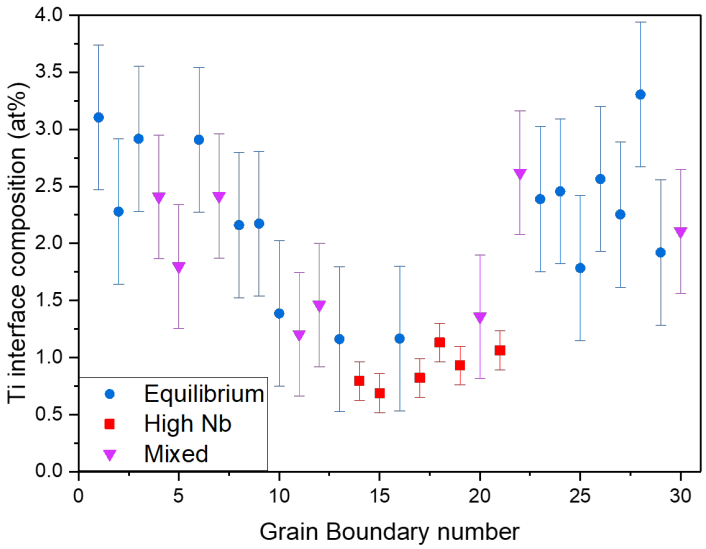


Figure 3.18: Ti at% at each grain boundary where the error is the standard deviation of each group of data.

The average compositions of high Nb, mixed and equilibrium boundaries have been plotted in table 3.2. Each boundary composition measurement is defined as the average composition between the edges of the solute Cu peak at each boundary, calculated by R-code used to calculate Γ_i detailed in section 2.6.4. The mixed and equilibrium boundaries have, within one standard deviation, the same segregation behaviour, whereas the high Nb boundaries retain higher concentrations of Nb and therefore systematically reduced amounts of Sn, Ti and Cu.

Boundary type	Nb at%	Sn at%	Ti at%	Cu at%
High Nb	72.8 ± 1.9	23.1 ± 1.4	1.0 ± 0.2	3.0 ± 0.4
Mixed	68.8 ± 1.8	24.8 ± 0.6	1.9 ± 0.5	4.5 ± 1.4
Equilibrium	69.5 ± 1.9	24.5 ± 1.9	1.9 ± 0.8	4.0 ± 1.5

Table 3.2: Grain boundary composition of high Nb, mixed and equilibrium grain boundaries from the as-received sample

3.4.4 Additional Features of Interest

In the as-received sample 3 of the 7 tips contain almost pure Nb nanoparticles. One of these reconstructions can be seen in Figure 3.19 where a 1D concentration profile has been extracted through the largest Nb particle. In total 7 Nb particles were found in the as-received datasets. Previous RRP® wires analysed through EDX have suggested the presence of residual pure Nb [20], however EDX did not detect Cu surrounding the Nb particle. The segregation of Cu to the Nb/Nb_3Sn interface suggests the interfaces could provide additional surface pinning to the Nb_3Sn wire. The Nb particles are likely to be residual Nb from the original Nb rods prior to heat treatment. The size distribution of Nb particles can be found in section 3.6.3. There is no obvious difference in Nb content in each grain which contains the Nb particles. For example if the matrix concentration of two grains from two tips which contain Nb particles are compared to the other grains in the tips which do not contain Nb, the average Nb content of the grains which contain Nb particles are 69.3 $\pm$ 0.2 at% and the grains without are 68.8 $\pm$ 0.9 at%. Within error there is no change in Nb content, this is likely due to the relatively small size of the Nb particles compared to the size of the grains.

In addition to residual Nb particles, there were also two different types of dislocations which could be observed in the as-received samples. The first type of dislocation takes the form of regular arrays of line dislocations which appear to form low angle grain boundaries. Figure 3.20 shows a regular dislocation array which is visible due to the segregation of Cu to the dislocations. There is a depletion in Nb at the dislocations, similar to what is seen at the grain boundaries. Obvious segregation of Ti is not present to these dislocations, therefore the Ti spectrum is not included. In total 7 linear arrays of dislocations were found in the as-received reconstructions.

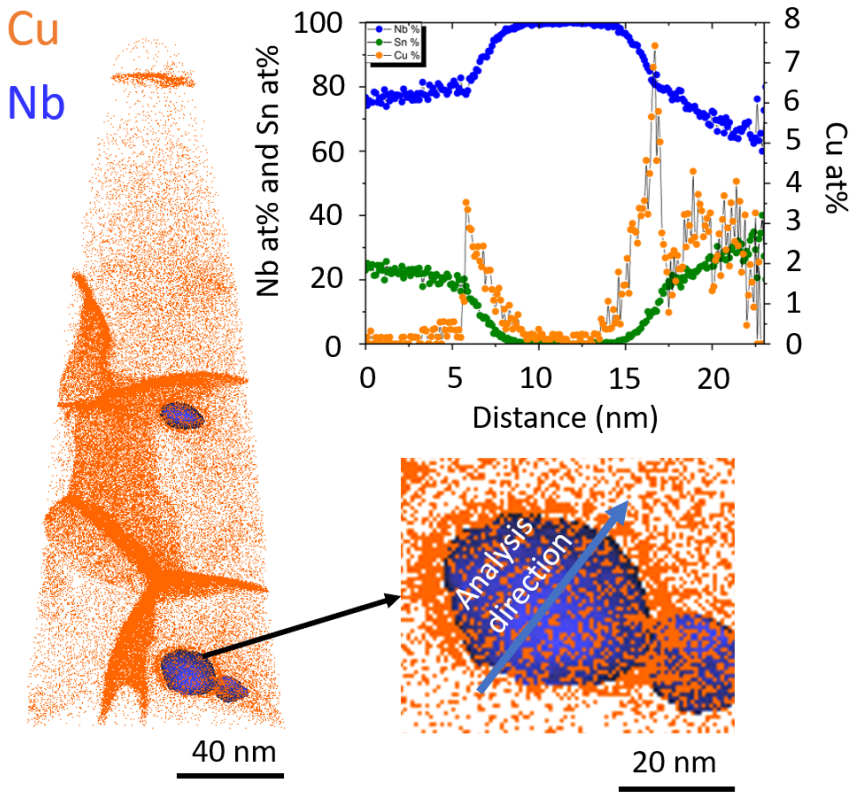


Figure 3.19: APT reconstruction of an as-received tip with Cu atoms and a Nb isosurface of 95 at% Nb. A 1D concentration profile has been taken through the largest particle showing the concentrations of Nb, Sn and Cu [189].

The second type of dislocation are individual linear dislocations which extend out of the plane of grain boundaries, as shown in Figure 3.21. In total 3 reconstructions contained out-of-plane dislocations which could occur either as a single dislocation or as multiple dislocations as shown in Figure 3.21. Previously, dislocation arrays have been seen in bronze processed Nb_3Sn [152, 198] and the presence of low-angle grain boundaries have been suggested in fine-grain regions [152], however individual dislocations can be difficult to image as their visibility is dependent on the TEM imaging conditions and sample thickness [20].

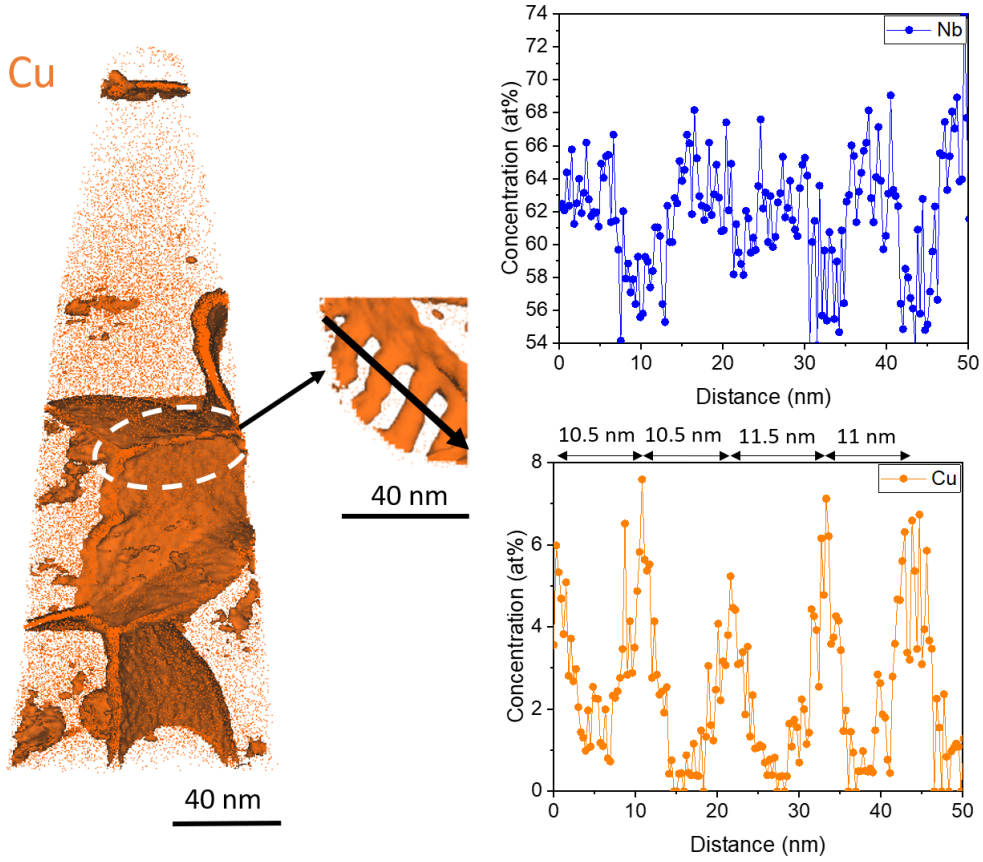


Figure 3.20: APT reconstruction of an as-received tip with Cu atoms and a Cu isosurface of 2 at% Cu. A 1D concentration profile has been extracted perpendicular to the dislocations and the concentration of Cu and Nb has been measured across the array. Adapted from [189]

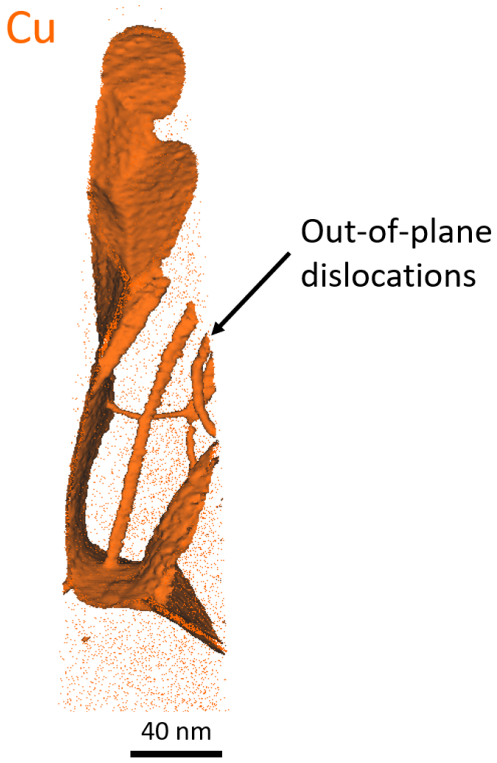


Figure 3.21: APT reconstruction of an as-received tip with Cu atoms and a Cu isosurface of 2 at% Cu showing typical out-of-plane dislocations

The final feature of interest found in the as-received sample is a boundary with sharp Ti segregation instead of the standard Cu segregation, Figure 3.22. There are 4 Cu clusters associated with the boundary and it separates two regions of high Nb Nb_3Sn. The large increase in Sn content and the depletion of Nb, as shown in Figure 3.22, identifies this as a grain boundary. There is a large increase in Sn at the boundary and a sharp increase in Ti, with the small peak in Cu associated with the clusters which could not be separated from the ROI which was used to generate the 1D concentration plots. In order to measure the amount of Ti segregation to the boundary, Γ_i analysis was conducted across the boundary using a 1D concentration profile, giving a Γ_{Ti} value of 13.8 $\pm$ 0.8 atoms/nm^2 across the interface. There is also a large excess of Sn associated with this boundary, however the Sn profile spreads over a wider distance and the solute peak is more difficult to define, so the error in Γ_i value is nearly as large as the value itself (19.5 $\pm$ 14.0 atoms/nm^2). To define the 4 Cu rich clusters, cluster analysis using the MSM has been used [186], with Cu identified as the solute atom and parameters of d_{max} = 0.8 nm, N_{min} = 29 and $d_{erosion}$ = 0 nm which clearly defined the 4 clusters. A cluster concentration profile has been produced which averages the concentrations of the 4 clusters and defines the normalised distance 1 as the defined edge of each cluster, Figure 3.23. The concentrations in Figure 3.23 have had the matrix count removed, this has been defined as the concentration of the species at the interface, at a normalised distance of 1. Although there is a slight peak in Sn at a normalised distance of 0, this does not correlate with the Cu profile, and therefore over a small number of 4 clusters this is likely to be matrix Sn rather than part of the clusters. The size of the clusters is dependent on the reconstruction parameters used and an estimate for the diameter in the z-direction (the direction with the highest spatial resolution [160]) has been made using the extent parameter in z direction, which is the maximum distance from the centre of mass of the cluster giving an average diameter of 2.1 $\pm$ 0.2 nm.

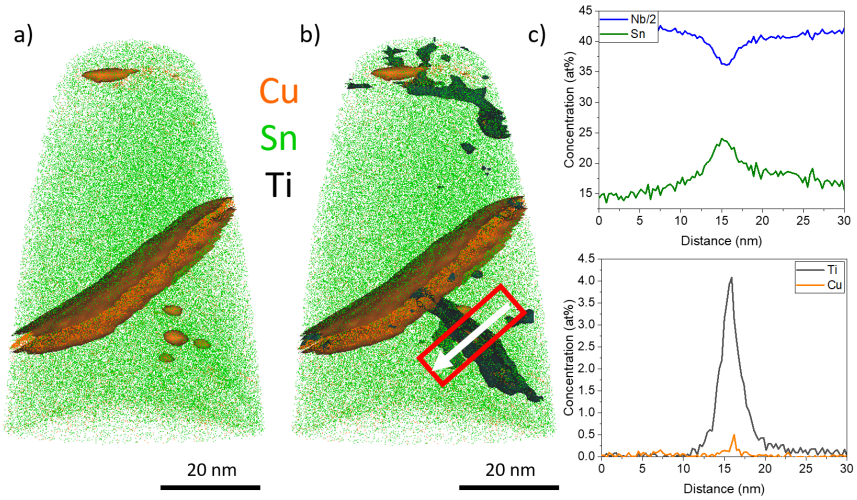


Figure 3.22: a) APT reconstruction of an as-received tip with Sn atoms and a Cu isosurface of 2 at% Cu highlighting a typical grain boundary and beneath this 4 Cu-rich clusters incorporated into a second grain boundary b) APT reconstruction including an additional Ti 2.5 at% isosurface to showing the second grain boundary which is Ti rich on the bottom right of the reconstruction c) A 1D concentration profile through the Ti rich boundary

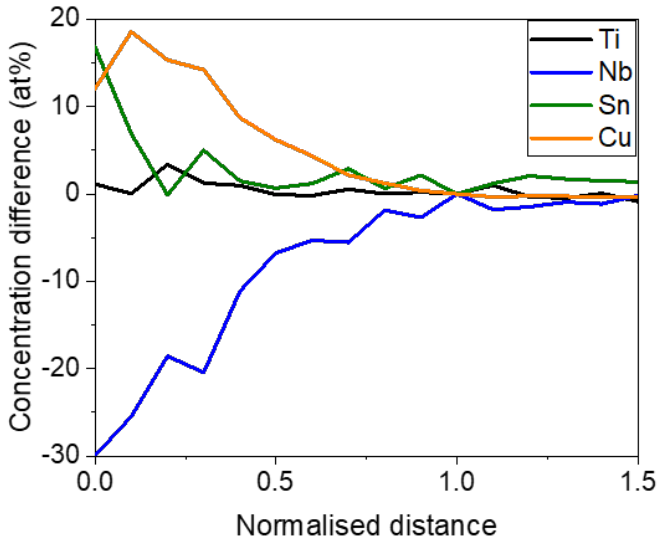


Figure 3.23: A normalised concentration profile of Nb, Sn, Cu, Ti across the four Cu clusters with a clear peak in Cu towards the centre of the clusters

3.5 Results from Atom Probe Tomography: Irradiated sample

To fairly compare the nanosegregation in the as-received sample and the irradiated sample, nanostructural features from the intra-grain, inter-grain regions, as well as additional features of interest, have been analysed across all 11 tips from the irradiated sample.

3.5.1 Intra-grain Compositional Analysis

In order to compare the intra-grain compositions of the irradiated sample, the same methodology has been followed as in section 3.4.1 and applied to the irradiated reconstructions. The high and low Nb regions are also present within the irradiated sample, with a ternary composition map of the high and low Nb Nb_3Sn regions shown in Figure 3.24, and the average composition of the high and low Nb regions shown in table 3.3. In total 12 low Nb regions and 14 high Nb regions were analysed from the irradiated sample.

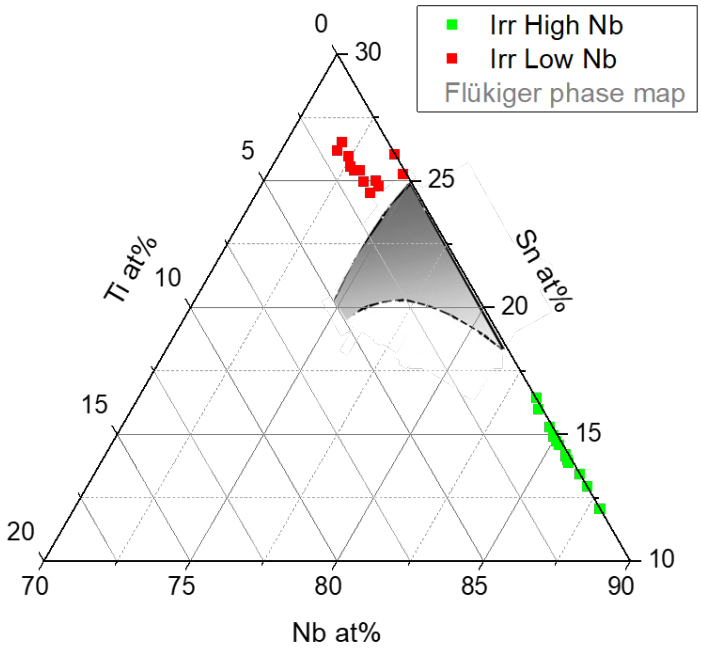


Figure 3.24: A ternary composition map showing the measured compositions of the high and low Nb regions in the as-received sample and a superimposed ternary composition map of the expected A15 composition when Nb_3Sn is doped with Ti from Flükiger *et al* [45].

Nb_3Sn regions	Nb at%	Sn at%	Ti at%	Cu at%
Low Nb	73.2 ± 0.6	25.5 ± 0.8	1.3 ± 0.4	0
High Nb	85.5 ± 1.2	14.1 ± 1.3	0.1 ± 0.1	0.3 ± 0.2

Table 3.3: Average composition of the high and low Nb regions in the irradiated sample

3.5.2 Grain Boundary Concentration Profiles

The grain boundaries in the irradiated sample show similar concentration profiles to those seen in the as-received sample. Figure 3.25 is an example of a mixed grain boundary which separates a region of low Nb on the upper side of the boundary to high Nb on the right side of the boundary. The m/q spectrum for this particular grain boundary profile has a minor overlap with the Nb^{3+} and Cu^{2+} peaks at 31.5 Da and 32.5 Da which explains why the Cu count does not go to zero on the low Nb side of the boundary.

Similar to the analysis of the as-received material in Figure 3.14, the number count of each type of grain boundary: equilibrium, mixed and high Nb has been established by plotting the Sn content in Grain A against Grain B in Figure 3.26. It is noticeable that there are no boundaries with high Nb content on both sides of the boundary for the irradiated sample.

3.5.3 Gibbsian Interfacial Excess

The grain boundaries have been numbered 1 - 27 for the irradiated sample. The Γ_{Cu} measurements for the irradiated sample have been plotted in Figure 3.27. The mean Γ_{Cu} of the equilibrium boundaries is 18.3 ± 6.2 atoms/nm^2 and for the mixed boundaries is 14.2 ± 5.7 atoms/nm^2.

The amount of Nb depletion for each boundary is shown in Figure 3.28, with the mean depletion for the equilibrium boundaries 7.8 ± 2.7% and 11.9 ± 3.2% for the mixed boundaries.

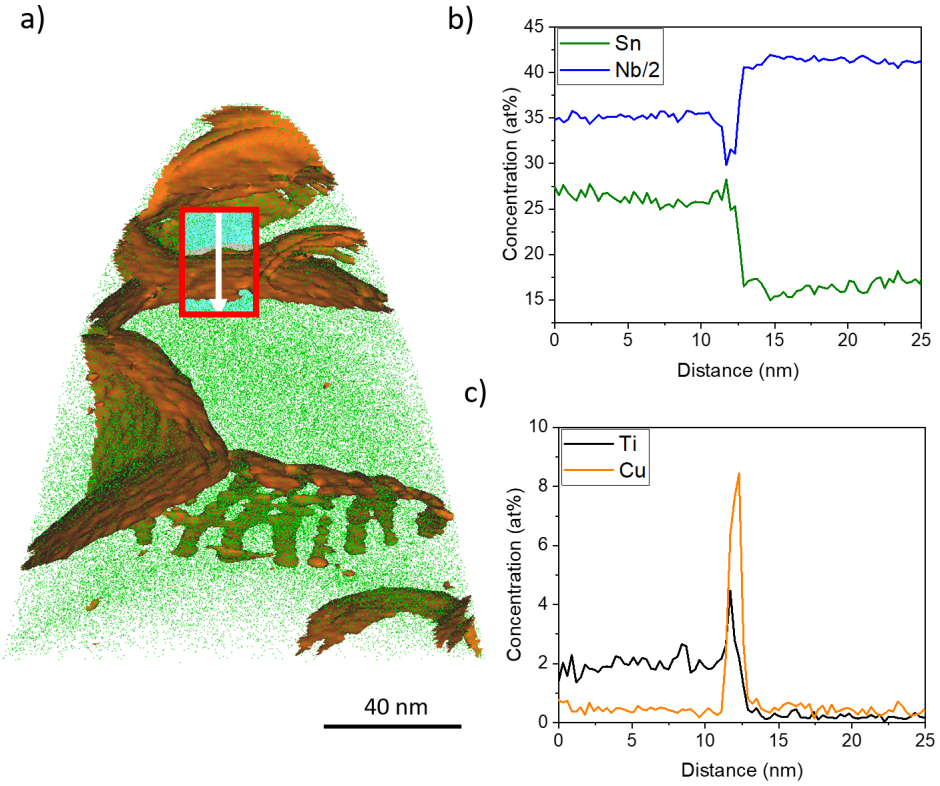


Figure 3.25: a) APT reconstruction from the irradiated sample with an ROI across a grain boundary with a 2 at% Cu isosurface in orange and Sn atoms in green b) 1D concentration profile of Nb/2 and Sn across the grain boundary c) 1D concentration profile of Cu and Ti across the grain boundary. All compositions of the high and low Nb regions in this tip, and all other irradiated tips, are included in Figure 3.35

The average amount of Ti in the grains either side of the boundaries in the irradiated sample are compared in Figure 3.29, with the errors representing the value of Ti in each grain either side of the grain boundaries. The average amount of Ti in the phases adjacent to the grain boundaries in the irradiated sample is 1.5 $\pm$ 0.3 at% for the equilibrium boundaries and 1.0 $\pm$ 0.3 at% for the mixed grain boundaries. The segregated composition of Ti at the interface of the irradiated samples can be seen in Figure 3.30, with the average amount of Ti at the interface being 2.3 $\pm$ 0.3 at% in the equilibrium boundaries and 2.3 $\pm$ 0.4 at% at the mixed boundaries. The average compositions of the equilibrium and mixed boundaries in the irradiated sample are presented in table 3.4.

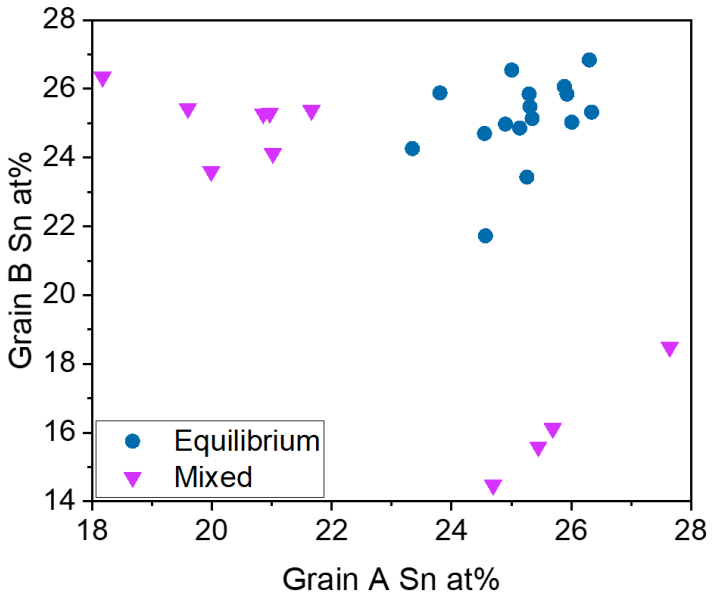


Figure 3.26: Sn at% measured in adjacent grains either side of each analysed grain boundary in the irradiated sample. Boundaries with equilibrium Nb either side of the boundary are in blue and mixed boundaries are shown in purple.

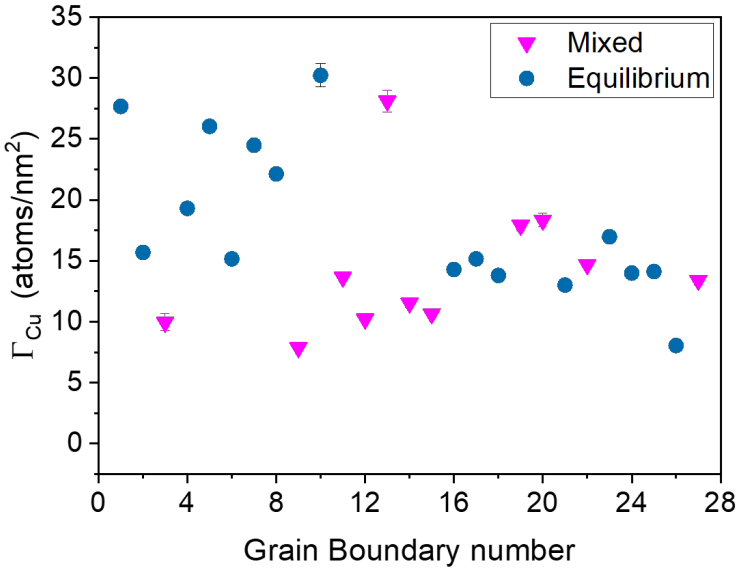


Figure 3.27: Γ_{Cu} at the grain boundaries in the irradiated material. Equilibrium concentration on either side of the boundary shown in blue, and mixed boundaries shown in purple. The error bars attached are those generated by the fit of the Poisson distribution to the solute profile and most are contained wholly within the symbol.

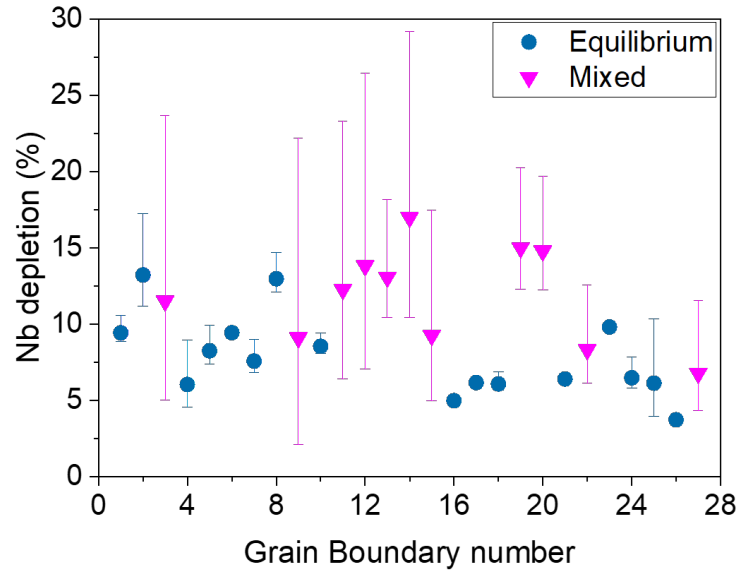


Figure 3.28: Nb depletion % of each grain boundary from the irradiated sample with the error bars taking into account the maximum and minimum Nb content on each side of the boundary.

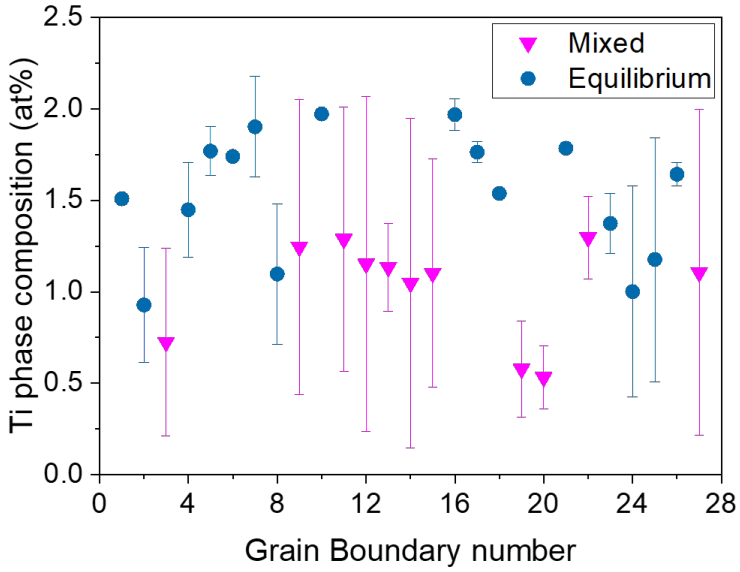


Figure 3.29: Average Ti at% of the grains either side of each boundary from the irradiated sample with the error bars taking into account the maximum and minimum Ti content on each side of the boundary.

Boundary type	Nb at%	Sn at%	Ti at%	Cu at%
Mixed	67.4 ± 2.6	24.7 ± 1.8	2.3 ± 0.4	5.6 ± 1.6
Equilibrium	67.4 ± 1.8	25.4 ± 0.7	2.3 ± 0.3	4.9 ± 1.5

Table 3.4: Grain boundary composition of mixed and equilibrium grain boundaries from the irradiated sample

3.5.4 Additional Features of Interest

Residual Nb and dislocation features were also present within the irradiated sample. In the irradiated sample only 3 residual Nb clusters were found, and a comparison of the volume of the residual Nb between samples can be found in section 3.6.3. Within the irradiated reconstructions analysed one sample contained a linear array of dislocations, as seen in the as-received sample, Figure 3.20, and 4 reconstructions contained dislocations out of the plane of the boundary, as seen in the as-received sample, Figure 3.21. The irradiated sample also contained boundaries which appeared to be formed from two orthogonal arrays of dislocations, as shown in Figure 3.31. To compare the relative segregation of these boundaries, Γ_{Cu}, Nb depletion, Ti average

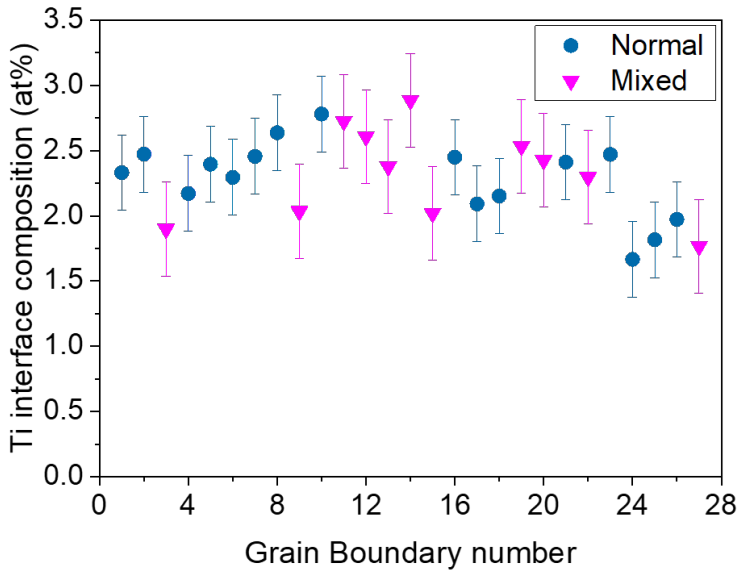


Figure 3.30: Segregated Ti at% at each grain boundary from the irradiated sample, where the error is the standard deviation of each group of data

phase composition, and Ti interface composition were calculated and are shown in table 3.5. The overall Ti composition of the grains adjacent to the boundaries and the Ti composition at the interface itself are lower than that seen at equilibrium and mixed boundaries in the irradiated sample. This suggests weaker segregation to these low angle orthogonal grain boundaries compared to the other grain boundaries in the irradiated sample.

Dis. Boundary	Γ_{Cu} (atoms/nm^2)	Nb depletion (%)	Ti phase av. (at%)	Ti interface (at%)
1	6.9 $\pm$ 1.7	5.1-11.1	0.56 $\pm$ 0.24	1.5 $\pm$ 0.3
2	12.3 $\pm$ 0.3	5.0-10.6	1.0 $\pm$ 0.5	1.8 $\pm$ 0.3

Table 3.5: Γ_{Cu}, Nb depletion, Ti average adjacent grain composition, Ti interface composition for the two grain boundaries which contain orthogonal dislocations in the irradiated sample

In addition to the orthogonal boundaries, one reconstruction contained a dislocation loop decorated by Cu segregation, as shown in Figure 3.32. The Cu segregated loop shows a decrease in Nb associated with an increase in both Cu and Ti. The dislocation loop appears to have similar segregation behaviour to a standard Cu grain boundary between two regions of low Nb Nb_3Sn. Interestingly, a second type of dislocation loop which showed only segregated Ti, as

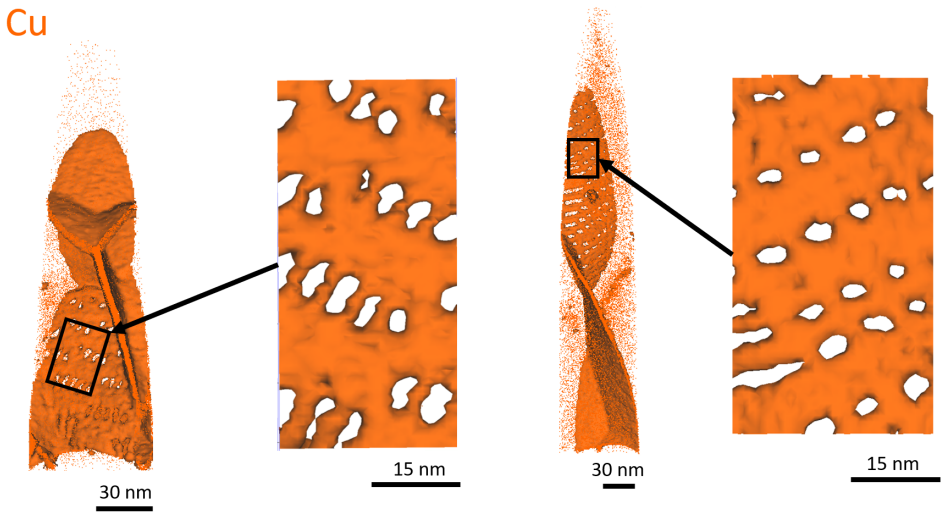


Figure 3.31: APT reconstructions of tips from the irradiated sample containing orthogonal arrays of dislocations decorated with Cu. The boundary is highlighted by a 2 at% Cu isosurface

shown in Figure 3.33, was also found. The Ti loop showed a depletion in Nb and an increase in Sn. Figure 3.33 shows the Ti loop is within a high Nb region, and the segregation is very similar to the Ti boundary seen in the as-received sample, Figure 3.18. Solute decorated dislocation loops are commonly seen in other neutron irradiated materials using APT, such as stainless steels [199] and zirconium alloys [200], and can be either vacancy or interstitial in type. It is likely that some of the *regions of disorder* seen using TEM in previous generations of Nb_3Sn wires [20, 143, 198, 201] could be dislocation loops that might increase the relative flux pinning in the irradiated material.

The irradiated sample does also contain Ti boundaries, with an example shown in Figure 3.34. This boundary cuts across two regions of low Nb and does not show any significant change in the amount of Nb or Sn at the boundary, unlike the Ti boundary for the as-received sample shown in Figure 3.22. No Cu clusters are associated with this boundary and the Γ_{Ti} at the boundary is 4.1 atoms/nm^2, with the error associated smaller than 0.01 atoms/nm^2.

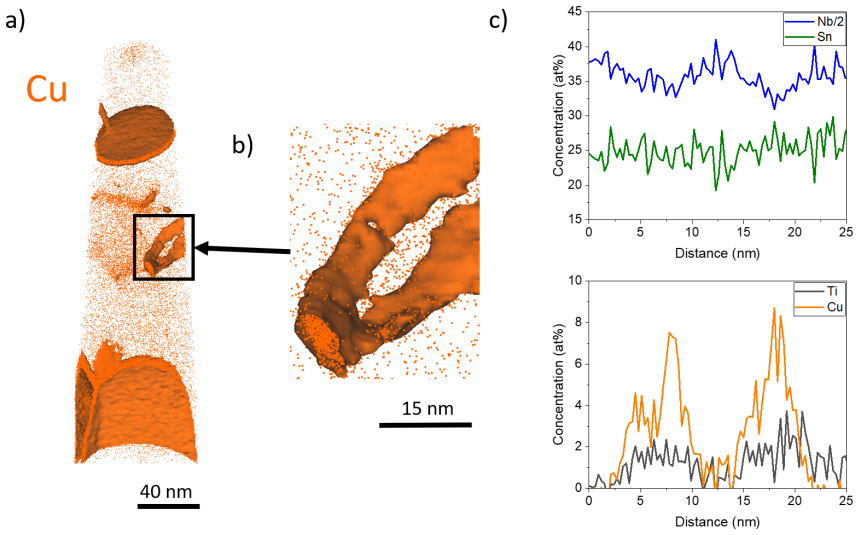


Figure 3.32: a) APT reconstruction of a tip from the irradiated sample with a Cu 2 at% isosurface to show the grain boundaries, an out of plane dislocation and a dislocation loop b) Inset of the dislocation loop c) 1D concentration profile across the Cu dislocation loop

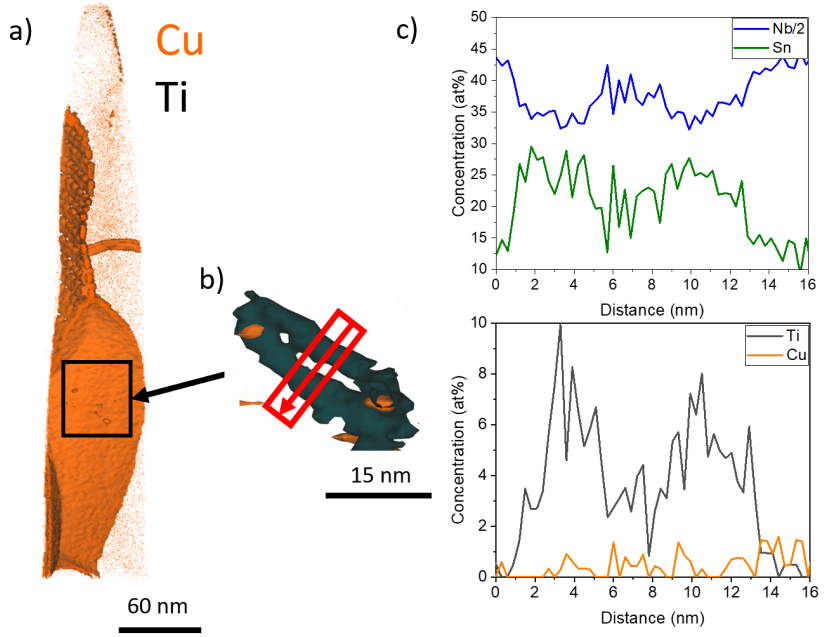


Figure 3.33: a) APT reconstruction of a tip from the irradiated sample with a Cu 2 at% isosurface to show the grain boundaries and an out of plane dislocation b) A dislocation loop extracted using a Ti 4 at% isosurface and a Cu 2 at% isosurface to show associated Cu clusters c) 1D concentration profile across the Ti dislocation loop

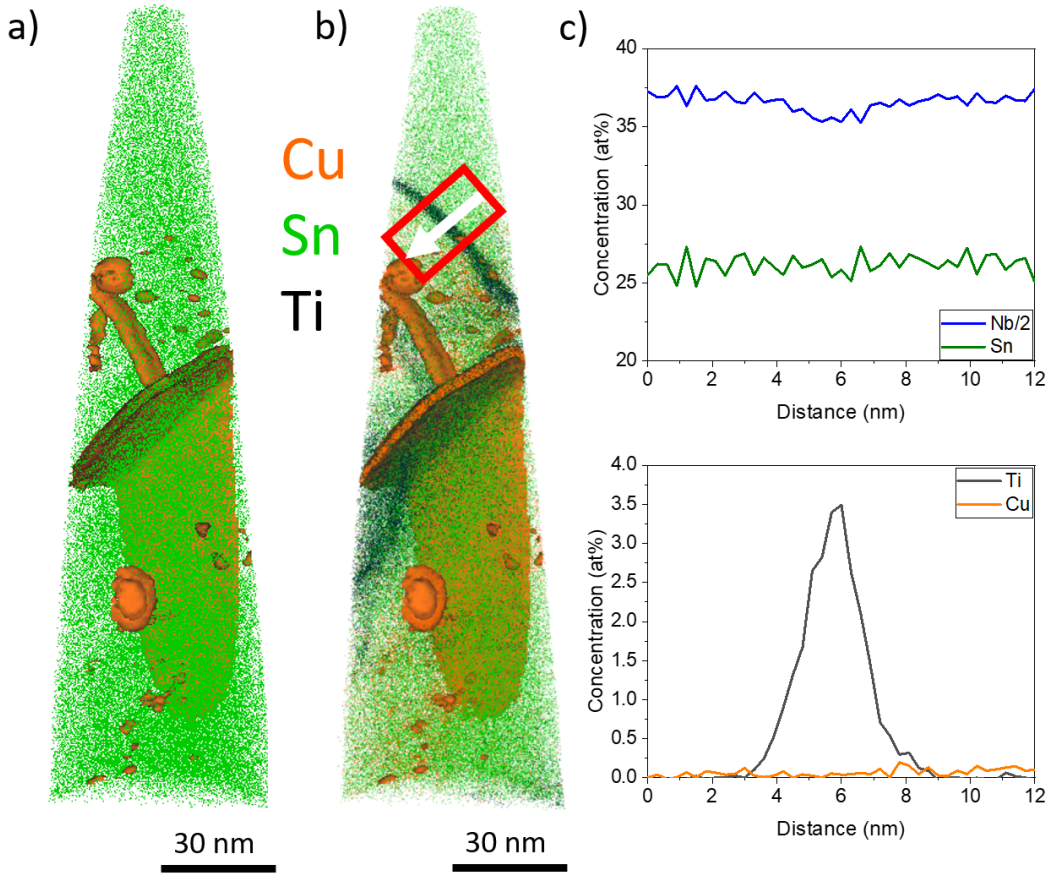


Figure 3.34: a) Reconstruction of an irradiated tip with Sn atoms and an isosurface of 2 at% Cu highlighting a typical grain boundary b) Reconstruction including Ti atoms to show a Ti boundary near the top of the reconstruction c) 1D concentration profile through the Ti boundary

3.6 Comparison of As-received and Irradiated results

3.6.1 Overall Composition

As discussed in sections 3.4.1 and 3.5.1 the individual small volumes analysed in the atom probe tips do not fit what would be predicted from the ternary composition map for Nb_3Sn doped with Ti [45]. However, this ternary composition map is calculated from data that averages over the overall sample, therefore it is important to consider how much of each region (low Nb, high Nb and grain boundaries) are present within the as-received and irradiated sample to see if it is consistent with the macro-scale composition of the samples. Grain boundary composition has been extracted from the Γ_i calculation, which defines the interface edges as the extents of the Cu solute peak. To estimate a volume for the amount of each tip which is grain boundary, a 2 at% Cu isosurface was fitted over the total volume of each reconstruction and the volume within this interface was defined as the grain boundary volume. The volume fraction of the high Nb regions were defined by a 80 at% Nb isosurface and any Nb particles were extracted with Nb isosurface 95 at%. The remaining volume fraction in each reconstruction was assumed to be low Nb regions which make up the majority of the reconstructions. The average composition for the as-received and irradiated samples were calculated by equation 3.5 for each species, where $x = Nb, Sn, Ti, Cu$, C is the concentration in at% and V_f is the volume fraction associated with each region and the error in C_x is given by $\sqrt{\sigma^2_{Low} + \sigma^2_{High} + \sigma^2_{GB}}$.

$$C_x(at\%) = (C_x^{HighNb} \times V_f^{HighNb}) + (C_x^{LowNb} \times V_f^{LowNb}) + (C_x^{GB} \times V_f^{GB}) \tag{3.5}$$

In total 7 atom probe tips from the as-received sample were analysed with an estimated total volume of 8.6 $\times$ 10^6 nm^3, and 11 atom probe tips from the irradiated sample were analysed with an estimated total volume of 5.8 $\times$ 10^6 nm^3. The average composition for the as-received material is $C_{Nb} = 74.5 \pm 3.6$ at%, $C_{Sn} = 23.8 \pm 2.0$ at%, $C_{Ti} = 1.2 \pm 0.9$ at% and $C_{Cu} = 0.5 \pm 1.5$ at%. The average composition of the irradiated sample is $C_{Nb} = 76.6 \pm 2.6$ at%, $C_{Sn} = 21.9 \pm 1.8$ at%, $C_{Ti} = 1.0 \pm 0.7$ at% and $C_{Cu} = 0.5 \pm 1.5$ at%. A ternary diagram

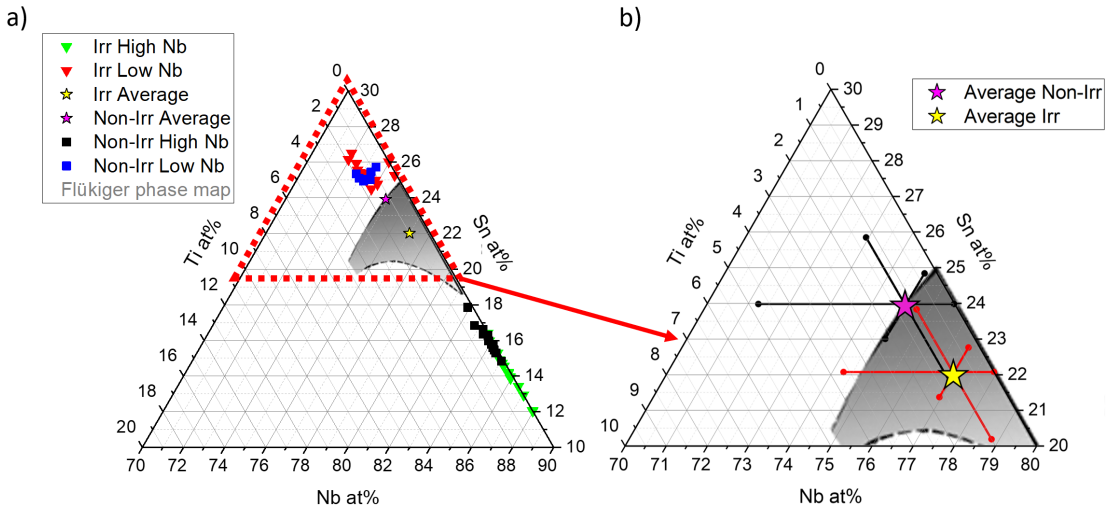


Figure 3.35: a) A ternary composition map which presents all the sampled low Nb and high Nb composition measurements from both the as-received and irradiated sample, respectively, and the predicted A15 phase composition map for Nb_3Sn doped with Ti [45] b) A close-up ternary composition map shows the average compositions of Nb, Sn and Ti for the irradiated and as-received samples as calculated by equation 3.5. The errors bars in the magnified image are the errors associated with C_x. Adapted from [189]

which displays the low Nb, high Nb and average compositions for each sample has been included in Figure 3.35. Both samples have a total average composition which maps directly onto the predicted Ti doped Nb_3Sn phase map developed by Flükiger from bulk composition measurements [45], Figure 3.35. The Cu composition has not been included in the composition map because the amount of Cu in solution in the low Nb regions is below the limits of detection and within the high Nb regions is negligible compared to the Ti content.

To compare the scatter in the composition measurements of the low Nb and high Nb regions between samples, Figure 3.36 includes magnified sections of Figure 3.35 which clearly distinguish the different regions. The Nb content in the high Nb regions in the irradiated sample is higher than the Nb content for the high Nb regions in the as-received sample. Average compositions of the low Nb and high Nb regions are compared in table 3.6. The composition of low Nb regions is approximately the same for both samples, however the regions of high Nb have a larger amount of Nb in the irradiated sample than in the as-received sample, therefore the high Nb regions in the irradiated sample are further from equilibrium stoichiometry.

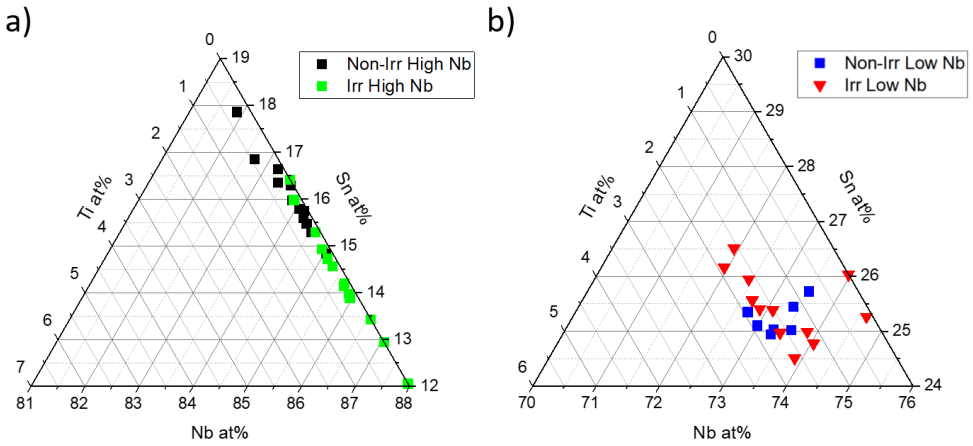


Figure 3.36: a) A ternary composition map which presents all high Nb composition measurements from both the as-received and irradiated sample b) A ternary composition map which shows all low Nb compositions for the irradiated and as-received samples

Sample	Nb (at%)	Sn (at%)	Ti (at%)	Cu (at%)
Non-Irr Low Nb	73.1 ± 0.6	25.5 ± 0.8	1.4 ± 0.4	0
Irr Low Nb	73.2 ± 0.6	25.5 ± 0.8	1.3 ± 0.4	0
Non-Irr High Nb	83.7 ± 0.9	16.0 ± 0.8	0.2 ± 0.1	0.1 ± 0.1
Irr High Nb	85.5 ± 1.2	14.1 ± 1.3	0.1 ± 0.1	0.3 ± 0.2

Table 3.6: The average compositions of the high and low Nb regions in the as-received and irradiated samples

3.6.2 Grain Boundary Segregation

To compare the composition of the grain boundaries between the two samples, first a comparison of the types of boundaries found in each sample is required. The as-received sample contained equilibrium, mixed and high Nb boundaries, whereas for the irradiated sample only equilibrium and mixed boundaries were detected. The likely reason that no high Nb boundaries were detected in the irradiated sample is due to the significantly reduced volumes of high Nb regions detected in each sample. Using an isosurface of 80 at% Nb to define all regions of high Nb, an estimation for the volume of high Nb regions could be generated as a percentage of the total volume. As a percentage, the volume fraction of high Nb in the as-received sample was 37.2% compared to 14.8% for the irradiated sample. The substantial reduction is unlikely

caused by random variation in the sampled microstructure, especially because, in comparison, the estimated percentage volume of grain boundaries (as defined by 2 at% Cu isosurface) did not change substantially between samples (11.8% in the as-received sample and 9.7% for the irradiated sample). For the as-received sample 6/30 boundaries were high Nb, 8/30 were mixed and 16/30 were equilibrium type boundaries and for the irradiated sample 11/27 boundaries were mixed and 16/27 boundaries were of the equilibrium type.

To compare the grain boundaries between each sample we can compare: Γ_{Cu} (atoms/nm^2), Nb depletion (%), Ti phase composition (at%) and Ti interface composition (at%) in table 3.7. Equilibrium boundaries, which are the majority boundary sampled in the as-received and irradiated case, show the strongest Γ_{Cu} for both samples, however the irradiated sample does appear to have stronger Cu segregation at the equilibrium boundaries. The largest amount of Nb depletion for both samples is associated with the mixed boundaries, again with the irradiated sample showing a slightly greater amount of depletion at the mixed boundaries. The Ti concentration in adjacent grains appears to be consistent across both samples too, as are the concentrations of Ti in the mixed and equilibrium boundaries. The interface concentration of Ti is consistent for equilibrium and mixed boundaries for each sample, however the irradiated sample does show stronger segregation to the boundaries than the as-received sample.

Sample/Boundary	Γ_{Cu} (atoms/nm^2)	Nb depletion (%)	Ti phase (at%)	Ti interface (at%)
Non-Irr Equilibrium	15.8 $\pm$ 4.8	8.1 $\pm$ 2.3	1.5 $\pm$ 0.6	1.9 $\pm$ 0.8
Irr Equilibrium	18.3 $\pm$ 6.2	7.8 $\pm$ 2.7	1.5 $\pm$ 0.3	2.3 $\pm$ 0.4
Non-Irr Mixed	14.5 $\pm$ 4.0	10.2 $\pm$ 2.0	1.2 $\pm$ 0.5	1.9 $\pm$ 0.5
Irr Mixed	14.2 $\pm$ 5.7	11.9 $\pm$ 0.3	1.0 $\pm$ 0.3	2.3 $\pm$ 0.3
Non-Irr High Nb	10.8 $\pm$ 1.7	9.6 $\pm$ 0.8	0.2 $\pm$ 0.1	1.0 $\pm$ 0.2

Table 3.7: The mean values of Γ_{Cu}, Nb depletion, Ti adjacent phase composition and Ti interface composition for specific boundary types for the as-received and irradiated samples.

The compositions of the interfaces can be found in tables 3.2 and 3.4, however the interface compositions are only really comparable when compared as enrichments or depletions compared to their adjacent grains. As the low Nb regions, which are either side of the equilibrium boundaries, are nearly the same between the as-received and irradiated sample, a valid comparison can be made between interface concentrations of the equilibrium boundaries for each sample, table 3.8. The irradiated sample appears to have a marginally lower Nb content at the boundary, with greater amounts of Sn, Ti and Cu than the as-received sample. However, this difference is within the statistical error of the measurements, therefore any correlation is suggested tentatively.

Sample	Nb at%	Sn at%	Ti at%	Cu at%
Non-Irr	69.5 $\pm$ 1.9	24.5 $\pm$ 1.9	1.9 $\pm$ 0.8	4.0 $\pm$ 1.5
Irr	67.4 $\pm$ 1.8	25.4 $\pm$ 0.7	2.3 $\pm$ 0.3	4.9 $\pm$ 1.5

Table 3.8: Grain boundary composition of the equilibrium grain boundaries from the as-received and irradiated samples

3.6.3 Additional Features of Interest

The as-received sample contained: residual Nb, linear dislocation arrays, out-of-plane dislocations and Ti boundaries. The irradiated sample contained all the features of interest listed for the as-received sample and additionally contained orthogonal sets of low angle dislocations which formed grain boundaries and both Ti and Cu decorated dislocation loops.

The amount and size of the residual Nb differed between the as-received and irradiated samples, with 7 Nb clusters found in the as-received sample compared to 3 found in the irradiated sample. To characterise a region as *pure Nb* an isosurface of 95 at% Nb was used to define each Nb cluster. A total volume of residual Nb in the as-received sample of 1.3 $\times$ 10^4 nm^3 and 620 nm^3 for the irradiated sample, this is approximately 0.15% of the total volume of the as-received sample and 0.01 % of the irradiated sample. The mean volume of each Nb cluster for the as-received sample is 1900 $\pm$ 1900 nm^3 and 210 $\pm$ 160 nm^3 for the irradiated sample. The as-received sample has significant scatter in residual Nb size, however the cluster volume

appears to decrease approximately by almost an order of magnitude in the irradiated sample. The dimensions of the Nb clusters is influenced by the implementation of the reconstruction calibration from each experiment. As an approximation to estimate the size of the Nb clusters an assumption of a perfectly spherical cluster was used to generate an approximate radius for each cluster. For the as-received sample the Nb average radius is 6.9 $\pm$ 2.5 nm and the irradiated sample is 3.4 $\pm$ 1.3 nm. Although there are only very few clusters, any additional pinning will be less effective in the irradiated material. However, any effect from residual Nb will be weak as there is relatively very little residual Nb in either sample which could be acting as additional pinning centres. The significant segregation of Cu to the Nb cluster interfaces, as seen in Figure 3.19, could also produce some additional surface type pinning for both samples.

As linear dislocation arrays and out-of-plane dislocations were found in similar quantities in each sample these will not be compared further. Both samples did contain Ti only boundaries, with the as-received sample showing associated Cu clusters to the boundary. However, the irradiated Ti boundary showed no sign of associated Cu clusters, potentially due to the irradiated Ti boundary being in the region of equilibrium Nb_3Sn which has no solubility for Cu and the as-received Ti boundary being between two high Nb regions which can dissolve a small amount of Cu.

Within the APT tips taken from the irradiated sample, two dislocation loops were found, one strongly segregated with Cu and weakly with Ti, and one strongly segregated by Ti with Cu clusters around the loop. Dislocation loops are formed by the collapse of excess point defect concentrations to form regions of interstitial or vacancy stacking faults bounded by the dislocation loops. Although APT is unable to visualise point defects, the presence of dislocation loops suggests an excess amount of point defects has been formed from neutron irradiation of the sample. Previous TEM conducted on fast neutron irradiated Nb_3Sn tapes revealed dislocation loops with a diameter 15 to 30 nm [145], which is consistent with the findings in Figures 3.32 and 3.33.

3.7 Discussion

The superconducting results from the as-received sample compared to the irradiated sample showed a decrease in T_c by approximately 1 K from 17.6 K to 16.6 K, a shift in F_p towards point pinning, an increase in F_p^{MAX} at all temperatures sampled and a small increase in the estimated B_{c2} value. Although the as-received sample and irradiated sample are not originally the same section of wire, and therefore may contain some random fluctuations in microstructure, these superconducting results are very similar to previous results of fast neutron irradiated RRP® wires [66, 151]. Baumgartner used the same type of RRP® wire as in this study, and showed that a fast neutron fluence of 2.2×10^{22} m^{-2} can produce an increase in peak J_c of approximately 50% at 4.2 K and 6 T [66]. The results from this study show an increase in J_c at from 1.4×10^{10} to 2.2×10^{10} Am^{-2}, which is 58% increase in J_c.

Some of the results of the APT findings above could be contributing towards the modification in behaviour between the as-received and irradiated samples. Initially it is important to focus on how the APT findings can help to understand the superconducting properties of Nb_3Sn in the as-received state. Previous studies relating unirradiated Nb_3Sn to T_c and B_{c2} have shown that bulk Sn content plays a large role in affecting these measured quantities [45]. However, all the data which Flükiger uses to show that a decrease in Sn content in the A15 phase reduces T_c and B_{c2} is either via SEM EDX [111, 197] or EPMA [117, 119], as detailed in section 3.4.1, and therefore does not take account for the significant local fluctuations in these parameters observed in this study. APT has shown in section 3.4.1 that the as-received sample has substantial compositional variations on the sub-granular level, with regions of high Nb Nb_3Sn and grain boundaries significantly off the ideal stoichiometry for good T_c and B_{c2} values. Off stoichiometry bulk Nb_3Sn is known to be dominated by antisite disorder [46], with the excess Nb occupying Sn sites (Nb_{Sn}) and a negligible vacancy concentration [47]. Sitaraman *et al* used DFT to model single crystal Nb_3Sn for SRF applications [48]. The DFT showed that the Nb_{Sn} defects in Nb_{Sn} cluster together to form Sn depleted regions in association with the free surfaces. The regions of high Nb seen in the APT data from the as-received sample are likely to be dominated by these Nb_{Sn} antisite defects, however as the grain size in the RRP® is

108 $\pm$ 48 nm [20] this may explain why the high Nb regions are not always directly associated with the grain boundaries. Sn has been shown to be the fastest diffusing species in forming Nb_3Sn using Kirkendell markers [202], despite first principle energy calculations predicting Nb to be the fastest diffusing species [47]. The discrepancy between theory and experiment can be explained by assuming that grain boundary diffusion is the dominant diffusion process [203]. The regions of high Nb suggest incomplete diffusion of Sn from the grain boundaries into the centre of the grains, and the residual Nb particles are further evidence of incomplete diffusion, section 3.4.4. The potential benefit of these high Nb regions is the additional pinning in addition to that from the grain boundaries. The grain boundaries have excess solute segregated to them, likely making them stronger pinning centres than sub-grain boundaries separating high Nb and low Nb regions which do not have strong segregation and should therefore perhaps be classified as weak boundaries. Figure 3.10 shows a boundary between a low and high Nb region, with the Nb and Sn content varying approximately over 5 nm and the Ti content varying over a wider 15 nm. Compositional changes at the sub-grain boundaries occurs over a distance which is similar to the coherence length in Nb_3Sn ($\sim$ 3 - 4 nm), therefore it is likely that these boundaries are contributing to the overall pinning force in as-received RRP® wires.

Further evidence from APT for the as-received sample has shown that grain boundaries can be categorised into equilibrium, mixed and high boundaries. The solute segregation behaviour differs for each type of boundary, with the largest Nb depletion and solute segregation of Ti and Cu seen in the mixed boundaries. Although the amount of segregation is not vastly different between boundaries, the number of each type of boundary, and their relative pinning strength, will be relevant in determining the overall surface pinning force in Nb_3Sn. In the same way, the number of dislocation features and their regularity within the Nb_3Sn will also contribute to the pinning force. Although it is not possible to calculate the Γ_i through a linear feature, from Figures 3.20 and 3.13 the peak Cu concentrations are similar for both boundaries and dislocations, although dislocations appear to have a weaker association with Ti than grain boundaries. In addition to the linear features present within the as-received sample, the presence of unreacted Nb could be providing additional pinning. Nb particles, as shown in Figure 3.19,

have Cu strongly segregated to the interface of Nb/Nb_3Sn in a similar way to Cu segregating to the grain boundaries. The large Nb particles, which are significantly larger than the coherence length, will not be contributing to point pinning, however, their interfaces may be contributing to surface pinning. The final type of boundary which needs to be considered is a Ti boundary, of which only 1 was sampled in the volume of material from this work. The Γ_i for the Ti boundary gave 13.8 $\pm$ 0.8 atoms/nm^2, which is slightly below, but comparable, to Γ_{Cu} for equilibrium and mixed grain boundaries. Crystallography of the adjacent grains around the Ti boundary is not possible to distinguish using APT in laser mode, therefore it is difficult to determine whether this boundary defines two grains or indeed defines a sub-grain. Attempts were made to run tips in voltage mode to retrieve crystallography information, however the tips fractured due to the brittle nature of Nb3Sn, so no crystallographic information is available.

The introduction of irradiation damage is expected to produce many point defects, such as vacancies, interstitials and Frenkel pairs which will reduce the local order of the A15 phase [204]. Neutron damage will affect the material uniformly, with radiation induced defects equally likely at the grain boundaries as within the grains. The introduction of point defects can help to explain the drop in T_c, the small increase in B_{c2} and the changes in segregation to features in the irradiated sample. When it is energetically favourable these point defects can agglomerate and produce larger defects on the nanoscale. Agglomerations of defects which produce changes in crystallography suggest the presence of these disordered regions which have been seen in HR-STEM and TEM on neutron irradiated Nb_3Sn wires [20, 145, 201, 205]. For samples irradiated in the TRIGA-II reactor an average diameter of 2 nm has been predicted by T. Baumgartner through energy displacement calculations [191]. Despite consensus that these *regions of disorder* exist, it is debated as to exactly what lies in these regions. It has been proposed that when the separation distance of these disordered regions approaches the coherence length that this causes a reduction in T_c [190]. The 1 K reduction in T_c for the irradiated material is therefore likely to contain nanoscale regions of disorder and some atomic scale defects. The regions of disorder, on a similar scale to the coherence length, are thought be adding additional point pinning to the irradiated samples, therefore causing the shift in

pinning curve towards a point pinning mechanism and overall increasing the pinning force in fast neutron irradiated RRP® wires [66, 151, 191]. Although APT cannot image point defects or detect changes in crystallography, associated solute segregation to these defects can be seen. Potential evidence for agglomeration of point defects are the Cu and Ti dislocation loops and the orthogonal dislocation arrays, which are only present in the irradiated sample.

In this work the irradiated sample has shown a reduction in size and volume of the high Nb regions, as well as small increase in the amount of Nb associated with these high Nb regions. It is expected that the large quantities of point defects produced in the irradiated sample, such as vacancies, accelerate diffusion and could potentially result in a reduction in the size of the metastable high Nb regions. Surface diffusion is already fast in Nb_3Sn [203], a small increase in surface diffusion may be predicted, which is supported by the increase in Cu solute excess at equilibrium grain boundaries. Bulk diffusion in Nb_3Sn is low [203], therefore the reduction in size of the metastable high Nb after irradiation supports the theory that there is increased bulk diffusivity caused by irradiation induced point defects. Further evidence of increased bulk diffusion in the irradiated sample is the reduction in number and size of residual Nb particles.

B_{c2} is dominated by the best interconnected superconducting path within the superconductor, so should be determined by current paths through the low Nb regions, bypassing the high Nb regions, due to their favourable superconducting properties. The observed decrease in T_c suggests the introduction of point defects into the irradiated sample, this atomic scale disorder is likely shifting the Nb_3Sn from the clean limit towards the dirty limit which may slightly increase B_{c2} [45, 206].

The increase in F_p and the shift in F_p towards point pinning is likely attributed to the nature of the *regions of disorder*. However, the increase in Cu segregation at the grain boundaries may also be modifying the surface pinning strength in the irradiated sample. The addition of dislocation loops, which have an approximate thickness on the scale of the coherence length, could be adding additional point pinning to the irradiated sample. However, it is difficult to quantify the amount of additional point pinning produced in the irradiated sample, as many of the *regions of disorder* will not show any obvious chemical segregation.

3.8 Conclusions

In depth nanoscale analysis of an as-received RRP® wire and a neutron irradiated RRP® wire have been compared in this chapter. APT has been used to explore the chemical segregation of both intra- and inter-grain regions in the two wires with the major finding that fine grain Nb_3Sn can be split into three different regions of composition: low Nb, high Nb and grain boundaries. The summed composition of these three distinct regions is in line with the predicted Nb-Sn-Ti A15 phase field, yet none of three regions themselves lie within the equilibrium phase field. The volume of high Nb in the A15 structure reduces after neutron irradiation, suggesting an increase in bulk diffusion caused by the production of irradiation induced point defects, leading to a predicted increase in B_{c2}. Finally, additional defect structures are present in the irradiated sample which could be acting as additional pinning sites, therefore promoting an increased F_p.

Chapter 4

APC RIT Sample

The effect of fast neutron irradiation on the superconducting properties and microstructure of Ti doped RRP® wires has been analysed in chapter 3. The alternative dopant known to increase B_{c2} in Nb_3Sn is Ta, as discussed in section 1.6. In this chapter the effect of Ta and the addition of APCs on the nanostructure of a Nb_3Sn RIT wire will be analysed and compared to the superconducting properties the wire.

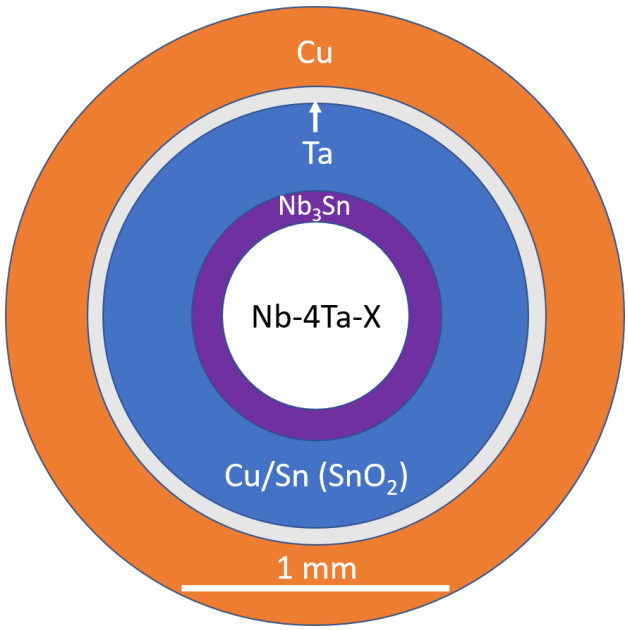


Figure 4.1: Schematic of a RIT layout produced by Balachandran *et al* [64]. A custom Nb alloy is placed in the centre, surrounded by the Cu/Sn (SnO_2) in a Ta barrier layer.

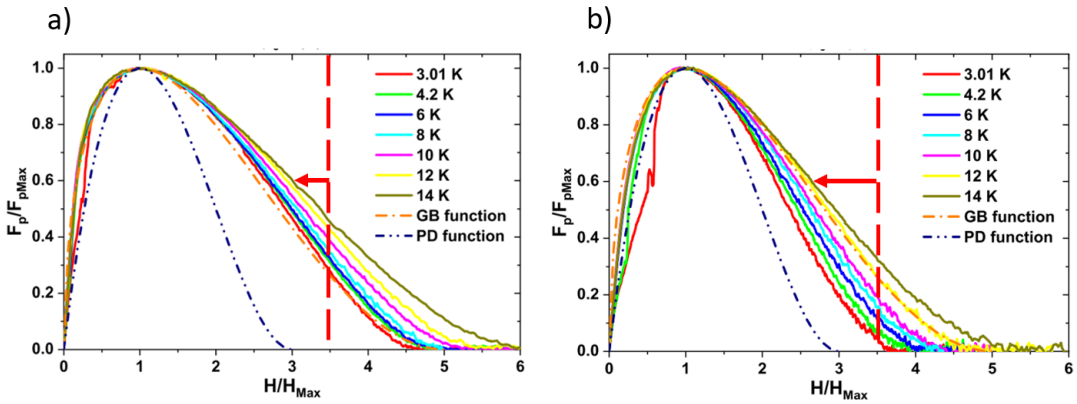


Figure 4.2: a) Normalised pinning force curve for the Nb-4Ta sample b) Normalised pinning force curve for the Nb-4Ta-1Hf sample adapted from Tarantini *et al* [58]. Red arrows show the shift in pinning force curve towards the point pinning function in the Nb-4Ta-1Hf sample.

The MagLab in Tallahassee, produced a selection of developmental RIT wires, with the aim to produce a wire which reached the equivalent RRP® non-Cu J_c 1500 Amm^{-2} at 16 T for the FCC target. Balachandran *et al* produced a variety of RIT wires with different custom Nb alloys: Nb-4Ta-1Hf, Nb-4Ta, Nb-4Ta-1Zr (at%) either with or without SnO_2 in the configuration shown in Figure 4.1 [64]. The samples were heat treated at 550°C for 100 hrs and 670°C for 100 hrs to produce the final Nb_3Sn layers. Previous work by Xu *et al* had shown that Zr and SnO_2 could produce ZrO_2 nanoparticles through internal oxidation [65]. Balachandran *et al* wanted to replicate the success of Xu *et al* with a high J_c wire and to verify whether HfO_2, which has a more negative formation energy than ZrO_2 [89, 207], could be produced through internal oxidation. The Nb-4Ta-1Hf sample without SnO_2 produced the highest equivalent RRP® non-Cu J_c at 16 T of 2230 $\pm$ 640 Amm^{-2} [64], estimated from field measurements up to 14 T, reaching the J_c target for the FCC. As can be seen in Figure 4.2, there is a shift in the pinning curve from surface pinning in the Nb-4Ta sample, to a combination of surface and point pinning in the Nb-4Ta-1Hf sample. F_p^{MAX} of the Nb-4Ta-1Hf wire occurs at $\sim 0.25H_{IRR}$ [58] which is between the values of $0.2H_{IRR}$ for surface pinning and $0.33H_{IRR}$ for point pinning [49] therefore implying both pinning mechanisms are active.

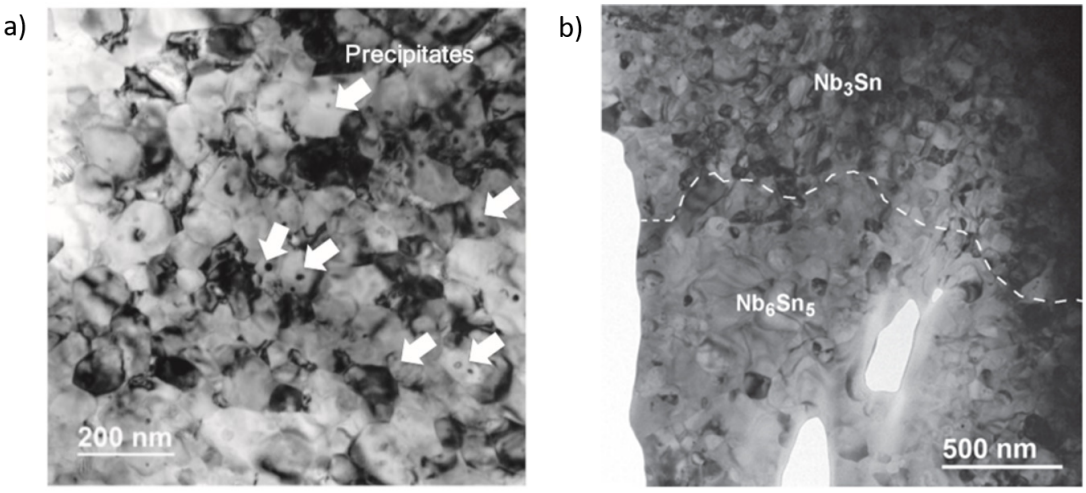


Figure 4.3: a) Bright field TEM image of Nb_3Sn grains near the alloy-rod interface, with white arrows indicating the presence of intergranular precipitates b) Bright field TEM image of Nb_3Sn-Nb_6Sn_5 interface with Nb_6Sn_5 grain sizes below 100 nm. Figures adapted from [64].

Microstructural investigations were carried out on the high J_c Nb-4Ta-1Hf wire with TEM showing evidence of precipitates, approximately 10 nm, as seen in a) from Figure 4.3, and evidence of a fine grain layer of Nb_6Sn_5 in contact with the Nb_3Sn layer [64], as seen in b) from Figure 4.3. The Nb_3Sn layer was found to have an average grain size of 68 $\pm$ 25 nm, substantially smaller than that which can be produced for commercial RRP® wires.

As oxygen was not intentionally added to the pre-heat treatment Nb-4Ta-Hf rod, APT and EPMA have been used been used in this work to determine the amount and distribution of oxygen within the pre-heat treatment Nb-4Ta-Hf alloy and the Nb-4Ta-Hf alloy after the final heat treatment. APT has then been used to analyse nanoparticles (from here on named clusters), intra-grain and inter-grain composition as well as additional features of interest such as Nb_6Sn_5 and Cu rich precipitates associated with the Nb_3Sn layer. An introduction to APT analysis on the Nb_3Sn layer sample has previously been published [208], however in depth analysis over a wider range of tips has been conducted in this work and then correlated with the measured pinning performance of the wire.

4.1 Pre-heat Treatment Nb-4Ta-1Hf Alloy

A polished cross section of a pre-heat treatment Nb-4Ta-1Hf RIT wire was sent from Florida, in the same configuration as that seen in the reacted state, Figure 4.8. The pre-heat treatment alloy of interest was located in the centre of the un-reacted RIT wire.

4.1.1 EPMA

To determine whether the pre-heat treatment Nb-4Ta-1Hf custom alloy did contain significant amounts of oxygen, EPMA was carried out. As the oxygen concentration peak is difficult to determine using EDX, EPMA was chosen to provide more reliable composition measurements for the alloy. EPMA mapping of Nb, Ta, Hf and O elements against a standard was carried out by C. Salter of Oxford Materials Characterisation Service. Figure 4.4 shows only the Ta and Hf maps from the as-received alloy which showed some weak inverse segregation highlighted in red. This shows evidence that there is some weak micro-segregation between Ta and Hf on the micron-scale, which may affect the overall composition of individual nanoscale APT tips. The Nb and O maps have not been included for this sample because there is no obvious segregation on the micron scale.

To calculate an overall composition for the as-received alloy, 30 line-scans were taken across the diameter of the cross section of the alloy and an average composition and standard deviation were calculated, table 4.1. It can be seen that the Ta and Hf concentrations are approximately as specified, but there is a non-negligible 5 at% concentration of oxygen present within the as-received Nb alloy. The custom alloy was arc-melted under 0.5 bar of high purity argon (C. Tarantini and D. Larbalestier, private communication, 28 Jul 2023) with the intention that very little oxygen would be trapped within the alloy. However, the binary Nb-O phase diagram shows that the maximum solubility of oxygen in Nb is $\approx$ 9 at% [209] at 1915°C, so it is possible that up to 9 at% oxygen could be present in the Nb alloy without oxides forming. However, this does not account for the presence of Ta in the alloy, which is more reactive with oxygen than Nb [89].

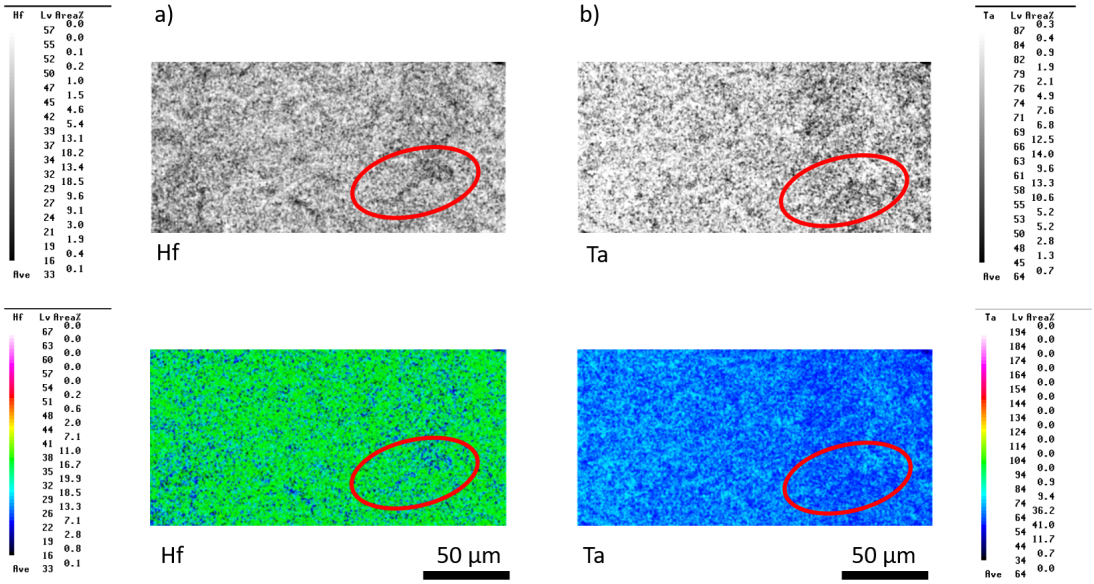


Figure 4.4: a) EPMA map and intensity scale for Hf in greyscale and colour b) EPMA map and intensity scale for Ta in greyscale and colour for the as-received Nb alloy

	Nb at%	Ta at%	Hf at%	O at%
Nb-4Ta-1Hf alloy	90.38 ± 0.62	3.62 ± 0.15	0.91 ± 0.06	5.09 ± 0.62

Table 4.1: EPMA composition measurements from the as-received Nb-4Ta-1Hf alloy

4.1.2 Atom Probe Tomography

To determine whether any nanoscale oxygen rich particles were present in the Nb-4Ta-1Hf alloy prior to reaction, 4 APT samples were extracted from the pre-heat treatment sample. The region selected for the atom probe lift-out was parallel to the edge of the alloy as this is the location in which the Nb_3Sn would form after reaction. APT samples were produced on the Crossbeam FIB instrument, using the lift-out procedure described in section 2.2.4. Samples were analysed using the same APT experimental conditions as the RIT Nb_3Sn sample: LEAP XS base temperature of 60 K, laser pulse energy of 80 pJ and frequency of 125 kHz at a detection rate of 0.3. The Nb alloy experiments could have been conducted at a lower laser energy because the alloy is less brittle than the Nb_3Sn layer, however the author wanted to be consistent in the application of experimental conditions across the pre-heat treatment, reacted Nb alloy and Nb_3Sn layer to understand which peaks may be missing from the Nb_3Sn layer due to overlaps. All data for this chapter was reconstructed using IVAS 3.8.16 software from CAMECA.

Nb^{3+} and Nb^{2+} peaks are the dominant Nb peaks in the m/q spectrum but there is also a peak at 61.9 Da for Nb_2^{3+}. A small peak is present at 92.9 Da which could be either Nb^+ or Nb_2^{2+}, however these counts have been indexed as Nb^+. This peak is over 100 times smaller than the largest Nb peak, therefore indexing this peak as Nb^+ instead of Nb_2^{2+} may only very slightly underestimate the amount of Nb present in each dataset. NbN and NbC compound ion peaks are present within the m/q spectrum suggesting some impurities of nitrogen and carbon were introduced during manufacture. Both Hf^{2+} and Hf^{3+} ions are present within the m/q spectrum, which is important for interpreting APT data from the reacted Nb_3Sn layer as the overlap of Hf^{3+} with Sn^{2+} peaks leads to an underestimation of Hf within the Nb_3Sn. The number of counts of Hf^{3+} and Hf^{2+} ions in this metallic alloy were compared as a ratio to estimate approximately how much Hf may be unaccounted for in the Nb_3Sn data, and this comparison can be found in section 4.3. In addition to the Hf ion peaks, there are also HfO^{2+} compound ions detected, as shown in Figure 4.5, with indications of HfO^{3+} and HfO^+ peaks, although these have a height of less than 10 counts and are hard to distinguish.

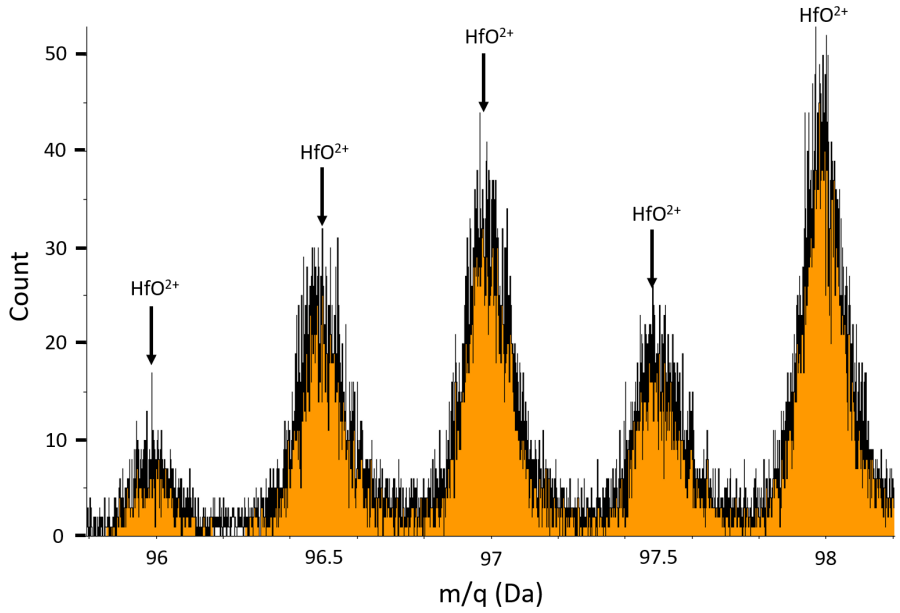


Figure 4.5: Close-up section of the m/q spectrum of the as-received Nb-4Ta-1Hf alloy showing HfO^{2+} peaks. The differing HfO^{2+} peaks are the different isotopes of Hf with masses: 176, 177, 178, 179 and 180.

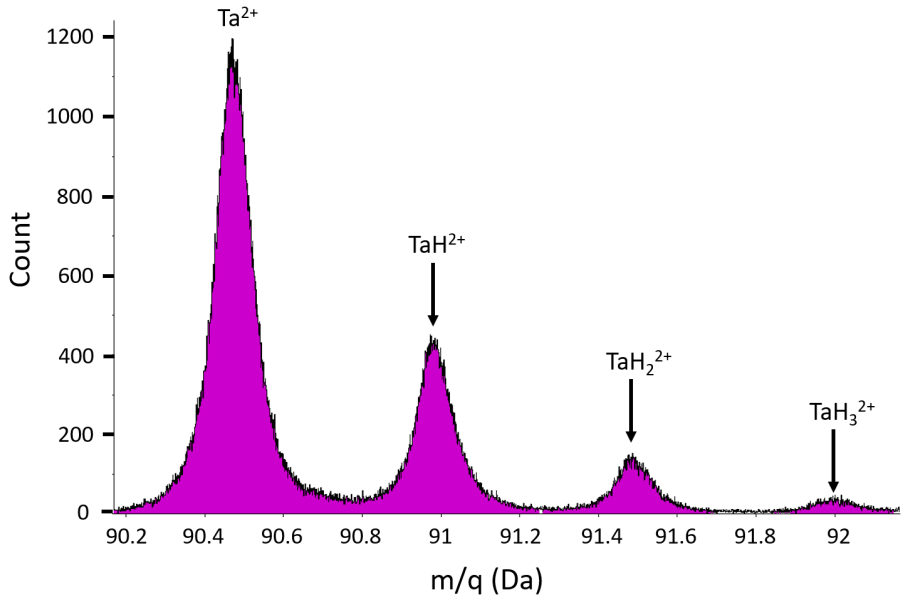


Figure 4.6: Close-up section of the m/q spectrum of the as-received Nb-4Ta-1Hf alloy showing Ta^{2+}, TaH^{2+}, TaH_2^{2+} and TaH_3^{2+} peaks.

The dominant Ta peaks are Ta^{3+} and Ta^{2+} with a series of what are likely Ta hydrides present at 90.5, 91.0, 91.5 and 92 Da, as shown in Figure 4.6, which are likely produced from residual hydrogen in the atom probe chamber. Although hydrides up to TaH_3 seem unlikely, care was taken to ensure these ions matched the location of the other Ta ions present and that no other possible ions could be producing these peaks. There are also TaO compound ion peaks present, with the largest peak TaO^{2+}, and the TaO^{+} and TaO^{3+} peaks between 10 to 30 times smaller than the TaO^{2+} peak. Moreover, there is the presence of Zr and ZrO impurity peaks within the m/q spectrum, examples of these can be found in section 4.3. A trace quantity of Zr is expected in Nb alloys as Zr is difficult to remove and these amounts are unlikely to effect the final microstructure. To verify whether Zr or ZrO ions did segregate these were ranged in the reconstruction and were seen to be randomly distributed within the tips.

Initially an overall bulk composition of the four APT reconstructions was determined, with the error given as the standard deviation. This composition can be found in table 4.2, suggesting a concentration of oxygen in the pre-heat treatment alloy of 2.53 $\pm$ 0.98 at%, about half of the value determined from EPMA analysis. To show the oxygen distribution in the APT tips one of the tips has been reconstructed and visualised in Figure 4.7 to show only HfO, TaO and TaO ions, as the O ion peak is negligible. There is no obvious HfO ion clustering in any of the as-received Nb-4Ta-1Hf alloy reconstructions, but as can be seen from Figure 4.7 there is a grain boundary present in one of the reconstructions. A 1D concentration profile has been measured across the profile with the compound ions decomposed into the elemental species, this shows a clear increase in O at the boundary, and not shown, a 2 - 3 at% depletion in Nb at the boundary. It is predicted that a boundary could be captured in an APT dataset as the grain size of the as-received alloy is 170 $\pm$ 30 nm [64]. Despite no obvious clustering, a nearest neighbour search was carried out for each compound ion: HfO, TaO, NbO. If clustering is present then it would be expected that the nearest neighbour distribution for a species, e.g. HfO ions, would have a peak at a closer distance than that of a random HfO ion distribution. At low nearest neighbour orders the distribution of ions for all three species tested appeared to be random, and at orders of 4 - 6 there was a small change in the distribution with HfO ions, so a cluster search

	Nb at%	Ta at%	Hf at%	O at%	Zr at%	N at%	C at%
Nb-4Ta-1Hf	92.98 ± 0.83	3.43 ± 0.4	0.84 ± 0.11	2.53 ± 0.98	0.03 ± 0.01	0.1 ± 0.03	0.09 ± 0.09

Table 4.2: APT composition measurements from the as-received Nb-4Ta-1Hf alloy

was conducted in accordance with section 2.6.6. However, no real clustering was found in the alloy, only some aberrant association with a crystallographic pole in one of the reconstructions.

The pre-heat treatment alloy contained a substantial amount of oxygen before the reaction to form Nb_3Sn, 5.09 ± 0.62 at% according to micron scale EPMA and 2.53 ± 0.98 at% using nanoscale APT, however no obvious evidence of HfO_2 clustering was found in the pre-heat treatment alloy. To determine whether diffusion during the reaction to form Nb_3Sn caused any change in oxygen concentration or production of clusters in the alloy the reacted Nb-4Ta-1Hf alloy was tested next.

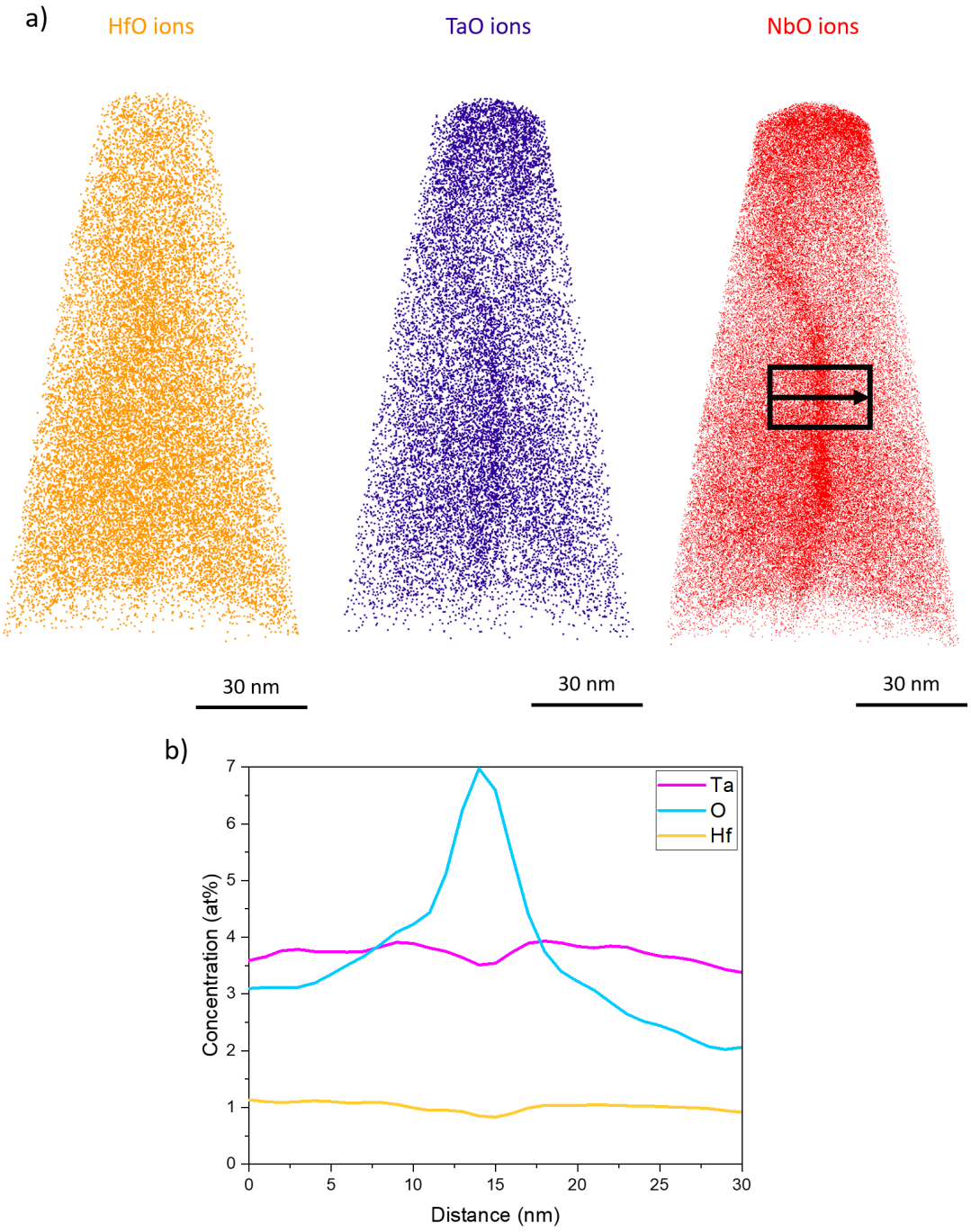


Figure 4.7: a) APT reconstruction of an as-received Nb-4Ta-1Hf tip showing HfO, TaO and NbO ions with no obvious oxide clusters present but a clear boundary most obvious in the NbO ion reconstruction b) A 1D concentration profile with the decomposed ions Ta, O and Hf, there is clearly a peak in O at the boundary. The Nb curve is not shown, but does show a dip in Nb content of 4 at%, corresponding with the increase in O at the boundary.

4.2 Reacted Nb-4Ta-1Hf alloy

A reacted RIT sample was also mounted and polished in conductive Bakelite to produce a cross-section of the overall wire with the reacted Nb-4Ta-1Hf alloy located in the centre of the wire, Figure 4.8, this was confirmed using EDX, Figure 4.9. This wire is designed as a test wire and therefore the ratios of Cu/Sn were not carefully controlled and produced significant pores in the original Cu-Sn powder region of the sample due to the Kirkendell effect. Surrounding the Nb-4Ta-1Hf layer, seen in Figure 4.8, is a non-homogeneous ring of Nb-Sn phases dispersed with trapped channels of Cu-Sn phases (shown in darker contrast), the exact location of the Nb_3Sn region will be discussed in section 4.3. Both EPMA measurements and APT experiments were carried out on the reacted Nb alloy to determine whether the oxygen concentration had changed and if any HfO_2 clusters had been produced.

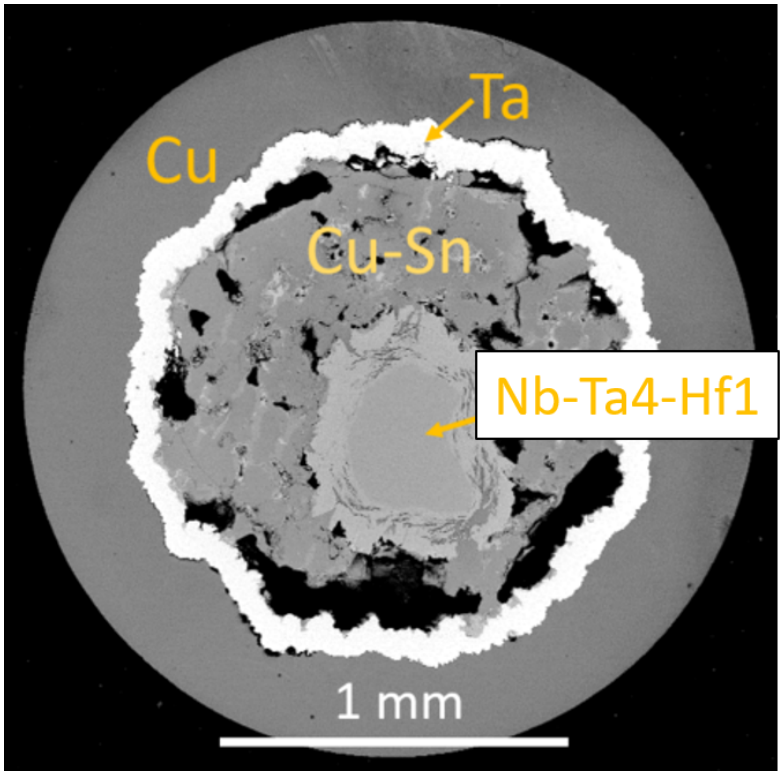


Figure 4.8: BSD image of the Nb-4Ta-1Hf RIT wire. The sample was heat treated at 550°C/100 hrs and 670°C/100 hrs to produce the Nb_3Sn layer which is located on the edge of the Nb-4Ta-1Hf central rod approximately 10 μm thick [64].

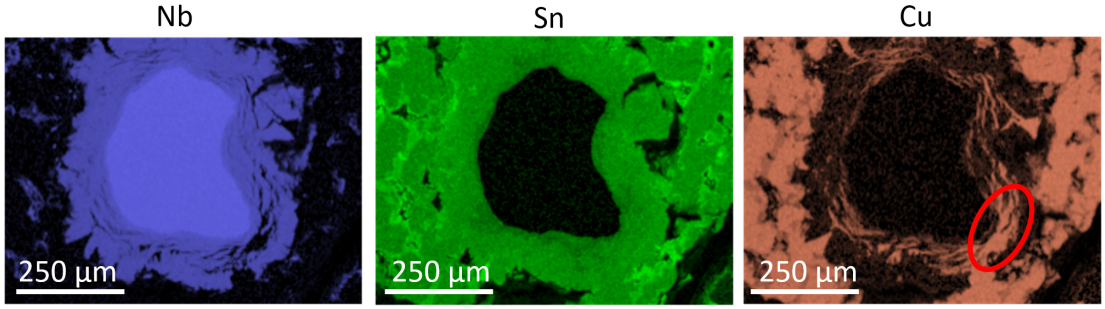


Figure 4.9: EDX map of Nb, Sn and Cu showing the central Nb custom alloy and an outer ring comprised on Nb-Sn phases which contain come trapped Cu-Sn phases, circled in red

4.2.1 EPMA

EPMA chemical mapping across the sample was conducted for Nb, Ta, Hf and O species. Like the as-received alloy, the only maps which showed some correlation in segregation were the Hf and Ta maps, where there again appeared to be inverse segregation of Hf and Ta, as shown in Figure 4.10 highlighted in red.

To give an overall composition for the reacted alloy, 30 line-scans were taken across the sample, from the top of the Nb4Ta1Hf alloy in Figure 4.8 to the bottom, and an average composition given in table 4.3. The amount of oxygen in the pre-heat treatment alloy of 5.09 $\pm$ 0.62 at% increased to 8.48 $\pm$ 1.43 at% in the reacted alloy, this shows that although some initial oxygen was present in the starting alloy that more oxygen diffused from the outer Cu/Sn region. From the binary Nb-O phase diagram at 670°C approximately 1 at% O can be dissolved in Nb before NbO is expected to also form [209], therefore in this more complicated alloy it would be expected that oxides may have formed. The EPMA map for oxygen has also been included, Figure 4.11, which on the micron scale does not show any signs of large oxide particles which may have formed, however the oxygen intensity does appear to vary, this suggests that APT results may show fluctuations in oxygen content.

	Nb at%	Ta at%	Hf at%	O at%
Nb-4Ta-1Hf	87.10 $\pm$ 1.34	3.56 $\pm$ 0.15	0.86 $\pm$ 0.06	8.48 $\pm$ 1.43

Table 4.3: EPMA composition measurements from the reacted Nb-4Ta-1Hf alloy

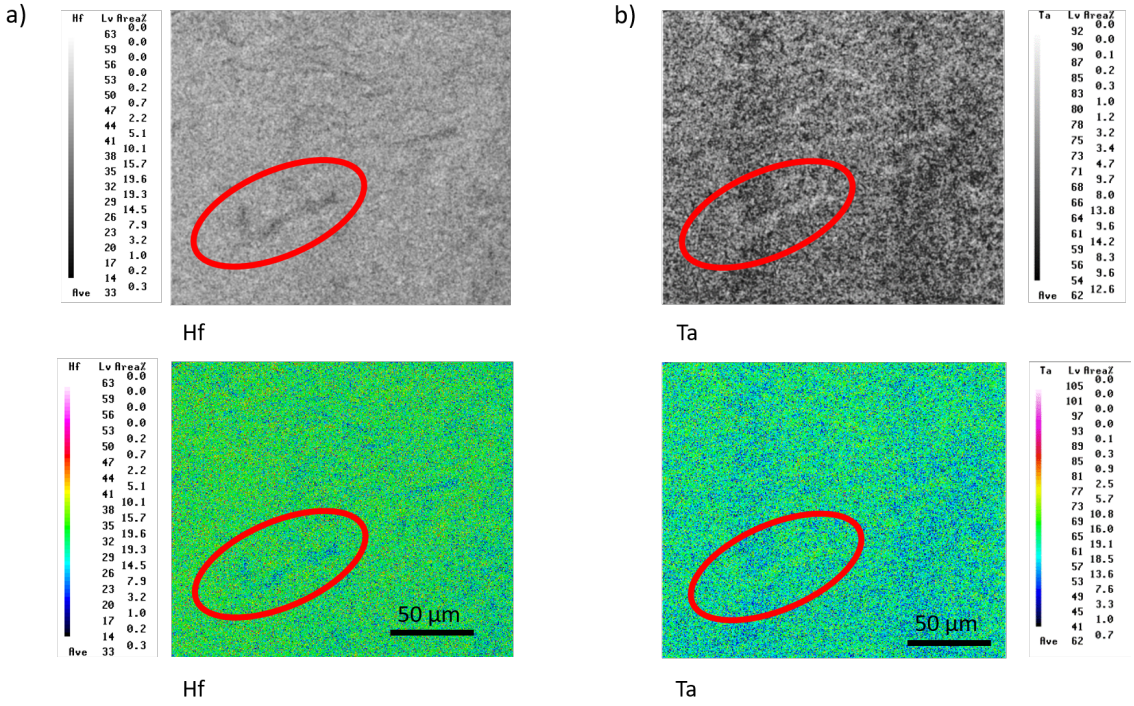


Figure 4.10: a) EPMA map and intensity scale for Hf in greyscale and colour for the reacted Nb-4Ta-1Hf alloy b) EPMA map and intensity scale for Ta in greyscale and colour for the reacted Nb-4Ta-1Hf alloy

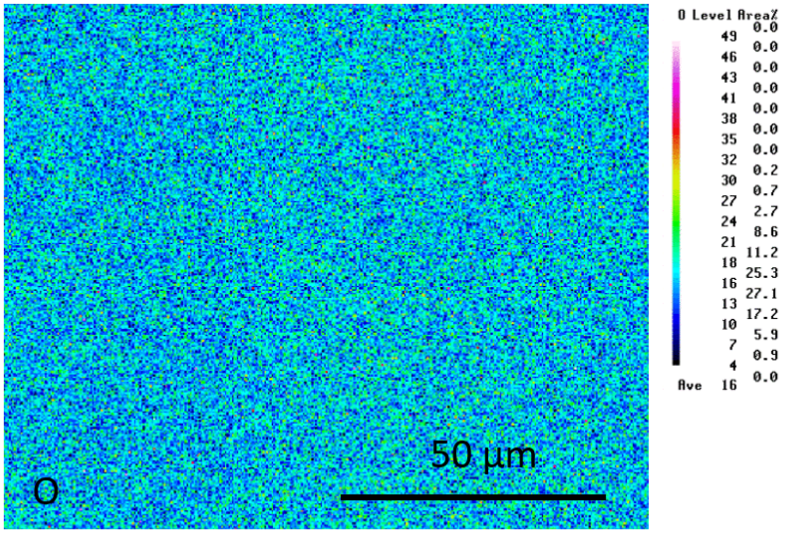


Figure 4.11: EPMA map and intensity in colour for oxygen for the reacted Nb-4Ta-1Hf alloy

4.2.2 Atom Probe Tomography

A lift-out of the reacted Nb alloy was conducted and 5 tips were produced. All tips were analysed under the same conditions as the later RIT Nb_3Sn tips: a base temperature of 60 K, a laser pulse energy of 80 pJ, a pulse frequency of 125 kHz at a detection rate of 0.3 on a LEAP XS. Figure 4.12 shows only the spatial distribution of HfO ions across 3 reconstructions from the reacted Nb alloy. It is clear that the first and third reconstructions contain clustering, whereas the second reconstruction has no obvious clustering. Three tips which contained HfO_2 clusters had an average oxygen content of 2.5 $\pm$ 1.1 at% and the two tips which did not contain any clusters had an average oxygen content of 2.4 $\pm$ 0.5 at%, therefore there is significant difference in oxygen concentration between the tips.

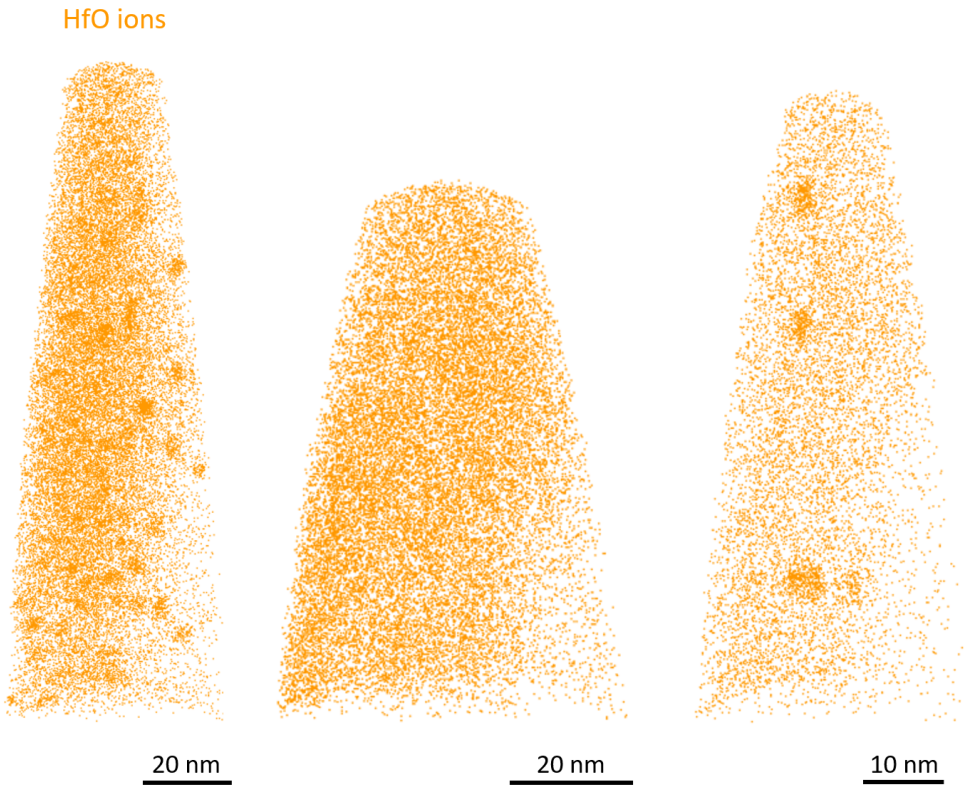


Figure 4.12: APT reconstructions of three tips from the reacted Nb-4Ta-1Hf alloy showing the distribution of HfO ions for visual clarity. For clarity the first tip contains 11.6 million ions, the second contains 7.3 million and the third contains 5.9 million ions.

Nb at%	Ta at%	Hf at%	O at%	Trace at%
93.05 ± 0.85	3.44 ± 0.12	0.76 ± 0.09	2.50 ± 0.80	0.25 ± 0.20

Table 4.4: APT composition measurements from the reacted Nb-4Ta-1Hf alloy

The same peaks from the m/q spectrum of the pre-heat treatment Nb alloy, such as NbN, NbC, NbO and Nb_2 ion peaks, were also present in the m/q spectrum of the reacted alloy sample. An overall bulk composition for the five reconstructions was produced and the standard deviation of each composition measurement calculated in table 4.4. Here, trace elements include N, C and Zr which were present in the mass spectrum. It is clear from the APT reconstructions that the local concentration of oxygen is lower than that seen on the micron scale by EPMA, this suggests that the oxygen is in-homogeneously distributed through the reacted Nb alloy, with potentially large oxides present at other regions of the alloy. The total volume sampled by the APT reconstructions is estimated to be 3.6 $\times$ 10^5 nm^3, which is much less than 1 μm^3, therefore the nanoscale variation can be very different to the bulk micron scale composition measurements.

Cluster searches were carried out on each reconstruction in accordance with section 2.6.6 using only HfO ions as the solute ions in the clusters, with further details discussed later for the Nb_3Sn layer in section 4.3.5. To demonstrate that the clusters are HfO_2, a proxigram, as discussed in section 2.6.3, was made of the largest 88 HfO ion clusters using a 3 at% HfO ion isosurface from the reacted Nb alloy reconstruction with the highest density of clusters, as shown in Figure 4.13. When the background matrix concentration is removed it is clear that the ratio of Hf:O is approximately 1:2 across a large amount of clusters of differing size and shape.

The values of number density and diameter of the cluster distribution can be found in table 4.5. Out of the 5 APT tips analysed from the reacted alloy, 2 of the reconstructions did not contain any clusters at all, hence producing a large standard deviation in number density. The location of clusters in 3 of the reconstructions are shown in Figure 4.14, where it is clear that the clusters appear to favour a certain plane in each of the 3 reconstructions. The second reconstruction in Figure 4.14 shows an obvious depletion in Nb atoms associated with the plane, this could suggest the presence of a grain boundary in this tip. However, there is no obvious

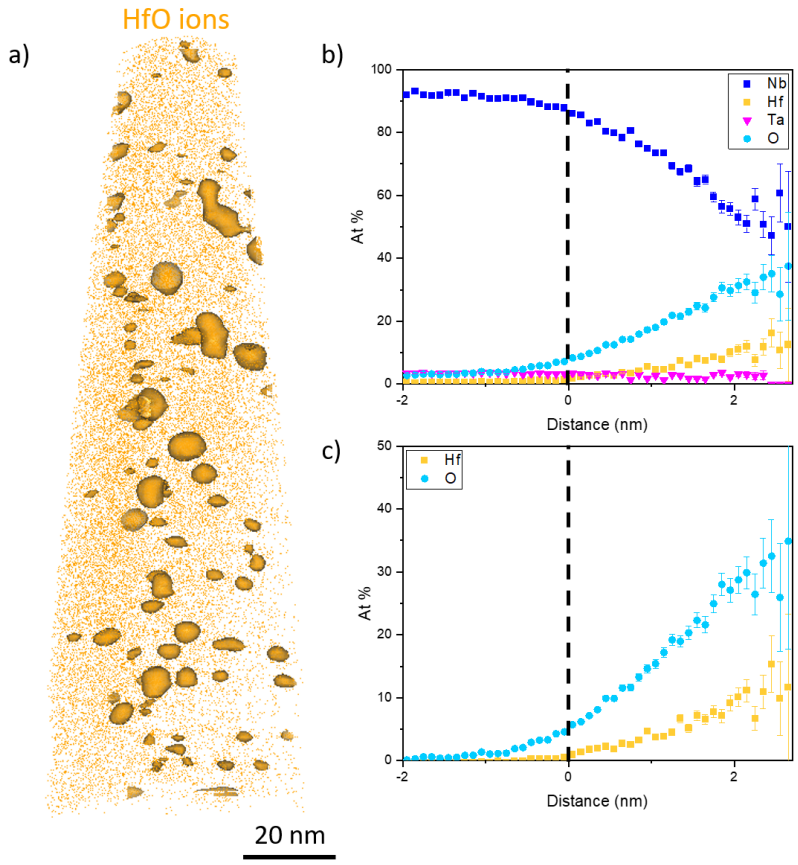


Figure 4.13: a) APT reconstruction of a reacted Nb alloy tip showing HfO ions and a 3 ionic% HfO isosurface to define the clusters b) A proxigram averaging over 88 clusters which shows decomposed Nb, Ta, Hf and O species with the interface defined at 0 and the clusters to the right of the interface c) Proxigram of decomposed Hf and O across the same 88 clusters with the background matrix removed, this is defined as concentration of each species at a distance of -2 nm.

change in any other species so it is difficult to define whether this is indeed a grain boundary. The large variation in number of HfO_2 clusters across the reconstructions sampled shows that the local amount of oxygen varies substantially, producing an inhomogeneous distribution of HfO_2 clusters cross the reacted Nb alloy. No clusters were present in the alloy pre-heat treatment, therefore the heat treatment encourages the formation of HfO_2 clusters in the Nb alloy, perhaps located at original grain boundaries. Evidence of HfO_2 in the reacted Nb alloy shows that precipitation of HfO_2 may occur in the precursor Nb alloy prior to the reaction with Sn and prior to A15 phase formation.

Reacted Nb-4Ta-1Hf alloy	N_D ($\times 10^{23}$ m^{-3})	Diameter (nm)
HfO_2 clusters	1.66 $\pm$ 1.98	1.65 $\pm$ 0.06

Table 4.5: N_D and diameter of the HfO_2 clusters in the reacted Nb-4Ta-1Hf alloy

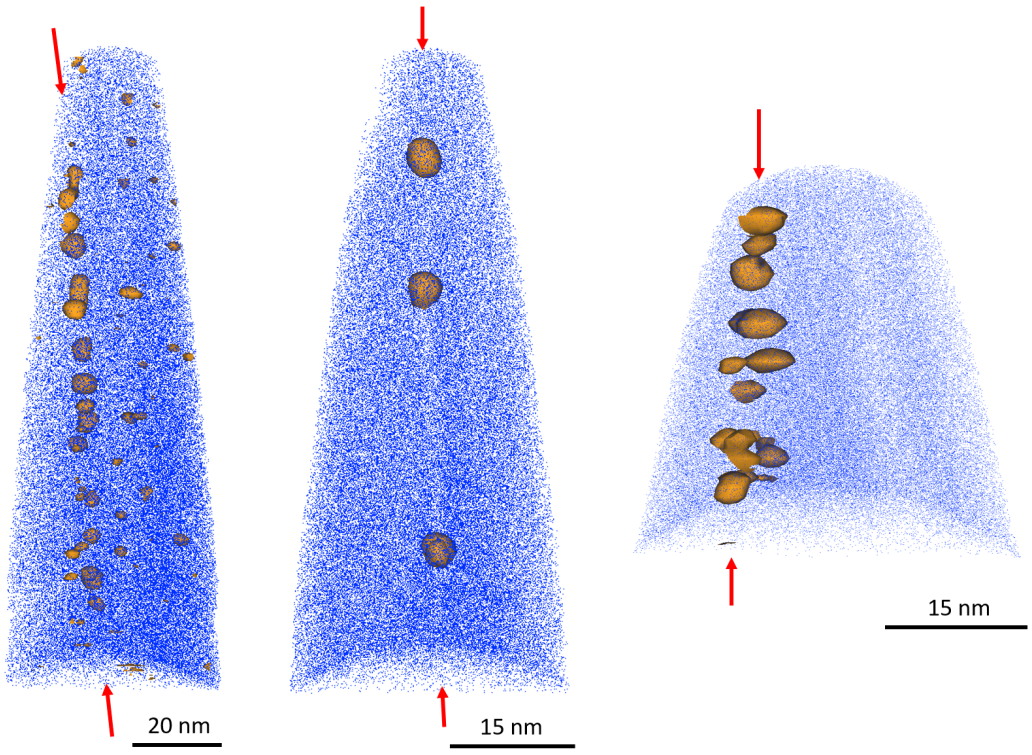


Figure 4.14: APT reconstructions of 3 tips from the reacted Nb-4Ta-1Hf alloy showing HfO isosurfaces of 4 ionic% in orange and Nb atoms in blue. The red arrows show planes where the distribution of HfO clusters appear to be concentrated, these are not associated with crystallographic poles.

4.3 APT analysis methods for the Nb_3Sn Layer

4.3.1 Identifying the Nb_3Sn

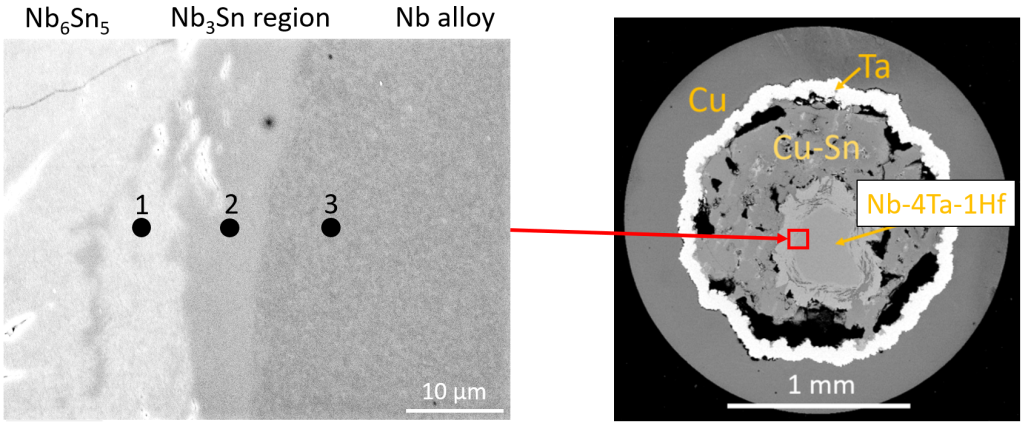


Figure 4.15: BSD image with EDX spots taken at the central Nb alloy and the two regions of contrast nearest to the central Nb alloy. Region 2 is the Nb_3Sn region of interest at a layer thickness 5 - 10 μm. A BSD image of the cross section of wire, from Figure 4.8, shows that the Nb_3Sn region is a very small, non-homogeneous ring around the central Nb alloy.

The BSD image of the reacted RIT wire, Figure 4.8, showed a layer several microns thick of Nb-Sn phases in the final RIT microstructure. As discussed in section 1.2.1 multiple binary phases of Nb and Sn exist: $NbSn_2$, Nb_6Sn_5 and Nb_3Sn. Previous work by Balachandran *et al* [64] had shown evidence of residual Nb_6Sn_5 in this sample, therefore care was taken in identifying the Nb_3Sn region. To confirm where the Nb_3Sn phase was situated, EDX spot measurements were taken at the edge of the custom Nb alloy, Figure 4.15. Nb_3Sn forms last out of the Nb/Sn phases, therefore it would be expected that the phase closest to the Nb alloy would be Nb_3Sn. Spot 1 gave a Nb:Sn ratio of 1.2, spot 2 gave a ratio of 2.5 and spot 3 only produced signal for Nb, Ta and Hf, clearly indicating the custom Nb alloy. The ratio of 1.2 for spot 1, suggested the presence of Nb_6Sn_5, whereas the ratio of 2.5, although slightly low for Nb_3Sn, suggested the presence of the Nb_3Sn layer. The estimated width of the Nb_3Sn layer is approximately 5 - 10 μm, therefore a standard FIB lift-out procedure to prepare the sample for APT analysis could be followed as detailed in section 2.2.4. Care was taken to select lift-outs of

Nb_3Sn from the widest sections of the Nb_3Sn layer to minimise the chance of selecting Nb_6Sn_5. However, due the inhomogeneity of the sample and the inability to see the phases beneath the surface some Nb_6Sn_5 was sampled, as detailed in section 4.9. During the FIB procedure, lower currents were required for the preparation of the RIT doped Nb_3Sn layer, which milled faster than the RRP® samples, further details can be found in section 2.2.4.

4.3.2 Atom Probe Tomography Experimental Parameters

Due to the inhomogeneous microstructure and the potential presence of nano-oxides or other impurities in the reacted RIT wire, the sample was more brittle than previous RRP® wires tested. Initially, APT parameters identical to the Ti doped RRP® samples were selected, however, this caused successive tip fractures, ending the experiment before useful information could be retrieved. To minimise the amount of fractures a higher base temperature of 60 K was chosen and an increased laser energy of 80 pJ, which meant that each tip started emitting at a lower voltage and therefore a lower field. A higher laser energy can produce increased surface migration and larger peak tails in the m/q spectrum [160]. The issues which arose with the Nb_3Sn layer in the Nb-4Ta-1Hf are discussed in section 2.5.

4.3.3 Ranging the Mass-to-charge-state Spectra

The m/q spectrum produced for the RIT is more complex than that generated for the RRP® wires. There are impurity peaks present in the Nb_3Sn spectrum which are likely due to the starting materials: the custom Nb alloy and Cu-Sn mixture produced in the Maglab facility. The common impurity peaks associated with Nb are NbC^{2+}, NbN^{2+} and NbO^{2+}, as seen in Figure 4.16, and there is also a small NbO^{+} peak at 108 Da. APT reconstructions with these ions were isolated to check the distribution of NbC and NbN ions within the tips, with distributions presented in Figure 4.17. To further investigate a region high in NbN and NbC ions a 1D concentration profile was taken through one of these regions, Figure 4.18. The 1D profile, Figure 4.18, shows the relative change in concentration of each species, where the interface at 6 nm is defined at 0 at% for each species. There is a clear increase in O, C, N

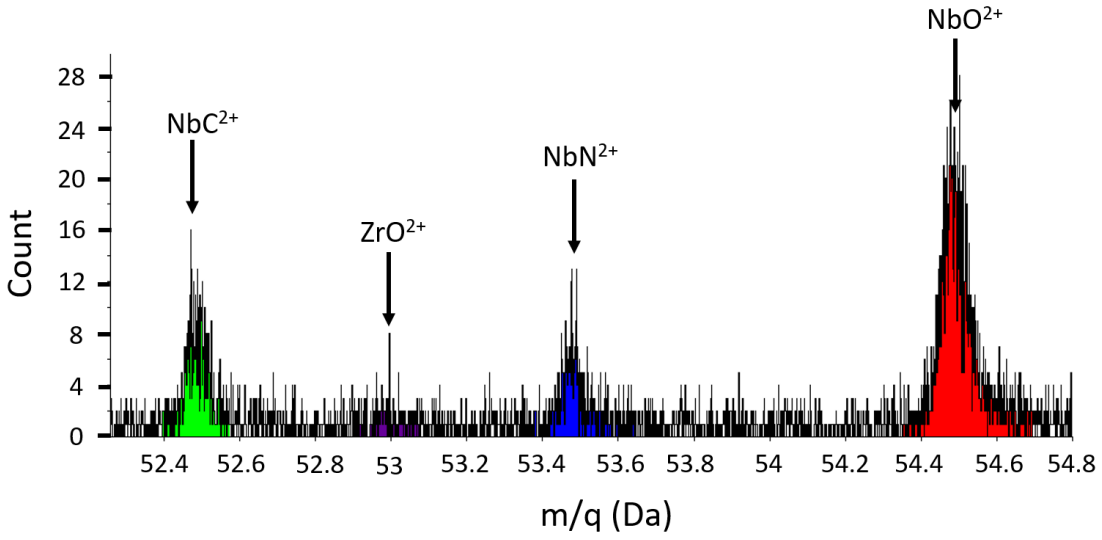


Figure 4.16: Close-up of part of the m/q spectrum for the Nb_3Sn region showing NbC^{2+}, NbN^{2+} and NbO^{2+} peaks. In between the peaks there is also a small ZrO^{2+} peak

and Hf, however the Hf and O increase is likely due to a HfO_2 nanoparticle present which is associated with the region - especially as the ratio of Hf to O is approximately 1:2. The Nb rich particles are therefore likely formed of Nb, C and N, and the potential effect of these particles on the superconducting properties is discussed in section 4.7.

As can be seen in Figure 4.16, there is also the presence of some Zr and ZrO ion peaks present within the Nb_3Sn spectrum, which were also seen in the original Nb-4Ta-1Hf alloy. The largest Zr^{2+} peak at 45 Da is often visible, with a peak height of only 8 counts in the sample used for Nb peaks m/q spectra, Figure 4.16. Zr is also used to produce nano-oxides to enhance the point pinning in Nb_3Sn [65], therefore care was required to determine whether the residual Zr was indeed helping to form ZrO_2 precipitates. However, both the Zr and ZrO ion distributions were homogeneous in the reconstructions and therefore considered as background counts. Further impurity peaks are Co^{2+} and Fe^{2+} peaks, as shown in Figure 4.19, which were not seen in the as-received or reacted Nb alloy. The correlation of each impurity species throughout the reconstruction was checked to make sure there was no association with features e.g. clusters. No segregation of ions associated to these peaks was observed, therefore these peaks were dismissed as non-influential trace impurity peaks.

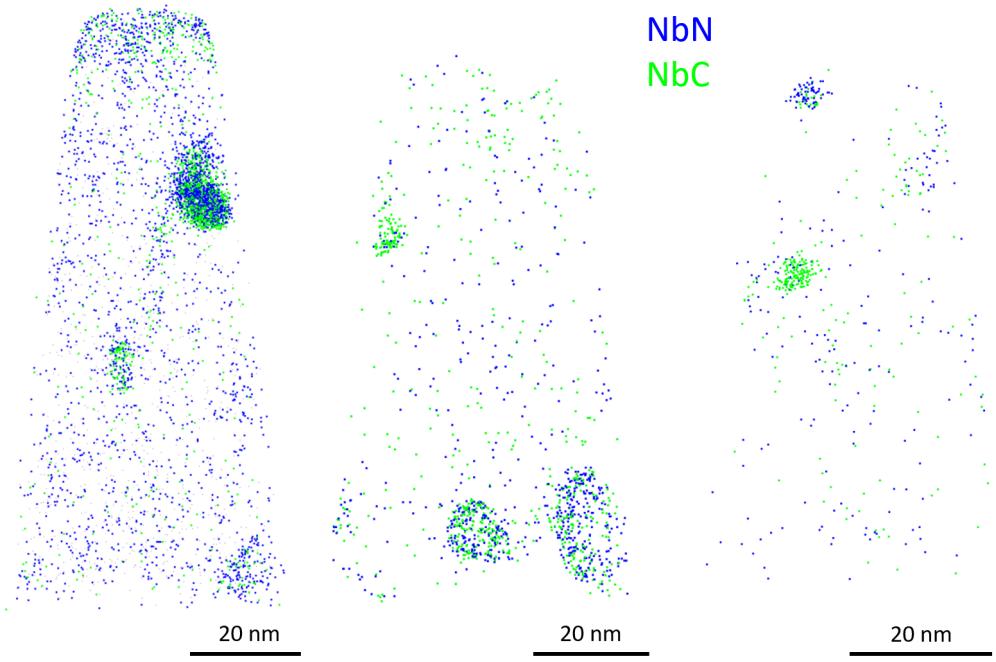


Figure 4.17: Three APT reconstructions showing the NbN and NbC ions in the RIT sample. Clusters of NbC and NbN ions are visually apparent in all three tips.

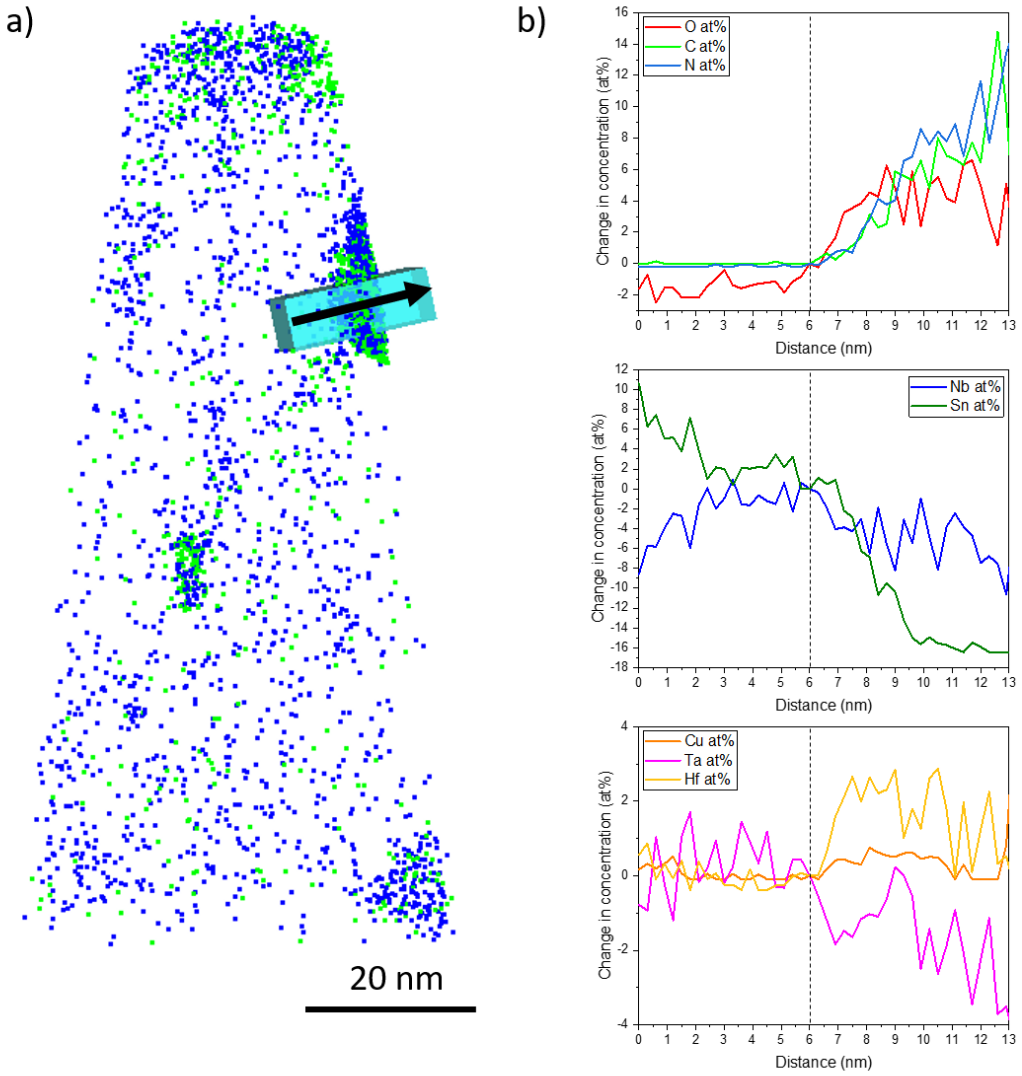


Figure 4.18: a) APT reconstruction of a Nb_3Sn tip from the RIT sample showing NbN and NbC ions and 1D concentration profile drawn through a dense NbN, NbC region b) 1D profiles showing the change in at% of each species in relation to an 'interface' defined as zero at a distance of 6 nm.

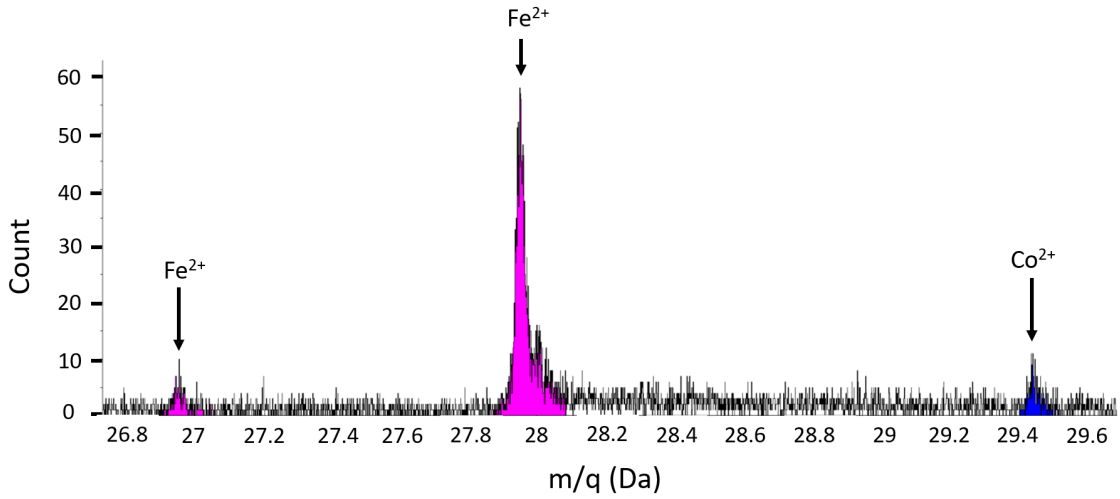


Figure 4.19: Close-up part of m/q spectrum for the Nb_3Sn region showing potential Fe^{2+} and Co^{2+} peaks. The isotopes of Fe 54 and Fe 56 are both visible above the background.

4.3.4 Peak Overlaps in the Mass-to-charge-state Spectra

The increased laser energy, and therefore reduced field, on the RIT samples compared to the RRP® wires has changed the relative ratios and charge-state peaks of Nb. As discussed for the as-received and reacted Nb alloy, there is a Nb_2^{3+} peak at 61.9 Da, which is not a problem in the Nb alloy m/q spectrum but does produce an overlap when Sn is also considered. Figure 4.20, shows the Sn^{2+} peak and Nb_2^{3+} overlap which, if ranged as Sn, produces an artificially low Nb:Sn ratio. For overall compositional measurements peak decomposition of the Nb_2^{3+}/Sn^{2+} overlap was solved through AtomProbeLab using the maximum likelihood method [210], however, the overlap does not affect the cluster analysis as both Nb and Sn ions are removed.

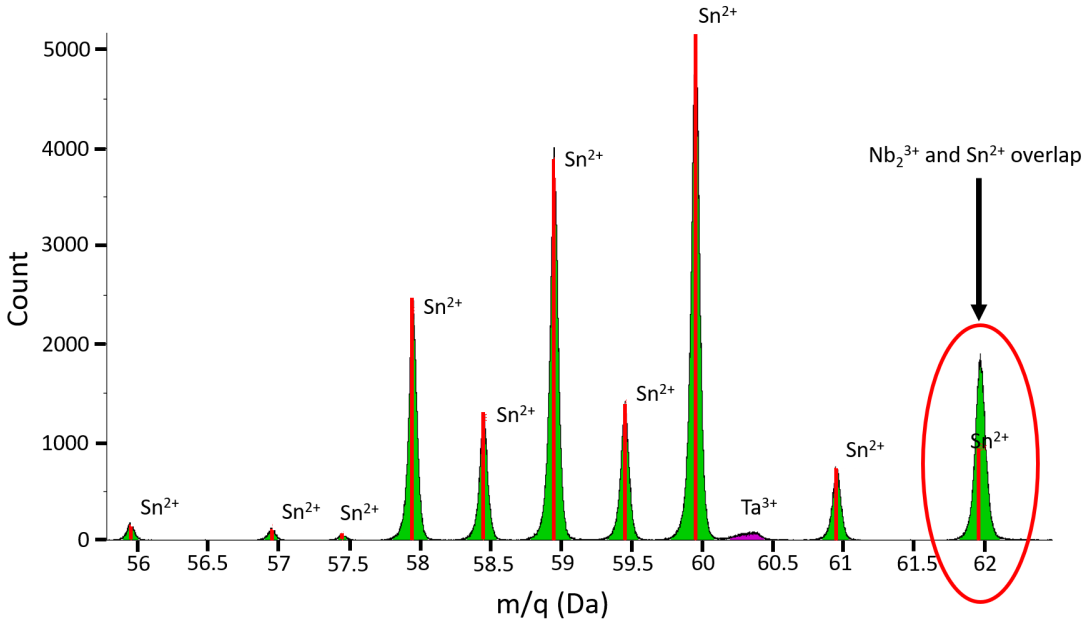


Figure 4.20: A section of the Nb_3Sn m/q spectrum from the RIT sample which shows the Sn^{2+} isotope peaks and Nb_2^{3+} peak overlap. The Nb_2^{3+} overlap occurs with 124 Sn^{2+}.

As discussed for the as-received Nb-4Ta-1Hf alloy in section 4.1.2, there are Hf^{3+} ions present in the Nb-4Ta-1Hf m/q spectrum, which under the same APT conditions would be expected to be present in the Nb_3Sn region, however these peaks are indistinguishable due to their overlap with the much larger Sn^{2+} peaks. One tip was analysed on the LEAP XR which has a longer flight path therefore improved mass resolution, this tip showed clear evidence of hidden Hf^{3+} peaks, Figure 4.21. Based on the ratio of Hf^{3+}:Hf^{2+} counts from the pre-heat treatment alloy, in section 4.1.2 the ratio of Hf^{3+} counts to Hf^{2+} counts ranged from 0.3 to 1.1, with the largest increase changing the Hf at% (not including HfO counts) from 0.21 at% to 0.45 at%, therefore it is reasonable to assume that the measured Hf count may indeed be up to double what is calculated from just the Hf^{2+} ions. The unoxidised Hf count probably does not play a major role in determining superconducting properties at so low a concentration, as it is not correlated with clustering and does not largely affect the Nb:Sn ratio, Hf^{3+} counts will not be estimated in Nb_3Sn samples as there is no accurate way of resolving the Hf^{3+} peaks from the Sn^{2+} peaks in the Nb_3Sn datasets.

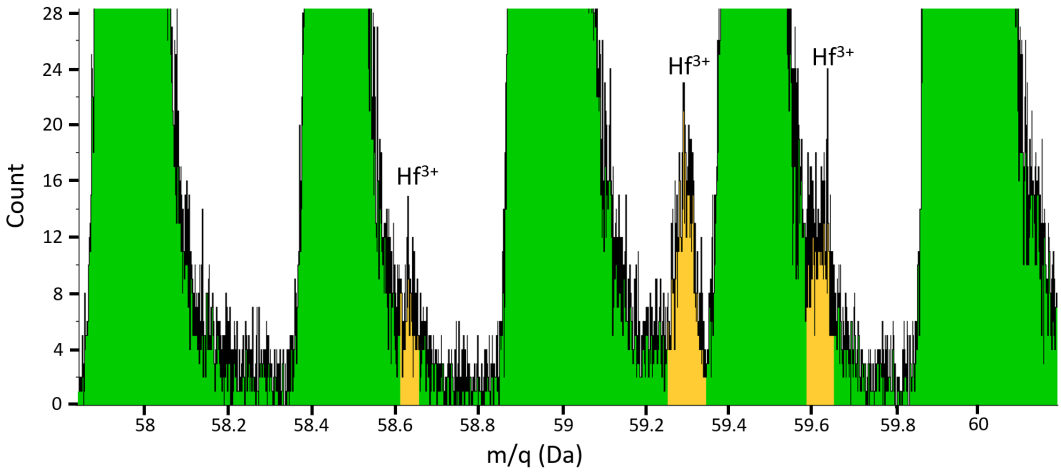


Figure 4.21: A section of the Nb_3Sn m/q spectrum from the RIT sample which shows the Sn^{2+} and Hf^{3+} isotope overlaps.

4.3.5 Cluster Analysis Considerations

From the initial reconstruction of the Nb_3Sn tips, it was clear that HfO ions were producing clusters within the Nb_3Sn regions. Examples of just the HfO ion clusters can be seen in Figure 4.22. To check whether the ions Hf or O had any association with the HfO ions, independent reconstructions were made of only the Hf and O ions, respectively, an example can be seen in Figure 4.23. The Hf (detected as single ions) is in solid solution in the Nb_3Sn with segregation behaviour determined by low and high Nb regions, as discussed in section 4.4.1, and O is randomly distributed within the APT reconstructions. In Figure 4.23, TaO and NbO ions are also plotted as there is some association of NbO and TaO ions with the HfO clusters. However, at the top of the reconstruction there are clearly some regions rich in NbO and TaO ions that do not correlate with the HfO clusters. There is no association between Hf and O detected as single ions, respectively, with HfO_2 clusters and unreliable NbO and TaO association with HfO_2 clusters, therefore only HfO ions will be used as solute ions in the cluster search.

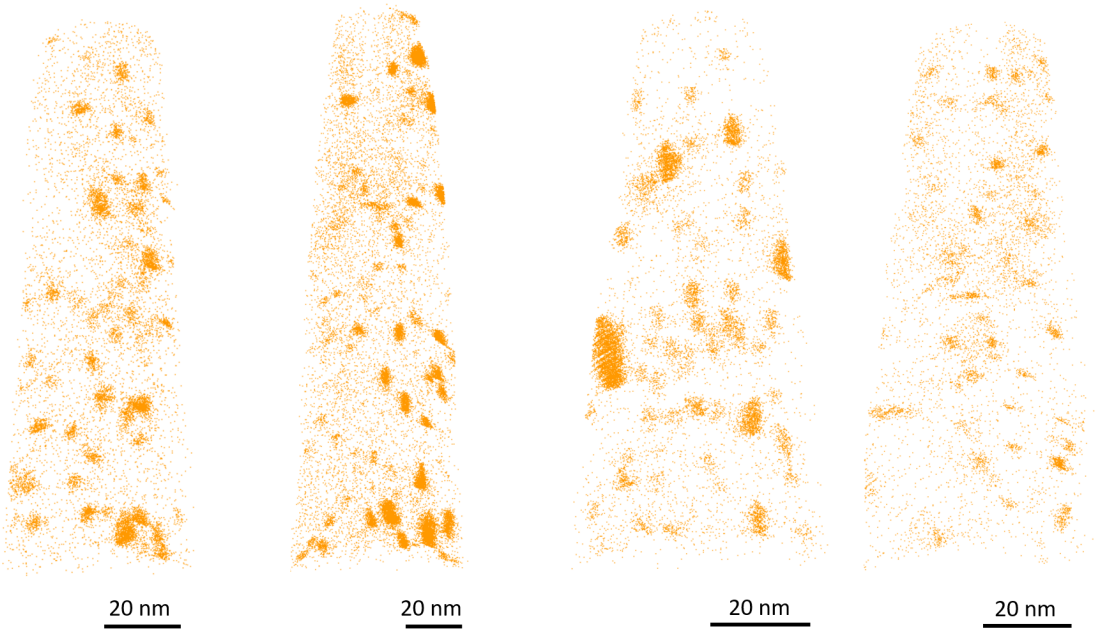


Figure 4.22: APT reconstructions of Nb_3Sn tips from the RIT sample showing only the HfO ions which are clearly forming clusters.

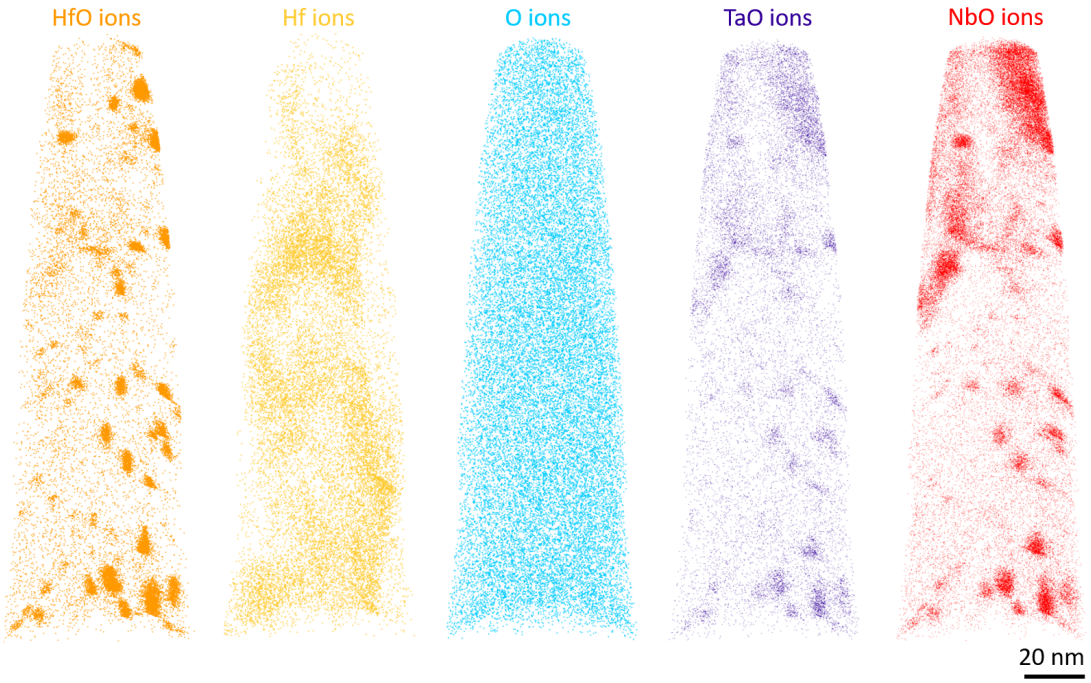


Figure 4.23: APT reconstructions of one Nb_3Sn tip from the RIT sample showing respective distributions of HfO, Hf, O, TaO, NbO ions. The top of the reconstruction has been removed to account for Ga damage or any oxide formation which was introduced during production of the tip.

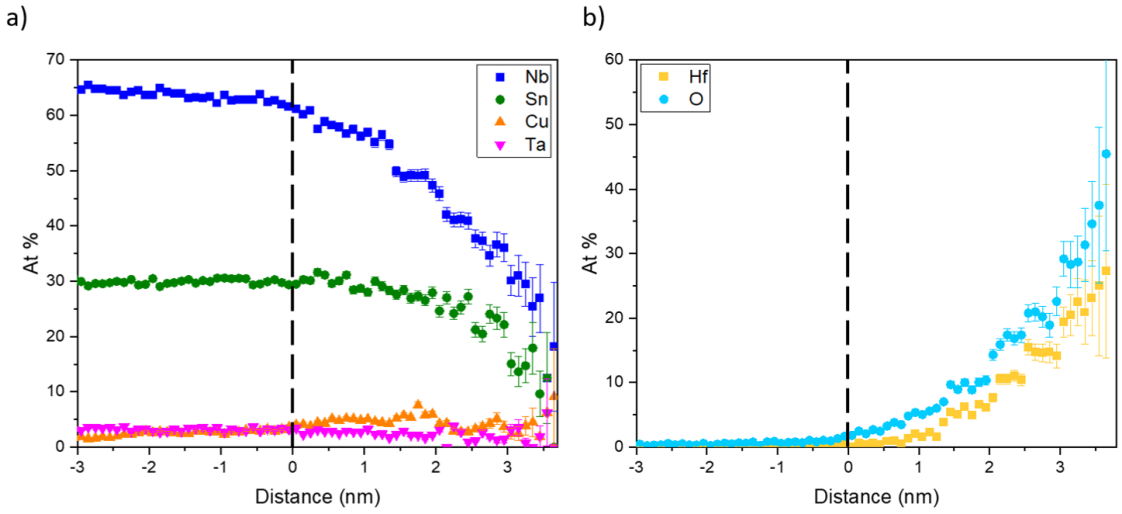


Figure 4.24: Proxigram analysis measured as an average over 7 clusters defined by a HfO 1 ionic% isosurface, with the interface defined at zero and the clusters on the right of the interface a) Decomposed Nb, Sn, Cu and Ta counts into the 7 clusters b) Decomposed Hf and O ions going into the clusters

Thermodynamically NbO and Ta_2O_5 have a highly negative free energy well below zero at 670°C [89], therefore both of these species are favourable under the conditions the wire was formed. However, HfO_2 has a lower standard free energy of formation [207], therefore if enough Hf is present in the sample it would be expected that HfO_2 forms as the most favourable oxide. There is residual Hf present in solution in the sample, as shown in Figure 4.23, therefore it is likely that the NbO and TaO ions present are actually Nb and Ta in the vicinity of the HfO_2 clusters reacting with the additional oxygen which has not evaporated as HfO ions. To confirm this, a HfO 1 ionic% isosurface was fitted to the clusters in Figure 4.23. Only the larger clusters which are near spherical and wholly within the reconstruction were selected to produce a proxigram. Figure 4.24 shows a proxigram from 7 defined clusters from the reconstruction in Figure 4.23. The matrix is defined to the left of the interface and the clusters are defined to the right of the interface, with each complex ion decomposed into its elemental counts. Figure 4.24 a) shows Nb and Sn concentration drops in the clusters, there is little change in the Ta count and there is a small increase in Cu closer to the edge of the clusters which is likely due to the proximity of a couple of the clusters to a Cu segregated boundary. Figure 4.24 b) shows a clear increase in Hf and O ion counts into the clusters, with a ratio of Hf:O which approaches 1:2. Based on the decomposed proxigram and thermodynamic predictions, only HfO ions will be used to conduct a cluster search and both Nb and Sn ions will be removed from the final cluster composition under the assumption that these are matrix counts.

4.4 Analysis from the Nb_3Sn Layer

In total 8 successful experiments were conducted from the Nb_3Sn layer, and 3 more experiments contained a combination of Nb_3Sn and Nb_6Sn_5 and will be discussed in section 4.9. Results of the intra-grain composition, grain boundary segregation and overall composition of the RIT will discussed in the same format as for the RRP® samples. In addition, analysis on the size and number density of clusters of HfO_2 will be discussed, and finally unexpected results such as residual Nb_6Sn_5 and Nb-C-N particles.

4.4.1 Intra-grain Compositional Analysis

The location of doped Ta and Hf within the Nb_3Sn structure is poorly understood in the literature. Ta is commonly added to wires to increase the upper critical field [45], whereas as Hf is usually added to wires with an oxygen source to form HfO_2 nanoparticles [64, 208]. Previously, work on Ta doped RRP® with 4 at% Ta used EXAFS to determine the site occupancy of the Ta on the Nb_3Sn lattice [120]. It was shown that Ta occupies both Nb and Sn sites, with between 21% to 32% of the Sn sites occupied. However, little is known about where any Hf not incorporated in HfO_2 clusters, may lie within the Nb_3Sn structure.

Upon initial investigation into the intra-grain composition of the Ta-Hf doped RIT sample, it can be seen that there are regions of high and low Nb Nb_3Sn, as shown in Figure 4.25, similar to that seen in the RRP® samples in chapter 3. Using a 1D concentration profile there is an indication that Cu and Hf may have a preference for the high Nb Nb_3Sn region, whereas Ta appears to vary more over the grain boundary than in the regions of low and high Nb.

To further investigate the intra-grain composition, measurements within discrete ROIs were taken within the grains in the 8 RIT tips analysed. The difference in selecting ROIs for the RIT sample compared to the RRP® samples was that the high and low Nb regions were far harder to clearly delineate with isosurfaces, and that the RIT tips had a larger volume of grain boundary due to the reduced grain size. Therefore, ROIs were selected which did not encounter any grain boundaries, however high and low Nb regions were not identified in precise volumes as they were difficult to define. In total 23 ROIs were extracted from the intra-grain

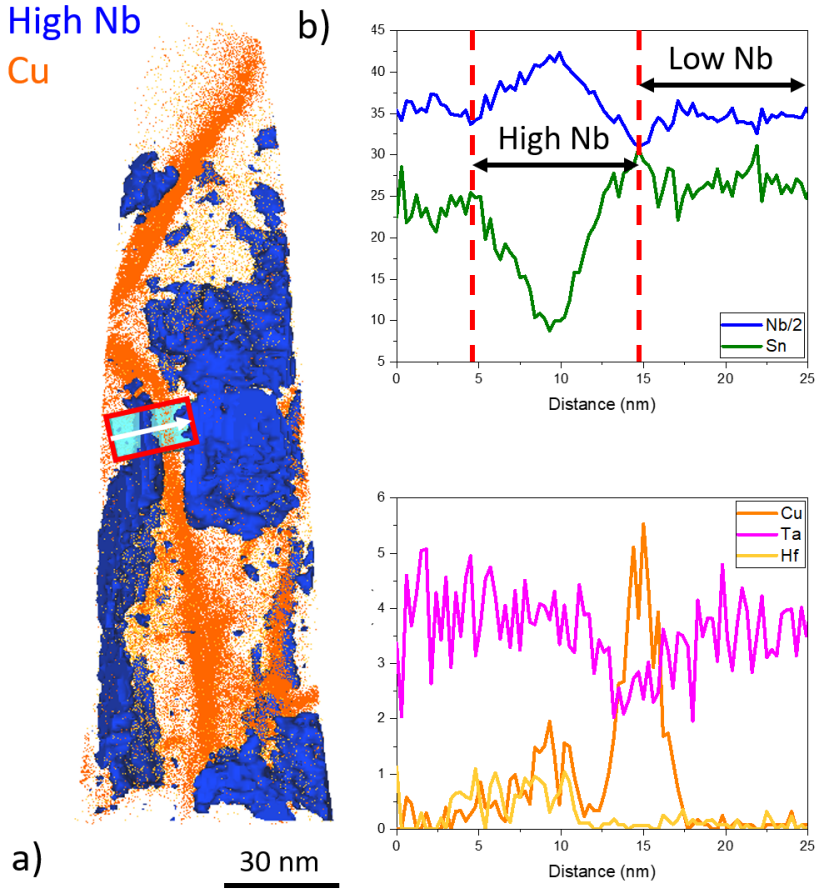


Figure 4.25: a) APT reconstruction of a Nb_3Sn tip from the RIT sample showing Cu atoms segregated to grain boundaries and high Nb regions with an isosurface of 75 at% Nb b) A 1D concentration profile through a high Nb Nb_3Sn region, through a grain boundary to a low Nb Nb_3Sn region

regions, with each m/q spectra individually ranged and the Nb_2^{3+}/Sn^{2+} peak decomposed using AtomProbeLab to produce a more accurate Nb:Sn composition. In most cases there was a small peak at 92.9 Da which has been consistently labelled as Nb^+, which could contain some some Nb_2^{2+} counts which are impossible to separate, as discussed in section 4.3.3. The peak at 92.9 Da is very small or non-existent in each of the ROIs, therefore the error in the relative composition of Nb is considered insignificant.

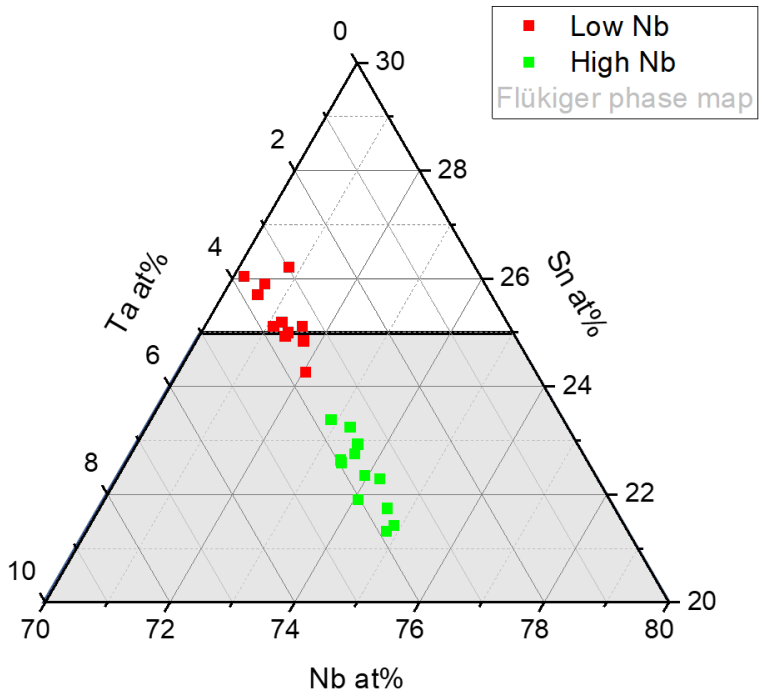


Figure 4.26: A ternary composition map showing the composition of high and low Nb Nb_3Sn regions in the RIT sample and a superimposed ternary composition map from Flükiger *et al* of the expected A15 composition when Nb_3Sn is doped with Ta [45]

To display the measured compositions of the intra-grain regions a ternary composition map of the high and low Nb regions has been placed on top of the Ta doped Nb_3Sn phase map from Flükiger *et al* [45], Figure 4.26. Only a section of compositions between 70 - 80 at% Nb is shown on the composition map as there is less variation in composition than that seen in the RRP® samples. To produce the ternary map of high and low Nb regions, the compositions of Cu, Hf and O (which are all below 0.5 at%) have been set to zero. From the ternary diagram it is clear that although the composition of Nb and Sn can vary in the A15 phase, the composition of Ta appears nearly constant throughout the high and low Nb regions. To display the variation of Ta, Hf and Cu with the amount of Nb, each species has been plotted against the concentration of Nb, Figure 4.27. The Ta concentration appears to be very slightly higher in the high Nb region compared to the low Nb region, however there is significant scatter associated and an anomalously low value of Ta for one specific region. In general for Hf there is

a trend of increasing Hf as the amount of Nb increases, but, the concentration of Hf measured is very small ($\leq$ 0.22 %), with some ROIs showing no Hf counts, therefore from Figure 4.27 the relationship between Nb and Hf is uncertain. The amount of Cu, although small, does seem to vary between low and high Nb regions, with high Nb regions seemingly containing up to 0.2 at% Cu.

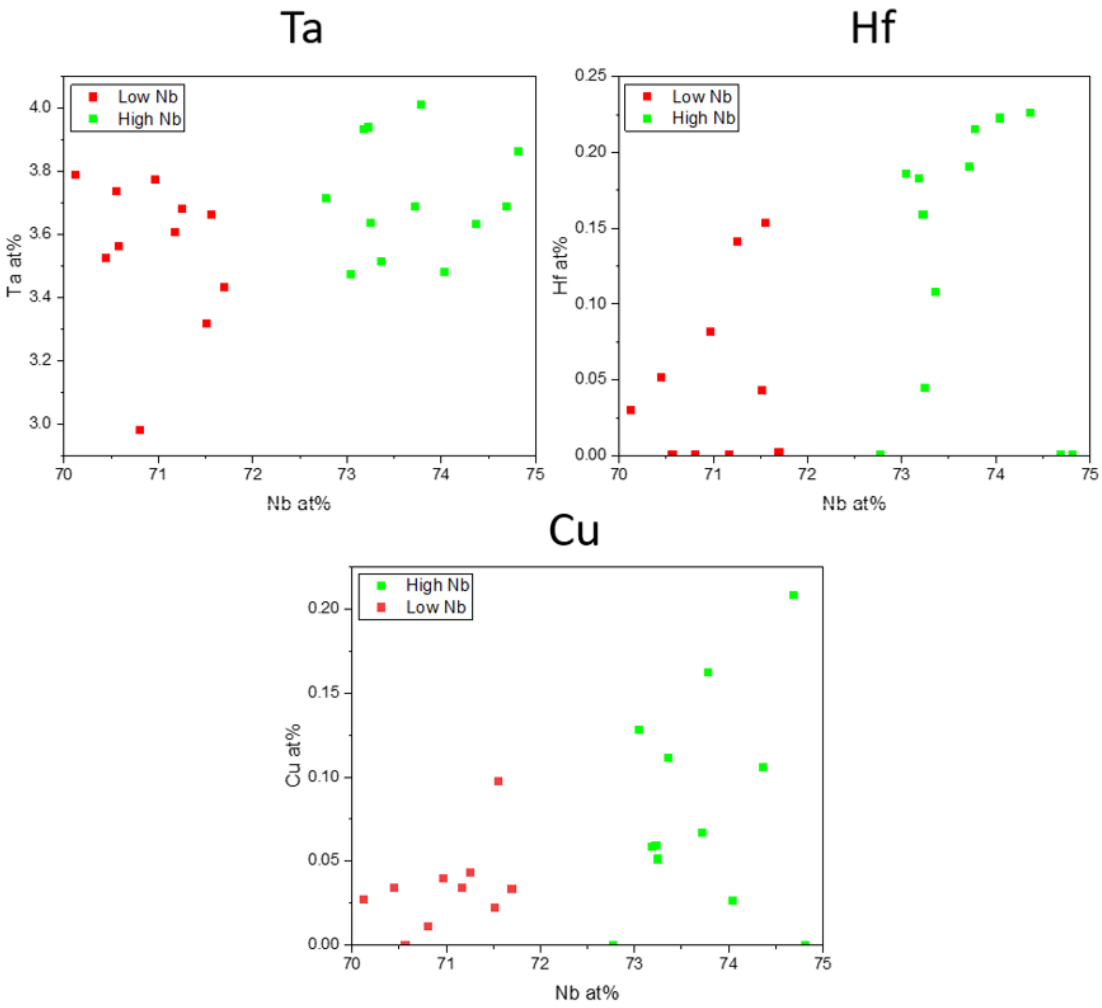


Figure 4.27: The variation of Ta, Hf and Cu, respectively, as a function of Nb in the intra-grain regions of the Nb_3Sn from the RIT sample.

Based on the ternary diagram, any ROI with a Nb concentration of $\geq$ 72.5 at% Nb was defined as high Nb and any ROI with $\leq$ 72.5 at% was defined as low Nb_3Sn regions. An average composition of these regions and their associated standard deviations is given in table 4.6. There is slightly more oxygen present within the low Nb regions than the high Nb regions, but these are not stark differences in composition compared to those found in the Ti doped RRP® samples.

Nb_3Sn regions	Nb at%	Sn at%	Ta at%	Cu at%	Hf at%	O at%
Low Nb	70.97 $\pm$ 0.51	25.24 $\pm$ 0.64	3.55 $\pm$ 0.24	0.03 $\pm$ 0.03	0.05 $\pm$ 0.06	0.16 $\pm$ 0.36
High Nb	73.69 $\pm$ 0.67	22.31 $\pm$ 0.67	3.71 $\pm$ 0.18	0.08 $\pm$ 0.06	0.14 $\pm$ 0.09	0.07 $\pm$ 0.11

Table 4.6: Average composition of the high and low Nb regions in the Nb_3Sn layer of the RIT sample.

4.4.2 Grain Boundary Concentration Profiles

Despite substantial evidence of Ti segregating to grain boundaries in Ti doped Nb_3Sn [154, 155] little is known about how Ta behaves at the grain boundaries in Nb_3Sn. In Figures 4.25 and 4.28 it is clear that Cu segregates strongly to the grain boundary, as expected in Nb_3Sn, and that the Ta concentration does not vary across the grain boundary. This solubility of Ta, both within the A15 phase and at the boundaries between grains, may be because Ta lies on both the Nb and the Sn sites [120]. There is also no obvious segregation of elemental Hf (not be mistaken for HfO_2) to grain boundaries, with Figure 4.29 showing how Hf is not evenly distributed through the Nb_3Sn grains, but that it does not have any preferential segregation to grain boundaries.

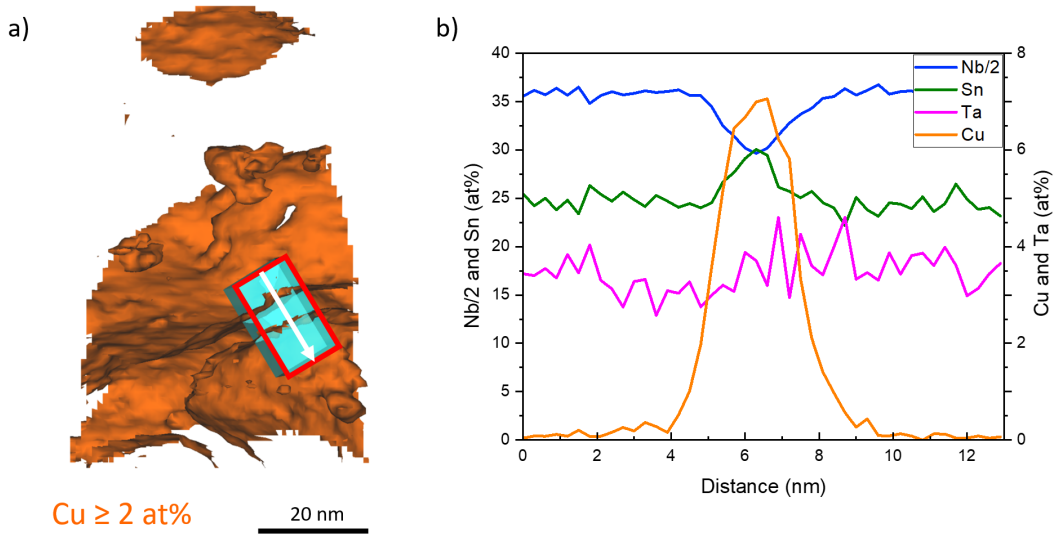


Figure 4.28: a) APT reconstruction of a Nb_3Sn tip from the RIT sample, showing only a 2 at% Cu isosurface and an ROI across a grain boundary b) A 1D concentration profile showing Nb/2, Sn, Ta and Cu in at%

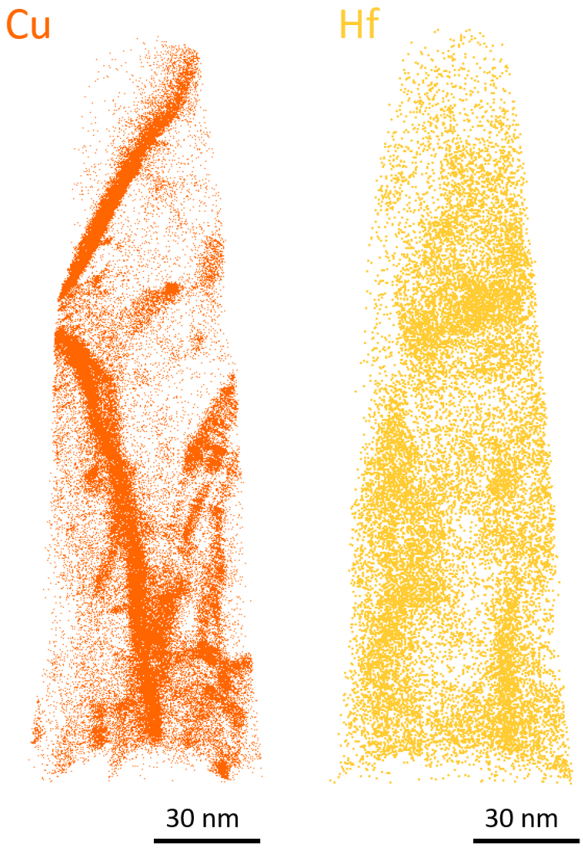


Figure 4.29: APT reconstruction of a Nb_3Sn tip from the RIT sample showing only Cu and Hf ions. The HfO ion distribution has no correlation with the Hf ion distribution.

4.4.3 Gibbsian Interfacial Excess

Across the 8 tips, 16 grain boundaries were extracted and Γ_i calculations conducted in accordance with methodology in section 2.6.4. The Γ_{Cu} was measured across each grain boundary and due to the increased laser energy used, the predominant Cu peaks were the Cu^+ peaks. Figure 4.30, shows that there is no overlap between the tail of the Nb^{2+} peaks and the Cu^{2+} peaks. The overlap between Sn^{2+} and the Nb^{3+} peak was present in each m/q spectrum and this was decomposed in accordance with methodology in section 4.3.4.

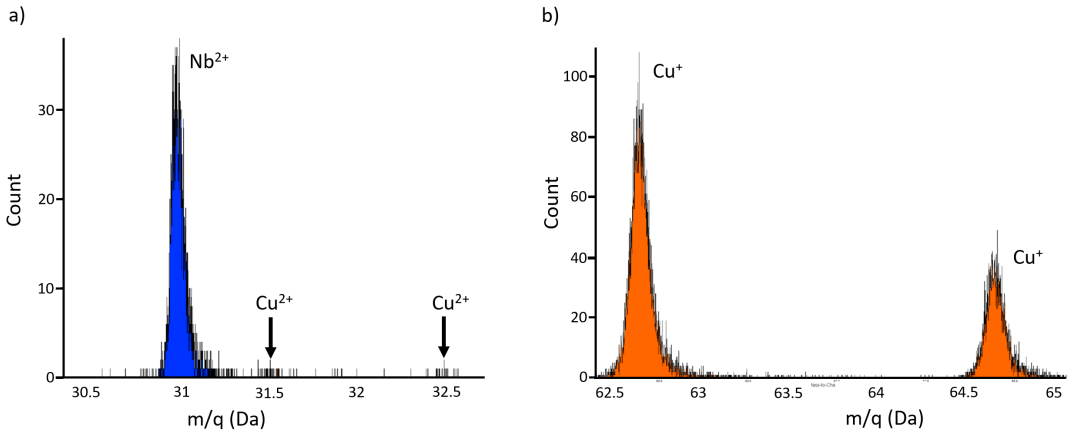


Figure 4.30: a) Section of m/q spectrum from a grain boundary in Nb_3Sn from the RIT showing the Nb^{2+} and Cu^{2+} peaks b) Section of the same m/q spectrum showing Cu^+ peaks

To check whether boundaries such as high Nb, mixed and equilibrium boundaries, defined in section 3.4.2, were present in this sample, the Sn content of Grain A and Grain B either side of the boundary were plotted against each other, as shown in Figure 4.31. Each boundary has been categorised by the interface Cu at% value, as the solubility for Cu in Nb_3Sn has been shown to be near zero in chapter 3, and unlike the RRP® samples there is no obvious presence of high Nb, equilibrium and mixed boundaries to the extent seen previously. Figure 4.32 shows Γ_{Cu} values for the Nb_3Sn grain boundaries in the RIT sample, with a larger spread in values than for the RRP® samples, with two boundaries which have Γ_{Cu} values of 164.9 $\pm$ 0.3 atoms/nm^2 and 90.3 $\pm$ 0.4 atoms/nm^2 respectively. These are far beyond what would be expected for a segregation process. If the assumption is made that that the grain boundaries are made up

of multiple layers of the densest packed planes of Nb_3Sn, which are (001), then each plane contains 10.7 atoms/nm^2. It is unphysical for a grain boundary to have 9 - 15 monolayers of segregated material, therefore further investigation into the nature of these grain boundaries was required.

To determine the nature of the two boundaries, the original 1D concentration profiles generated to produce the Γ_{Cu} measurements are plotted in Figure 4.33. One of the boundaries reaches over 30 at% Cu and the other reaches over 45 % Cu, which suggests the presence of an intermetallic phase at the grain boundary which is rich in Cu. The Cu 20 at% isosurface in Figure 4.33 shows that many regions high in Cu are present within the reconstructions, often associated with grain boundaries. Further analysis on these two boundaries and possible Cu-Sn phases is conducted in section 4.6.

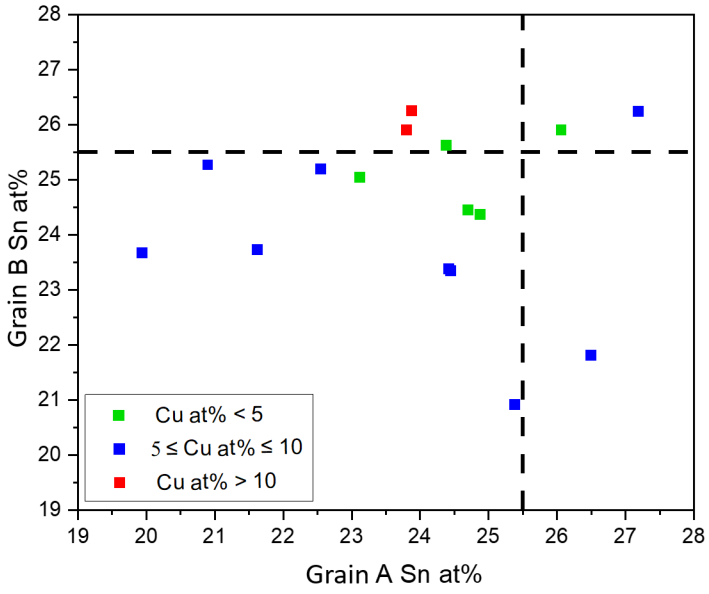


Figure 4.31: Sn content of Grain A and Grain B adjacent to the grain boundaries in Nb_3Sn from the RIT sample. Each value is categorised by colour depending on Cu at% associated with that boundary. The dashed lines below 25.5 at% Sn show the limits of the equilibrium Sn composition for the binary Nb_3Sn phase.

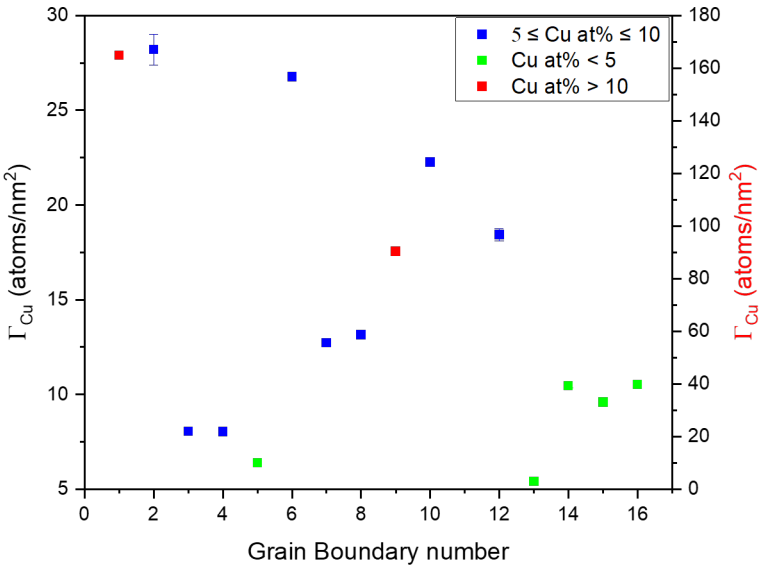


Figure 4.32: Γ_{Cu} values of grain boundaries in the Nb_3Sn region of the RIT sample, and their associated errors, most of which are contained within the data point symbol. The left y-axis is only for interface Cu at% $\leq$ 10 and the right y-axis is for interface Cu at% $>$ 10 with data points coloured in red.

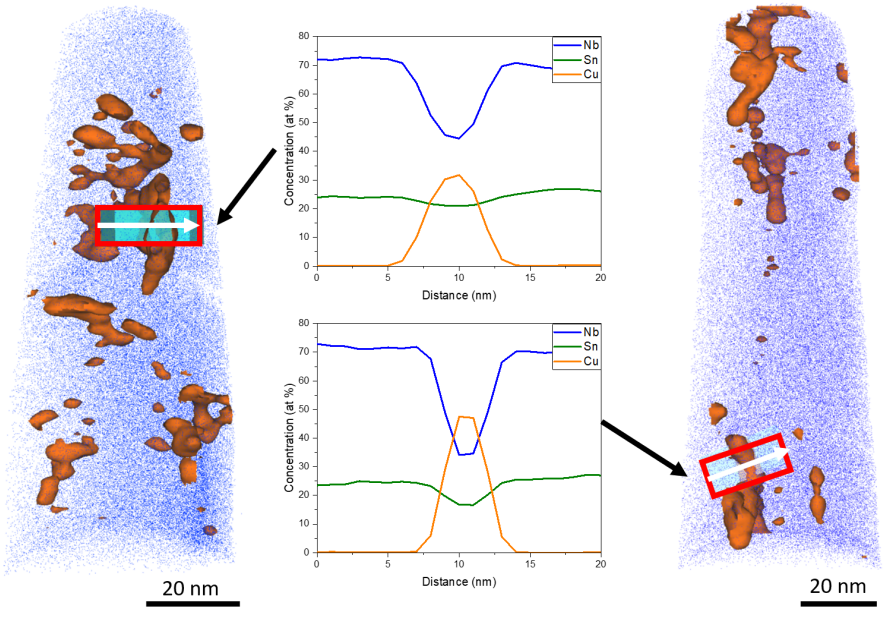


Figure 4.33: APT reconstructions of two Nb_3Sn tips from the RIT sample showing Nb atoms in blue, Cu 20 at% isosurface in orange and two 1D concentration profiles through the high Cu regions which produced the two highest measured Γ_{Cu} values.

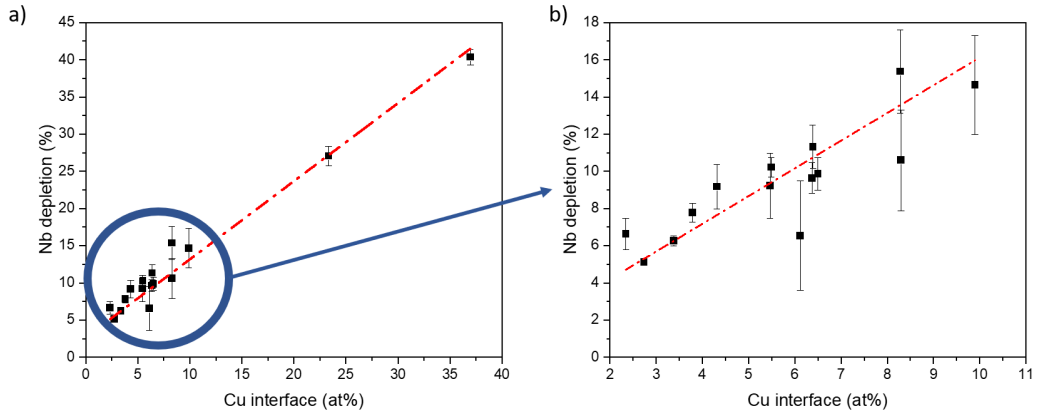


Figure 4.34: a) Nb depletion plotted against the interface Cu concentration at each boundary, with the error in each point taking into account the minimum and maximum Nb content on each side of the boundary. A linear fit to the data can be seen in red with an $R^2 = 0.97$ b) A close-up of Nb depletion against the interface Cu concentration at each boundary for Cu at% ≤ 10, with the error in each point taking into account the minimum and maximum Nb content on each side of the boundary. A linear fit to the data can be seen in red with an $R^2 = 0.90$.

To determine the relationship between the amount of Cu at the interface and the amount of Nb depletion at the interface, Nb depletion has been plotted against Cu interface concentration in Figure 4.34. A linear relationship shows that as the amount of Nb at the boundary decreases, the amount of Cu at the interface increases. As seen in Figure 4.30 there is no Nb^{2+}/Cu^{2+} overlap in the m/q spectrum for this sample, therefore the inverse relationship between Cu and Nb plotted in Figure 4.34 is not affected by this issue. The Ta depletion has been plotted against the Cu interface concentration in Figure 4.35 with a linear relationship showing that there is some correlation between the increase in Cu at the interface and a depletion in Ta, however this is a weaker correlation than that seen for Nb. One boundary shows an enrichment in Ta at the boundary but overall there is a mild depletion in Ta at the boundary which is weakly correlated with the amount of Cu at the interface.

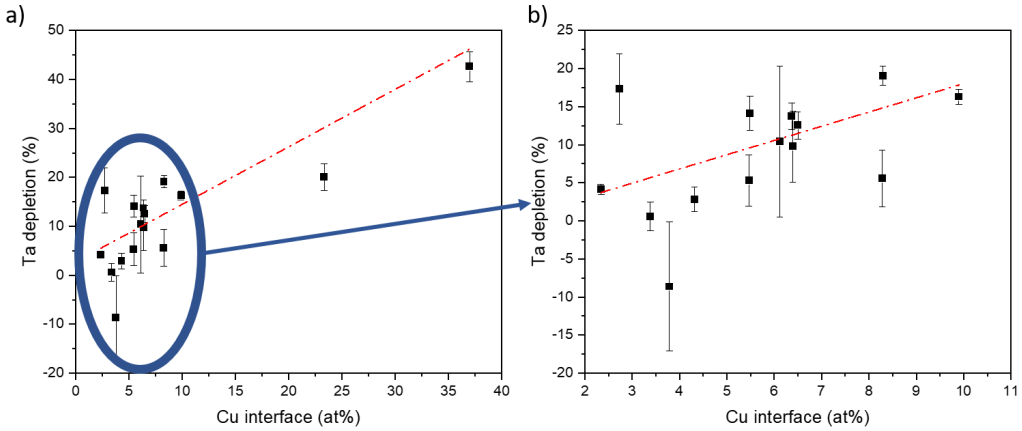


Figure 4.35: a) Ta depletion against the interface Cu concentration at each boundary, with the error in each point taking into account the minimum and maximum Nb content on each side of the boundary. A linear fit to the data can be seen in red with an $R^2 = 0.74$ b) Ta depletion against the interface Cu concentration at each boundary for Cu at% ≤ 10, with the error in each point taking into account the minimum and maximum Nb content on each side of the boundary. A linear fit to the data can be seen in red with an $R^2 = 0.77$.

Nb_3Sn regions	Nb at%	Sn at%	Ta at%	Cu at%	Hf at%	O at%
Cu at% < 5	66.34 $\pm$ 0.69	26.78 $\pm$ 0.78	3.50 $\pm$ 0.34	3.31 $\pm$ 0.79	0.01 $\pm$ 0.02	0.06 $\pm$ 0.05
$5 \leq$ Cu at% ≤ 10	64.55 $\pm$ 1.92	25.21 $\pm$ 1.79	2.98 $\pm$ 0.21	6.98 $\pm$ 1.51	0.08 $\pm$ 0.09	0.20 $\pm$ 0.26
Cu at% > 10	47.15 $\pm$ 6.76	20.10 $\pm$ 2.17	2.42 $\pm$ 0.51	30.16 $\pm$ 9.65	0.02 $\pm$ 0.03	0.15 $\pm$ 0.18

Table 4.7: Average composition of the grain boundaries in the Nb_3Sn region of the RIT sample

The composition of the grain boundaries can be found in table 4.7. There is clearly no obvious segregation of Hf or O to the grain boundaries, however the amount of Nb, Sn, Ta and Cu do vary between boundary types

4.5 Solute Cluster Analysis from the Nb_3Sn Layer

As discussed in section 2.6.6, selection of cluster parameters for the RIT sample followed the core-linkage method with only HfO ions selected as solute ions for the cluster search. To calculate a number density of clusters for each reconstruction, edge clusters were identified and excluded from the calculations as these could bias the estimation of size distribution.

4.5.1 Number Density and Size of HfO_2 Clusters

The N_D and diameter of HfO_2 clusters in the Nb_3Sn region can be found in table 4.8. For normal pinning sites to have the greatest effect on pinning, it is important that the size of such defects is on the scale of the coherence length ($\sim$ 3 - 4 nm in Nb_3Sn) and ideally the diameter of such defects should be double the coherence length, approximately 6 - 8 nm in Nb_3Sn. As described in section 2.6.6, the volume of each cluster is calculated, assuming each cluster is spherical, then a measurement of diameter is calculated from this volume. The average diameter for the HfO_2 clusters is found to be 1.9 $\pm$ 0.3 nm, table 4.8. Although the cluster size is smaller than predicted to provide maximum point pinning, the clusters also have the additional benefit of pinning grain boundaries (Zener pinning) during the A15 reaction to minimise the final A15 grain size.

Nb_3Sn	N_D ($\times 10^{23}$ m^{-3})	Diameter (nm)
HfO_2 clusters	1.93 $\pm$ 0.98	1.9 $\pm$ 0.3

Table 4.8: N_D and diameter of the HfO_2 clusters in Nb_3Sn

To further consider the size and shape of the clusters, the aspect ratio and oblateness have been considered. If we consider a cluster in 3D, there are three dimensions (L) in x, y and z. In this case the parameter L is defined by the radius of gyration. To define oblateness and aspect ratio these dimensions need to be ordered in terms of size, where $L_1 > L_2 > L_3$ and using equations 4.1 and 4.2.

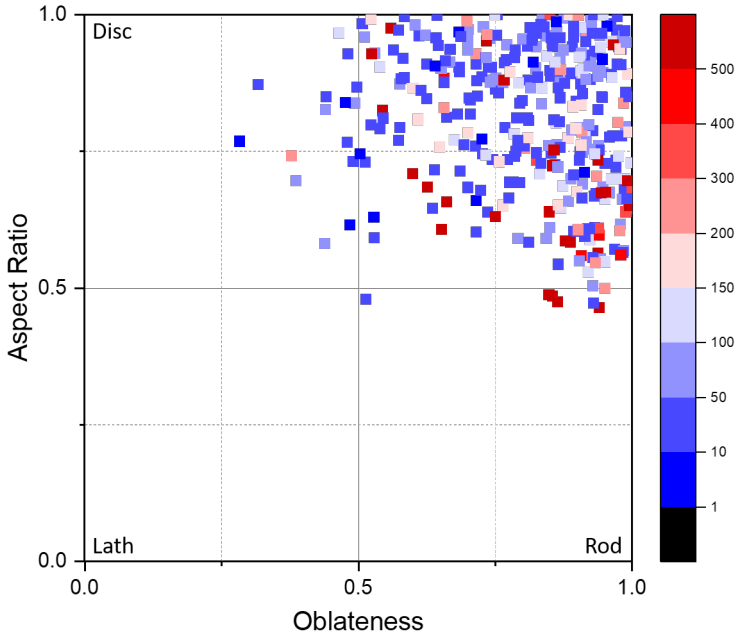


Figure 4.36: Aspect ratio against oblateness for the HfO_2 clusters distributed within the Nb_3Sn layer of the RIT sample. The intensity of each point corresponds to the number of HfO ions associated with each cluster. Correlation with the top right corner evidences the spherical nature of the clusters

$$Oblateness = \frac{L_3}{L_1} \tag{4.1}$$

$$AspectRatio = \frac{L_2}{L_1} \tag{4.2}$$

Once calculated for each cluster, the aspect ratio can be plotted against oblateness to determine the shape of the clusters in the samples, Figure 4.36. The clusters are tending towards an oblateness and aspect ratio of 1, this evidences the spherical nature of the majority of the clusters. Some of the larger clusters, with over 500 HfO ions associated, tend to have a lower aspect ratio, with four such clusters tending slightly towards a rod shape. Overall this shows that assuming spherical clusters to approximate the diameter, is a valid assumption for this system.

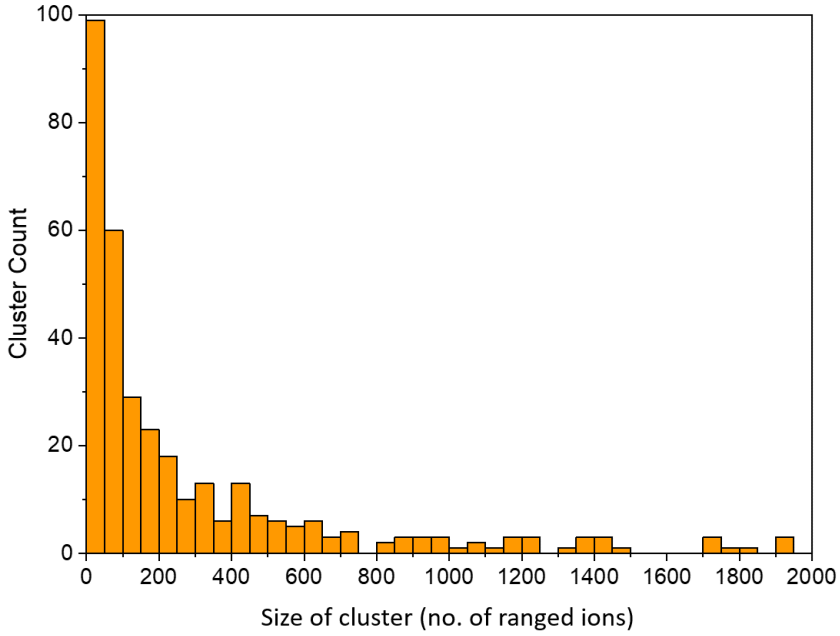


Figure 4.37: Cluster count against the no. of ranged ions within each cluster in Nb_3Sn

It should also be noted that, the exact size of the clusters may be distorted to some extent by the method of reconstruction of each tip or due to evaporation effects, as described in section 2.5. The HfO_2 clusters appear to have a slightly higher density of ions/nm^3 in the reconstruction than the surrounding matrix, this is likely due to the clusters evaporating at a lower field compared to the matrix, therefore a flattening on the surface occurs as the ions are evaporating producing an increase in the number of ions at the detector [160] producing LME as discussed in section 2.5.1. As these clusters are often less than 4 nm in diameter a density of the clusters has not been calculated and compared with HfO_2 density because defining the centre of the cluster for density calculations is challenging when clusters are so small. To remove the influence of shape, the number of ranged ions in each cluster has been plotted against the cluster count in Figure 4.37, to investigate the distribution of cluster sizes. From Figure 4.37, 27.3% of clusters have $\leq$ 50 ranged ions and 57.7% of all clusters have $\leq$ 200 ranged ions.

4.5.2 Location of HfO_2 Clusters

The location of HfO_2 clusters in the reacted Nb alloy, as shown in Figure 4.14, shows that the HfO_2 clusters are preferentially aligned along boundaries within the Nb alloy. To see whether the same pattern of behaviour is occurring for the Nb_3Sn layer, reconstructions of two atom probe tips showing HfO_2 clusters using a 2 at% HfO isosurface, and their association with any grain boundaries is shown in Figure 4.38. The HfO iosurface does not show all the clusters present but it visually shows the alignment of clusters present in the reconstructions. From the side view of the reconstructions there is some vertical association between HfO_2 clusters in both reconstructions, however this becomes more obvious when the top down view of the reconstruction is visualised. Reconstruction a) has HfO_2 clusters arranged vertically, just to the right of centre of the reconstruction whereas b) has HfO_2 clusters in a plane dominating the bottom right corner of the top down view. Although the correlation of HfO_2 clusters and specific planes, is potentially less obvious than in the case of the reacted Nb alloy, and more affected by Cu grain boundaries, there do appear to be planes of HfO_2 clusters which are not fully associated with grain boundaries in the Nb_3Sn. The planes of HfO_2 did not correlate with crystallographic poles, and are therefore not likely to be analysis artefacts.

As can be seen from Figure 4.38, some of the clusters are associated with features within the Nb_3Sn structure and others are not. To determine locations of HfO_2 clusters, Figure 4.39 shows one reconstruction with HfO_2 clusters, as 2 at% HfO ions in light blue and a 2 at% Cu isosurface which highlights grain boundaries, dislocations and any residual Cu. Grain boundaries are identified as the planar Cu segregated features and dislocations are defined as linear Cu segregated features, e.g. the linear Cu features on the left hand side of the reconstruction in Figure 4.39. To confirm that dislocations and a boundary are real in this tip, density slices from the same reconstruction are shown in Figure 4.40. Each density map looks at the total density of all ions detected and density is expected to be higher at boundaries and dislocations as these have a structure which is irregular compared to the matrix. The 2 at% HfO isosurface does not show all the clusters present, but it does make it possible to separate the association of HfO_2 and Cu into four different categories, these are: intra-grain HfO_2 particle with no Cu, intra-grain

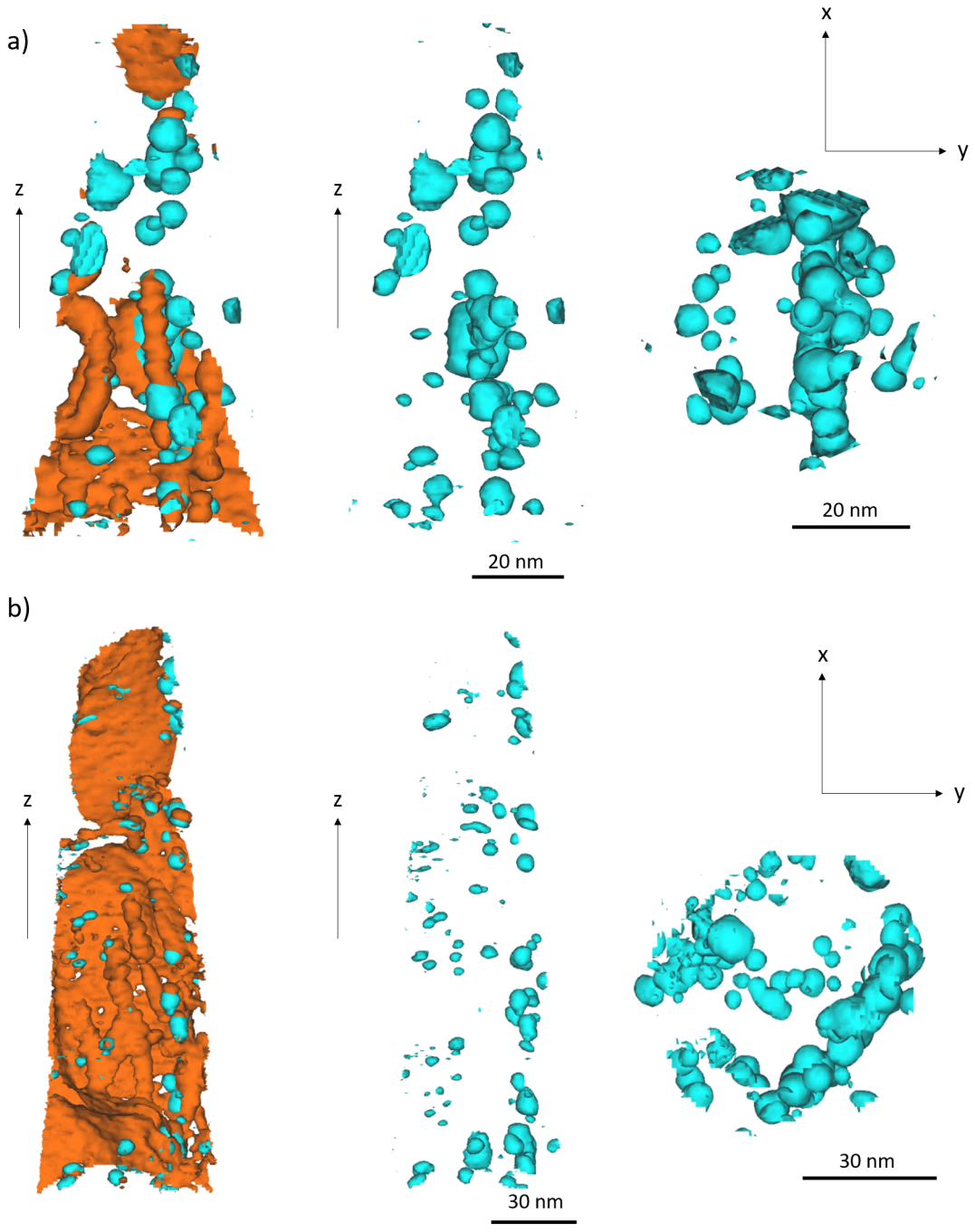


Figure 4.38: a) APT reconstruction of a tip showing a 2 ionic% HfO isosurface in blue and 2 at% Cu isosurface in Cu, a reconstruction just showing just the HfO isosurface and a top down view of the HfO isosurface b) Second reconstruction showing the same three isosurface reconstructions as a)

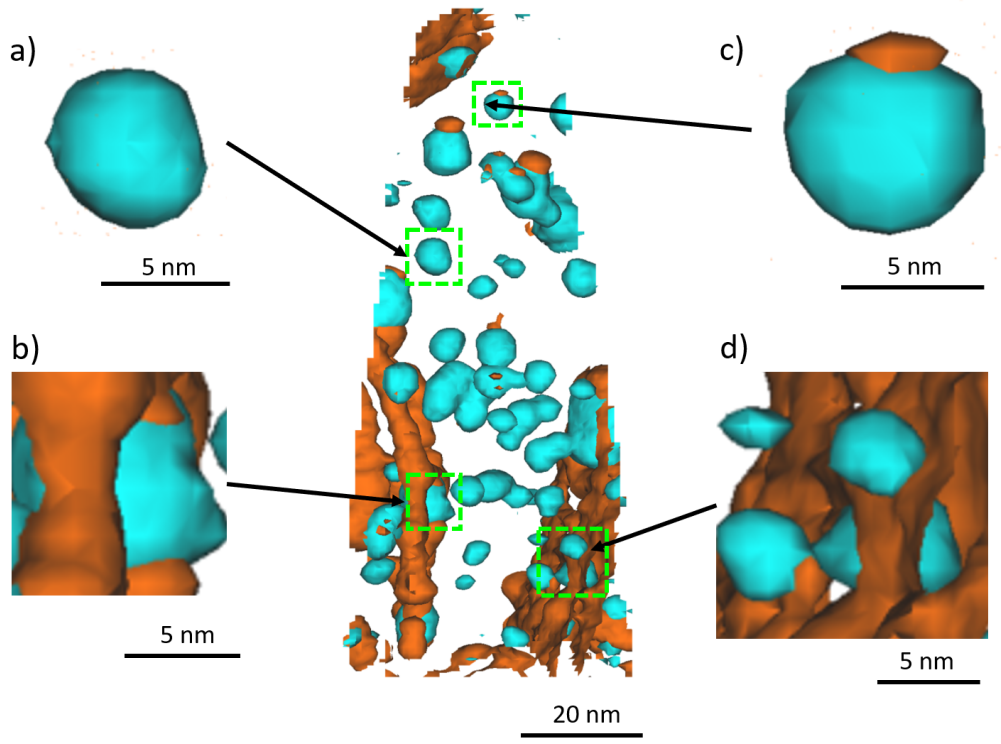


Figure 4.39: APT reconstructions of a Nb_3Sn tip from the RIT sample showing an isosurface of 2 at% Cu in orange and 2 at% HfO ions in light blue. HfO_2 clusters are shown close-up with different associations to the Nb_3Sn microstructure shown inset: a) HfO_2 cluster with no association to Cu b) HfO_2 cluster with association to a Cu segregated dislocation c) HfO_2 cluster with association to Cu within a Nb_3Sn grain d) HfO_2 cluster in association with a Cu segregated grain boundary

HfO_2 particle with Cu, HfO_2 particle associated with a Cu segregated dislocation and HfO_2 particle associated with a Cu segregated grain boundary. Dislocations are normal regions which will modify the pinning landscape in a similar way to grain boundaries, the main difference is that dislocations can pin fluxons in 1D whereas grain boundaries can pin dislocations along a 2D plane. Therefore, there are two main types of location of HfO_2 clusters which need to be considered, these are intra-grain HfO_2 and inter-grain HfO_2 clusters. It may be expected that HfO_2 clusters which are associated with the intra-grain regions act solely as APCs, whereas ones which interact with inter-grain regions have a summation of both APCs and surface pinning.

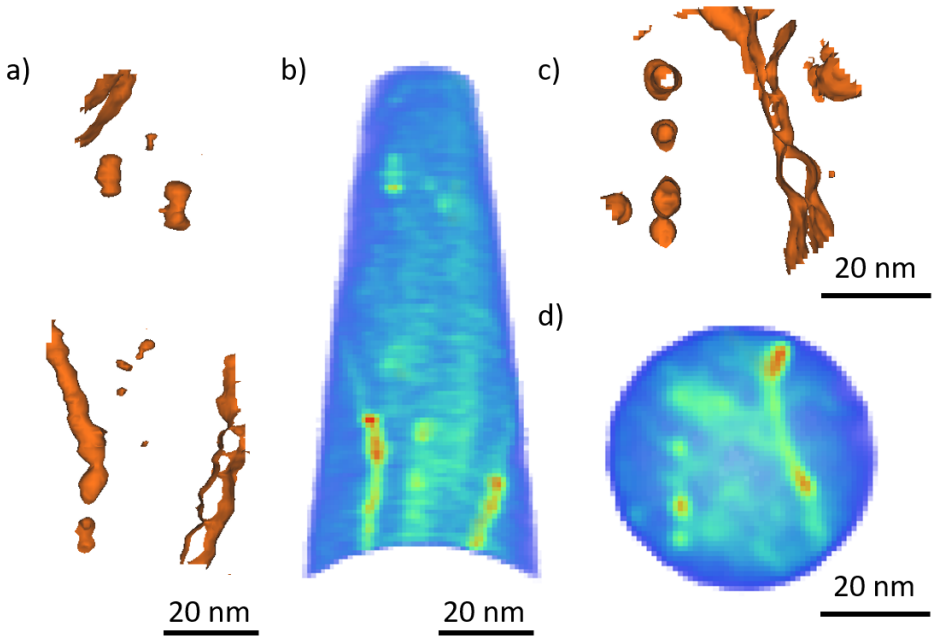


Figure 4.40: Slices of the APT reconstruction shown in Figure 4.39. a) A thin slice in the z-direction showing a 2 at% Cu isosurface with a dislocation on the left and a grain boundary on the right b) A density map of the same z-slice showing an increase in density at the dislocation and the boundary c) A thin slice from the base of the same reconstruction, looking down the axis of the tip, with a 2 at% Cu isosurface showing the dislocations and the boundary d) A density map of the c) slice showing an increase in density associated with the dislocations and the grain boundary

Although it is not possible to, with total certainty, determine whether the HfO_2 clusters are intra-grain or inter-grain, one measure that can help to determine where the cluster resides is the amount of Cu incorporated into the composition of each cluster. Clusters which are intra-grain and have no association with Cu (as seen in Figure 4.39) are not expected to have significant counts of Cu associated with their composition. Clusters which are inter-grain e.g. d) from Figure 4.39, are embedded within the grain boundary therefore there will be significant amounts of Cu associated. To confirm that Figure 4.39 does contain dislocations and a boundary, a density map is shown in Figure 4.40. To determine the location of the HfO_2 clusters, the Cu count within each individual cluster was taken as a percentage of the total atom count of each cluster. Figure 4.41 shows the percentage of clusters which have $\leq$ Cu% e.g. the first point on the graph is the percentage of clusters where Cu% ≤ 0. In Figure 4.41 there are two distinct gradients present, one Cu% ≤ 3 and the second $3 <$ Cu% ≤ 7, which suggests that the Cu% ≤ 3 HfO_2 clusters which have limited association can be considered to be intra-grain, and those $3 <$ Cu% ≤ 7 can be considered to be inter-grain or associated with Cu segregated dislocation features. This method is a first approximation to defining the location of the HfO_2 clusters, however it can be noted that 114 out of the 366 clusters sampled contained 0% Cu, which to 2 s.f. is 31% of the HfO_2 clusters. By using the metric of Cu% ≤ 3 the total percentage of clusters which are deemed to be intra-grain are 79%, therefore the percentage of clusters which are intra-grain and have some association with Cu are 48%. This leaves 21% of clusters which are in close association with dislocation features or grain boundaries. These percentages should be considered as estimates, and it is likely that the some of the inter-grain clusters which are weakly associated with boundaries or dislocations may be included within the Cu associated intra-grain percentages. However, this estimate suggests that up to 80% of clusters are intra-grain and 20% are inter-grain. The intra-grain clusters will be acting as purely point pinning centres, however the clusters associated with the inter-grain regions will be modifying, and likely strengthening, the surface pinning behaviour associated with the dislocations and grain boundaries.

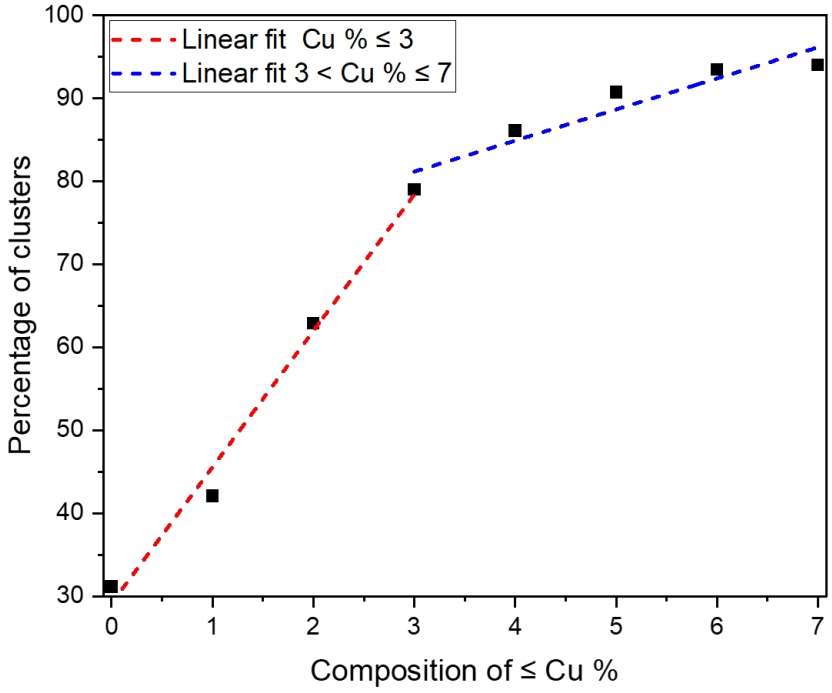


Figure 4.41: Percentage of clusters which incorporate a composition of $\leq$ Cu% with two linear regions of best fit at $\leq$ 3% Cu and 3 $<$ Cu% $\leq$ 7.

4.6 Residual Cu Rich Phases

As presented in section 4.4.3 and shown in Figure 4.33, two grain boundaries were found to have very different segregation behaviour, with Γ_{Cu} values of 164.9 $\pm$ 0.3 atoms/nm^2 and 90.3 $\pm$ 0.4 atoms/nm^2, up to 20 times larger than that seen for other grain boundaries. This excess of Cu is unphysical, therefore additional phases must be present at these boundaries. Other compositional analysis in this work has used compositional measurements from ROIs to determine the composition of different phases, however these high Cu regions were not much thicker than grain boundaries and very small, therefore enclosed isosurfaces and proxigram analysis were used to estimate the composition of these regions/grain boundaries.

A series of increasing Cu isosurfaces were applied to each Nb_3Sn reconstruction: 20 at% Cu and 30 at% Cu. At each isosurface concentration, proxigram analysis was conducted on every enclosed volume, with the composition of each region of high Cu phase given as the plateau in composition towards the centre of the shape. Selecting the composition towards the centre of the shape minimised the contribution of matrix counts and produced an estimate for the composition of each high Cu phase. Figure 4.42 shows the composition of every high Cu region in the Nb_3Sn reconstructions, with a concentration of 20 at% Cu and 30 at% Cu on two ternary Nb-Sn-Cu composition maps, with Hf, Ta and O measured to be approximately zero in these regions. The secondary 30 at% Cu isosurface was used to investigate whether the composition of the regions stayed in the same place on the ternary map, or whether, when any contributions from the surrounding Nb_3Sn matrix were reduced, the composition moved towards one of the binary phases indexed. A number density of high Cu phases was calculated at 20 at% Cu and 30 at% Cu producing a number density range of between 2.1 - 2.4 $\times$ 10^{22} m^{-3}.

From first observation the majority of points in a) and b) from Figure 4.42, are shifting towards the Cu corner of the ternary map, however there are some points at the centre of the diagram which appear stationary, suggesting a ternary phase may be present. Figure 4.43 includes regions from Figure 4.42 with a composition which stays consistent at both 20 at% and 30 at% Cu isosurfaces. The average composition of this ternary phase is calculated as Cu = 41.6 $\pm$ 6.7 at%, Sn = 29.8 $\pm$ 4.7 at% and Nb = 28.6 $\pm$ 6.0 at%, which would suggest

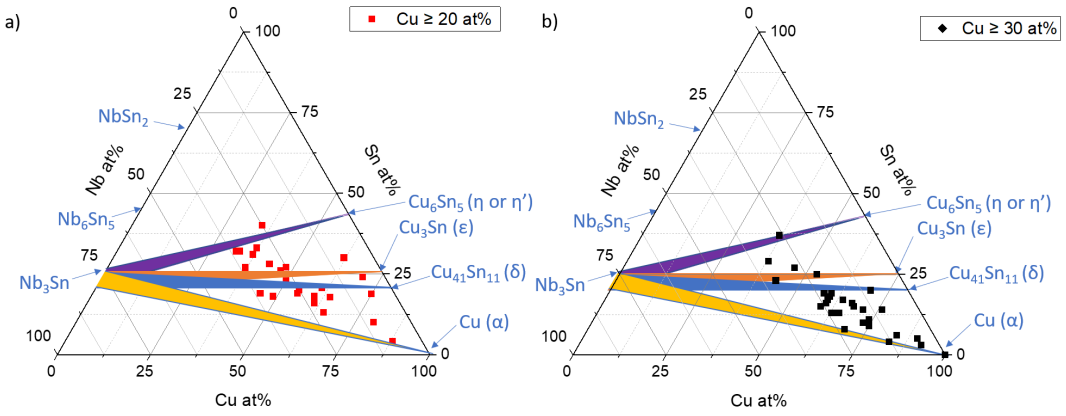


Figure 4.42: Ternary Nb-Sn-Cu composition map a) Cu 20 at% isosurface used to define the abnormally high Cu regions in Nb_3Sn b) Cu 30 at% isosurface. Nb-Sn and Cu-Sn binary phases within the compositions of interest have been included on the ternary composition map. The four tie-lines are the compositions which would be expected if Nb_3Sn and one of the four indexed Cu-Sn phases were present in equilibrium in the APT volumes analysed.

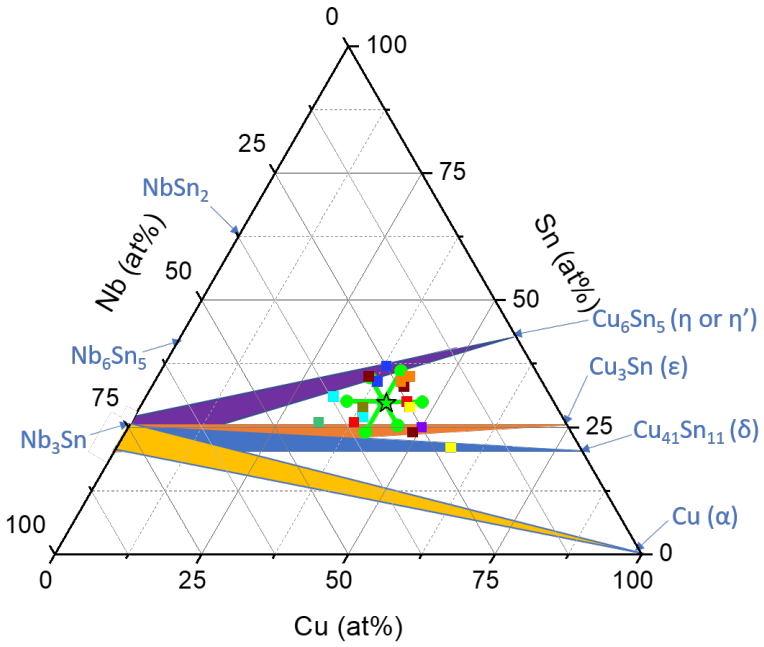


Figure 4.43: Ternary Nb-Sn-Cu composition map with each colour showing the composition of a region with a 20 at% and 30 at% Cu isosurface. Only regions which did not show significant shift towards the Cu-α corner are included. An average composition for these regions is shown by a green star and the error associated shown with green error bars.

a ratio of $Cu_3Sn_2Nb_2$. To the author's knowledge, the only ternary phase identified in the literature is nausite ($Nb_{0.75}Cu_{0.25}Sn_2$) which contains approximately 56 - 64 at% Sn [103, 211, 212], however this phase is far too low in Cu to be the phase present in the RIT data. The nausite reaction pathway has previously been shown to produce coarse grain Nb_3Sn [98, 102], however little is known as to how the presence of APCs affects the nausite reaction pathway.

The remaining regions which appear to show a shift towards the Cu corner in Figure 4.42 can be found in Figure 4.44. If the Cu concentration was above 40 at% for a region, an additional point was plotted to show the composition at an isosurface concentration of $>$ 40 at% Cu. Although the majority of the points are shifted towards Cu there is a suggestion that there may be some amount of Cu_3Sn (ϵ) or $Cu_{41}Sn_{11}$ (δ) present in the sample. Previous literature on RRP® wires has shown the presence of ϵ and η phases, with η dominant at the Sn core after heat treatment at 400°C and ϵ dominant after the final heat treatment at 665°C [98, 213]. However evidence of the ϵ and η phases has focused on the micron scale using SEM EDX, therefore little is known about residual nanoscale Cu-Sn phases within the Nb_3Sn microstructure. δ phase, which would not be predicted to exist at room temperature under equilibrium conditions, see Figure 1.18, has been seen in contact with Nb_3Sn in RRP® bundles on the micron scale (P.Lee, private communication, 7 Aug 2023). Although no studies have previously looked at Cu-Sn phase formation at the nanoscale within the Nb_3Sn, the presence of δ and ϵ on the micron scale suggests even finer Cu-Sn particles could be present.

Nanoscale binary or ternary Cu rich phases in the Nb_3Sn microstructure have not been previously discussed in the literature, however these nanoscale phases might, unintentionally, be acting as additional pinning centres.

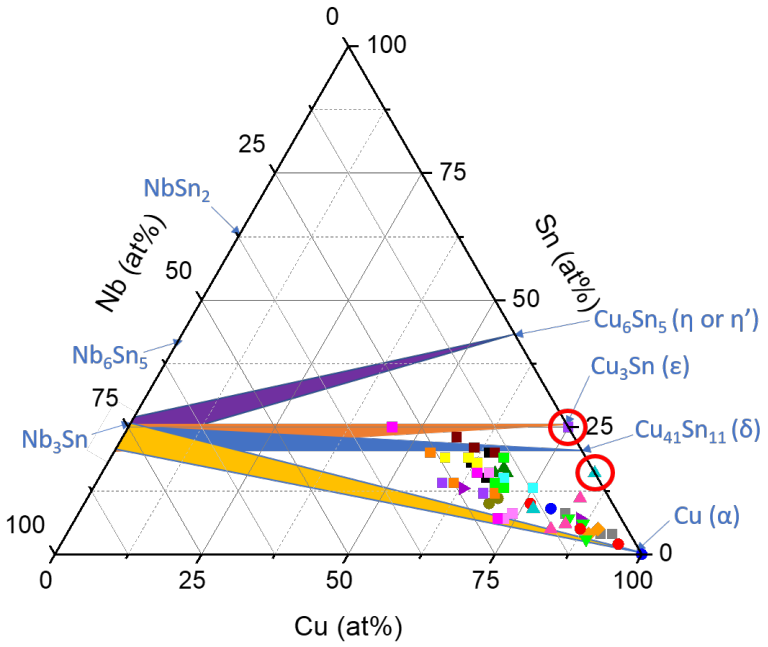


Figure 4.44: Ternary Nb-Sn-Cu composition map with each colour showing the composition of a region with a 20 at%, a 30 at% Cu and if possible a 40 at% Cu isosurface. There is a clear shift in compositions towards the Cu corner but there are points, circled in red, implying the presence of δ or ϵ Cu-Sn phases.

4.7 Carbon and Nitrogen Rich Particles

As discussed in section 4.3.3, there is some evidence of Nb rich particles which contain an amount of carbon and/or nitrogen. Nb can form multiple phases with C and N species. At 670°C there are four different Nb and C phases which could be present, these are Nb_2C, Nb_4C_{3-x}, Nb_6C_5 and NbC_{1-x} [214] and Nb and N have three phases which are stable, Nb_2N, Nb_4N_3 and NbN [215, 216]. The particles found in the Nb_3Sn layer of the RIT appear to contain some amount of C and N, for example the particle in Figure 4.18 contains approximately 70 at% Nb, 15 at% C and 15 at% N which produces a ratio of approximately $NbN_{0.2}C_{0.2}$. Although the ratio is not exact, there is evidence in the literature of Nb-C-N phases, such as $Nb(C_{0.3}N_{0.7})$ which do superconduct and have a T_c value of 17.8 K [217], just below that of Nb_3Sn.

Nb-C-N particles with a T_c only slightly below the Nb_3Sn regions would be expected to contribute to the overall superconducting performance of the sample and may broaden the T_c transition. Although, these particles are approximately 10 - 20 nm in diameter they will not be contributing to the point pinning force of the wire because they are superconducting regions. As can be seen from Figure 4.18 there is no sharp segregation of solute to the edge of these Nb-C-N particles, therefore any boundary pinning from the edges of these regions is likely to be very weak. Although these particles are unlikely to have a substantially negative effect on the Nb_3Sn performance, these particles were formed through a lack of control over the processing environment of the wire. If enough of these particles were present within the Nb_3Sn layer this could contribute to Zener pinning, however this will be negligible compared to the effect of HfO_2 as Zener pinning centres, as these are more evenly distributed throughout the Nb_3Sn layer.

4.8 Overall Composition of the Nb_3Sn

To determine whether the overall composition of the intra-grain regions and inter-grain regions are consistent with the A15 Nb-Sn-Ta composition map produced by Flükiger *et al* [45], at between 700°C and 750°C, an overall composition for 8 Nb_3Sn reconstructions was calculated. The estimated composition map determined by Flükiger *et al* used EPMA [109, 111, 117] and TEM EDX [91] to determine the limits of the A15 Nb-Sn-Ta composition map. As previously discussed in chapter 1, prior studies using EPMA and TEM EDX consider composition on the micron scale, therefore it is unknown as to how these compositions vary at the nano-scale.

The overall composition of the Nb_3Sn region in the RIT can be considered to be made up of low Nb Nb_3Sn, high Nb Nb_3Sn, HfO_2 clusters and high Cu features which are usually associated with grain boundaries but can include dislocations and some Cu clustering. Although the volume fraction of HfO_2 clusters is very small (0.17%), the majority of Hf and O counts are contained within the clusters therefore these need to be included in the overall composition calculation. The average intragrain compositions for low and high Nb Nb_3Sn regions have been determined from section 4.4.1, and the average grain boundary composition is from section 4.4.3. To calculate the volume of each region within the overall volume of Nb_3Sn analysed, the total reconstructed volume of each tip was measured in IVAS. The grain boundary volume was calculated by defining these regions with an isosurface of 2 at% Cu, the high Nb volume was calculated as an isosurface 72.5 at% Nb (from section 4.4.1), the composition of HfO_2 was assumed to be 33.3% Hf and 66.6% O and the low Nb Nb_3Sn volume was assumed to be the total volume minus the high Nb and grain boundary volumes.

The average composition of the Nb_3Sn for the RIT sample was calculated by equation 3.5, previously shown in chapter 3, with an additional term used for the HfO_2 clusters, equation 4.3, for each species, where x = Nb, Sn, Ta, Cu, Hf, O, C is the concentration in at%, and V_f is the volume fraction associated with each region. The error in C_x does not include the HfO_2 cluster term which vastly skews the error associated with the Hf and O species, therefore the error is given by $\sqrt{\sigma_{Low}^2 + \sigma_{High}^2 + \sigma_{GB}^2}$.

$$C_x(at\%) = (C_x^{HighNb} \times V_f^{HighNb}) + (C_x^{LowNb} \times V_f^{LowNb}) + (C_x^{GB} \times V_f^{GB} + (C_x^{GB} \times V_f^{HfO_2}) \tag{4.3}$$

The average composition for the A15 is $C_{Nb} = 69.90 \pm 6.67$ at%, $C_{Sn} = 24.83 \pm 2.71$ at%, $C_{Ta} = 3.49 \pm 0.54$ at%, $C_{Cu} = 1.37 \pm 8.97$ at%, $C_{Hf} = 0.13 \pm 0.13$ at% & $C_O = 0.29 \pm 0.43$ at%. The amount of Hf present here will be a slight underestimation of the Hf in the sample due to the Hf^{3+}/Sn^{2+} overlap described in section 4.3.4, therefore up to 0.26 at% may be present within the sample. The overall composition, only including Nb, Sn and Ta normalised to 100, can be seen in the ternary composition map, Figure 4.45, with the overall composition just outside the high Sn region of the A15 phase field. This is interesting to note because A15 with high Sn is known to have increased B_{c2} and T_c values [45]. Although the RIT sample contains additional elements such as Hf, O and Cu, the Flükiger *et al* A15 composition map is a fairly good fit to the overall composition of the RIT sample. The volume fractions of the different Nb_3Sn regions are 15.4% grain boundary, 11.3% high Nb and 73.3% low Nb.

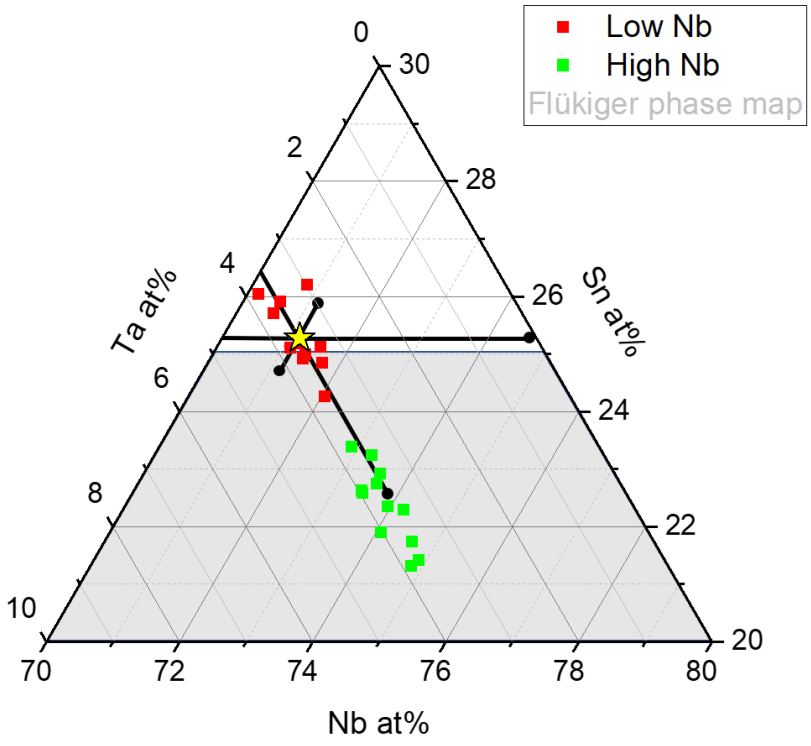


Figure 4.45: A Nb-Sn-Ta Nb_3Sn ternary composition map showing the average composition of the Nb_3Sn with a yellow star and both the low and high regions of Nb_3Sn overlaid on the Nb-Sn-Ta composition map from Flükiger *et al* [45]. Error bars associated with the average composition are shown in black.

4.9 Residual Nb_6Sn_5

As discussed in section 4, Figure 4.3 showed previous evidence that a residual fine grain Nb_6Sn_5 layer was present next to the Nb_3Sn layer in the RIT sample [64]. In Figure 4.46, the heat treatment process to form Nb_3Sn proceeds by a $NbSn_2$ and Nb_6Sn_5 pathway. Incomplete reaction of the Nb and Sn to form Nb_3Sn will leave residual Nb-Sn phases which do not contribute to the superconducting properties of the wire. When targeting the Nb_3Sn layer during the FIB lift-out process, it is not always clear exactly where the Nb_3Sn layer stops and the Nb_6Sn_5 layer begins, particularly below the surface of the sample. Therefore, 3 tips which were intended to be taken from the Nb_3Sn regions contained mainly Nb_6Sn_5.

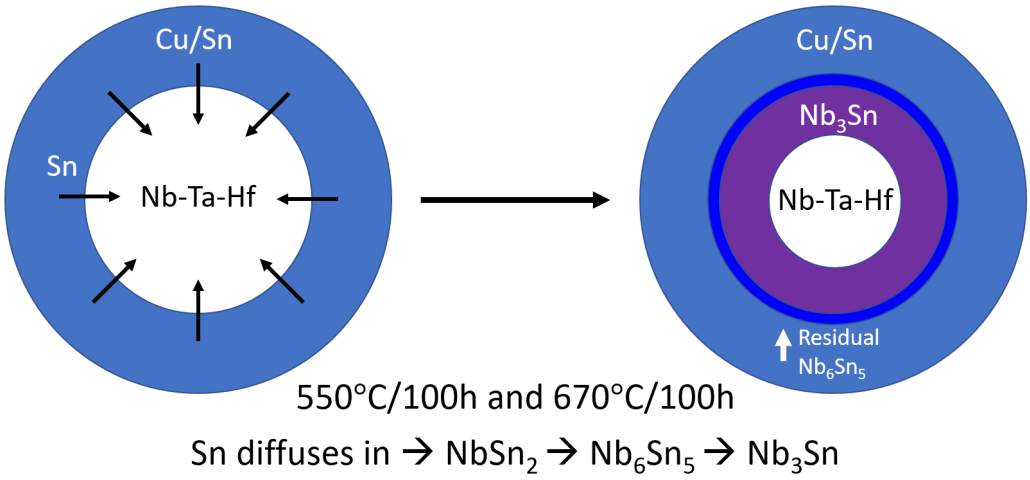


Figure 4.46: Reaction of the RIT sample occurred in two stages, initially at 550°C for 100 hrs where Sn diffuses into the Nb-Ta-Hf alloy, forming the higher Sn content Nb-Sn phases. The 670°C heat treatment for 100 hrs aims to promote the formation of Nb_3Sn.

Although collecting data on Nb_6Sn_5 was unintentional, key compositional measurements, such as the composition of Hf, Cu and Ta in the Nb_6Sn_5 phase can be measured as well as the distribution of HfO_2 clusters within the Nb_6Sn_5 which will help show if HfO_2 is formed prior to the A15 phase. Figure 4.47 shows 2/3 analyses which contain Nb_6Sn_5.

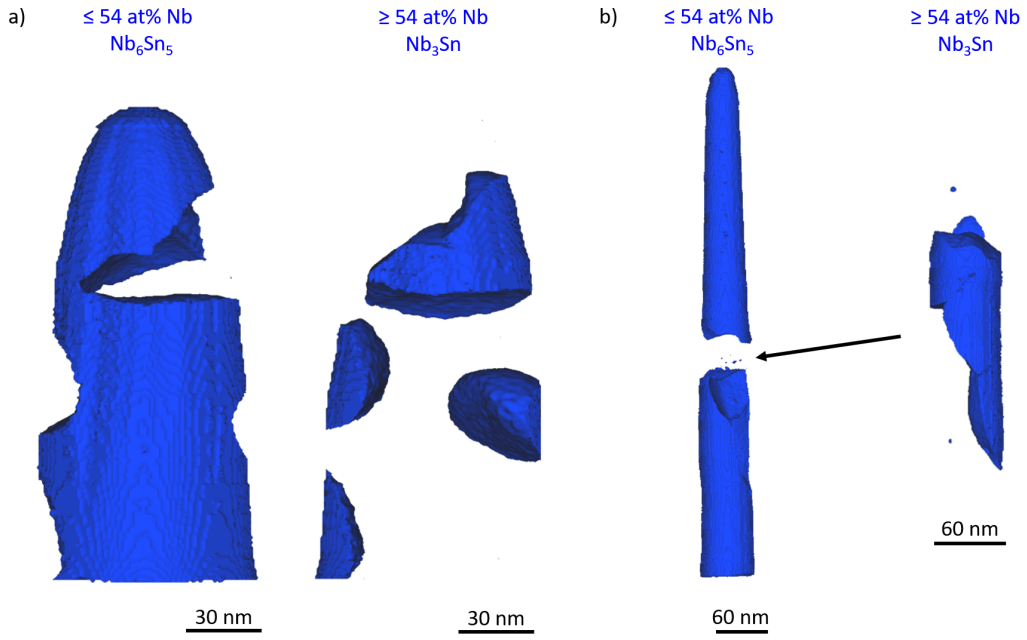


Figure 4.47: Two APT reconstructions, a) and b), to which a Nb isosurface 54 at% Nb is applied, identifying the Nb_3Sn regions with $\leq$ 54 at% Nb and the Nb_6Sn_5 regions with $\geq$ 54 at% Nb

4.9.1 Intra-grain Compositional Analysis

Unlike Nb_3Sn, Nb_6Sn_5 is a line compound at 54.5 at% Nb and 45.5 at% Sn [44]. However, within this sample the presence of Cu, Ta and Hf may be segregating differently in Nb_6Sn_5 compared to Nb_3Sn. By understanding which species prefer to segregate in each phase, we can better design wire structures and heat treatments for optimising Hf and Ta doped Nb_3Sn.

To extract composition data, ROIs were extracted from distinct regions of the samples, with decomposition of the Nb_2^{3+}/Sn^{2+} peak overlaps in the mass spectra, as discussed in 4.3.4. Out of the 3 reconstructions which contained Nb_6Sn_5 regions, 9 ROIs were extracted and within which 3 distinct compositions were established. To best demonstrate the differing composition, only the Nb, Sn and Cu have been included in a normalised ternary composition map, Figure 4.48.

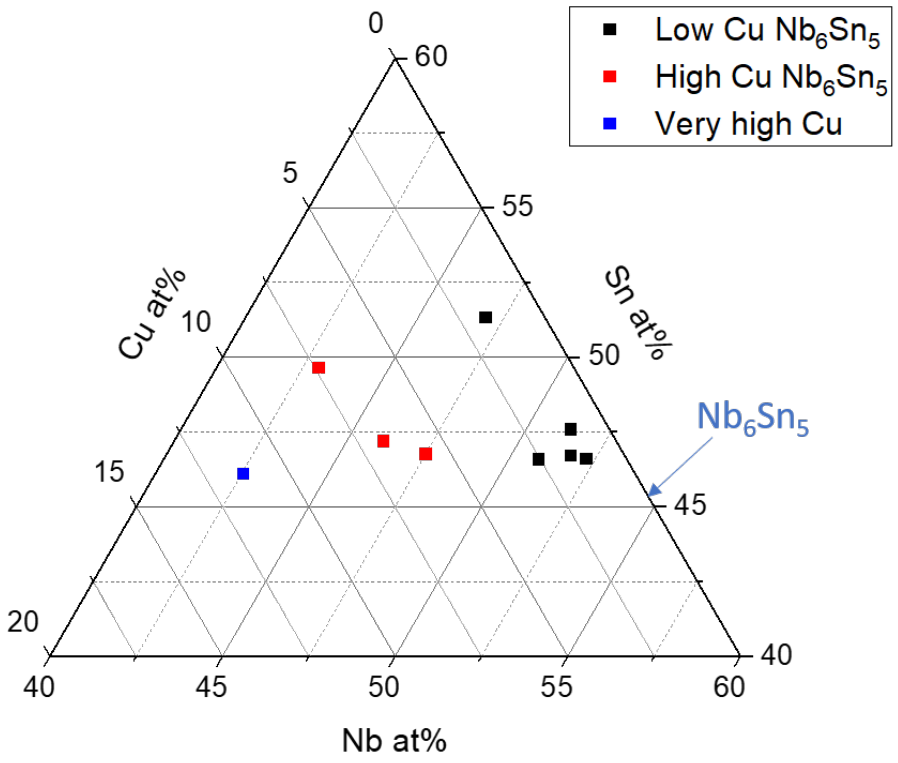


Figure 4.48: Ternary composition map of Nb, Sn and Cu within the Nb_6Sn_5 phase, normalised to visually show the difference in Cu between differing Nb_6Sn_5 regions.

To show the correlation of Nb and Sn concentrations with Cu, Nb and Sn have been plotted against Cu in Figure 4.49, which shows that as Cu increases there is a linear decrease in Nb and no clear change in Sn. These data suggest that Cu is substituting onto the Nb lattice site in the Nb_6Sn_5 phase. Figure 4.50 shows 2 Nb_6Sn_5 reconstructions with only the Cu atoms, there are clearly 3 distinct regions of low Cu, high Cu and very high Cu, over 10 at%. The average compositions for these distinct regions are included in table 4.9 along with the composition for the very high Cu region. The regions with higher Cu appear to have a lower Nb and Ta concentration, however the Hf and HfO ion content appears consistent in all three regions. Cu appears to have significantly more solubility in Nb_6Sn_5, with the maximum solubility of Cu in the Nb_3Sn 0.5 at% for the irradiated RRP® sample, from table 3.3. Previous work in the literature has shown that Nb_6Sn_5 can contain more Cu than Nb_3Sn, with reports of 3.4 at% [218] and 5 at% Cu [219]. The Nb_6Sn_5 converts to Nb_3Sn, which has lower solubility of Cu, therefore if the Cu cannot be pushed out to the grain boundaries within the nanostructure, then this may explain why some Cu becomes trapped in the intra-grain region and often becomes associated with HfO_2 clusters, as shown in Figure 4.39. Only 1 of the 3 reconstructions sampled contained considerably more oxygen than the other reconstructions, with the average oxygen content of the Nb_6Sn_5 regions in 2 of the reconstructions 0.19 $\pm$ 0.05 at% compared to the average of 4.14 $\pm$ 0.92 at% in the third reconstruction. Due to the small sample size of reconstructions, the high oxygen reconstruction is skewing the measured oxygen concentrations for the low and very high Cu regions, therefore a larger sample size is required to determine the correlation of oxygen with each Cu region in Nb_6Sn_5.

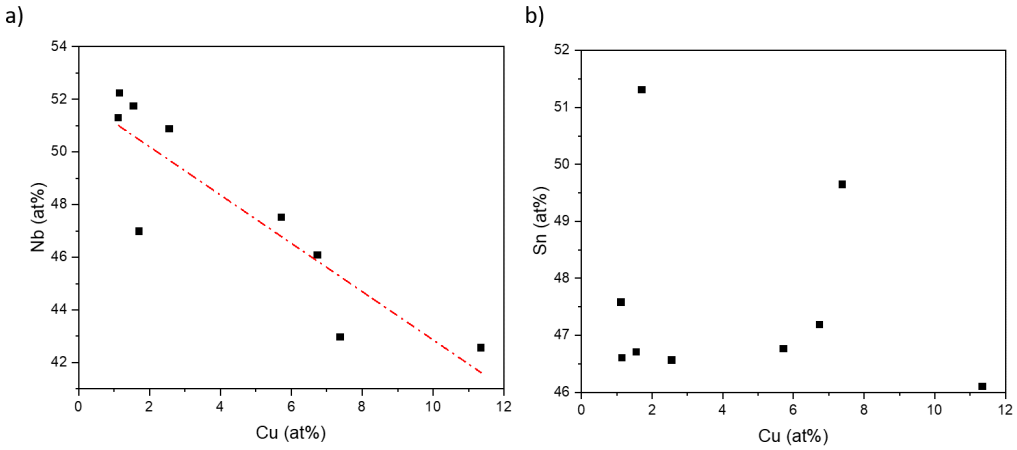


Figure 4.49: a) Nb concentration plotted against Cu concentration for the Nb_6Sn_5 regions and a linear relationship with $R^2 = 0.74$ b) Sn concentration against Cu concentration for the Nb_6Sn_5 regions with no obvious correlation.

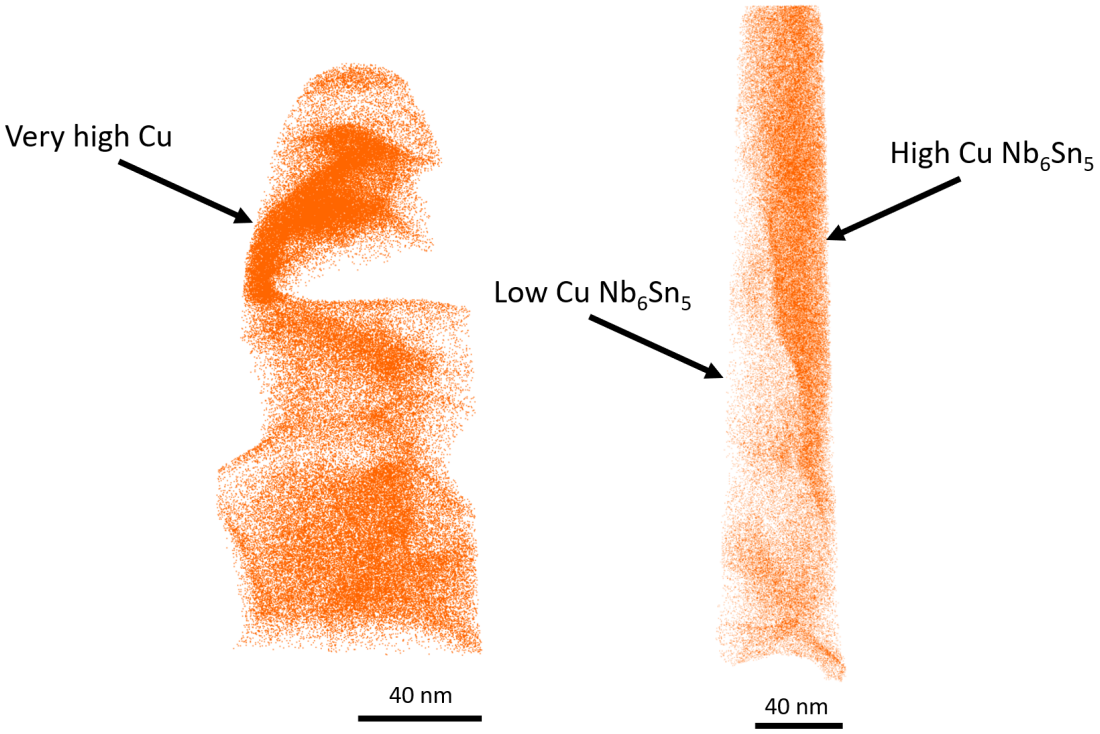


Figure 4.50: APT reconstruction of two regions of Nb_6Sn_5, showing only Cu ions, from the tips in Figure 4.47 which within the Nb_6Sn_5 phase contain low, high and very high Cu regions

	Nb at%	Sn at%	Cu at%	Ta at%	Hf at%	O at%
Low Cu Nb_6Sn_5	48.34 ± 3.51	45.51 ± 1.12	1.54 ± 0.52	2.36 ± 0.15	0.29 ± 0.10	1.95 ± 2.43
High Cu Nb_6Sn_5	44.56 ± 3.74	46.76 ± 0.30	6.45 ± 0.63	1.78 ± 0.23	0.22 ± 0.08	0.23 ± 0.05
Very high Cu	40.80	44.20	10.88	0.62	0.23	3.27

Table 4.9: Compositions of differing Nb_6Sn_5 regions

4.9.2 Number Density and Size of HfO_2 Clusters

As can been seen from table 4.9, HfO ions are present within the Nb_6Sn_5 regions. To understand whether the HfO_2 clusters have differing number densities or sizes in Nb_6Sn_5 compared to Nb_3Sn, cluster calculations were performed on the Nb_6Sn_5 regions.

To extract the Nb_6Sn_5 regions for cluster analysis, an isosurface $\leq$ 53 at% Nb was applied to each reconstruction, as shown in Figure 4.47. Each distinct region of Nb_6Sn_5 in each of the 3 reconstructions was extracted and an individual cluster search conducted on each region. This method did not separate the Nb_6Sn_5 into low Cu and high Cu regions, but instead addressed the total cluster size and number density within each region. Cluster analysis was followed in line with section 2.6.6 using HfO ions as the selected solute and performing an erosion step to remove matrix atoms which may have been included in the calculation. Table 4.10 shows the N_D and diameter of the HfO_2 clusters in Nb_6Sn_5. The size distribution of the clusters is presented in Figure 4.51 in terms of the number of ranged ions, with a bin width of 50 ranged ions, which is the same used for the clusters identified in the Nb_3Sn phase. From Figure 4.51, 16.9% of clusters have $\leq$ 50 ranged ions and 41.7% of all clusters have $\leq$ 200 ranged ions, further evidence that the clusters in the Nb_6Sn_5 are marginally larger than those seen in Nb_3Sn.

Nb_6Sn_5	N_D ($\times 10^{22}$ m^{-3})	Diameter (nm)
HfO_2 clusters	9.4 $\pm$ 4.0	2.4 $\pm$ 0.3

Table 4.10: N_D and diameter of the HfO_2 clusters in Nb_6Sn_5

Although the volume of Nb_6Sn_5 sampled is smaller than the volume of Nb_3Sn sampled, the N_D of HfO_2 clusters in Nb_6Sn_5 is in the lower quartile of that sampled in the Nb_3Sn and the diameter of the HfO_2 nanoparticles is marginally larger than those seen in the Nb_3Sn. If the volume fraction of HfO_2 clusters is compared, Nb_3Sn contains an average 0.17 $\pm$ 0.21 % HfO_2 and Nb_6Sn_5 contained an average volume fraction of 0.10 $\pm$ 0.05 % HfO_2. It is clear that HfO_2 clusters are found in both phases, and with so little volume of Nb_6Sn_5 present it is difficult to have any certainty in whether there is an obvious difference in size and N_D between the two phases. The presence of HfO_2 nanoparticles in the Nb_6Sn_5 phase is evidence that the HfO_2 is not formed by a late stage reaction in the A15 compound.

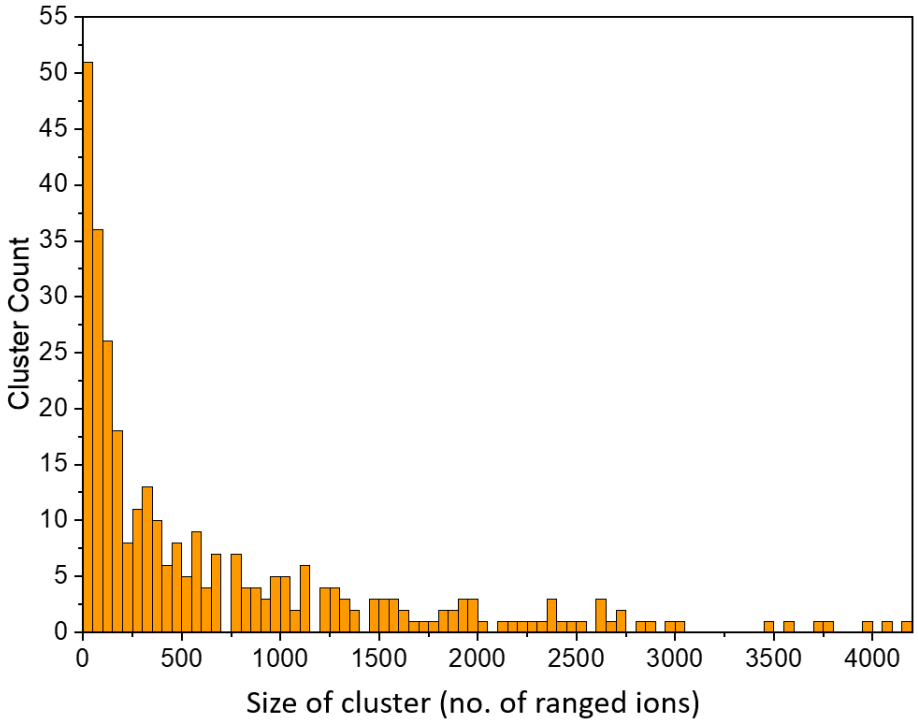


Figure 4.51: Cluster count against the no. of ranged ions within each cluster in Nb_6Sn_5

4.10 Linking Cluster Properties to Superconducting Properties

As discussed in section 1.3, pinning in Nb_3Sn is a combination of grain boundary and point pinning mechanisms. The pinning force is:

$$F_p = A_{GB}\left(\frac{H}{H_{irr}}\right)^{0.5}\left(1-\frac{H}{H_{irr}}\right)^2 + A_{PD}\left(\frac{H}{H_{irr}}\right)\left(1-\frac{H}{H_{irr}}\right)^2 \tag{4.4}$$

In this case the field is defined as the H field and the maximum field is the irreversible H_{irr}, instead of using B and B_{c2}. Dew-Hughes developed the theory for grain boundary (normal surface) and point (normal point) pinning in 1974 [49] with the factors which multiply each pinning function defined more precisely as:

$$A_{GB} = \frac{\mu_0 S_v H_{irr}^2}{4\kappa^2} \tag{4.5}$$

$$A_{PD} = \frac{\mu_0 V_f H_{irr}^2}{4.64 a\kappa^2} \tag{4.6}$$

where μ_0 is the permeability of free space, S_v is the grain boundary surface pinning area per unit volume in the direction of F_L, κ is the Ginzburg-Landau parameter which is a property of the material, V_f is the fraction of flux lines which lie inside the nanoparticles and a is the effective nanoparticle diameter. A value of A_{PD}/A_{GB} can be determined from the fit of equation 4.4 to the pinning force curves for this sample. The pinning force curves for this sample can be found in work by Tarantini *et al* [58], and the ratio of A_{PD}/A_{GB} for this sample was found to be 0.57 from additional work by Tarantini *et al* [208]. A previous approximation of point and grain boundary pinning was made for this sample using limited APT data collected in 2021 [208], however since publication further APT analyses have been taken from this sample and therefore the numbers discussed here will be slightly different based on the larger volume of collected data.

	N_D ($\times 10^{23}$)	a (nm)	d (nm)	Rigid A_{PD}/A_{GB}	Flex A_{PD}/A_{GB}
Lower Limit	0.95	1.63	43	0.009	1.690
Upper Limit	2.92	2.25	93	0.119	5.316

Table 4.11: Upper and lower limits for the A_{PD}/A_{GB} value for either fully rigid or fully flexible flux lines

To determine whether the full set of results from APT are consistent with the measured pinning force curves, a value for $A_{PD}/A_{GB} = \frac{V_f}{1.16 a S_v}$ can be determined by assuming the $S_v \approx 1/d$ where d is grain size, V_f is between $(a/l)^3$ for a rigid flux lines and a/l for flexible flux lines, and l is the average nanoparticle spacing. l can be calculated from N_D ($l \approx N_D^{-\frac{1}{3}}$) and d is taken from SEM grain size measurements, determined to be 68 $\pm$ 25 nm [64].

Using the lower and upper limits for N_D, a and d from the APT data the expected range of A_{PD}/A_{GB} has been calculated for the rigid and flexible flux line condition, table 4.11, using equation 4.7 and 4.8 respectively.

$$\left(\frac{A_{PD}}{A_{GB}}\right)_{Rigid} = \frac{N_D a^2 d}{1.16} \tag{4.7}$$

$$\left(\frac{A_{PD}}{A_{GB}}\right)_{Flex} = \frac{N_D^{1/3} d}{1.16} \tag{4.8}$$

From the APT data the range A_{PD}/A_{GB} is calculated to be between 0.009 to 5.316, as shown in table 4.11. Tarantini *et al* measured a A_{PD}/A_{GB} value of 0.57 from the pinning force curve for the RIT sample, which is consistent with the range of values of A_{PD}/A_{GB} from the APT data. The value of 0.57 is consistent with a more rigid flux line condition.

Here we have assumed the reduction in grain size is not close enough to the flux line spacing, predicted to be 12 nm at 16 T from equation 1.6, to cause any additional $\Delta\kappa$ pinning. This is a reasonable assumption based on the grain size being $\sim$ 5 times larger than the flux line spacing. It is also assumed that the regions of binary or ternary Cu phases are having a negligible effect on pinning compared to the HfO_2 particles. The number density of the Cu phases is 10 times smaller than that of the HfO_2 particles and the size of the Cu phases are very difficult to define.

The shift in pinning force curve to an F_p^{MAX} value of $0.25H_{IRR}$ for the Nb-4Ta-1Hf sample compared to the F_p^{MAX} values of $0.2B_{IRR}$ for the Nb-4Ta sample strongly evidences the introduction of point pinning [58]. This work has shown the presence of HfO_2 clusters using APT and that the number density and size distribution of HfO_2 clusters are consistent with the pinning force curve for the Nb-4Ta-1Hf sample. The additional effect of the HfO_2 particles is Zener pinning which has reduced the grain size of the Nb_3Sn grains in the Nb-4Ta-1Hf sample to 68 $\pm$ 25 nm, compared to $\sim$ 110 nm for the Nb-4Ta sample which did not contain HfO_2 nanoparticles [64]. The reduction in grain size will have increased the surface pinning, but only the addition of point pinning from the HfO_2 particles can explain the shift in the pinning force.

Consistency between the nanoscale segregation and quantitative measurements, and the superconducting pinning curve is key evidence to show how important the nanoscale structure is in affecting the measured superconducting properties of the sample.

4.11 Discussion

The RIT sample produced an impressive equivalent RRP® non-Cu J_c of 2230 $\pm$ 640 Amm^{-2} at 16 T [64], when extrapolated from 14 T results, reaching the FCC target. It was initially unclear as to why a sample with no oxygen source could be producing a pinning force curve with a clear shift towards point pinning.

4.11.1 Pre- and Post-heat treatment Nb alloys

An investigation into the macroscale segregation behaviour of the original Nb-4Ta-1Hf rod using EPMA showed that there was potentially some macroscale inverse segregation of Hf and Ta, as shown in Figure 4.4, but that there was no obvious Nb or O segregation. Using EPMA line-scans the measured oxygen content of the as-received Nb alloy was 5.09 $\pm$ 0.62 at%, as shown in table 4.1, which is evidence of the presence of oxygen within the original starting alloy. The EPMA map of oxygen did not show any macroscale oxides present in the starting material, however under equilibrium conditions below $\sim$ 1400°C, less than 5 at% of oxygen could be in solution in Nb, therefore it may be expected that some oxide precipitates would form. APT tips were taken from the as-received Nb alloy to determine whether HfO_2 or other oxide particles/clusters were present. No clusters were found in the as-received Nb alloy, as shown in Figure 4.7, and the average oxygen content across the reconstructions was 2.53 $\pm$ 0.98 at%, as shown in table 4.2. APT on the as-received alloy is consistent with EPMA, showing that there is some oxygen present in the original alloy, however the smaller amount of oxygen present in APT suggests that the oxygen is not evenly distributed across the as-received alloy, this could further imply the presence of oxide precipitates in other regions. This could be studied further with TEM to see if oxides are present across a larger area of the Nb alloy.

To determine if the final heat treatment of the wire at 670°C produced oxide clusters in the Nb alloy, both EPMA and APT were carried out on the reacted alloy. EPMA mapping again showed the residual weak inverse segregation of Hf and Ta present, as shown in Figure 4.10, in the as-received Nb alloy, but no obvious Nb or O segregation could be seen on the macroscale. EPMA line scans produced an average oxygen concentration of 8.48 $\pm$ 1.43 at%, as shown in

table 4.3, higher than that seen in the as-received alloy. Although oxygen was present in the original Nb alloy, this increase in oxygen content does suggest some oxygen may have diffused in from the outer Cu/Sn region during the heat treatment process. APT on the reacted Nb alloy produced mixed results with regards to HfO_2 clusters, with 2 out of 5 reconstructions showing no HfO_2 clustering at all. The 3 reconstructions which did contain HfO_2 clusters showed their preferential alignment within specific planes, as shown by Figure 4.14. The planes of clusters may correspond to grain boundaries, where the diffusion of oxygen will be higher than that of the bulk, accelerating the nucleation of HfO_2 clusters at the boundaries. The average size of these clusters is 1.65 $\pm$ 0.06 nm and the average number density, taking into account the two reconstructions with zero clusters, is 1.66 $\pm$ 1.98 $\times$ 10^{23} m^{-3}. Evidence from the as-received and reacted Nb alloy shows that a substantial amount of oxygen was present in the original alloy, however the amount of oxygen increased upon formation of the final heat treated wire. It is therefore likely that the unintentional additional oxygen was a product of both the initial Nb alloy and the atmosphere under which the alloy was heat treated to produce the final wire. As discussed in chapter 3, Kirkendell markers have shown that Sn is the fastest diffusing species in forming binary Nb_3Sn, therefore during the heat treatment Sn and Cu diffuse into the original Nb alloy to form the final A15 phase. The A15 phase is formed in what was originally the Nb alloy, therefore it is important to understand the original concentrations of Ta, Hf and O present in the starting alloy.

4.11.2 Nb_3Sn

Once clusters were observed in the reacted Nb alloy, it was highly likely that clusters would also be present in the Nb_3Sn layer which is formed on the edge of the original Nb alloy. Before cluster analysis was conducted, careful consideration of the m/q spectrum of the Nb_3Sn region was conducted in section 4.3.3, which showed that there were some impurities present, with a small amount of Zr in both the Nb alloy and in the final Nb_3Sn region. Within the tips sampled there are particles which contain Nb-C-N only regions, as shown in figure 4.17, and although their exact composition is not previously discussed in the literature, $Nb(C_{0.3}N_{0.7})$ has been found to produce a T_c of 17.8 K [113], just below that expected of Nb_3Sn. As these particles are likely superconducting with a similar T_c to the Nb_3Sn, these will potentially be contributing to the interconnected superconducting path.

In a similar format to that used in chapter 3, the intra-grain and inter-grain properties of the Nb_3Sn layer and the individual segregation behaviour of each species are considered. The intra-grain regions of Nb_3Sn show distinct high and low Nb Nb_3Sn regions, however these are less pronounced in Nb content than that seen in the RRP® wire in chapter 3. Hf is highly reactive with O, therefore if there was residual oxygen present in the sample it may be expected that Hf would react with all the O available to form HfO_2 with no residual oxygen remaining. However, Hf ions can be detected from the Nb_3Sn layer which do not correspond with the location of the HfO_2 clusters, as shown in Figure 4.23. When the composition of the regions of low and high Nb Nb_3Sn are considered, the high Nb regions suggest an increased segregation of Hf and Cu, with Ta appearing the same (within error) in both the low and high Nb regions, as shown in table 4.6. Small quantities of Cu are present within both the low and high Nb regions, with distinguishable Cu^+ peaks present within the m/q spectrum. Slightly more Cu is present in the high Nb regions, 0.08 $\pm$ 0.06 at% compared to 0.03 $\pm$ 0.03 at% for the low Nb regions.

The grain boundaries in Nb_3Sn show a strong segregation of Cu, a depletion in Nb, a weak increase or no change in Sn, with a weak depletion or little change in Ta across the boundary, as shown in Figure 4.28. Figure 4.29 shows that the residual unoxidised Hf ions in the Nb_3Sn layer are not correlated with the grain boundaries, this suggests that any Hf which was present at

the grain boundaries has reacted with oxygen, forming HfO_2 clusters. Further evidence of this HfO_2 cluster formation at boundaries is supported by the low Hf and O concentrations at grain boundaries, as seen in table 4.7. Ta depletion across the boundary varies between boundaries, with one boundary showing an excess in Ta, however as Cu at the boundary increases there is a weak correlation of depletion in Ta. If any segregation of Ta is taking place it is very weak, far weaker than Nb, and often within error.

The majority of grain boundaries for the RIT samples had Γ_{Cu} values between 5 to 30 atoms/nm^2 as shown in Figure 4.32, which when the densest packed (001) layer is considered, this means an excess of 0.5 - 2.8 of the densest packed monolayers at the boundary. Two boundaries produced Γ_{Cu} values with unphysical fractional monolayers of 9 - 15 of the densest packed Nb_3Sn planes. These exceptional boundaries, with 30 at% and 45 at% Cu, evidence the presence of residual binary or ternary Cu phases.

The average composition of the Nb_3Sn layer lies within error of the ternary composition map expected for Ta doped Nb_3Sn by Flükiger *et al* [45], as shown in Figure 4.45. However, the ternary composition map does not consider the non-negligible amount of Cu or Hf which are present in the Nb_3Sn layer which may modify the expected phase composition. Furthermore, the composition map is based on micron scale measurements which used EPMA [109, 111, 117] and TEM EDX [91] to determine the limits of the A15 Nb-Sn-Ta composition map. This work has shown that within the microstructure of a Ta-Hf doped wire that there are substantial fluctuations in the A15 composition on the nanoscale.

4.11.3 HfO_2 Clustering

Within the Nb_3Sn layer of the RIT sample there is clear evidence of HfO_2 clustering, as shown in Figure 4.22, with an average diameter of 1.9 $\pm$ 0.3 nm & N_D of 1.93 $\pm$ 0.98 $\times$ 10^{23} m^{-3}. The size of these clusters are slightly smaller than those in the reacted Nb alloy in the centre of the sample which have a diameter of 1.65 $\pm$ 0.06 nm and N_D of 1.66 $\pm$ 1.98 $\times$ 10^{23} m^{-3}. The clusters are smaller than the optimum 6 - 8 nm in diameter required to maximise the pinning force, and when Nb and Sn ions are included the cluster diameter increases to within error of the 1.9 $\pm$ 0.3 nm calculated. As discussed in section 4.5.2, some HfO_2 clusters are associated with residual Cu, which is likely trapped from the higher solubility Cu in the precursor Nb_6Sn_5. This associated Cu has not been defined as a solute for the HfO_2 clusters, therefore any clusters which are attached to an isolated Cu region will be larger than that shown from the cluster calculations. The strain associated with each cluster may be expected to be slightly larger than the given cluster size, therefore producing a slightly larger effective pinning site. However, it is important to note that even smaller clusters have a significant effect on the overall pinning behaviour and J_c of the RIT wire. As can be seen from Figure 4.38, there are some planes of HfO_2 clusters which do not appear to be directly associated with grain boundaries in the Nb_3Sn. Based on the location of HfO_2 clusters in the reacted Nb alloy, it is possible that the planes seen in the Nb_3Sn are previous grain boundaries from the original Nb alloy prior to A15 formation. The location of the clusters is approximately split 80% intra-granularly and 20% inter-granularly. It would be expected that the clusters located within the grains would be acting as APCs in the traditional model postulated by Dew-Hughes [49]. However, the clusters which are located at grain boundaries and at dislocations are instead expected to modify the pinning environment in these regions to a combination of grain boundary and point pinning. Finally, the HfO_2 clusters have contributed to Zener pinning, with a reduction in Nb_3Sn grain size from $\sim$ 110 nm for the Nb-4Ta sample to the Nb-4Ta-1Hf sample with a Nb_3Sn grain size of 68 $\pm$ 25 nm [64].

The HfO_2 nanoparticles have increased the amount of surface pinning present in the sample via grain size reduction and produced additional point pinning which will all contribute to the high F_p measured.

4.11.4 Residual Cu Rich Phases

Further investigation into the two high Cu boundaries in the Nb_3Sn suggested that additional Nb-Sn-Cu or Cu-Sn phases were present within some of the Nb_3Sn layer. A Nb-Sn-Cu ternary phase diagram has been used to help understand whether the composition of the high Cu regions indicate the presence of alternative binary or ternary phases at these boundaries. The only Nb-Sn-Cu phase known to exist is nausite with a composition $Nb_{0.75}Cu_{0.25}Sn_2$ [211, 212, 220], however, multiple regions high in Cu appear to have a composition close to $Cu_3Sn_2Nb_2$, as shown in Figure 4.43, which has not been seen in previous literature. These regions are nanoscale and it is difficult to produce a precise composition due to potential counts from the external A15 matrix, however there is a indication of a ternary phase present. Two binary phases are expected to both be present when a composition lies on a tie line between two binary phases. However, some of the high Cu regions, although tending towards the Cu and Nb_3Sn tie lines appear to lie between Nb_3Sn, Cu and δ phases or Nb_3Sn, Cu and ϵ phases. δ has been seen to exist in contact with Nb_3Sn in RRP® wires on the micron scale (P.Lee, private communication, 7 Aug 2023) and ϵ has been seen in on the micron scale in Nb_3Sn wires after a final heat treatment of 665°C [98, 213]. It is therefore possible that these phases could be producing some of the high Cu regions within the the Nb_3Sn layer. No previous evidence of Cu-Sn phases has been seen on the nanoscale or at grain boundaries in Nb_3Sn, therefore the author can only speculate that these regions may be changing the pinning landscape at boundaries where they are present. These residual phases are discontinuous and therefore unlikely to be blocking the current path, but maybe, unintentionally, increasing the overall pinning force.

4.11.5 Nb_6Sn_5

Evidence of residual Nb_6Sn_5 both from APT and TEM experiments [64] at the outer edge of the Nb_3Sn layer, enables a greater understanding of how the Nb_6Sn_5 phase forms Nb_3Sn and how it can be better controlled during processing to maximise the formation of Nb_3Sn area. Much like Nb_3Sn, Nb_6Sn_5 has regions of differing composition which have been defined as low Cu, high Cu and very high Cu regions, as seen in Figure 4.50. Cu is known to have a

higher solubility in Nb_6Sn_5, of up to 5 at% [218, 219], compared to the negligible solubility of Cu in Nb_3Sn, as shown in chapter 3. As the Nb_6Sn_5 forms Nb_3Sn, during the final heat treatment, the Cu is pushed out of the grains and forced either into the grain boundaries or isolated islands within Nb_3Sn grains. The solubility of Ta in the Nb_6Sn_5 phase appears to be lower than that seen for Nb_3Sn, whereas the concentration of Hf appears marginally higher in the Nb_6Sn_5 regions, as seen in table 4.9. From the limited data collected sampling this phase, it is not possible to draw a conclusion as to whether the oxygen content varies between Nb_3Sn and Nb_6Sn_5 because 1 of the 3 reconstructions had an average oxygen content of 4.14 $\pm$ 0.92 at% compared to 0.19 $\pm$ 0.05 at% for the other two reconstructions.

The Nb_6Sn_5 in this sample shows equiaxed grains with a diameter $\leq$ 100 nm [64], which is much smaller than Nb_6Sn_5 grains commonly seen in PIT wires [221]. This reduced grain size is likely due to the presence of pre-existing HfO_2 clusters which are limiting the grain growth of the Nb_6Sn_5 by Zener pinning. The volume fraction of HfO_2 clusters is, within error, the same for Nb_6Sn_5 and Nb_3Sn, further suggesting that the HfO_2 clusters are formed prior to the Nb-Sn phases.

4.11.6 Linking Cluster Properties to Superconducting Properties

As discussed in section 4.10, a shift in the F_p curve was seen in the Nb-4Ta-1Hf sample compared to the Nb-4Ta sample, from surface pinning to a combination of surface and point pinning, with an F_p^{MAX} at $0.25H_{IRR}$ [58]. Using the Dew-Hughes models of point and surface pinning, a lower and upper estimate for the contribution of point pinning has been made. N_D and size of the HfO_2 clusters in the Nb_3Sn layer has been correlated with the value of A_{PD}/A_{GB} generated by Tarantini *et al* [58, 208] in table 4.11, showing that the flux lines tend towards the rigid condition.

4.12 Conclusions

This work is an extensive study using APT to probe the nanoscale structure of an APC RIT Nb_3Sn wire. This is the first in depth study which addresses the chemical segregation, size and distribution of APCs within Nb_3Sn wires. EPMA and APT have shown that significant oxygen was present in the starting Nb custom alloy and that HfO_2 clusters formed during the heat treatment. The presence of HfO_2 clusters in the reacted Nb alloy, seemingly along original grain boundaries, suggests HfO_2 clusters formed prior to the Nb-Sn phases and then were incorporated into Nb_6Sn_5 and Nb_3Sn layers. The pre-formed HfO_2 clusters likely acted as Zener pinning sites to pin the grain boundaries and reduce the grain size from 170 $\pm$ 80 nm in the original Nb-4Ta-1Hf alloy to $\sim$ 100 nm in Nb_6Sn_5, to the final Nb_3Sn grain size of 68 $\pm$ 25 nm [64].

The intra-grain and inter-grain regions in the A15 layer were probed with clear high and low Nb regions, and the presence of residual Cu-Sn or Nb-Sn-Cu phases at some grain boundaries. Residual Hf in solution was found at intra-grain regions within the A15 layer, suggesting higher densities of HfO_2 clusters could be produced with better control over oxygen concentration, and selective heat treatments. A direct relationship between HfO_2 cluster observations from APT has been made with the pinning force curve for the APC sample, enabling further comparisons for future APC wires. Further optimisation of APC wires is required to increase homogeneity, reduce cracks and increase the area of Nb_3Sn to produce a commercially viable wire.

Chapter 5

Conclusions

To develop Nb_3Sn wires which can be useful for future applications, such as particle accelerators or fusion reactors it is important to understand how the nanoscale structure of high J_c and neutron irradiated wires varies in order to understand the superconducting properties. This work has shown nanoscale analysis of the two different methods which produce point pinning in Nb_3Sn, irradiation and APCs, in two different wire types, RRP® and RIT wires. The RIT wire is a test wire, therefore the heat treatment and geometry of the wire were not carefully controlled during manufacture, whereas the commercial RRP® wire has a more predictably homogeneous A15 layer without the presence of residual Nb-Sn-Cu phases. The reaction pathway within commercial RRP® wires is well understood, with care taken to minimise nausite formation and form fine grain Nb_3Sn through a $NbSn_2$ to Nb_6Sn_5 pathway. However, it is unknown as to how the APCs may affect the formation of Nb-Sn phases prior to Nb_3Sn.

The final heat treatment of RRP® wires was 665°C for 48 hours compared to 670°C for 100 hours for the monofilament sample. Although similar final temperatures were used, the RIT sample contained a high fraction of Nb_6Sn_5 which had not transformed to Nb_3Sn. The temperature at which Nb_3Sn starts to form has been shown to vary substantially between wire types. RRP® wires form Nb_3Sn at temperatures as low as 510°C and RIT wires as high as 680°C for certain grain orientations. The smaller subelement size of the RRP® wires reduces the diffusion distance of the Sn [103], therefore residual Nb_6Sn_5 is more likely in RIT type wires.

5.0.1 Intra-grain Compositional Analysis

Both the RRP® and RIT samples had an inhomogeneous intra-grain composition with distinct regions of high and low Nb Nb_3Sn present. The difference in high and low Nb composition is most pronounced for the RRP® sample where both the low and high Nb regions lie out of the expected Nb_3Sn phase field, as seen in Figure 3.11. Across the two wires types a variety of different dopants were studied: Ti, Ta, Cu and Hf. Ti and Ta are commonly added to Nb_3Sn wires to increase B_{c2}, Cu is added to reduce the A15 temperature of formation and Hf was added to the RIT to react with oxygen to produce APCs. The relative segregation of each species in the low and high Nb_3Sn regions is displayed in table 5.1 with more Ti segregating to the low Nb, whereas Ta shows no obvious preference for low or high Nb regions. This segregation behaviour supports previous work using EXAFS which showed Ti to only segregate to the Nb lattice site and that Ta can segregate to both Nb and Sn lattice sites in Nb_3Sn [120].

Nb_3Sn regions	Ti	Ta	Cu	Hf
Low Nb	↑	-	↓	↓
High Nb	↓	-	↑	↑

Table 5.1: Relative comparison of segregating dopant species in low and high regions of Nb_3Sn

5.0.2 Inter-grain Compositional Analysis

Γ_i and grain boundary compositions were determined for each sample, with the as-received RRP® boundary types classified into: equilibrium, mixed and high Nb grain boundaries. Of the APT tips sampled, the irradiated RRP® wire only contained equilibrium and mixed grain boundary types, likely due to the large reduction in volume of high Nb regions in the irradiated sample. The grain boundaries from the RIT sample can be classed as equilibrium boundaries for Cu $\leq$ 5 at% and mixed boundaries for 5 $\geq$ Cu at% $\geq$ 10. As seen in previous literature [77, 154, 157], Cu strongly segregated to the grain boundaries in both wire types due to its limited solubility in the A15 phase and Nb is depleted at the grain boundaries. Segregation behaviour

of Ti, Ta, Cu and Hf is summarised in table 5.2. Ti segregated to the grain boundaries, which supports previous literature in bronze processed wires [154] and Ta showed a weak depletion at the grain boundaries, previously not seen in the literature. The RIT sample contained Hf, however any residual Hf was concentrated in the intra-grain regions, likely due to the formation of HfO_2 at grain boundaries, depleting residual Hf. Two grain boundaries in the RIT sample contained unphysically high Γ_i of Cu, which after further investigation were determined to be residual binary or ternary Cu phases within the Nb_3Sn.

Nb_3Sn regions	Ti	Ta	Cu	Hf
Grain boundaries	↑↑	↓	↑↑↑	↓

Table 5.2: Relative comparison of segregating dopant species at grain boundaries in Nb_3Sn

5.0.3 Overall Nb_3Sn composition

The volume fraction of high Nb decreased from 37.2% in the as-received RRP® sample to 14.8% in the irradiated RRP® sample with the grain boundary volume approximately constant in both wires. The reduction in high Nb, which is further from equilibrium, is likely due to radiation induced diffusion caused by the large concentration of vacancies produced during neutron irradiation. The volume fraction of high Nb in the RIT sample is 11.3%, much lower than the as-received RRP® sample, this is because the Nb_3Sn reaction is dominated by grain boundary diffusion [203], therefore a smaller grain size in the RIT sample, reduces the distance elements need to travel to reach equilibrium. The smaller grain size of the RIT sample (68 $\pm$ 25 nm [64] compared to 108 $\pm$ 48 nm [20] for the RRP® samples) is also evidenced by an increased grain boundary volume fraction of 15.4% compared to 9.7% and 11.8% for the RRP® samples.

5.0.4 Summary

APT has been used to conduct an in depth study into the nanoscale chemical segregation in a selection of Nb_3Sn wires. Apart from a TEM EDX profile which showed a fluctuation in Nb/Sn content through a Nb_3Sn grain [20], this is the first time the Nb_3Sn composition has been seen to have two distinct regions of high and low Nb which would be expected to affect the local B_{c2} and T_c values of the Nb_3Sn. Segregation preferences of Ti, Ta, Cu and Hf has been determined both in the low and high Nb regions, as well as at the grain boundaries. After neutron irradiation a reduction in the high Nb regions implies radiation induced diffusion has occurred.

Although previous work has briefly examined the presence of oxide nanoparticles in Nb_3Sn this work has determined the origin of the HfO_2 nanoparticles from oxygen in the original Nb alloy and shown that HfO_2 were also present in the residual Nb_6Sn_5, therefore HfO_2 was formed prior to the A15 phase and could act as Zener pinning sites to reduce the grain size. The number density, size distribution, shape and inter-/intra-grain location of the HfO_2 clusters have been determined in the RIT wire. The A15 phase in the RIT sample was found to be more complicated than first anticipated with residual intra-grain Hf, Nb-C-N particles and residual Cu binary or ternary phases.

This work has shown that APT is a valuable tool in understanding the nanoscale chemistry in Nb_3Sn wires which can help to design better wires with APCs to improve J_c performance and can help understand how irradiation affects the superconducting properties of Nb_3Sn.

Chapter 6

Future Work

6.1 RRP® and Neutron Irradiation

To further distinguish how the superconducting properties, e.g. T_c, B_{c2} are affected by the nanoscale structure of the wire a series of neutron irradiations should be performed on lengths of an RRP® wire, in a similar way to that studied by Baumgartner [151], with corresponding APT conducted at each fluence. It would be beneficial to conduct APT on fluences above the 2.82 $\times$ 10^{22} neutrons m^{-2} studied here to see whether the concentration of dislocations, orthogonal low angle boundaries and dislocation loops is correlated to the fluence of irradiation. To study the dislocation features at each fluence it would also be beneficial to have correlative TEM at each dose.

This work focuses only on RRP® wires and for future high J_c requirements, such as FCC, PIT is also a contender to produce the high J_c and large RRR required [84]. Properties for each type of wire can vary, therefore it may be beneficial to compare a set of comparable RRP® and PIT wires with the same doping e.g. 2 at% Ti, which have undergone the same heat treatment. Correlative APT across the highest Sn at% A15 regions of each wire may show significant differences in the nanoscale composition of the intra- and inter-grain regions which could then be linked to each sample's corresponding superconducting properties.

Both Ta and Ti are commonly used to increase B_{c2} therefore a direct comparison to an RRP® wire doped with the optimum 4 at% Ta (for high T_c and B_{c2} [45]) heat treated in an identical way to the as-received sample, would show clearly how Ta segregates in the Nb_3Sn. Chapter 4 does discuss how Ta segregates in a more complex system, however understanding Ta segregation in a commercial RRP® will help to understand Ta doping in more complex systems.

6.2 Optimising APC Wires

This work has shown that APT is a vital tool in understanding the nanoscale segregation in APC wires. The RIT test wire studied in this work produced an impressive J_c performance without careful control over the manufacturing procedure of the wire. A key reason why this wire had good superconducting properties was due to the amount of oxygen and the grain size of the original Nb alloy. The RIT wire should be replicated with careful control over the production of the custom Nb alloy, ideally producing a fine grain ($\leq$ 100 nm) Nb-4Ta-1Hf alloy with approximately 5 at% oxygen dissolved homogeneously through the alloy. The same heat treatments can be repeated but extensive SEM EDX should be conducted at several points during the heat treatments to determine the binary and ternary phases formed during reactions to produce the final A15 phase. Further work should then be conducted on the heat treatment of each wire, applying what has been learnt from C. Sanabria on Cu-Sn mixing in RRP® wires [98] to APT RIT type wires. A similar process can be applied to ZrO_2 APC wires to optimise the conditions required to increase J_c. Once multiple wires containing APCs, which appear to have homogeneous A15 layers, are produced, then APT can be used systematically to look at the size, location and distribution of APCs within the A15 wires. Taking APT samples from the inner to the outer edge of the A15 region would help to determine whether the distribution of APCs is indeed homogenous. APT is a very time intensive technique and not all samples extracted by FIB produce APT results, therefore APT should be used sparingly as a technique in combination with other micron scale techniques such as EPMA and SEM EDX to design the best wire for the FCC application.

Bibliography

1. Onnes, H. K. Further experiments with liquid helium. C. On the change of electric resistance of pure metals at very low temperatures etc. IV. The resistance of pure mercury at helium temperatures. **13** (1911).

2. Bardeen, J, Cooper, L. N. & Schrieffer, J. R. Theory of Superconductivity. *Physical Review* **108,** 1175–1204 (1957).

3. Maxwell, E. Isotope Effect in the Superconductivity of Mercury. *Physical Review* **78,** 477–477 (1950).

4. Reynolds, C. A., Serin, B, Wright, W. H. & Nesbitt, L. B. Superconductivity of Isotopes of Mercury. *Physical Review* **78,** 487–487 (1950).

5. Bednorz, J. G. & Müller, K. A. Possible high T_c superconductivity in the Ba- La- Cu- O system. *Zeitschrift für Physik B Condensed Matter* **64,** 189–193 (1986).

6. Drozdov, A., Eremets, M., Troyan, I., Ksenofontov, V. & Shylin, S. I. Conventional superconductivity at 203 kelvin at high pressures in the sulfur hydride system. *Nature* **525,** 73–76 (2015).

7. Hahn, S. *et al.* 45.5-tesla direct-current magnetic field generated with a high-temperature superconducting magnet. *Nature* **570,** 496–499 (2019).

8. Schoerling, D. *et al.* Considerations on a Cost Model for High-Field Dipole Arc Magnets for FCC. *IEEE Transactions on Applied Superconductivity* **27,** 1–5 (2017).

9. Keckert, S. *et al.* Critical fields of Nb_3Sn prepared for superconducting cavities. *Superconductor Science and Technology* **32,** 075004 (2019).

10. Matthias, B., Geballe, T., Geller, S & Corenzwit, E. Superconductivity of Nb_3Sn. *Physical Review* **95,** 1435 (1954).

11. Hardy, G. F. & Hulm, J. K. Superconducting silicides and germanides. *Physical Review* **89,** 884 (1953).

12. Hanak, J. J., Strater, K. & Cullen, G. W. Preparation and properties of vapor-deposited Niobium Stannide. *Radio Corporation of America Review (U.S.)* **25** (1964).

13. Cheng, D. *et al.* Limits of NbTi and Nb_3Sn, and development of W & R Bi-2212 High Field Accelerator Magnets. *IEEE Transactions On Applied Superconductivity* **17** (2007).

14. Apollinari, G., Brüning, O, Nakamoto, T. & Rossi, L. High-luminosity large hadron collider (HL-LHC). *arXiv preprint arXiv:1705.08830* (2017).

15. Bordini, B. *et al.* Nb_3Sn 11 T Dipole for the High Luminosity LHC (CERN), 223–258 (2019).

16. Todesco, E. *et al.* Progress on HL-LHC Nb_3Sn magnets. *IEEE Transactions on Applied Superconductivity* **28,** 1–9 (2018).

17. Ciazynski, D. Review of Nb_3Sn conductors for ITER. *Fusion Engineering and Design* **82,** 488–497 (2007).

18. ITER.org. *Facts and Figures* `https://www.iter.org/factsfigures`.

19. Tommasini, D. *et al.* The 16 T Dipole Development Program for FCC. *IEEE Transactions on Applied Superconductivity* **27,** 1–5 (2017).

20. Pfeiffer, S. *The microstructure of Nb_3Sn superconductors for the Future Circular Collider project and its impact on the performance* PhD thesis (Wien, 2020).

21. Stewart, G. R., Newkirk, L. R. & Valencia, F. A. Impurity stabilized A15 Nb_3Nb - a new superconductor. *Physical Review B* **21,** 5055–5064 (1980).

22. Dew-Hughes, D. Superconducting A-15 compounds: A review. *Cryogenics* **15,** 435–454 (1975).

23. Flükiger, R, Kupfer, H, Jorda, J & Muller, J. Effect of atomic ordering and composition changes on the electrical resistivity of Nb_3Al, Nb_3Sn, Nb_3Ge, Nb_3Ir, V_3Si and V_3Ga. *IEEE transactions on magnetics* **23,** 980–983 (1987).

24. Devantay, H, Jorda, J., Decroux, M, Muller, J & Flükiger, R. The physical and structural properties of superconducting A15-type Nb-Sn alloys. *Journal of Materials Science* **16,** 2145–2153 (1981).

25. Flükiger, R. Atomic ordering, phase stability and superconductivity in bulk and filamentary A15 type compounds (1987).

26. Godeke, A. A review of the properties of Nb_3Sn and their variation with A15 composition, morphology and strain state. *Superconductor Science and Technology* **19,** R68 (2006).

27. Godeke, A *et al.* The upper critical field of filamentary Nb_3Sn conductors. *Journal of applied physics* **97,** 093909 (2005).

28. Toffolon, C, Servant, C & Sundman, B. Thermodynamic assessment of the Nb-Sn system. *Journal of phase equilibria* **19,** 479 (1998).

29. Toffolon, C, Servant, C, Gachon, J. & Sundman, B. Reassessment of the Nb-Sn system. *Journal of phase equilibria* **23,** 134 (2002).

30. Mailfert, R, Batterman, B. & Hanak, J. Low temperature structural transformation in Nb_3Sn. *Physics Letters A* **24,** 315–316 (1967).

31. Chu, C. & Vieland, L. The superconducting transition temperature and its high-pressure behavior of tetragonal Nb_3Sn. *Journal of Low Temperature Physics* **17,** 25–29 (1974).

32. Vieland, L. The system $Nb_3Sn_{1-x}Sb_x$ and the density of states model for Nb_3Sn. *Journal of Physics and Chemistry of Solids* **31,** 1449–1454 (1970).

33. Vieland, L. & Wicklund, A. The martensitic transformation in the system $Nb_3Sn_{1-x}Al_x$. *Physics Letters A* **34,** 43–44 (1971).

34. Van Ooijen, D., Van Vucht, J. & Druyvesteyn, W. Superconductivity of $NbSn_2$. *Physics Letters* **3** (1962).

35. Enstrom, R. E. Superconducting properties of Nb_6Sn_5 and of multi-phase Nb-Sn Alloys. *Journal of Applied Physics* **37,** 4880–4882 (1966).

36. Charlesworth, J. The superconducting transition temperatures of Nb_6Sn_5 and $NbSn_2$. *Physics Letters* **21,** 501–502 (1966).

37. Elen, J., van Beijnen, C. & van der Klein, C. Multi-filament V_3Ga and Nb_3Sn superconductors produced by the ECN-technique. *IEEE Transactions on Magnetics* **13,** 470–473 (1977).

38. Junod, A, Jarlborg, T & Muller, J. Heat-capacity analysis of a large number of A 15-type compounds. *Physical Review B* **27,** 1568 (1983).

39. Guritanu, V *et al.* Specific heat of Nb_3Sn: The case for a second energy gap. *Physical Review B* **70,** 184526 (2004).

40. Arko, A. *et al.* de Haas-van Alphen effect in the high-T_c A15 Superconductors Nb_3Sn and V_3Si. *Physical Review Letters* **40,** 1590 (1978).

41. Orlando, T., McNiff Jr, E., Foner, S & Beasley, M. Critical fields, pauli para-magnetic limiting, and material parameters of Nb_3Sn and V_3Si. *Physical Review B* **19,** 4545 (1979).

42. Foner, S & McNiff Jr, E. Upper critical fields of cubic and tetragonal single crystal and polycrystalline Nb_3Sn in DC fields to 30 tesla. *Solid State Communications* **39,** 959–964 (1981).

43. Jewell, M., Godeke, A, Lee, P. & Larbalestier, D. The upper critical field of stoichiometric and off-stoichiometric bulk, binary Nb_3Sn. **711,** 474–484 (2004).

44. Charlesworth, J., Macphail, I & Madsen, P. Experimental work on the niobium-tin constitution diagram and related studies. *Journal of Materials Science* **5,** 580–603 (1970).

45. Flükiger, R, Uglietti, D., Senatore, C. & Buta, F. Microstructure, composition and critical current density of superconducting Nb_3Sn wires. *Cryogenics* **48,** 293–307 (2008).

46. Welch, D., Dienes, G., Lazareth Jr, O. & Hatcher, R. Defects and diffusion mechanisms in Nb_3Sn. *Journal of Physics and Chemistry of Solids* **45,** 1225–1242 (1984).

47. Besson, R., Guyot, S. & Legris, A. Atomic-scale study of diffusion in A15 Nb_3Sn. *Physical Review B* **75,** 054105 (2007).

48. Sitaraman, N. *et al.* Ab Initio Calculations on the Growth and Superconducting Properties of Nb_3Sn, 39–43 (2019).

49. Dew-Hughes, D. Flux pinning mechanisms in type II superconductors. *Philosophical Magazine* **30,** 293–305 (1974).

50. Scanlan, R., Fietz, W. & Koch, E. Flux pinning centers in superconducting Nb_3Sn. *Journal of Applied Physics* **46,** 2244–2249 (1975).

51. Shaw, B. J. Grain size and film thickness of Nb_3Sn formed by solid-state diffusion in the range 650–800° C. *Journal of Applied Physics* **47,** 2143–2145 (1976).

52. Schauer, W & Schelb, W. Improvement of Nb_3Sn high field critical current by a two-stage reaction. *IEEE Transactions on Magnetics* **17,** 374–377 (1981).

53. West, A. W. & Rawlings, R. D. A transmission electron microscopy investigation of filamentary superconducting composites. *Journal of Materials Science* **12,** 1862–1868 (1977).

54. Fischer, C. M. Investigation of the relationships between superconducting properties and Nb_3Sn reaction conditions in powder-in-tube Nb_3Sn conductors. *Master of Science Thesis, University of Wisconsin-Madison* (2002).

55. Lee, P. J. & Larbalestier, D. C. Niobium-titanium superconducting wires: Nanostructures by extrusion and wiredrawing. *Wire Journal International* **36,** 61–66 (2003).

56. Kramer, E. J. Scaling laws for flux pinning in hard superconductors. *Journal of Applied Physics* **44,** 1360–1370 (1973).

57. Godeke, A, ten Haken, B., ten Kate, H. H. J. & Larbalestier, D. A general scaling relation for the critical current density in Nb_3Sn. *Superconductor Science and Technology* **19,** R100 (2006).

58. Tarantini, C. *et al.* Ta, Ti and Hf effects on Nb_3Sn high-field performance: temperature-dependent dopant occupancy and failure of Kramer extrapolation. *Superconductor Science and Technology* **32,** 124003 (2019).

59. Summers, L., Guinan, M., Miller, J. & Hahn, P. A model for the prediction of Nb_3Sn critical current as a function of field, temperature, strain, and radiation damage. *IEEE Transactions on Magnetics* **27,** 2041–2044 (1991).

60. Godeke, A, Jewell, M., Golubov, A., Ten Haken, B & Larbalestier, D. Inconsistencies between extrapolated and actual critical fields in Nb_3Sn wires as demonstrated by direct measurements of H_{c2}, H* and T_c. *Superconductor Science and Technology* **16,** 1019 (2003).

61. Witcomb, M. J. & Dew-Hughes, D. Superconductivity of heat-treated Nb-65 at.% Ti alloy. *Journal of Materials Science* **8,** 1383–1400 (1973).

62. Dew-Hughes, D. Hard superconductors. *Materials Science and Engineering* **1,** 2–29 (1966).

63. Uglietti, D. *Electromechanical properties, microstructure and critical current of Nb_3Sn wires* PhD thesis (University of Geneva, 2006).

64. Balachandran, S. *et al.* Beneficial influence of Hf and Zr additions to Nb4at.% Ta on the vortex pinning of Nb_3Sn with and without an O source. *Superconductor Science and Technology* (2019).

65. Xu, X, Sumption, M, Peng, X & Collings, E. Refinement of Nb_3Sn grain size by the generation of ZrO_2 precipitates in Nb_3Sn wires. *Applied Physics Letters* **104,** 082602 (2014).

66. Baumgartner, T *et al.* Performance boost in industrial multifilamentary Nb_3Sn wires due to radiation induced pinning centers. *Scientific reports* **5,** 1–7 (2015).

67. Dietderich, D. & Godeke, A. Nb_3Sn research and development in the USA-Wires and cables. *Cryogenics* **48,** 331–340 (2008).

68. Xu, X, Majoros, M, Sumption, M. & Collings, E. Persistent-Current Magnetization of Nb_3Sn Strands: Influence of Applied Field Angle and Transport Current. *IEEE Transactions on Applied Superconductivity* **25,** 1–4 (2014).

69. Benz, M. Superconducting properties of diffusion processed niobium-tin tape. *IEEE Transactions on Magnetics* **2,** 760–764 (1966).

70. Kantrowitz, A. & Stekly, Z. A new principle for the construction of stabilized superconducting coils. *Applied Physics Letters* **6,** 56–57 (1965).

71. Swartz, P. & Bean, C. A model for magnetic instabilities in hard superconductors: The adiabatic critical state. *Journal of Applied Physics* **39,** 4991–4998 (1968).

72. Levi, F. Permanent magnets obtained by drawing compacts of parallel iron wires. *Journal of Applied Physics* **31,** 1469–1471 (1960).

73. Sanabria, C. *New Understanding of the Heat Treatment of Nb-Sn Superconducting Wires* PhD thesis (2017).

74. Ballarino, A. & Bottura, L. Targets for R&D on Nb_3Sn Conductor for High Energy Physics. *IEEE Transactions on Applied Superconductivity* **25,** 1–6 (2015).

75. Tachikawa, K. *Development of metallic superconductors in Japan* in *IEEE/CSC & ESAS European Superconductivity News Forum (ESNF)* (2011).

76. Suenaga, M, Horigami, O & Luhman, T. Effects of Sn concentration on the critical current density of Nb_3Sn formed at the Nb-(Cu-Sn alloy) interface. *Applied Physics Letters* **25,** 624–627 (1974).

77. Suenaga, M & Jansen, W. Chemical compositions at and near the grain boundaries in bronze-processed superconducting Nb_3Sn. *Applied physics letters* **43,** 791–793 (1983).

78. Smathers, D. & Larbalestier, D. The Layer Thickness Dependence of the Transition Temperature in Niobium-Tin. *Advances in Cryogenic Engineering Materials,* 415–424 (1982).

79. Howlett, B. *Method of fabricating a composite superconductor* US Patent 3,728,165. 1973.

80. Luhman, T., Pande, C. & Dew-Hughes, D. Flux pinning in bronze-processed Nb_3Sn. *Journal of Applied Physics* **47,** 1459–1463 (1976).

81. Miyatake, T. *et al.* Influence of wire parameters on critical current versus strain characteristics of bronze processed Nb_3Sn superconducting wires. *IEEE transactions on applied superconductivity* **22,** 4805005–4805005 (2011).

82. Zhang, P. *et al.* Fabrication and characterization of internal Sn and bronze-processed Nb_3Sn strands for ITER application. *Superconductor Science and Technology* **23,** 034013 (2010).

83. Mitchell, N, Breschi, M & Tronza, V. The use of Nb_3Sn in fusion: lessons learned from the ITER production including options for management of performance degradation. *Superconductor Science and Technology* **33,** 054007 (2020).

84. Ballarino, A. & Bottura, L. Targets for R&D on Nb_3Sn conductor for high energy physics. *IEEE transactions on applied superconductivity* **25,** 1–6 (2015).

85. Kunzler, J. Superconductivity in high magnetic fields at high current densities. *Reviews of Modern Physics* **33,** 501 (1961).

86. Elen, J, Van Beijnen, C & Van der Klein, C. Multifilament V_3Ga and Nb_3Sn superconductors produced by the ECN-technique. *IEEE Transactions on Magnetics* **13,** 470–473 (1977).

87. Van Beijnen, C & Elen, J. Multifilament Nb_3Sn superconductors produced by the ECN technique. *IEEE Transactions on Magnetics* **15,** 87–90 (1979).

88. Boutboul, T. *et al.* Heat treatment optimization studies on PIT Nb_3Sn strand for the NED project. *IEEE transactions on applied superconductivity* **19,** 2564–2567 (2009).

89. Xu, X. A review and prospects for Nb_3Sn superconductor development. *Superconductor Science and Technology* **30,** 093001 (2017).

90. Hashimoto, Y, Yoshizaki, K & Tanaka, M. Processing and properties of superconducting Nb_3Sn filamentary wires (1974).

91. Abächerli, V *et al.* The influence of Ti doping methods on the high field performance of (Nb, Ta, Ti)$_3$Sn multifilamentary wires using Osprey bronze. *IEEE transactions on applied superconductivity* **15,** 3482–3485 (2005).

92. Peng, X *et al.* Composition profiles and upper critical field measurement of internal-Sn and tube-type conductors. *IEEE transactions on applied superconductivity* **17,** 2668–2671 (2007).

93. Parrell, J., Field, M., Zhang, Y & Hong, S. Nb$_3$Sn conductor development for fusion and particle accelerator applications. **711,** 369–375 (2004).

94. JA, P., MB, F., Y, Z. & S, H. Advances in Nb$_3$Sn strand for fusion and particle accelerator applications. *IEEE Transactions on Applied Superconductivity* **15,** 1200–1204 (2005).

95. Field, M., Parrell, J., Zhang, Y. & Hong, S. *Critical current density in Nb$_3$Sn superconducting wire* US Patent 7,368,021. 2008.

96. Cooley, L., Ghosh, A., Dietderich, D. & Pong, I. Conductor specification and validation for high-luminosity LHC quadrupole magnets. *IEEE Transactions on Applied Superconductivity* **27,** 1–5 (2017).

97. Ferracin, P *et al.* Development of MQXF: The Nb$_3$Sn Low-β Quadrupole for the HiLumi LHC. *IEEE Transactions on applied superconductivity* **26,** 1–7 (2015).

98. Sanabria, C. *et al.* Controlling Cu-Sn mixing so as to enable higher critical current densities in RRP® Nb$_3$Sn wires. *Superconductor Science and Technology* **31,** 064001 (2018).

99. Fürtauer, S, Li, D, Cupid, D & Flandorfer, H. The Cu-Sn phase diagram, Part I: new experimental results. *Intermetallics* **34,** 142–147 (2013).

100. Naus, M. T., Lee, P. J. & Larbalestier, D. C. The influence of the starting Cu-Sn phase on the superconducting properties of subsequently reacted internal-Sn Nb$_3$Sn conductors. *IEEE transactions on applied superconductivity* **11,** 3569–3572 (2001).

101. Mattafirri, S., Barzi, E., Fineschi, F. & Rey, J.-M. Kinetics of phase growth in the Cu-Sn system and application to composite Nb_3Sn strands. *IEEE transactions on applied superconductivity* **13,** 3418–3421 (2003).

102. Scheuerlein, C *et al.* Coarse Nb_3Sn grain formation and phase evolution during the reaction of a high Sn content internal tin strand. *IEEE transactions on applied superconductivity* **21,** 2554–2558 (2010).

103. Scheuerlein, C *et al.* Phase transformations during the reaction heat treatment of Nb_3Sn superconductors. **234,** 022032 (2010).

104. Ghosh, A. *et al.* Effects of reaction temperature and alloying on performance of Restacked-Rod-Process Nb_3Sn. *IEEE transactions on applied superconductivity* **17,** 2623–2626 (2007).

105. Cogan, S, Holmes, D. & Rose, R. On the elimination of Kirkendall voids in superconducting composites. *Applied Physics Letters* **35,** 557–559 (1979).

106. McDonald, W. K. *Composite construction process and superconductor produced thereby* US Patent 4,262,412. 1981.

107. Sheth, M. *et al.* Study of filament cracking under uniaxial repeated loading for ITER TF strands. *IEEE transactions on applied superconductivity* **22,** 4802504–4802504 (2011).

108. Cody, G., Hanak, J., McConville, G. & Rosi, F. Superconducting properties of the (Nb, Ta, V)$_3$Sn system. *Radio Corporation of America Review (US)* **25** (1964).

109. Livingston, J. Effect of Ta additions to bronze-processed Nb_3Sn superconductors. *IEEE Transactions on Magnetics* **14,** 611–613 (1978).

110. Tachikawa, K, Asano, T & Takeuchi, T. High-field superconducting properties of the composite-processed Nb_3Sn with Nb-Ti alloy cores. *Applied Physics Letters* **39,** 766–768 (1981).

111. Suenaga, M, Welch, D., Sabatini, R., Kammerer, O. & Okuda, S. Superconducting critical temperatures, critical magnetic fields, lattice parameters, and chemical compositions of 'bulk' pure and alloyed Nb_3Sn produced by the bronze process. *Journal of applied physics* **59,** 840–853 (1986).

112. Suenaga, M. Optimization of Nb_3Sn. *IEEE Transactions on Magnetics* **21,** 1122–1128 (1985).

113. Sekine, H, Takeuchi, T & Tachikawa, K. Studies on the composite processed Nb-Hf/Cu-Sn-Ga high-field superconductors. *IEEE Transactions on Magnetics* **17,** 383–386 (1981).

114. Uglietti, D, Abächerli, V, Buta, F, Seeber, B & Flükiger, R. The effect of Ti addition on critical parameters and transport properties of quaternary (Nb, Ta, Ti)$_3$Sn wires. *Superconductor Science and Technology* **19,** 1185 (2006).

115. Abächerli, V *et al.* Investigation on the effect of Ta additions on J_c and n of (Nb,Ti)$_3$Sn bronze processed multifilamentary wires at high magnetic fields. *IEEE transactions on applied superconductivity* **17,** 2564–2567 (2007).

116. Flükiger, R *et al.* Optimization of Nb_3Sn and MgB_2 wires. *Superconductor Science and Technology* **21,** 054015 (2008).

117. Tafto, J, Suenaga, M & Welch, D. Crystal site determination of dilute alloying elements in polycrystalline Nb_3Sn superconductors using a transmission electron microscope. *Journal of applied physics* **55,** 4330–4333 (1984).

118. Tachikawa, K, Itoh, K, Kamata, K, Moriai, H & Tada, N. Improved multifilamentary Nb_3Sn conductors produced by the titanium-bronze process. *Journal of nuclear materials* **133,** 830–833 (1985).

119. Asano, T., Iijima, Y., Itoh, K. & Tachikawa, K. Effects of titanium addition to the niobium core on the composite-processed Nb_3Sn. *Transactions of the Japan institute of metals* **27,** 204–214 (1986).

120. Heald, S. M. *et al.* Evidence from EXAFS for Different Ta/Ti Site Occupancy in High Critical Current Density Nb_3Sn Superconductor Wires. *Scientific reports* **8,** 1–9 (2018).

121. Flükiger, R, Specking, W, Klemm, M & Gauss, S. Composite core Nb_3Sn wires: preparation and characterization. *IEEE transactions on magnetics* **25,** 2192–2199 (1989).

122. Dietderich, D. R. & Scanlan, R. M. Nb_3Sn artificial pinning microstructures. *IEEE transactions on applied superconductivity* **7,** 1201–1204 (1997).

123. Rodrigues, C. A. & Rodrigues Jr, D. Development and analysis of superconductors with projected nanostructured pinning centers. *Physica C: Superconductivity* **408,** 921–922 (2004).

124. Rodrigues, D, Da Silva, L., Rodrigues, C., Oliveira, N. & Bormio-Nunes, C. Optimization of Heat Treatment Profiles Applied to Nanometric-Scale Nb_3Sn Wires With Cu-Sn Artificial Pinning Centers. *IEEE transactions on applied superconductivity* **21,** 3150–3153 (2010).

125. Motowidlo, L. R., Lee, P. J. & Larbalestier, D. C. The Effect of Second Phase Additions on the Microstructure and Bulk Pinning Force in Nb_3Sn PIT Wire. *IEEE transactions on applied superconductivity* **19,** 2568–2572 (2009).

126. Martin, D. L. & Benz, M. G. *Method of making superconductors containing flux traps* US Patent 3,429,032. 1969.

127. Rumaner, L., Benz, M. & Hall, E. The role of oxygen and zirconium in the formation and growth of Nb_3Sn grains. *Metallurgical and Materials Transactions A* **25,** 213–219 (1994).

128. Rumaner, L. & Benz, M. Effect of oxygen and zirconium on the growth and superconducting properties of Nb_3Sn. *Metallurgical and Materials Transactions A* **25,** 203–212 (1994).

129. Zeitlin, B. A. *et al.* Results on mono element internal tin Nb_3Sn conductors (MEIT) with Nb7.5Ta and Nb (1Zr+ O_x) filaments. *IEEE transactions on applied superconductivity* **15,** 3393–3398 (2005).

130. Xu, X., Sumption, M. D. & Peng, X. Internally oxidized Nb_3Sn strands with fine grain size and high critical current density. *Advanced Materials* **27,** 1346–1350 (2015).

131. Motowidlo, L. R. *et al.* An intermetallic powder-in-tube approach to increased flux-pinning in Nb_3Sn by internal oxidation of Zr. *Superconductor Science and Technology* **31,** 014002 (2017).

132. Xu, X., Rochester, J., Peng, X., Sumption, M. & Tomsic, M. Ternary Nb_3Sn superconductors with artificial pinning centers and high upper critical fields. *Superconductor Science and Technology* **32,** 02LT01 (2019).

133. Buta, F *et al. Properties and microstructure of binary and ternary Nb_3Sn superconductors with internally oxidized ZrO_2 nanoparticles* in *Applied Supercond. Conf* (2018).

134. Xu, X., Peng, X., Rochester, J., Lee, J.-Y. & Sumption, M. High critical current density in internally-oxidized Nb_3Sn superconductors and its origin. *Scripta Materialia* **186,** 317–320 (2020).

135. Xu, X. *et al.* APC Nb_3Sn superconductors based on internal oxidation of Nb-Ta-Hf alloys. *Superconductor Science and Technology* **36,** 035012 (2023).

136. Bovone, G *et al.* Effects of the oxygen source configuration on the superconducting properties of internally-oxidized internal-Sn Nb_3Sn wires. *Superconductor Science and Technology* **36,** 095018 (2023).

137. Xu, X., Peng, X., Sumption, M. & Collings, E. Recent progress in application of internal oxidation technique in Nb_3Sn strands. *IEEE Transactions on Applied Superconductivity* **27,** 1–5 (2016).

138. Sborchia, C *et al.* Design and specifications of the ITER TF coils. *IEEE transactions on applied superconductivity* **18,** 463–466 (2008).

139. Fuger, R, Eisterer, M, Hengstberger, F & Weber, H. Influence of neutron irradiation on high temperature superconducting coated conductors. *Physica C: Superconductivity* **468,** 1647–1651 (2008).

140. Bett, R. The effects of neutron irradiation damage on the superconducting properties of Nb_3Sn. *Cryogenics* **14,** 361–366 (1974).

141. Soell, M, Bauer, H, Boening, K & Bett, R. Effect of low temperature neutron irradiation on superconducting properties of Nb_3Sn. *Physics Letters A* **51,** 83–84 (1975).

142. Brown, B., Blewitt, T., Scott, T. & Wozniak, D. Critical-current changes in neutron-irradiated Nb_3Sn as a function of irradiation temperature and initial metallurgy. *Journal of Applied Physics* **49,** 4144–4148 (1978).

143. Pande, C. Effect of nuclear irradiation on the superconducting transition temperatures of A15 materials. *Solid State Communications* **24,** 241–245 (1977).

144. Küpfer, H & Manuel, A. Summation and Saturation Behaviour of the Volume Pinning Force in Neutron Irradiated V_3Si. *Physica status solidi (a)* **54,** 153–165 (1979).

145. Holdway, P & Rawlings, R. Microstructure and radiation damage of commercially produced Nb_3Sn tapes. *Cryogenics* **24,** 137–142 (1984).

146. Hahn, P., Guinan, M., Summers, L., Okada, T & Smathers, D. Fusion neutron irradiation effects in commercial Nb_3Sn superconductors. *Journal of nuclear materials* **179,** 1127–1130 (1991).

147. Spina, T *et al.* Correlation Between the Number of Displacements Per Atom and T_c After High-Energy Irradiations of Nb_3Sn Wires for the HL-LHC. *IEEE Transactions on Applied Superconductivity* **26,** 1–5 (2016).

148. Haindl, S *et al.* Neutron irradiation effects on A15 multifilamentary wires. *IEEE transactions on applied superconductivity* **15,** 3414–3417 (2005).

149. Nishimura, A. *et al.* Neutron irradiation effects on superconducting wires and insulating materials. *Fusion engineering and design* **84,** 1425–1428 (2009).

150. Cullen, G. & Novak, R. Effect of Neutron-Induced Defects on the Current-Carrying Behavior of Vapor-Deposited Niobium Stannide. *Journal of Applied Physics* **37,** 3348–3352 (1966).

151. Baumgartner, T. *et al.* Effects of neutron irradiation on pinning force scaling in state-of-the-art Nb_3Sn wires. *Superconductor Science and Technology* **27,** 015005 (2013).

152. Wu, I. *et al.* The microstructure and critical current characteristic of a bronze-processed multifilamentary Nb_3Sn superconducting wire. *Journal of applied physics* **54,** 7139–7152 (1983).

153. Rose, J., Goringe, M., Smith, G. & Moore, A. Field ion microscopy and atom probe microanalysis of Nb_3Sn wires. *Le Journal de Physique Colloques* **47,** C2–281 (1986).

154. Sandim, M. *et al.* Grain boundary segregation in a bronze-route Nb_3Sn superconducting wire studied by atom probe tomography. *Superconductor Science and Technology* **26,** 055008 (2013).

155. Cantoni, M., Abächerli, V., Uglietti, D., Seeber, B. & Flükiger, R. Analytical TEM of Nb_3Sn multifilament superconductor wires. *Microscopy and Microanalysis* **14,** 1146–1147 (2008).

156. Lee, J. *et al.* Grain-boundary segregation behavior in Nb_3Sn coatings on Nb for superconducting radiofrequency cavity applications. *Acta Materialia* **188,** 155–165 (2020).

157. Santra, S *et al.* Insight into the effect of Ti-addition on diffusion-controlled growth and texture of Nb_3Sn intermetallic superconductor phase. *Materialia* **6,** 100276 (2019).

158. Xu, X, Sumption, M., Lee, J, Rochester, J & Peng, X. Persistent compositions of non-stoichiometric compounds with low bulk diffusivity: A theory and application to Nb_3Sn superconductors. *Journal of Alloys and Compounds* **845,** 156182 (2020).

159. Thompson, K *et al.* In situ site-specific specimen preparation for atom probe tomography. *Ultramicroscopy* **107,** 131–139 (2007).

160. Gault, B., Moody, M. P., Cairney, J. M. & Ringer, S. P. *Atom probe microscopy* (Springer Science & Business Media, 2012).

161. Gault, B. *et al.* Atom probe tomography. *Nature Reviews Methods Primers* **1,** 1–30 (2021).

162. Chang, A. S. & Lauhon, L. J. Atom probe tomography of nanoscale architectures in functional materials for electronic and photonic applications. *Current Opinion in Solid State and Materials Science* **22,** 171–187 (2018).

163. Cerezo, A, Godfrey, T., Sijbrandij, S., Smith, G. & Warren, P. Performance of an energy-compensated three-dimensional atom probe. *Review of Scientific Instruments* **69,** 49–58 (1998).

164. Gault, B. *et al.* Advances in the reconstruction of atom probe tomography data. *Ultramicroscopy* **111,** 448–457 (2011).

165. Bas, P, Bostel, A., Deconihout, B. & Blavette, D. A general protocol for the reconstruction of 3D atom probe data. *Applied Surface Science* **87,** 298–304 (1995).

166. Reddy, S. M. *et al.* Atom probe tomography: Development and application to the geosciences. *Geostandards and Geoanalytical Research* **44,** 5–50 (2020).

167. Gault, B., Danoix, F., Hoummada, K., Mangelinck, D. & Leitner, H. Impact of directional walk on atom probe microanalysis. *Ultramicroscopy* **113,** 182–191 (2012).

168. Gault, B *et al.* Influence of surface migration on the spatial resolution of pulsed laser atom probe tomography. *Journal of Applied physics* **108,** 044904 (2010).

169. Jenkins, B., Grovenor, C. & Moody, M. The Effect of Analysis Conditions on the Fidelity of Atom Probe Data of Zirconium Alloys. *Microscopy and Microanalysis* **27,** 2468–2470 (2021).

170. Haydock, R. & Kingham, D. R. Some predictions of a theory of post-ionization of field-evaporated ions. *Surface Science* **104,** 194–198 (1981).

171. Kingham, D. R. The post-ionization of field evaporated ions: A theoretical explanation of multiple charge states. *Surface Science* **116,** 273–301 (1982).

172. Maruyama, N., Smith, G. & Cerezo, A. Interaction of the solute niobium or molybdenum with grain boundaries in α-iron. *Materials Science and Engineering: A* **353,** 126–132 (2003).

173. Sauvage, X *et al.* Solid state amorphization in cold drawn Cu/Nb wires. *Acta Materialia* **49,** 389–394 (2001).

174. Gault, B. *et al.* Atom probe tomography and transmission electron microscopy characterisation of precipitation in an Al–Cu–Li–Mg–Ag alloy. *Ultramicroscopy* **111,** 683–689 (2011).

175. Saxey, D. Correlated ion analysis and the interpretation of atom probe mass spectra. *Ultramicroscopy* **111,** 473–479 (2011).

176. Cerezo, A, Godfrey, T. & Smith, G. Application of a position-sensitive detector to atom probe microanalysis. *Review of Scientific Instruments* **59,** 862–866 (1988).

177. Kolli, R. P. & Seidman, D. N. Co-precipitated and collocated carbides and Cu-rich precipitates in a Fe–Cu steel characterized by atom-probe tomography. *Microscopy and Microanalysis* **20,** 1727–1739 (2014).

178. Haley, D., Choi, P & Raabe, D. Guided mass spectrum labelling in atom probe tomography. *Ultramicroscopy* **159,** 338–345 (2015).

179. Oltman, E, Ulfig, R & Larson, D. Background removal methods applied to atom probe data. *Microscopy and Microanalysis* **15,** 256–257 (2009).

180. Krakauer, B. W. & Seidman, D. N. Absolute atomic-scale measurements of the Gibbsian interfacial excess of solute at internal interfaces. *Physical Review B* **48,** 6724 (1993).

181. Jenkins, B. *Improving the Safety and Reliability of Reactor Pressure Vessel Steels* PhD thesis (2019).

182. Oberdorfer, C., Eich, S. M. & Schmitz, G. A full-scale simulation approach for atom probe tomography. *Ultramicroscopy* **128,** 55–67 (2013).

183. Vaumousse, D, Cerezo, A & Warren, P. A procedure for quantification of precipitate microstructures from three-dimensional atom probe data. *Ultramicroscopy* **95,** 215–221 (2003).

184. Kolli, R. P. & Seidman, D. N. Comparison of compositional and morphological atom-probe tomography analyses for a multicomponent Fe-Cu steel. *Microscopy and Microanalysis* **13,** 272–284 (2007).

185. Morley, A, Sha, G, Hirosawa, S, Cerezo, A & Smith, G. Determining the composition of small features in atom probe: bcc Cu-rich precipitates in an Fe-rich matrix. *Ultramicroscopy* **109,** 535–540 (2009).

186. Hyde, J., Marquis, E., Wilford, K. & Williams, T. A sensitivity analysis of the maximum separation method for the characterisation of solute clusters. *Ultramicroscopy* **111,** 440–447 (2011).

187. Stephenson, L. T., Moody, M. P., Liddicoat, P. V. & Ringer, S. P. New techniques for the analysis of fine-scaled clustering phenomena within atom probe tomography (APT) data. *Microscopy and Microanalysis* **13,** 448–463 (2007).

188. Crow, J., Strongin, M., Thompson, R. & Kammerer, O. The superconducting transition temperatures of disordered Nb, W, and Mo films. *Physics Letters A* **30,** 161–162 (1969).

189. Wheatley, L. E. *et al.* Understanding the nanoscale chemistry of as-received and fast neutron irradiated Nb_3Sn RRP® wires using Atom Probe Tomography. *Superconductor Science and Technology* **36,** 085006 (2023).

190. Karkin, A., Arkhipov, V., Goshchitskii, B., Romanov, E. & Sidorov, S. Radiation effects in the superconductor Nb_3Sn. *Physica status solidi (a)* **38,** 433–438 (1976).

191. Baumgartner, T. *Effects of fast neutron irradiation on critical currents and intrinsic properties of state-of-the-art Nb_3Sn wires* PhD thesis (2013).

192. Spina, T., Ballarino, A., Bottura, L., Scheuerlein, C. & Flükiger, R. Artificial pinning in Nb_3Sn wires. *IEEE Transactions on Applied Superconductivity* **27,** 1–5 (2017).

193. Cooley, L. D., Fischer, C. M., Lee, P. J. & Larbalestier, D. C. Simulations of the effects of tin composition gradients on the superconducting properties of Nb_3Sn conductors. *Journal of applied physics* **96,** 2122–2130 (2004).

194. Uglietti, D, Seeber, B, Abächerli, V, Cantoni, M & Flükiger, R. Strain and Field Scaling Laws for Internal Sn and Bronze Route Nb_3Sn Wires up to 21T. **824,** 528–535 (2006).

195. Helfand, E & Werthamer, N. Temperature and purity dependence of the superconducting critical field, H_{c2}. *Physical Review Letters* **13,** 686 (1964).

196. Pfeiffer, S. *et al.* Analysis of inhomogeneities in Nb_3Sn wires by combined SEM and SHPM and their impact on J_c and T_c. *Superconductor Science and Technology* **36,** 045008 (2023).

197. Takeuchi, T, Asano, T, Iijima, Y & Tachikawa, K. Effects of the IVa element addition on the composite-processed superconducting Nb_3Sn. *Cryogenics* **21,** 585–590 (1981).

198. Pande, C. Transmission electron microscopy of radiation damage in Nb_3Sn. *Physica status solidi (a)* **52,** 687–696 (1979).

199. Chen, D. *et al.* Formation of Ni-Si clusters and their relationship with dislocation loops in irradiated stainless steels. *Journal of Nuclear Materials* **578,** 154366 (2023).

200. Eriksson, J, Sundell, G, Tejland, P, Andrén, H.-O. & Thuvander, M. An atom probe tomography study of the chemistry of radiation-induced dislocation loops in Zircaloy-2 exposed to boiling water reactor operation. *Journal of Nuclear Materials* **550,** 152923 (2021).

201. Jenkins, M., Roller, G, Katerbau, K.-H. & Wilkens, M. TEM studies of displacement cascades in Nb_3Sn. *Journal of Nuclear Materials* **108,** 603–613 (1982).

202. Kumar, A. & Paul, A. Interdiffusion and growth of the superconductor Nb_3Sn in Nb/Cu (Sn) diffusion couples. *Journal of electronic materials* **38,** 700–705 (2009).

203. Oh, S.-H. *et al.* Diffusion in A15 Nb_3Sn: An atomistic study. *Acta Materialia* **234,** 118050 (2022).

204. Fähnle, M. The influence of fast neutron irradiation on the critical current densities in Nb_3Sn. *Physica status solidi (b)* **84,** 245–251 (1977).

205. Pande, C. Direct observation of defects in A15 compounds produced by fast neutron irradiation, 349–353 (1980).

206. Li, Y. & Gao, Y. GLAG theory for superconducting property variations with A15 composition in Nb_3Sn wires. *Scientific reports* **7,** 1133 (2017).

207. Kornilov, A., Ushakova, I., Huber Jr, E. & Holley Jr, C. The enthalpy of formation of hafnium dioxide. *The Journal of Chemical Thermodynamics* **7,** 21–26 (1975).

208. Tarantini, C. *et al.* Origin of the enhanced Nb_3Sn performance by combined Hf and Ta doping. *Scientific reports* **11,** 17845 (2021).

209. Okamoto, H., Massalski, T., *et al.* Binary alloy phase diagrams. *ASM International, Materials Park, OH, USA* **12** (1990).

210. London, A. J. Quantifying uncertainty from mass-peak overlaps in atom probe microscopy. *Microscopy and Microanalysis* **25,** 378–388 (2019).

211. Naus, M. T. *Optimization of internal-Sn Nb_3Sn composites* (University of Wisconsin–Madison, 2002).

212. Pong, I., Oberli, L.-R., Bottura, L. & Scheuerlein, C. Longitudinal and Transverse Cross-Sectional Microstructure and Critical Current Density in Nb_3Sn Superconductors. *IEEE transactions on applied superconductivity* **21,** 2537–2540 (2011).

213. Pong, I., Oberli, L.-R. & Bottura, L. Cu diffusion in Nb_3Sn internal tin superconductors during heat treatment. *Superconductor Science and Technology* **26,** 105002 (2013).

214. Smith, J., Carlson, O. & De Avillez, R. The niobium-carbon system. *Journal of Nuclear Materials* **148,** 1–16 (1987).

215. Mayr, W *et al.* Nitridation of Ti/Nb alloys and solid-state properties of δ-(Ti, Nb) N. *Journal of alloys and compounds* **262,** 521–528 (1997).

216. Dhakal, P. Nitrogen doping and infusion in SRF cavities: A review. *Physics Open* **5,** 100034 (2020).

217. Matthias, B. Transition temperatures of superconductors. *Physical Review* **92,** 874 (1953).

218. Neijmeijer, W. L. & Kolster, B. H. Microstructure and Kinetics of the Formation of Nb_3Sn From Reaction Between Nb_6Sn_5 and Nb. *International Journal of Materials Research* **81,** 314–321 (1990).

219. Segal, C., Tarantini, C., Lee, P. J. & Larbalestier, D. C. Improvement of small to large grain A15 ratio in Nb_3Sn PIT wires by inverted multistage heat treatments. **279,** 012019 (2017).

220. Lachmann, J., Kriegel, M. J., Leineweber, A., Shang, S.-L. & Liu, Z.-K. Thermodynamic re-modelling of the Cu-Nb-Sn system: Integrating the nausite phase. *Calphad* **77,** 102409 (2022).

221. Segal, C. *et al.* Evaluation of critical current density and residual resistance ratio limits in powder in tube Nb_3Sn conductors. *Superconductor Science and Technology* **29,** 085003 (2016).